



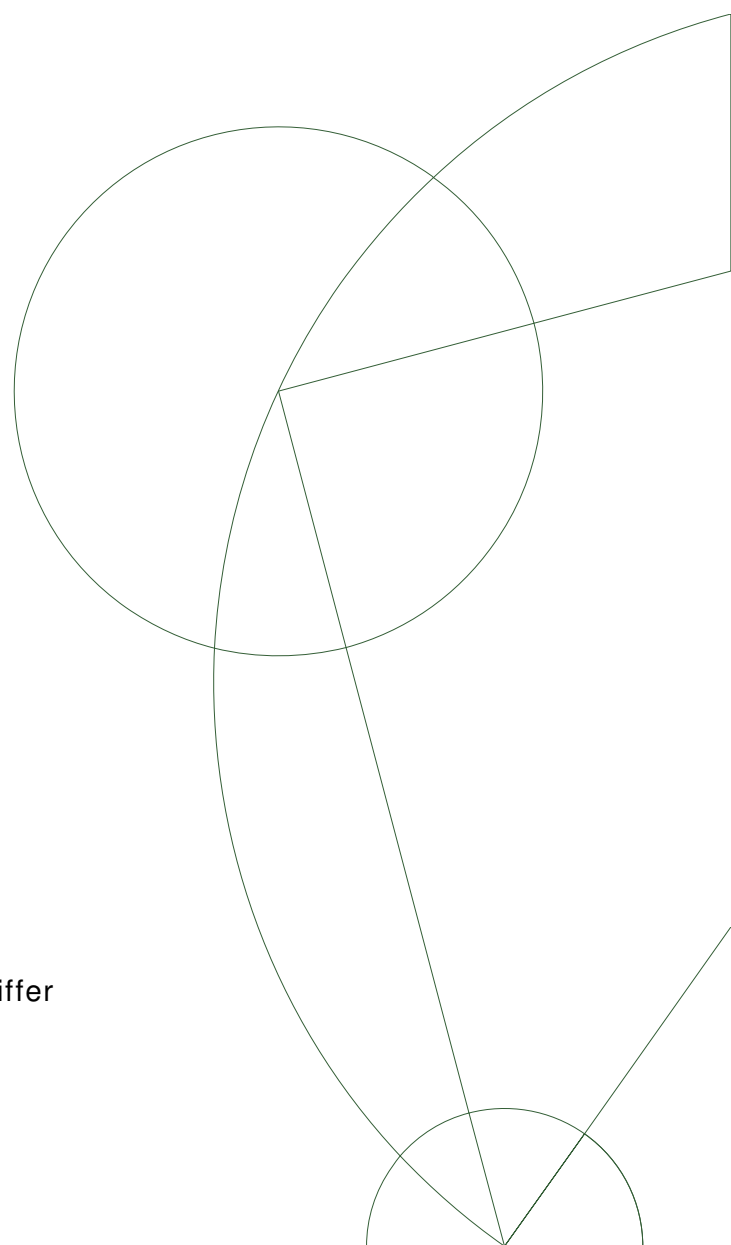
PhD thesis

Torben Haugaard Jensen

Refraction and scattering based x-ray imaging

Supervisors: Robert Feidenhans'l and Franz Pfeiffer

October, 2010



Refraction and Scattering based x-ray imaging

Submitted to:
The Graduate School of Science
Faculty of Science
Niels Bohr Institute
University of Copenhagen
Denmark

For the PhD degree

by

Torben Haugaard Jensen
Niels Bohr Institute
University of Copenhagen
Universitetsparken 5
2100 Copenhagen
Denmark

October 2010

Abstract

A number of novel refraction and scattering based x-ray imaging contrast mechanisms and their applications are presented in this thesis. The presentation is based on six original papers prepared during the PhD.

The methods include grating based x-ray phase-contrast computed tomography (PCT). We demonstrate how PCT can be used to identify metastatic deposits in human lymph nodes and thus can be used for diagnosis and staging of breast cancer. We also demonstrate food industrial applications of PCT using porcine fat and rind. Important for both these results is that grating based PCT works well with a standard x-ray tube source. The results can thus achieve widespread application.

The method of directional x-ray dark-field imaging is also presented. The method provides nano- and micro-textural information and can be used to probe e.g. the orientation of fibers in a sample. These results were also obtained with a standard x-ray tube source.

Finally high-resolution small-angle x-ray scattering computed tomography (SAXS-CT) is presented. SAXS-CT is used for nondestructive imaging of molecular parameters of neuronal myelin sheaths in a brain. These parameters are important for the understanding of a number of neurodegenerative diseases. SAXS-CT is also used for imaging of both functional areas in the brain as well as brain tumor morphology.

Copies of the six original papers are attached at the end of the thesis.

Dansk resumé

I denne afhandling præsenteres en række nye brydnings- og spredningsbaserede røntgenbilledkontrastmekanismer og deres anvendelser. Præsentationen er baseret på seks originalartikler udarbejdet i løbet af ph.d.-studiet.

Metoderne inkluderer gitterbaseret røntgen fase-kontrast tomografi (PCT). Vi demonstrerer, hvordan PCT kan bruges til at identificere metastaser i humane lymfeknuder, og dermed kan bruges til diagnosticering og stadiebestemmelse af brystkræft. Vi præsenterer også en anvendelse af PCT indenfor fødevareindustrien. Vi bruger PCT til visualisering og analyse af svinefedt og svær. Vigtigt for begge disse resultater er det, at gitterbaseret PCT kan udføres med et almindeligt røntgenrør. Resultaterne, som er opnået med phase-contrast tomography kan således opnå udbredt anvendelse.

Metoden ”directional x-ray dark-field imaging” (DDFI) bliver også præsenteret og demonstreret i afhandlingen. Metoden kan bruges til at bestemme nano- og mikro-teksturen i en prøve. Dette kan bruges til eksempelvis at bestemme den lokale orientering af fibre i fiberforstærkede materialer. Disse resultater er også opnået med et almindeligt røntgenrør.

Endelig bliver højopløsnings småvinkel røntgensprednings tomografi (SAXS-CT) præsenteret. SAXS-CT bruges til ikke-invasiv bestemmelse af den rummelige variation af de molekulære parametre for nervecellers myelinskeder i en hjerne. Disse parametre er vigtige for forståelsen af en række neurodegenerative sygdomme, som eksempelvis multipel sklerose og Alzheimers. Vi præsenterer også, hvordan SAXS-CT bruges til visualisering af både funktionelle områder i hjernen, samt til at studere morfologien af hjernesvulster.

Til sidst i afhandling er vedhæftet en kopi af de seks originalartikler.

Publications on which this thesis is based

Publication I

T.H. Jensen, M. Bech, T. Binderup, A. Böttiger, C. David, T. Weitkamp, I. Zanette, E. Reznikova, J. Mohr, F. Rank, R. Feidenhans'l, A. Kjær, L. Højgaard and F. Pfeiffer

Imaging of Metastatic Lymph Nodes by X-ray Phase Contrast Tomography
Submitted to Radiology

Publication II

T.H. Jensen, A. Böttiger, M. Bech, I. Zanette, T. Weitkamp, S. Rutishauser, C. David, E. Reznikova, J. Mohr, L. Bager Christensen, E. Olsen, R. Feidenhans'l, and F. Pfeiffer

X-ray phase-contrast tomography of porcine fat and rind
Submitted to Meat Science

Publication III

T.H. Jensen, M. Bech, O. Bunk, T. Donath, C. David, R. Feidenhans'l and F. Pfeiffer

Directional x-ray dark-field imaging
Physics in Medicine and Biology 55 (2010) 3317-3323.

Publication IV

T.H. Jensen, M. Bech, I. Zanette, T. Weitkamp, C. David, H. Deyhle, S. Rutishauser, E. Reznikova, J. Mohr, R. Feidenhans'l and F. Pfeiffer

Directional x-ray dark-field imaging of strongly ordered systems
Submitted to Physical Review B

Publication V

T.H. Jensen, M. Bech, O. Bunk, M. Thomsen, A. Menzel, A. Bouchet, G. Le Duc, R. Feidenhans'l and F. Pfeiffer

Brain tumor imaging using small-angle x-ray scattering tomography
Submitted to Physics in Medicine and Biology

Publication VI

T.H. Jensen, M. Bech, O. Bunk, A. Menzel, A. Bouchet, G. Le Duc, R. Feidenhans'l and F. Pfeiffer

Molecular x-ray computed tomography of myelin in a brain
Submitted to *Nature Communications*

Other co-authored publications

Publication VII

O. Bunk, M. Bech, **T.H. Jensen**, R. Feidenhans'l, T. Binderup, A. Menzel and F. Pfeiffer

Multimodal x-ray scatter imaging

New Journal of Physics 11 (2009) 123016.

Publication VIII

M. Bech, **T.H. Jensen**, O. Bunk, T. Donath, C. David, T. Weitkamp, G. Le Duc, A. Bravin, P. Cloetens and F. Pfeiffer

Advanced Contrast Modalities for X-ray Radiology: Phase-Contrast and Dark-Field Imaging using a Grating Interferometer

Zeitschrift für medizinische Physik 20, 1 (2010) 7–16.

Publication IX

M. Bech, **T.H. Jensen**, R. Feidenhans'l, O. Bunk, C. David and F. Pfeiffer

Soft-Tissue Phase-Contrast Tomography with X-Ray Tube Sources

Physics in Medicine and Biology 54 (2009) 2747–2753.

Acknowledgements

First of all I would like to thank my two supervisors Robert Feidenhans'l and Franz Pfeiffer for their enthusiasm, commitment and inspiration. Thanks also for allowing me to spend three years working on a range of fascinating projects. It has been a privilege and a pleasure to work with you.

A special thanks to Martin Bech for introducing me to the field, and for the many shared valuable discussion, and experiments. Thanks also for the good times and for providing excellent company.

This thesis has been possible through a scholarship from the Niels Bohr Institute. Many of the experiments could not have been conducted without the financial support from DanScatt.

Nowadays research is really a team effort. A lot of people thus took part in the experiments on which this thesis is based on. It has been a privilege to work with such a wide range of experts. Thanks to all of you. Without these collaborators I would never have come this far. Now for a long list of people I feel indebted to.

For the production of gratings for a number of experiments I owe great thanks for the help and support from the group of Christian David at the PSI, including Christian Grünzweig and Simon Rutishauser. Also thanks to the group of Jürgen Mohr at KIT, including Elena Reznikova.

To perform interesting experiments one needs relevant samples to study. I would like to express a special thanks to a fruitful collaboration with Tina Binderup, Andreas Kjær and Liselotte Højgaard from the Faculty of Health Sciences and Rigshospitalet. After several tries we did manage to succeed. Thanks for your sustained effort and tireless work. Also thanks to Hans Deyhle from Unibas and PSI for on several occasions having provided teeth samples. Thanks to Géraldine Le Duc and Audrey Bouchet from ESRF for providing brain samples. Thanks to Lars Bager Christensen and co-workers from DMRI/TI for providing a range of meat and fat samples and introducing me to the science of meat.

Not all experiments produce publishable results. That does not mean the experiments or sample preparation require less work. On that account I owe thanks to Rie Hansen and Anne-Marie Heegaard of FARMA for providing bone samples. Thanks to Carole Poitry-Yamate of EPFL for providing the most beautiful set of rat brain slices I have ever seen. Thanks also to Ron Ruth and the people at Lyncean Tech. Inc. for inviting us to work with their exciting new Compact Light Source. The John and Birthe Meyer Foundation is greatly acknowledged for granting funds to establish a project on phase-contrast imaging at the Compact Light Source.

Thanks also to the tireless local contacts for support and discussions.

Thanks to Oliver Bunk and Andreas Menzel and the rest of the people at the PSI. Thanks to Irene Zanette and Timm Weitkamp at the ESRF.

I appreciate the work by a number of students and the many interesting discussions that ensued. It has been a pleasure, sometimes also a challenge. Thanks to Arvid Böttiger, Maria Thomsen, Gregoire Dougniaux, Mikkel Schou Nielsen, Signe Dam, Christine Hartmann and Tine Straasø.

During my PhD I had the pleasure of a stay at the PSI in Switzerland. I would like to thank all of the people who helped me during my stay. A special thanks to Franz, Ebru, Oliver and Carola for taking me in, and out when I was away from home. A special thanks to Oliver Bunk for all of the help and support - working with you has been an inspiration. It was a pleasure to get to know, work with and learn from a number of people. So thanks to Christian David, Tilman Donath, Martin Dierolf, Edith Perret, Andreas Menzel, Cameron Kewish, Pierre Thibault and more.

At the NBI I have now spend several years in the same group. We were a whole group of people that have shared many great moments together. Thanks to Simon Mariager, Andreas 'AI' Kring, Martin Bech, Henrik Lemke, Kristoffer 'Kreuff' Haldrup, Anette Vickory, Søren Kynde, Louise Sperling, Søren Lodberg, Morten Christensen, Thomas Nørskov Nielsen and all the rest. Now I will as the last person of this group move on and leave it up to a new and younger crowd to continue the work.

Thanks also to Jens Als-Nielsen for many interesting discussions. I also want to thank Keld Theodor for the support and the pleasure of having worked with him for several years. Thanks also to Bente Juhl Andersen, Hanne Tulinius and Jannis Bouchikas for help along the way.

Finally I owe a great thanks to my wife Signe, my family and friends. For listening to me talking on and on about x-rays and our latest and craziest ideas. For sharing the joy, excitements and the ups and downs. Your support has been indispensable.

Also a thought to Axel, whom I know would have been as proud as anyone on seeing this final product.



Torben H. Jensen



Copenhagen, October 2010

Contents

1	Introduction	1
1.1	General motivation	1
1.2	Outline	2
1.3	Review of phase-contrast imaging methods	3
2	Grating interferometer	7
2.1	Theory	7
2.1.1	Refractive index	7
2.1.2	Grating interferometer	10
2.2	Experimental set-up	16
2.2.1	The grating interferometer in the laboratory	17
2.2.2	The grating interferometer at the synchrotron	22
3	Phase-contrast tomography results	25
3.1	Theory	25
3.2	Introduction to Paper I and Paper II	29
3.2.1	Introduction to Paper I	30
3.2.2	Introduction to Paper II	32
3.3	Outlook and applications	35
3.3.1	Dose considerations	36
4	Directional x-ray dark-field imaging	39
4.1	Theory	39
4.2	Introduction to Paper III and Paper IV	49
4.2.1	Introduction to Paper III	50
4.2.2	Introduction to Paper IV	51
4.3	DDFI vs SAXS mapping	54
4.4	Outlook and applications	63
5	Small-angle x-ray scattering tomography	67
5.1	Theory	67

5.2	Introduction to Paper V and Paper VI	72
5.2.1	Introduction to Paper V	73
5.2.2	Introduction to Paper VI	78
5.3	Outlook and applications	81
6	Conclusion	85
6.1	Outlook	86
	Bibliography	91
A	Matlab script for directional dark-field imaging	101
B	Publications	105
	Publication I	107
	Publication II	119
	Publication III	133
	Publication IV	145
	Publication V	155
	Publication VI	163

Chapter 1

Introduction

The purpose of this thesis is to describe a number of novel refraction and scattering based x-ray imaging contrast mechanisms and their applications. The reader is assumed to have a basic knowledge of x-ray physics, though the most important theoretical background is included. The thesis is written as a synopsis, thus primarily working as an introduction to and presentation of the six attached papers.

This first chapter will provide a brief motivation for the need for new x-ray imaging methods, followed by an outline of the following chapters. In the end we will provide a brief introduction to a number of existing x-ray phase-contrast imaging methods.

1.1 General motivation

X-ray imaging has been widely used since the discovery of x-rays in 1895 (Röntgen 1895). The imaging technique has been used in hospitals for diagnostics. This includes 2D radiographic images and since the 1970s also 3D tomographic images (Hounsfield 1973, Cormack 1963). Besides hospitals x-ray imaging has been widely applied in the industry for non-destructive inspection and testing and for a number of specialized research purposes.

The most widely used x-ray imaging technique is based on the absorption of the x-rays. This was the imaging principles presented by W.C. Röntgen in 1895. Sometimes the contrast available in absorption images is not sufficient for the intended purpose. This lack of contrast is often an issue when imaging soft tissue, where the variations in absorption are minute. Imaging of these subtle differences can be necessary for diagnostic purposes. Another issue is the standard x-ray absorption images lack of sensitive to specific properties one would like to image. This could include textural or nanostructural infor-

mation, which can be of relevance when studying the integrity and function of tissue or materials.

A number of supplementary imaging methods have been developed which address some of these issues. For soft tissue imaging Magnetic Resonance Imaging (MRI) and ultrasound are two examples. The aim of this thesis is to present a number of novel refraction and scattering based x-ray imaging methods which addresses these issues as well as a number of novel applications for these methods. Some of the methods are aimed at biomedical imaging, and some are more focused on industrial applications. Some of the methods have potential for widespread use in hospitals or in the industry and some have their main application within scientific research. The developed contrast mechanisms all provide new possibilities.

1.2 Outline

The thesis is outlined as follows.

In this chapter we introduce, motivate and outline the thesis. We also present a number of existing refraction and scattering based x-ray imaging methods.

In Chapter 2 we introduce the x-ray grating interferometric method. The chapter provides the background for the experiments and methods presented in Chapter 3 and Chapter 4 and Papers I-IV. In Chapter 2 we explain how phase-contrast imaging can provide contrast superior to standard absorption-contrast imaging. We also present the three basic radiographic contrasts mechanism available with a grating interferometer: absorption-contrast, phase-contrast and dark-field contrast.

Chapter 3 introduces phase-contrast tomography and works as an introduction to Paper I and Paper II. These papers demonstrate two applications of the phase-contrast tomographic method. Paper I is related to the diagnosis of cancer in human lymph nodes from breast cancer patients. Paper II investigates the increased contrast attainable with phase-contrast tomographic imaging of porcine fat.

Chapter 4 presents the method of directional x-ray dark-field imaging and works as an introduction to Paper III and Paper IV. The method provides textural information about structures smaller than the actual image resolution. Paper III and Paper IV originally introduced the method and are presented in this chapter. The chapter further includes a detailed comparison between the grating based directional x-ray dark-field imaging and results obtained using small-angle x-ray scattering mapping. The comparison further supports the claims of directional x-ray dark-field imaging.

In Chapter 5 we present the method of small-angle x-ray scattering computed tomography (SAXS-CT). This chapter serves as an introduction to Paper V and Paper VI. The two papers demonstrated for the first time high resolution SAXS-CT of soft tissue, where the full differential scattering cross section is reconstructed volume resolved inside an extended sample.

Chapters 3-5 are based on six papers in total. The papers are referred to by roman numerals as Paper I-VI and are included in their full length in Appendix B. A list of the papers appear on page vi. Paper III has already been published, while the remaining five have been submitted for publication. The publications contain most of the work presented in this thesis, only section 4.3 has not yet been prepared for publication.

1.3 Review of phase-contrast imaging methods

In the following we will shortly review a number of important refraction and scattering based x-ray imaging methods. The methods can be grouped into four categories: (1) Propagation Based Imaging (PBI), (2) Analyzer Based Imaging (ABI), (3) Crystal interferometric methods and (4) Grating Based Imaging (GBI). In these few pages we can not provide a full review of each of the methods, but will shortly present each of them. Investigations of the advantages and drawbacks of the different methods are still being conducted as the methods are being developed. We will shortly discuss some of the benefits and limitations of the different methods.

Propagation Based Imaging

In propagation based imaging (PBI) no optical elements are needed. The method is based on fresnel diffraction. By increasing the distance between the sample and the detector one lets the x-rays propagate to see the effects of refraction from the sample. A sketch of a PBI set-up is shown in Figure 1.1a. The method measures the the laplacian of the phase (Cloetens et al. 1997). The first radiographic images made using this method were presented in the 1990's (Snigirev et al. 1995, Cloetens et al. 1996). Later the method was also demonstrated with a laboratory based x-ray source (Wilkins et al. 1996). While there are no stringent requirements on the temporal coherence, a high degree of spatial coherence is necessary (Gureyev et al. 2009). In the laboratory the necessary spatial coherence can be achieved by using microfocus x-ray sources.

Using PBI both the absorption and the phase can be determined quantitatively if images are recorded with several different sample to detector dis-

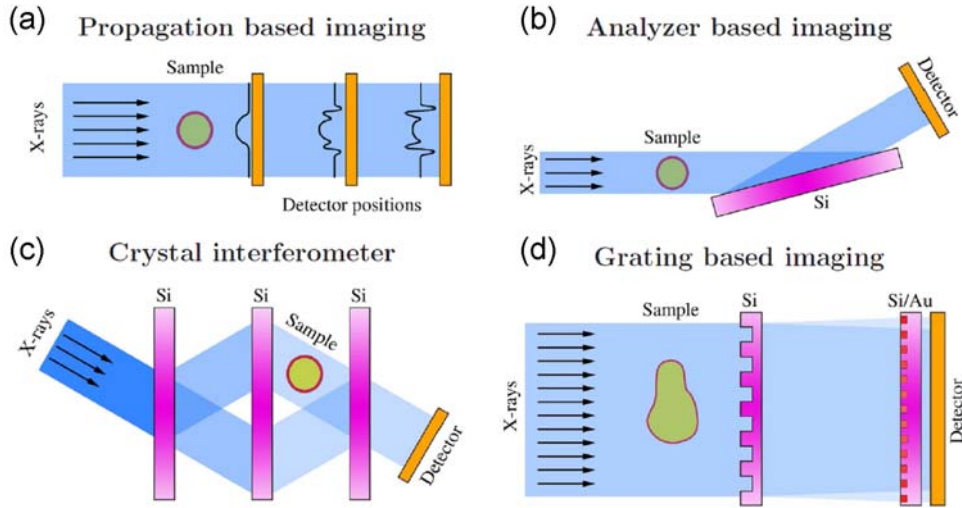


Figure 1.1. Refraction and scattering based x-ray imaging methods

Schematic overview of the four different refraction and scattering based x-ray imaging methods. (a) Propagation Based Imaging (PBI). (b) Analyzer Based Imaging (ABI). (c) Crystal interferometric method. (d) Grating Based Imaging (GBI). Figure adapted from (Bech 2009).

tances or if the sample is a pure phase object (Cloetens et al. 1999a, Gureyev et al. 2009). The complex refractive index can thus also be reconstructed tomographically (Cloetens et al. 1999a).

The method of PBI does not provide the possibility of dark-field imaging. Scattering is generally neglected within the framework of the method, and strongly scattering samples can thus not be imaged correctly.

One limitation for using this method in a laboratory set-up is the need for spatial coherence, which limits the available flux. Another limitation is the need for a relatively high resolution detector to resolve the interference caused by the fresnel diffraction. The need for high resolution detectors, limits the field of view available for imaging or require detectors with a very large number of pixels. Finally the method is limited in that it cannot easily deal with strongly scattering samples. Compared to other methods PBI is also claimed to generally provide lower contrast than other phase-contrast imaging methods (Nesterets & Wilkins 2008).

Analyzer Based Imaging

As a well collimated x-ray beam passes through a sample, the beam is slightly refracted. In analyzer based imaging (ABI) the refraction is imaged using the

Bragg reflection of one or multiple analyzer crystals. A sketch of an ABI set-up is shown in Figure 1.1b. The method measures the derivative of the phase. The method was first introduced by Goetz et al. (1979), Ingal & Beliaevskaya (1995), Davis et al. (1995), Chapman et al. (1997). Using Bragg reflections from crystals the method is limited to a temporal coherence of $\frac{\Delta\lambda}{\lambda} \sim 10^{-4}$. Chapman et al. (1997) demonstrated that it is possible to determine the phase quantitatively for pure phase objects. Later the same was shown in general (Pagot et al. 2003, Wernick et al. 2003, Rigon et al. 2003). The method is difficult to extend to tomography as the crystals are normally aligned such that the derivative of the refractive index is measured in the direction parallel to the tomographic axis. The tomographic reconstruction thus provides the out-of-plane derivative of the phase $\left(\frac{\partial\delta(x,y)}{\partial z}\right)$ and the apparent absorption reconstruction.

In the beginning of the 2000's it was demonstrated that ABI can also be used to generate dark-field images if projections are recorded at a number of crystal rotations thus covering the full rocking curve (Zhong et al. 2000, Ando et al. 2002, Pagot et al. 2003, Wernick et al. 2003, Rigon et al. 2003, Levine & Long 2004, Ando et al. 2005).

If the method is to be used with a laboratory source the main limitations are the need for temporal coherence, which limits the available flux. Due to the diffraction angles and sizes of the analyzer crystals the field of view will normally also be limited.

Crystal interferometry

Crystal interferometers were first used for imaging by Bonse & Hart (1965). The method uses a number of crystal reflections to split an x-ray beam in two and let one part of the beam pass through the sample before the two beams are recombined. A sketch of a crystal interferometer set-up is shown in Figure 1.1c. The method has later been extended to cover tomography (Momose 1995, Momose et al. 1996). As the method is based on the optical path length difference between the two beams, there are very stringent requirements to the stability of the interferometer. The interferometer has to be stable to better than a part of the x-ray wavelength (Momose 2003b). Resolving the stability issue can be aided through the use of monolithic crystal optics. Using Bragg reflections from crystals the method is limited to a temporal coherence of $\frac{\Delta\lambda}{\lambda} \sim 10^{-4}$. A high degree of spatial coherence is also needed (Momose 2003b).

The method is very good for synchrotron use and high resolution studies. It was originally demonstrated with a laboratory x-ray source (Bonse & Hart

1965), but the temporal coherence limits the available flux. The method is limited in the field of view by the size of the crystal optics. The widespread use is also limited by the need for stability where small vibrations can change the optical path length enough to disturb the measurements.

Using crystal interferometry it is possible to quantitatively reconstruct the full complex refractive index. There has however not been demonstrated any dark-field contrast using crystal interferometers.

Grating Based Imaging

A sketch of a grating based imaging (GBI) set-up is shown in Figure 1.1d. One grating is used to produce an interference pattern. The change in position of the interference pattern is then used to determine how the x-rays have been refracted through the sample and is normally probed using a second grating. The method was first demonstrated in the beginning of the 2000's (David et al. 2002, Momose et al. 2003a, Weitkamp et al. 2005, Pfeiffer et al. 2006). In general there are no requirements for the temporal coherence of the beam (Engelhardt et al. 2008). As the method is based on interference produced by the first grating a certain degree of spatial coherence is needed. In a laboratory set-up the necessary coherence can be achieved by using a third grating producing an array of line source (Pfeiffer et al. 2006). In this way source sizes of up to a square millimeter can be used even in compact set-ups. The field of view is limited only by the size of the gratings used, and should be scalable to tens of centimeters. In a tomographic set-up it is possible to reconstruct the full complex refractive index (Weitkamp et al. 2005, Momose et al. 2006, Pfeiffer et al. 2007a,b,c). GBI also provides the possibility of dark-field imaging (Pfeiffer et al. 2008a, 2009).

Further details on the workings of the grating interferometer, its development, possibilities and limitations will be presented in the following chapters.

Chapter 2

Grating interferometer

The following Chapter 3 and 4 and Papers I-IV are based on experiments made with an x-ray grating interferometer. In this chapter we will provide the necessary background and a short introduction to the working principles of a grating interferometer. There exists a wide range of implementations of x-ray grating interferometers. We will in this text describe the type of grating interferometers used for the experiments in this thesis. For a more thorough introduction to x-ray grating interferometry we refer to Bech (2009).

2.1 Theory

2.1.1 Refractive index

To understand how the grating interferometer works we will have to start by looking at the refractive index of x-rays. For x-rays the refractive index is often described as,

$$n = 1 - \delta + i\beta, \quad (2.1)$$

where both δ and β are small quantities ($< 10^{-5}$). From Als-Nielsen & McMorrow (2001) we know that the real and imaginary part of the refractive index at energies above the absorption edges of the elements can be written as,

$$\delta = \frac{\lambda}{2\pi} \rho_A (\lambda r_0 Z) = \frac{\lambda}{2\pi} \rho_A \sigma_p, \quad (2.2)$$

$$\beta = \frac{\lambda}{4\pi} \rho_A \sigma_a, \quad (2.3)$$

where λ is the wavelength, $r_0 = 2.82 \times 10^{-15} m$ is the Thomson scattering length, Z is the atomic number, and ρ_A the atomic number density. σ_p

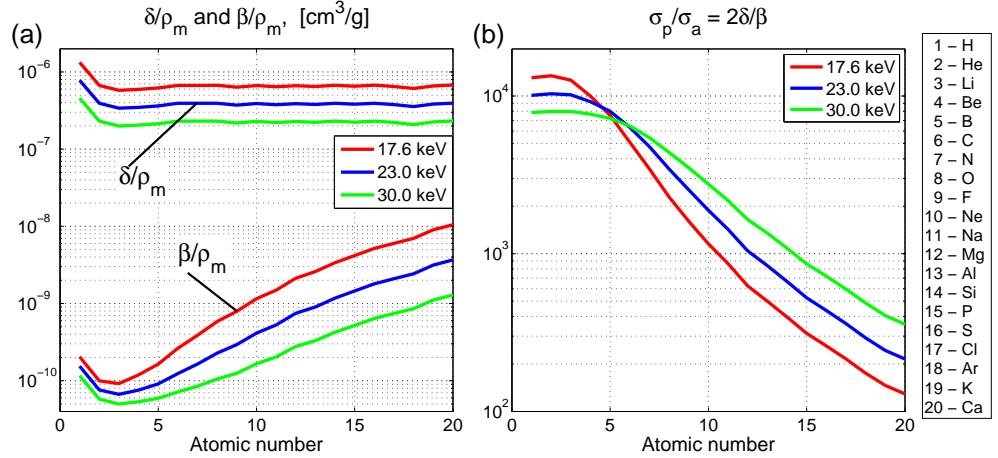


Figure 2.1. Refractive index. (a) The real part (δ) and the imaginary (β) part of the refractive index per mass unit are plotted for various elements at various energies. (b) The ratio between the phase-shift and the absorption cross sections is plotted for various elements at various energies. Note that the ratio is between $10^2 - 10^4$ for these low Z elements, and except for the lowest atomic number this ratio increases with energy. (Data from Henke et al. (1993)).

and σ_a are the phase-shift cross section and the absorption cross section respectively. From equations (2.2)-(2.3) we see that the ratio between the two cross sections is given as,

$$\frac{\sigma_p}{\sigma_a} = \frac{2\delta}{\beta}. \quad (2.4)$$

In Figure 2.1a the refractive index per mass unit is plotted for elements with atomic number lower than or equal to 20 for a number of different x-ray energies (data from Henke et al. (1993)). For water at 23.0 keV, $\delta = 4.36 \times 10^{-7}$ and $\beta = 2.20 \times 10^{-10}$. In Figure 2.1b the ratio between the phase-shift cross sections and the absorption cross sections is plotted. We see that the ratio is in the range $10^2 - 10^4$ (for water at 23.0 keV, $\sigma_p/\sigma_a = 3.97 \times 10^3$). The cross section for the phase-shift is thus 2-4 orders of magnitude greater than the cross section for the absorption. It is this large difference that is one of the motivations for performing phase-contrast imaging, as phase-contrast imaging has the potential to deliver contrast that is orders of magnitude better than standard absorption images. Phase-contrast imaging is especially beneficial for soft tissue as it mainly consists of materials of low atomic number (C, O and H). From Figure 2.1b we also see that except for the lowest atomic numbers the cross section ratio increases with energy.

The two cross sections are measured using different types of experiments. In the end the achieved contrast differences depends on how precisely the phase-shift and the absorption can be measured respectively[†]. The benefits of phase-contrast over absorption-contrast will be illustrated in Chapter 3.

Having seen how the real and imaginary part of the refractive index varies for different energies and elements we will now move on to see how the refractive index is used to describe the x-rays interaction with matter. Using the refractive index the electric field of a plane wave of x-rays through a material can be described as follows,

$$E = E_0 e^{i n \mathbf{k} \cdot \mathbf{r}} = E_0 e^{i(1-\delta) \mathbf{k} \cdot \mathbf{r}} e^{-\beta \mathbf{k} \cdot \mathbf{r}}, \quad (2.5)$$

where \mathbf{k} is the wave vector and \mathbf{r} is the position vector and E_0 is the amplitude of the electric field. In Figure 2.2 an example of how a plane wave changes

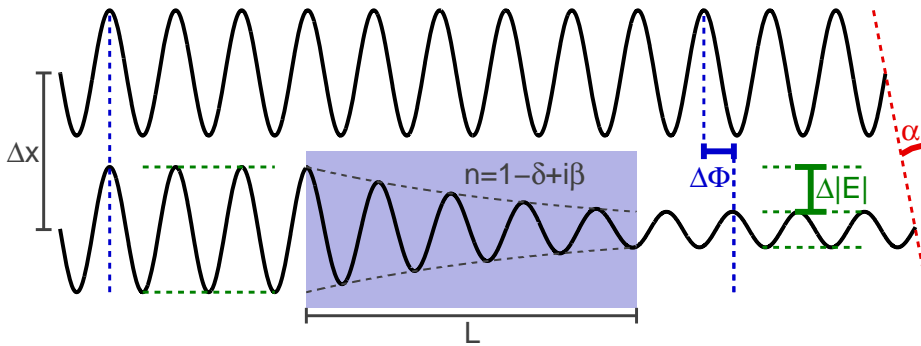


Figure 2.2. Refractive index. A plane wave passes through a material with refractive index, n . This material absorbs a part of the wave, resulting in a change in amplitude, $\Delta|E|$. As the wave passes through the object the phase changes, $\Delta\Phi$, resulting in a change in direction by the angle α .

as it interacts with a block of material is displayed. The imaginary part of the refractive index describes the attenuation, here illustrated by the loss in amplitude. The change in amplitude is given by $\Delta|E| = E_0 (1 - e^{-\beta k L})$, where L is the length of the block of material. The transmission is then given as,

$$T(x) \equiv \frac{I}{I_0}, \quad (2.6)$$

$$= \frac{|E|^2}{|E_0|^2}, \quad (2.7)$$

$$= e^{-\int 2k\beta(x,y)dy}. \quad (2.8)$$

[†]'Det er eksperimentet, som afgører sagen'. (It is the experiment that provides the final answer.) - J.M. Knudsen

The absorption length, μ , is defined as $\mu \equiv 2\beta k$, so that the transmission can be written as,

$$T(x) = e^{-\int \mu(x,y)dy}. \quad (2.9)$$

The second part of the refractive index is the real part, δ . The real part describes the change in wavelength of the x-rays inside the material. The change in wavelength causes a phase difference between the x-rays that pass through the material and the x-rays that do not. This change in phase is,

$$\Delta\Phi = \delta k L. \quad (2.10)$$

In general this can be rewritten as,

$$\Delta\Phi = k \int \delta(x,y)dy. \quad (2.11)$$

The change in phase also results in a change in direction of the x-rays as seen in Figure 2.2. The angular change in the direction is given as $\alpha = \frac{\Delta\Phi/k}{\Delta x}$, or in more general terms,

$$\alpha(x) = \frac{\partial\Phi(x,y)/k}{\partial x} = \frac{\partial}{\partial x} \int \delta(x,y)dy. \quad (2.12)$$

From the derivations above we now see how the real and the imaginary parts of the refractive index describe the behavior of x-rays as they pass through the material. These descriptions can be used to determine how to measure the real and imaginary parts of the refractive index.

Above we have seen how the phase-shift cross section is much larger than the absorption cross section. We also saw how the derivative of the phase could be determined by measuring the change in direction of the x-rays, and the absorption by measuring the change in intensity. To determine the phase-shift one method is thus to measure the change in direction of the x-rays. As we saw in section 1.3 there are several ways to probe the change in direction of the x-rays. In the following we will present the one of them in detail - the grating interferometric method.

2.1.2 Grating interferometer

The grating interferometer consists of two x-ray gratings. A sketch of the grating interferometer can be seen in Figure 2.3. The first grating is a beam splitting phase grating, G1. The grating is designed with a 0.5 duty cycle, such that the width of the phase shifting part of the grating is half of the period, g_1 of the grating. The grating is designed so that the phase shifting

part of the grating introduces a π -phase shift at the design energy. Using these parameters it can be shown that the grating produces a box shaped interference pattern of alternating high and low intensity at uneven fractional Talbot distances, $d_T^{(n)}$, behind the grating (Pfeiffer et al. 2005, Weitkamp et al. 2006). The fractional Talbot distance is given as,

$$d_T^{(n)} = n \frac{g_1^2}{8\lambda}, \quad n \in 1, 3, 5, \dots, \quad (2.13)$$

where λ is the wavelength of the x-rays. Figure 2.3 shows an example of how the interference behind such a phase grating will be if the incoming beam is a plane wave. We note that the maximum intensity variation take place at the uneven fractional Talbot distances. We also note that the period of the interference pattern is half the period of the phase grating. In Figure 2.3 the 5th, 9th and 11th fractional Talbot distances are marked with red dashed lines. These three distances corresponds to the distances used in Papers I(9th), II(11th), III(5th) and IV(11th).

If an object is placed in front of the phase grating it will change the intensity and the direction of the x-rays as described by the refractive index and explained above. As the direction of the x-rays changes, the vertical position of the interference pattern will also change. The principle idea of the grating interferometric imaging method is thus to determine the refraction of the x-rays through the sample, by performing measurements with and without sample and determine the change in position of the interference pattern caused by the sample.

To follow the reasoning behind the construction of the grating interferometer we need to introduce some typical numbers for the gratings. The phase grating typically has a period of around $4 \mu\text{m}$. The interference pattern thus has a period of around $2 \mu\text{m}$. One way to measure the position of the interference pattern is to use a high-resolution detector to resolve the interference fringes. This will require a very high resolution detector and thus limit the field of view significantly. Our main focus has been to measure with relatively large fields of view (greater than 10 mm). A high resolution detector has thus not been a suitable approach for our experiments. A second approach, which we used, is to determine the position of the interference pattern using an analyzer grating. We used a gold analyzer absorption grating. This second grating, G2, also has a duty cycle of 0.5 and a period that is matched to the period of the interference pattern $g_2 = \frac{g_1}{2}$ (see Figure 2.3). Behind G2 is a detector that can have a pixel size that is many times the period of the interference pattern, thus allowing imaging of larger fields of view. (In Papers I, II and IV the pixel size was $d_p \approx 3g_2$ while in Paper III the pixel size was $d_p \approx 86g_2$.) The idea is then to replace a high-resolution detector with

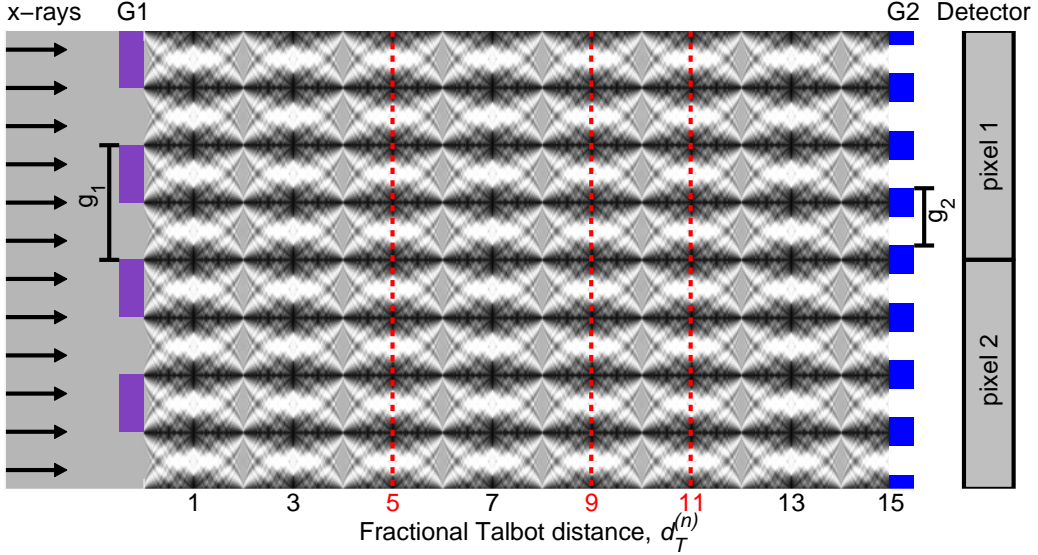


Figure 2.3. *The grating interferometer.* On the left a phase grating, G_1 , of period, g_1 , splits the incoming plane wave. As a result an interference pattern is produced behind the grating. At uneven fractional Talbot distances, $d_T^{(n)}$, the interference pattern produces lines of alternating high and low intensity. The intensity pattern can be analyzed using an absorption grating, G_2 , of period $g_2 = g_1/2$. Depending on the alignment of the second grating it will either block or transmit the x-rays. A detector is placed behind the second grating. By scanning the second grating the position of the interference pattern can be determined.

a high precision motor to scan G_2 in small increments perpendicular to the grating lines to detect the position of the interference pattern. An example of the result of scanning G_2 is shown in Figure 2.4. When G_2 is aligned with the interference pattern all the x-rays will pass through the grating and high intensity will be recorded in the detector pixel behind the grating (Figure 2.4a). When G_2 is moved half a period most of the x-rays will be absorbed in the gold, and low intensity will be recorded in the detector pixel behind the grating (Figure 2.4c). It can be shown that for real life set-ups the intensity variations when scanning one of the gratings will be well approximated by a first order Fourier expansion (Pfeiffer et al. 2008a),

$$\begin{aligned} I(j, k, x_g) &= \sum_{n=0}^{\infty} a_n(j, k) \cos \left[\frac{2\pi n}{g_2} x_g - \phi_n(j, k) \right], \\ &\approx a_0(j, k) + a_1(j, k) \cos \left[\frac{2\pi}{g_2} x_g - \phi_1(j, k) \right], \end{aligned} \quad (2.14)$$

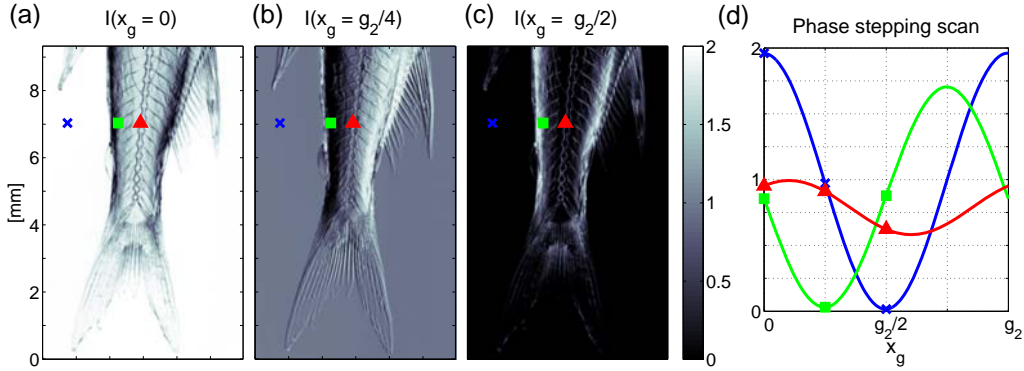


Figure 2.4. Stepping the grating. (a)-(c) Projections of a fish for the grating positioned at $x_g = [0; g_2/4; g_2/2]$ respectively. (d) Plot of the intensity in three pixels as a function of the grating position. The three points are marked in panels (a)-(c). Note how the phase and amplitude of the oscillation varies.

where (j,k) refers to the pixel numbers, a_n are the amplitude coefficients, ϕ_n the corresponding phase coefficients, and g_2 the period of G2. An example of such an intensity variation is seen in Figure 2.5. The parameter a_0 describes

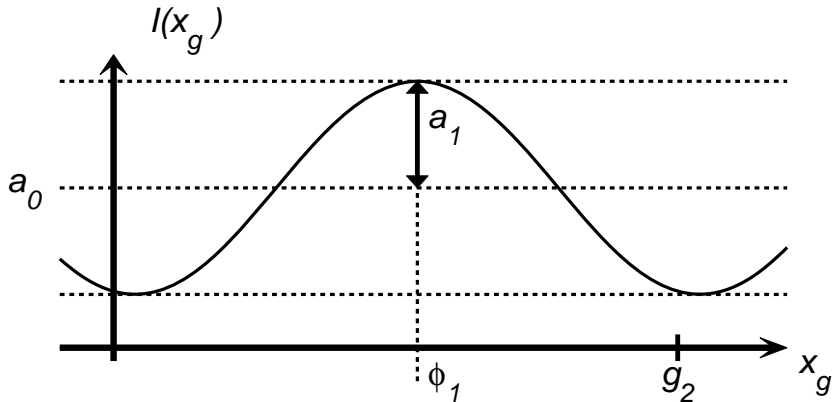


Figure 2.5. Intensity variation in a single pixel. The parameter a_0 describes the average intensity, a_1 the oscillation amplitude and ϕ_1 the position of the interference pattern.

the average intensity, a_1 the oscillation amplitude and ϕ_1 the position of the interference pattern.

When using a grating interferometer for imaging, then measurements are made with and without a sample in the beam. The transmission can then be

determined as,

$$T(x, z) = \frac{a_0^{(s)}}{a_0^{(r)}}, \quad (2.15)$$

where (x, z) describes a position on the detector and the superscripts s and r denote the values measured with the specimen in place (s) and as a reference without (r). In Figure 2.4d the intensity in three pixels are plotted as a function of grating position, x_g . The influence of absorption is in Figure 2.4 seen as the difference between the point, \times , where there is no sample and the average intensity is 1, and the point, \blacktriangle , where the average intensity has fallen to 0.8 due to absorption in the fish. The absorption can be related to the refractive index through μ as seen in equation (2.9) on page 10.

$$-\log(T(x)) = \int \mu(x, y) dy. \quad (2.16)$$

The differential phase shift used to generate differential phase-contrast images can be determined from the change in position of the interference pattern.

$$\frac{\partial \Phi(x, z)}{\partial x} = k\alpha(x, z) = k \frac{\left(\phi_1^{(s)} - \phi_1^{(r)}\right) \frac{g_2}{2\pi}}{d_T^{(n)}}, \quad (2.17)$$

where $\alpha(x, z)$ is the refraction angle and Φ is given as,

$$\Phi(x, z) = \int \delta(x, y) dy. \quad (2.18)$$

In Figure 2.4 the phase-shift difference is illustrated in the difference between the point, \times , and the point, \blacksquare . The first point (\times) has the maximum intensity in when the grating is placed at $x_g = 0$, while the second point (\blacksquare), has the maximum intensity when the grating is placed at $x_g = \frac{3}{2}g_2$. The interference pattern has thus changed position because the x-rays have changed direction as they passed through the fish.

Finally there is the parameter a_1 describing the oscillation amplitude (Figure 2.5). The reduction in the relative oscillation amplitude is called the visibility,

$$V(x, z) \equiv \frac{a_1^{(s)}/a_0^{(s)}}{a_1^{(r)}/a_0^{(r)}}. \quad (2.19)$$

The visibility is a measure of the integrated small-angle scattering intensity of the sample (Pfeiffer et al. 2008a). When the sample scatters it will smear the interference pattern, resulting in a reduction in oscillation amplitude and hence V will be reduced. As the visibility is a map of the scattering from

the sample, the images produced with this contrast mechanism are named dark-field images. In Figure 2.4 this is seen as the difference between the point, \times , where $a_1 = a_0$, and the point, \blacktriangle , where $a_1 = 0.2 = 5a_0$. The oscillation amplitude of the interference pattern in the point, \blacktriangle , has thus been decreased by the scattering taking place in the fish. A more thorough discussion of how the visibility is related to the scattering of the sample will be given in Chapter 3.

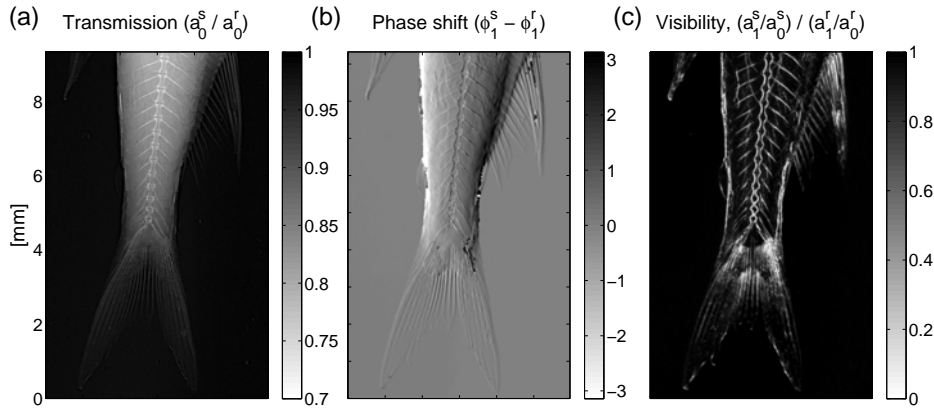


Figure 2.6. The three types of images. Three types of images are recorded with the grating interferometer. (a) The transmission, which is the standard x-ray absorption-contrast image. (b) The differential phase-contrast image, which is very sensitive to e.g. soft tissue. (c) The dark-field image, which shows the scattering structures of the sample.

In Figure 2.6 an example of the three types of images produced with a grating interferometer is presented. The imaged specimen is a small fish. We can now see the individual strengths of the three different imaging modalities. The absorption image (Figure 2.6a) is the classical x-ray image, showing both the tissue and the bone of the fish. Figure 2.6b shows the differential phase-contrast image. These images illustrate how the phase-contrast can provide added contrast especially for soft tissue as described in the beginning of this chapter. Finally the dark-field image (Figure 2.6c) shows that the microstructure of the bones produce a lot of scattering. The dark-field signal thus delineates the bones even more clearly than the standard absorption image. It is important to note here that the three types of signals are all recorded simultaneously.

We have now seen the working principle of the grating interferometer. We also introduced the three basic types of images that are recorded with a grating interferometer: Absorption, differential phase-contrast and dark-field images. In the following we will move on to the practical implementation of

the grating interferometer.

How the three types of signals can be extended from radiography to three dimensional tomography or used for other advanced contrast mechanisms will be covered in the following chapters when needed.

2.2 Experimental set-up

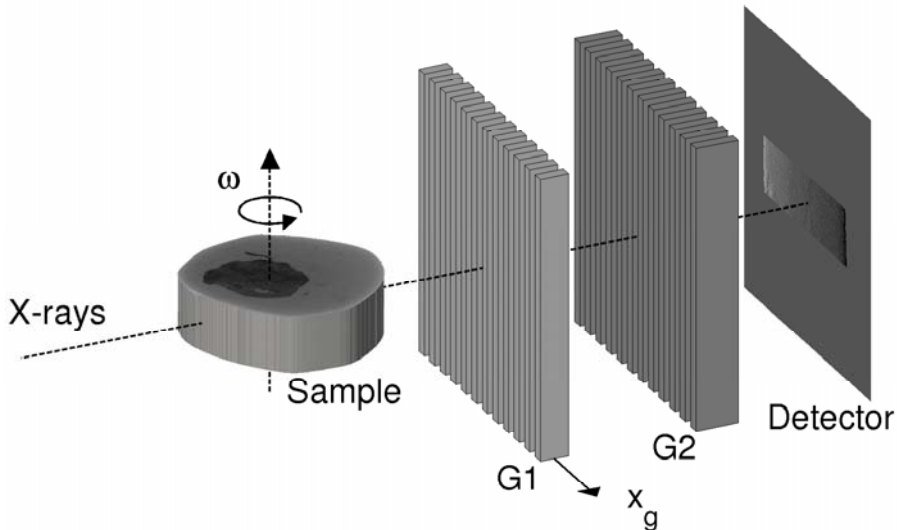


Figure 2.7. Experimental set-up. Set-up with a phase grating G_1 and an analyzer absorption grating G_2 . The sample is placed in front of G_1 , and the detector behind G_2 . Not to scale.

We have in Section 2.1 so far discussed only the theoretical basis of the grating interferometer. In this section we will discuss some of the relevant details for the practical implementation of the grating interferometer. Figure 2.7 shows a sketch of a grating interferometric set-up. The grating interferometer consists of the phase grating, G_1 , and the analyzer absorption grating, G_2 . The sample is placed in front of G_1 and the detector immediately behind G_2 . In this case it is indicated how G_1 can be scanned in a direction perpendicular to the grating lines to probe the interference pattern. The experiments presented in Chapters 3-4 were performed with two different types of x-ray sources. Some were performed with a laboratory x-ray tube source, and some with a 3rd generation synchrotron source. In the following we will highlight some of the advantages and limitations of these two types of x-ray sources.

2.2.1 The grating interferometer in the laboratory

We have so far presented how a grating interferometer works under ideal conditions with monochromatic, non-divergent and fully coherent x-ray beam. In real life and especially with a laboratory x-ray tube source these conditions are not fulfilled. We will below shortly outline some of the limitations and how these are dealt with when using a grating interferometer in a laboratory.

Divergent beam

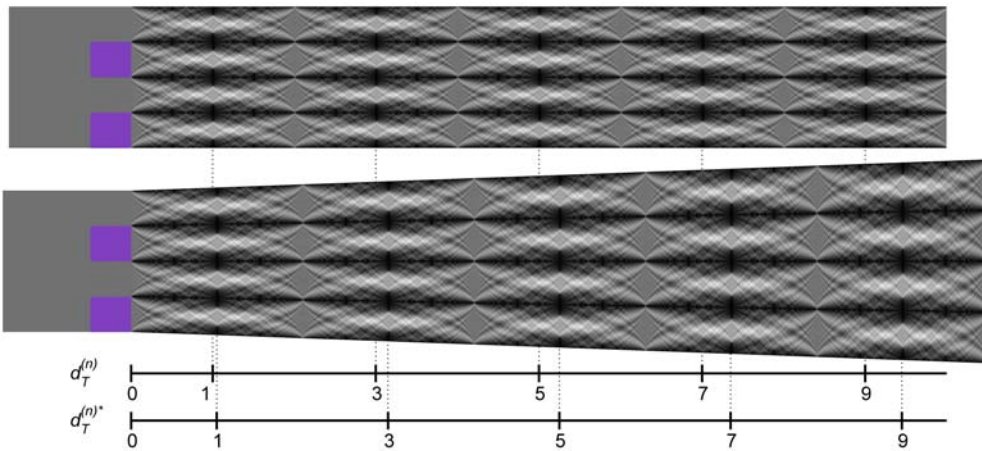


Figure 2.8. Divergence of beam. Interference patterns behind the phase grating for a non-divergent (top) and a divergent (bottom) beam respectively. We note that the fractional Talbot distances and the period of the interference pattern both increases if the x-ray beam is divergent.

If the x-ray beam is divergent this will influence the interference pattern created behind the phase grating. Due to the divergence the interference pattern will be magnified and the Talbot distance will be slightly increased. From simple geometry one can derive that the new Talbot distance $d_T^{(n)*}$ will be given as,

$$d_T^{(n)*} = \frac{r}{r - d_T^{(n)}} d_T^{(n)}, \quad (2.20)$$

where r is the distance between the source and G1 (Weitkamp et al. 2006). The increase in the period of the interference pattern can similarly be calculated to be,

$$g_2 = \frac{d_T^{(n)*} + r}{r} \frac{g_1}{2}, \quad (2.21)$$

which again is a slight increase relative to the case of the non-divergent beam. The correction for divergence is taken into account when the gratings are designed and produced, and this issue can thus be completely avoided.

Monochromaticity

The grating interferometer is designed for a specific energy. As the phase grating is designed to introduce a π -phase shift it only works at the design energy[†]. It has however been shown that when using a π -phase shifting grating there is no general limitation of the acceptable bandwidth $\frac{\Delta E}{E}$ (Engelhardt et al. 2008). The relative oscillation amplitude of the interference pattern might be reduced a little, but the interferometer will work adequately even with the bremsstrahlung spectrum of an anode x-ray source. The grating interferometer will thus function fine in laboratory set-up. This is one point where the grating interferometric method has a great advantage compared to other phase-contrast imaging methods. Most other methods requires a highly monochromatic x-ray beam, but this is not the case for the grating interferometer.

However when using a broad energy spectrum this may introduce artifacts. In absorption imaging we can observe artifacts due to beam hardening. This is caused by the fact that imaginary part of the refractive index, β , is energy dependent. Since the real part of the refractive index, δ , is also energy dependent artifacts due to beam hardening can also be observed in the phase-contrast images. There are different strategies to deal with these artifacts both during exposure and in the subsequent data processing. Beam hardening artifacts have not played a role in the experiments presented in this thesis, and we will thus not dwell more with this issue.

Transverse coherence

One important issue for the grating interferometer is the degree of transverse coherence in the x-ray beam. As the grating interferometer relies on interference between different parts of the beam, a specific phase relation is needed between the parts that should interfere. The larger the distance is between the two gratings the larger will the original spatial separation of the interfering parts of the beam be and the larger coherence length is needed. The coherence length is normally given as,

$$l_t = \frac{r\lambda}{D}, \quad (2.22)$$

[†]At uneven fractions ($\frac{1}{2m-1}$) of the design energy the phase grating will actually produce a phase shift equivalent to π .

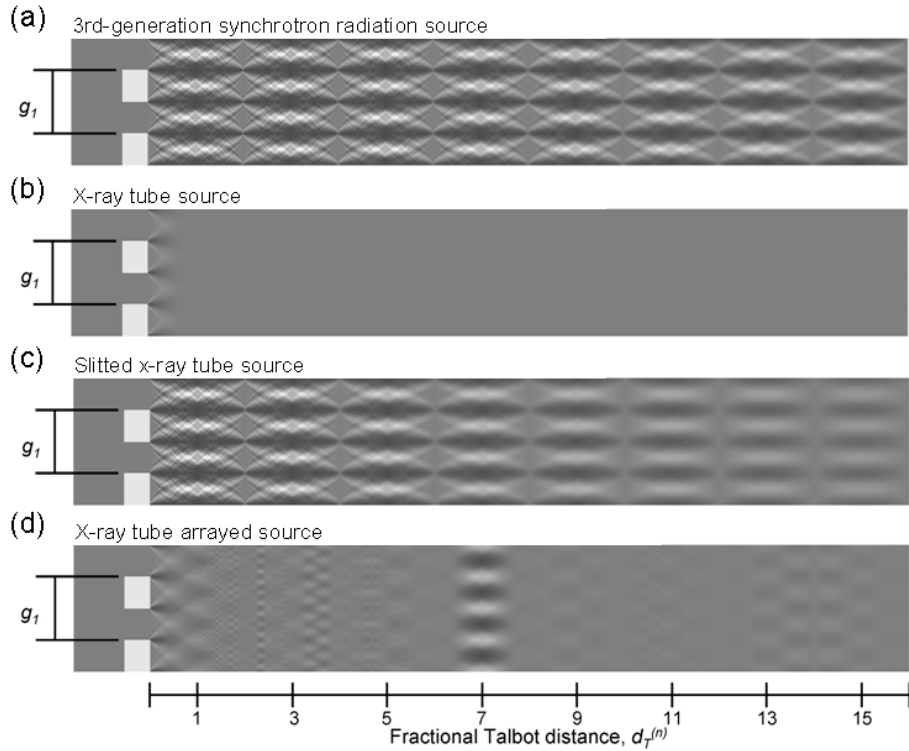


Figure 2.9. Interference limited by transverse coherence. The interference pattern behind the phase grating depends on the transverse coherence of the beam. Here is shown the interference for parameters typical for four different experimental set-ups. The following parameters were used: $E = 14.4 \text{ keV}$, $g_1 = 4.0 \mu\text{m}$. (a) At a synchrotron source. ($D = 50 \mu\text{m}$, $r = 40 \text{ m}$). (b) At an x-ray tube source. ($D = 250 \mu\text{m}$, $r = 2 \text{ m}$). (c) At a slitted x-ray tube source. ($D = 6.15 \mu\text{m}$, $r = 2 \text{ m}$). (d) At an x-ray tube source with 10 equidistant line sources interspaced by $24.6 \mu\text{m}$. ($D_1 = 6.15 \mu\text{m}$, $D_{total} = 250 \mu\text{m}$, $r = 2 \text{ m}$). Figure adapted from (Weitkamp et al. 2006).

where D is the source size and r the distance to the source. It has been shown (David et al. 2002, Weitkamp et al. 2005) that the minimum required transverse coherence length for the grating interferometer is given as,

$$l_t > n \frac{g_1}{2}, \quad (2.23)$$

where n is the fractional talbot order.

Panel	(a)	(b)	(c)	(d)
Energy, [keV]	14.4	14.4	14.4	14.4
g_1 , [μm]	4.0	4.0	4.0	4.0
D_1 , [μm]	50	250	6.15	6.15
D_{total} , [μm]	-	-	-	250
r , [m]	40	2	2	2
l_t , [μm]	69	0.69	28	28

Table 2.1. List of experimental parameters used for the simulation generating the images in the four panels in Figure 2.9.

For the laboratory set-up which has a very small source to G1 distance the needed coherence places stringent requirements on the source size. Figure 2.9 shows the influence a limited transverse coherence has on the interference pattern produced behind the phase grating (Figure adapted from (Weitkamp et al. 2006)). The four different panels show the interference pattern as simulated for typical numbers of four different experimental set-ups. The parameters used for the simulations are summarized in Table 2.1. Figure 2.9a shows the results for a synchrotron beamline with a source size of $D = 50 \mu\text{m}$ and a source to interferometer distance of $r = 40 \text{ m}$. We see that the further we move away from the phase grating the more influence does the limited coherence length have. We also see that when the transverse coherence is limited, this will reduce the oscillation amplitude of the interference pattern.

For a typical laboratory source with a source size of $D = 250 \mu\text{m}$ and a source to interferometer distance of $r = 2 \text{ m}$, the coherence length is $l_t = 0.7 \mu\text{m}$. In Figure 2.9b we see that this coherence length is not even enough to produce interference at the first fractional Talbot distance. One way to solve this problem is by reducing the source size. As the coherence is needed only in the direction perpendicular to the grating lines a narrow tall slit can be used. Figure 2.9c shows the interference when the source width has been reduced to $D = 6.15 \mu\text{m}$. We see that with this line source of reduced width the interference is again visible for several fractional Talbot distances. However with a limited source size the available flux is also severely limited. The intensity was in this case reduced by a factor of 50.

Pfeiffer et al. (2006) showed that the flux could be significantly increased by introducing a third grid to produce an array of line sources. A set of individually coherent narrow slits are arranged such that the interference pattern generated by each slit overlaps at the position of G2. The distance between the slits thus has to be determined for the specific geometry of the set-up. In Figure 2.9d an array of 10 line sources of width $D_1 = 6.15 \mu\text{m}$ have been placed with a period of $24.6 \mu\text{m}$. The distance is chosen so that the interference patterns of each of the 10 line sources overlap at the 7th fractional Talbot distance. The total extension of the arrayed source is thus $250 \mu\text{m}$ as in Figure 2.9c, while the line sources are of the same size as in Figure 2.9b. In Figure 2.9d we see that the depth of the interference pattern at the 7th fractional Talbot order is the same for both the arrayed source and the single line source. In this way it is thus possible to increase the flux 10 fold. In practice a source of size $1 \times 1 \text{ mm}^2$ can be used resulting in a great increase in the available flux. In the case of Paper III, an array of 56 slits were used. Paper III is the only paper that include results made at a fixed tube source with a three grating interferometer. Key parameters for the set-up used in Paper III are presented in Table 2.2 on page 23.

We have now seen how a limited transverse coherence can limit the oscillation amplitude and hence the applicability of the grating interferometer. To achieve a reasonable flux through the grating interferometer at a standard x-ray tube source one can then use an array of line sources. We have discussed a number of limitations for the use of the grating interferometer with an x-ray tube source and also seen how each of these limitations can be dealt with. There are thus no fundamental limitations that prevent the use of a grating interferometer with a laboratory x-ray tube source. This is a very important feature for the widespread application of the results obtained with, and the methods developed for, a grating interferometer. If newly developed methods should achieve widespread application, it is not enough that they work well with synchrotron x-ray sources. The number of these synchrotron sources and the access to them is highly limited. For widespread application it is thus paramount that the methods also function with standard x-ray tube sources.

Accessability is not the only limitation for synchrotron x-ray sources. The synchrotron beams for hard x-rays are often limited in size to tens of millimeters. The tube sources on the other hand are much less restricted in the possible beam sizes. This is very important for the measurements of larger samples of tens of centimeters.

2.2.2 The grating interferometer at the synchrotron

Above we discussed some of the limitations when using the grating interferometer with a laboratory x-ray tube source. Several of the experiments presented in this thesis were performed at a 3rd generation synchrotron source. Key experimental parameters for the set-ups of the four papers using a grating interferometer are printed in Table 2.2.

For the synchrotron experiments the divergence correction of the gratings and the Talbot distance were still performed. However as seen in Table 2.2 the divergence and hence the correction is much smaller than for the laboratory set-up. This is most easily seen as the divergence correction to g_2 (
$$g_2 = \frac{d_T^{(n)*} + r}{r} \frac{g_1}{2}$$
). For the synchrotron experiments this correction is around 0.2% while for the laboratory experiment with much shorter distances the correction is around 14%.

The transverse coherence for the synchrotron experiments was much greater than for the laboratory experiment. This is primarily due to the fact that the experiments were conducted at a long beamline, with a source to interferometer distance of 150 meters. At the same time the beamline staff and designers have done an excellent job at preserving the coherence all the way from the source to the interferometer, avoiding unnecessary optical components in the beam. Even with this long beamline the transverse coherence is limited, and this is the reason why only the 9th and 11th fractional Talbot distances were used. As seen in Figure 2.9a even with high transverse coherence the oscillation amplitude of the interference pattern will decrease with distance to the phase grating. The choice of the specific fractional Talbot distance to work at is then a trade-off between the sensitivity which comes with high distances versus the loss in oscillation amplitude.

In this chapter we have now introduced the working principles of an x-ray grating interferometer. We have also discussed issues of importance for the practical implementations of a grating interferometric set-up. We will in the following chapters move on to present two imaging methods based on an x-ray grating interferometer as well as a number of applications of these methods.

	ESRF ID 19			PSI Lab Set-up
Paper	I	II	IV	III
Energy	23.0 keV	17.6 keV	17.6 keV	~28 keV
Monochromatic	Yes	Yes	Yes	No
Talbot Order	9	11	11	5
Talbot distance	480 mm	447 mm	447 mm	200 mm
Dist. Source-GI	150 m	150 m	150 m	1.40 m
$a_1^{(r)}/a_0^{(r)}$	~0.4	~0.5	~0.5	0.1
FOW (h,v), [mm]	15.3×13.7	15.3×15.3	ø15.3	ø26
Grating orient.	Vert.	Vert.	Horiz.	Vert.
g_1	4.785 µm	4.79 µm	4.79 µm	3.5 µm
g_2	2.400 µm	2.40 µm	2.40 µm	2.0 µm

Table 2.2. List of experimental parameters for x-ray grating experiments of Papers I-IV.

Chapter 3

Phase-contrast tomography results

In the previous chapter we saw how a grating interferometer can be used to determine two dimensional absorption, differential phase-contrast and dark-field images. In this chapter we will demonstrate how the two dimensional radiographic phase-contrast images can be extended to three dimensions using tomography. This chapter will work as an introduction to Paper I (Jensen et al. 2010a) and II (Jensen et al. 2010b) both of which rely on phase-contrast tomography. The use of the grating interferometer for phase-contrast tomography has been demonstrated a number of times (Weitkamp et al. 2005, Momose et al. 2006, Pfeiffer et al. 2007a,b,c). As such the method of phase-contrast tomography was developed and demonstrated prior to this PhD. The focus has thus been on demonstrating new applications of phase-contrast tomography.

3.1 Theory

Absorption tomography

We begin our description of phase-contrast tomography by recalling the method of absorption tomography. The method of absorption x-ray tomography has been widely used since it was first introduced by Godfrey Hounsfield (Hounsfield 1973) and Allan M. Cormack (Cormack 1963) in the 1960s and 1970s. The basic idea is to reconstruct the three dimensional distribution of the absorptionlength from a number of line integrals. The method of tomography can be described as follows:

Let the projection, $p_\theta(x')$, describe the transmission through a sample in the direction described by y' , where (x', y') describes a coordinate system

which is rotated by an angle θ around the z axis (see Figure 3.1). Recalling the results from equation (2.16) on page 14, the projection is then given as,

$$p_\theta(x') \equiv -\log(T(x')), \quad (3.1)$$

$$= -\log\left(\frac{a_0^{(s)}}{a_0^{(r)}}\right), \quad (3.2)$$

$$= \int \mu(x', y') dy'. \quad (3.3)$$

Many textbooks describe how once these projections are known for a sufficient number of angles of θ , they can be used to reconstruct the spatial distribution of the absorption length, μ . One way to perform the reconstruction is as described in Kak & Slaney (2001) using the filtered back-projection algorithm,

$$\mu(x, y) = \int_0^\pi \mathcal{FT}^{-1} [\tilde{p}_\theta(v') \tilde{k}(v')] d\theta, \quad (3.4)$$

$$\tilde{k}(v') = |v'|, \quad (3.5)$$

where $\tilde{p}_\theta = \mathcal{FT}(p_\theta)$ and \tilde{k} is the filter function. Equation (3.4) thus describes how to reconstruct $\mu(x, y)$ for a slice through the sample. Extending the method to the the third dimension, z , is done by repeating the above procedure for several height steps with different values of z .

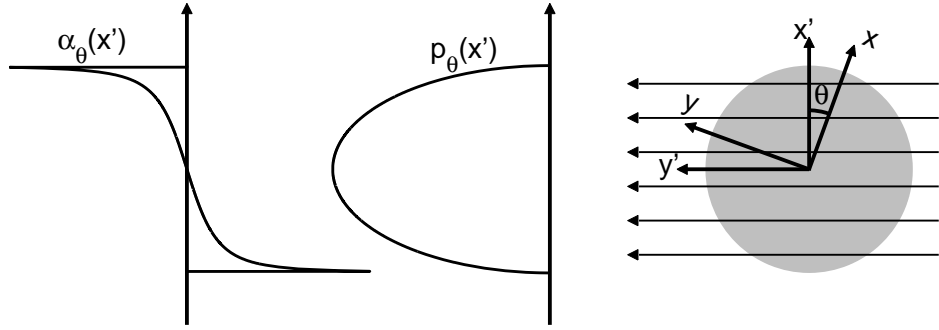


Figure 3.1. Projection geometry. The sample is rotated by the angle, θ , and illuminated in the direction along y' . Shown are the projection, p_θ of the sample, and the refraction angle, α_θ .

Phase-contrast tomography

After having recalled how x-ray absorption tomography works we will now move on to phase-contrast tomography. In phase-contrast imaging we mea-

sure the angular change in direction of the x-rays, which we recall from equation (2.17) on page 14 is given as,

$$\alpha_\theta(x') = \frac{(\phi_1^{(s)} - \phi_1^{(r)})}{d_T^{(n)}} \frac{g_2}{2\pi}, \quad (3.6)$$

$$= \int \frac{\partial}{\partial x'} \delta(x', y') dy'. \quad (3.7)$$

We note that equation (3.7) is very similar to equation (3.3). The only difference being that we measure the derivative of δ in equation (3.7) as opposed to just β in equation (3.3). A general property of fourier transforms is that taking the fourier transform of a derivative is the same as taking the fourier transform of the original function and multiplying by $2\pi i v'$. The integration of δ can thus be done in fourier space. In that way the filtered backprojection algorithm can be adjusted to phase-contrast tomography by replacing the original filter function with a complex filter function. In the end the filtered backprojection algorithm for phase-contrast tomography will be as follows,

$$\delta(x, y) = \int_0^\pi \mathcal{FT}^{-1} [\tilde{\alpha}_\theta(v') \tilde{h}(v')] d\theta, \quad (3.8)$$

$$\tilde{h}(v') = |v'| \frac{1}{2\pi i v'}, \quad (3.9)$$

where $\tilde{\alpha}_\theta = \mathcal{FT}(\alpha_\theta)$ and \tilde{h} is the complex filter function. The two filters used for the reconstruction of the absorption and phase-contrast respectively are shown in Figure 3.2. The use of the complex filter function for direct reconstruction was for grating based x-ray tomography introduced by Pfeiffer et al. (2007a). We have now seen how it is possible to reconstruct the spatial variation of δ using refraction data recorded with a grating interferometer and a filtered backprojection algorithm with a complex filter-function. We have also seen how the projections needed for the tomographic reconstructions of both the absorption length, μ , and the real part of the refractive index, δ , can be recorded using a grating interferometer. In this way we have now seen how to generate three dimensional tomographic reconstructions of μ and δ .

Grating interferometry for x-ray phase-contrast tomography was introduced the early 00's (Weitkamp et al. 2005, Momose et al. 2006, Pfeiffer et al. 2007a,b,c). The use of the complex filter function was introduced by Pfeiffer et al. (2007a). Before then the phase-contrast reconstructions were made by integrating the phase for each projection. Several of the first phase-contrast tomography publications include images of different small insects.

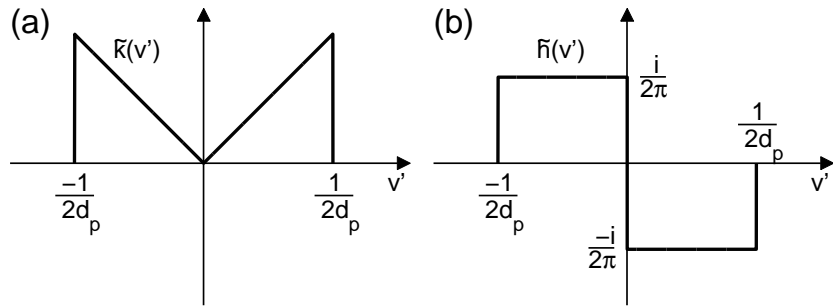


Figure 3.2. *Filter functions for filtered backprojection algorithms.*

(a) The filter used for absorption tomography reconstructions. (b) The complex filter used for phase-contrast tomography reconstructions.

A number of biomedical studies using phase-contrast tomography have later been published. All of them have so far been studies on single samples. Weitkamp et al. (2008) and Bech et al. (2009b) each imaged a single healthy heart of a rat and a chicken with a synchrotron and a lab source respectively. Cancer invaded tissue has also been imaged. Pfeiffer et al. (2007c) imaged a single rat brain with a tumor, and Momose et al. (2006) a single rabbit liver with cancer. The first human and so far only published human study was the imaging of an infant human hand by Donath et al. (2010). So far there have thus been no systematic studies on a series of samples using grating interferometry. In the following we will introduce two studies we did on new applications of phase-contrast tomography. One of them will be a study on a series of human lymph nodes, demonstrating that the increased contrast available with phase-contrast tomography has important diagnostic value.

3.2 Introduction to Paper I and Paper II

In this section we summarize the most important points of Papers I (Jensen et al. 2010a) and II (Jensen et al. 2010b). These two papers investigate two applications of phase-contrast tomography. Important key figures are included. For the full details of the papers the reader is referred to the full version of the papers in Appendix B.

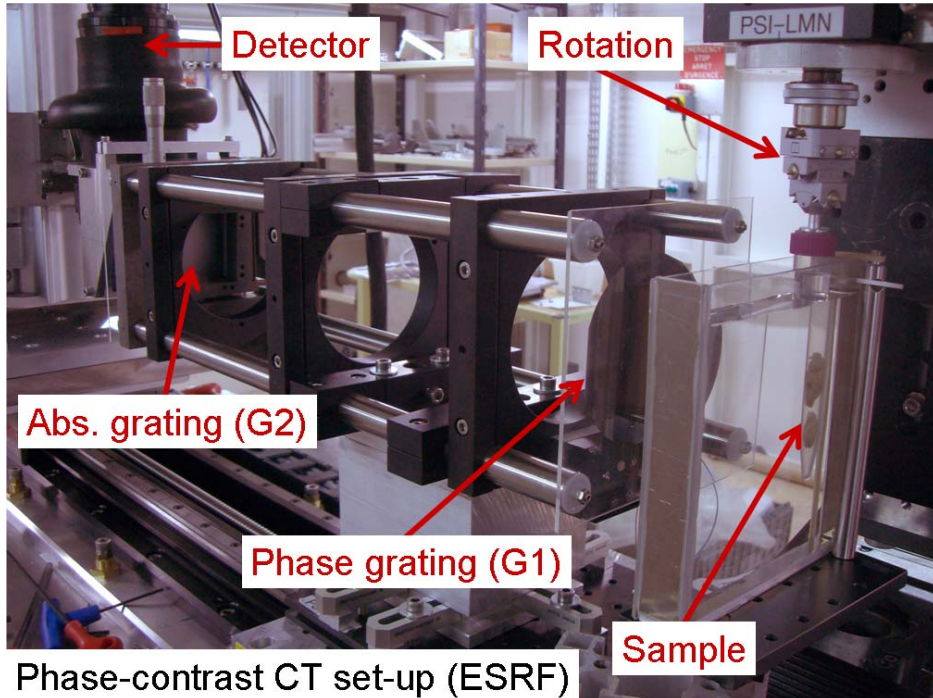


Figure 3.3. Picture of the experimental set-up for phase-contrast tomography. Picture of interferometric set-up at ID19 at the ESRF. The set-up consists of a phase grating G1 and an analyzer absorption grating G2. The sample is rotated around a vertical axis parallel to the grating lines. G1 is scanned in the horizontal direction.

Shown in Figure 3.3 is a photograph of the experimental set-up at ID19 at the ESRF. This set-up was used for the experiments in Paper I and II. On the right is the sample mounted with the tomographic rotation from above. The water bath in which the sample container is submerged was used to minimize phase-wrapping in Paper II. The sample can be translated sideways out of the beam, for collection of flat field images. The sample is placed right in front of the phase grating. More than 40 centimeters away the gold absorption grating is placed, with the detector immediately behind. The experimental details can be found in Table 2.2 on page 23.

3.2.1 Introduction to Paper I

Paper I has the title: 'Imaging of Metastatic Lymph Nodes by X-ray Phase-Contrast Micro-Tomography' (Jensen et al. 2010a). The paper presents the first high contrast biomedical application of phase-contrast tomography. We investigate the diagnostic capabilities of phase-contrast tomography for identification of malignant humane lymph nodes.

Breast cancer is the leading cause of death in cancer among women (Ferlay et al. 2007). Early diagnosis and accurate staging of the disease is crucial for proper treatment and improved prognosis. It is of major importance whether the cancer is confined to the breast or has spread to the adjacent lymph nodes. The current state of the art method to investigate the spread is an invasive method called the sentinel node technique (Veronesi et al. 2006). Besides being invasive the method is not feasible for all patients. The development of a safe pre-operative, noninvasive imaging technique to identify lymph node metastases is of paramount interest. Such an imaging technique could spare the patient axillary surgery if negative, and if positive, the primary tumor and the affected nodes could be removed during the same operation and proper treatment initiated faster.

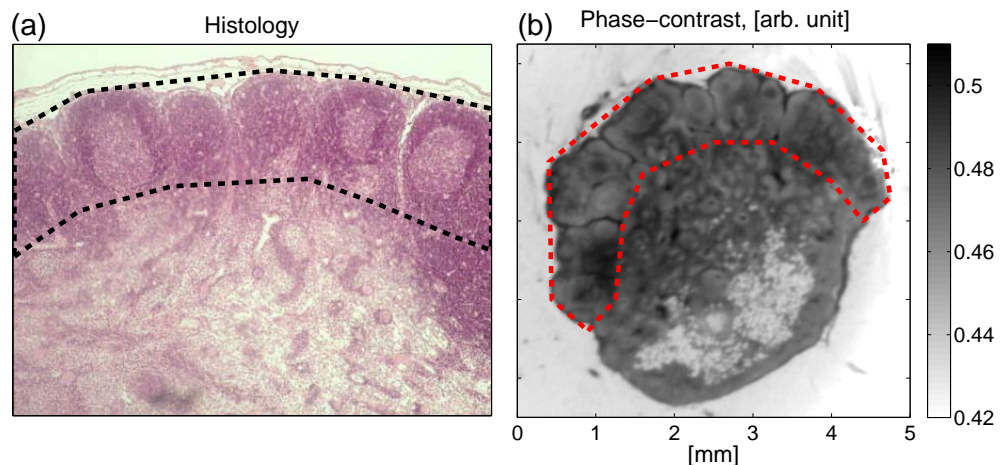


Figure 3.4. Benign lymph node. (a) Histology of a benign lymph node. The lymphoid follicles in the outer cortex are marked. (Image from Gunin (2009).) (b) Phase-contrast image of a different benign lymph node. The lymphoid follicles in the outer cortex are marked. This demonstrates that phase-contrast imaging provides details about functional areas.

In Paper I we demonstrate grating based x-ray phase-contrast tomography to be a noninvasive method to diagnose and stage breast cancer. Using phase-contrast tomography we demonstrate the identification of metastatic

deposits with high accuracy and specificity on 17 excised humane lymph nodes. The density variations caused by cancer in the lymph nodes are generally too small to visualize using standard x-ray absorption-contrast methods. Paper I demonstrates that x-ray phase-contrast tomography provides enough additional contrast to precisely diagnose excised lymph nodes.

Figure 3.4 shows an example of how one of the benign lymph nodes we studied looked like. In Figure 3.4a a histological slice shows the ordered structure of the lymph node is shown. Marked is the collection of lymphoid follicles in the outer cortex. The histological slice is not from a lymph node from the present study (Gunin 2009). In Figure 3.4b the same lymphoid follicles are seen in a phase-contrast tomography slice of a benign lymph node. An overview, showing a single slice from each of the 17 lymph nodes and their diagnosis is attached with the paper in Appendix B.

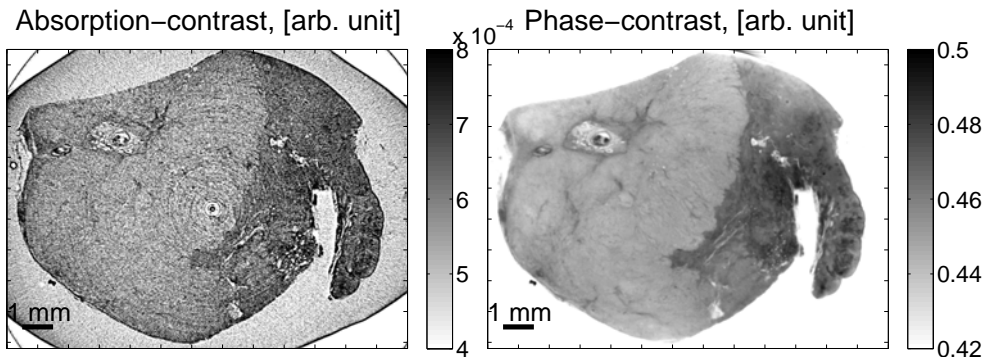


Figure 3.5. Malignant lymph node. (a) Standard absorption-contrast image of malignant lymph node. (b) Phase-contrast image of the same slice as shown in (a). In phase-contrast the border between the cancer infiltrated and the non-infiltrated part of the lymph node can be seen with a clear color difference due to the changed density of the tissue caused by the cancer infiltration.

Figure 3.5b shows an example of a malignant lymph node. In this case some of the follicle structure is still visible in the right part of the lymph node, while in the left part there is a large region of cancerous tissue. The cancer infiltrated tissue has a different density and shows up clearly in the phase-contrast images. Shown in panel (a) of Figure 3.4 is the corresponding absorption-contrast image. In the standard absorption-contrast image we can see the outline of the lymph node, but contrary to (b) there is insufficient contrast to see details in the tissue. Comparing with Figure 3.5b we can again recognize the boundary between infiltrated and non-infiltrated tissue in panel (a), but the level of details would be insufficient for diagnosis. The

diagnostic method is outlined in detail in the paper.

Once this x-ray phase-contrast imaging methodology has been developed into a clinical routine it will have a great impact on diagnosis and treatment of patients with breast cancer. The present sentinel node technique might then be replaced by a noninvasive preoperative x-ray phase-contrast evaluation of lymph node involvement in patients with breast cancer, and surgical intervention could be reduced to one operation. The method of grating-based x-ray phase-contrast imaging has already been demonstrated using standard laboratory x-ray sources (Pfeiffer et al. 2006, Bech et al. 2009b, Donath et al. 2010), making its use in the clinic feasible. We believe that the results presented in Paper I will constitute the next step towards a new concept for imaging cancer and possibly other diseases.

3.2.2 Introduction to Paper II

Paper II has the title: 'Phase-contrast tomography of pig fat' (Jensen et al. 2010b). It investigates the possibilities of using phase-contrast tomography in the food industry. In collaboration with the Danish Meat Research Institute we investigated two pieces of porcine fat and rind in a pilot study.

The Danish pig industry produces more than 27 million pigs per year and pork products represent around 5% of the total Danish export (*Landbrug & Fødevarer* 2010). X-ray computed tomography (CT) has lately received increased attention in the food science community as a possibly new tool for quality testing and automation aid (Judas et al. 2006, Vester-Christensen et al. 2009). In Paper II we demonstrate how grating based phase-contrast CT can provide contrast superior to standard absorption based CT. We apply the method of phase-contrast CT to porcine subcutaneous fat and rind.

Figure 3.6 shows an example of the results. Two pieces of fat are mounted in a small plastic cylinder. The bottom sample (sample B) is mounted so that the dermis is on top and two layers of subcutaneous fat below. The top most sample (sample A) is mounted sideways with the dermis to the right. Both images are scaled with two times the standard deviation. We notice that in the absorption image (Figure 3.6a) we can distinguish the fat from the water it is submerged in, but there is no difference in contrast between the dermis and the water in the sample container. In the phase-contrast image, this is much different. We can clearly separate the dermis and the water. It is even possible to see contrast differences within the dermis.

To provide a quantitative comparison of the absorption-contrast to phase-contrast, Figure 3.6a displays the values along the dashed lines in Figures 3.6a,b. The two axes have been scaled for the curves to overlap. We observe that the difference between the water and the dermis in the absorption-

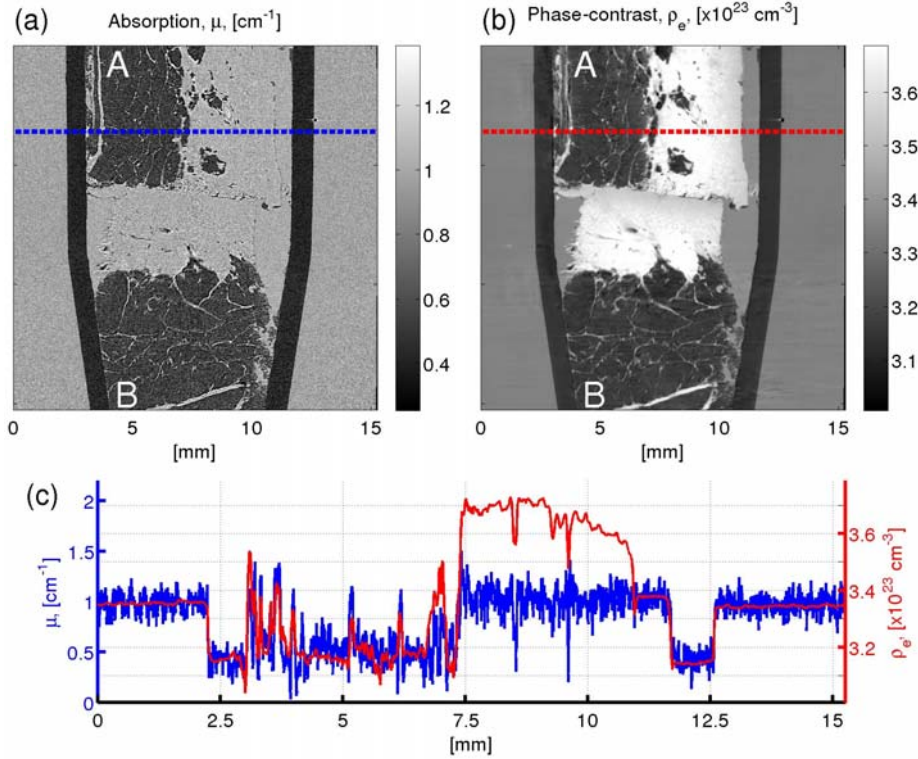


Figure 3.6. (a) Frontal slice through the tomographic reconstruction of the absorption-contrast. (b) Frontal slice through the tomographic reconstruction of the phase. (a) and (b) are scaled displayed on a linear gray scale corresponding to $\pm 2\sigma$, where σ is the standard deviation of the pixel gray values in the image. (c) Plot of the absorption-contrast and phase-contrast through the lines marked in (a) and (b).

contrast is lower than the noise level, whereas it is clearly resolved in the phase-contrast. We also note the clear difference in signal to noise ratio. The noise is significantly reduced in the phase-contrast images. Based on the standard deviation of the gray values in water regions of the reconstructed tomographic slices, we deduced from the phase-contrast measurements an electron density sensitivity of 9.0×10^{20} cm $^{-3}$ corresponding to a mass density sensitivity of approximately 2.7 mg cm $^{-3}$ for aqueous specimens. From the absorption-contrast measurements we deduced a measurement sensitivity for the absorption length of 0.10 cm $^{-1}$ corresponding to a mass density sensitivity of approximately 100 mg cm $^{-3}$ for aqueous specimens. The phase-contrast measurements thus have a forty-fold increase in sensitivity for aqueous specimens in this experiment.

These differences can be further explored by studying the histogram rep-

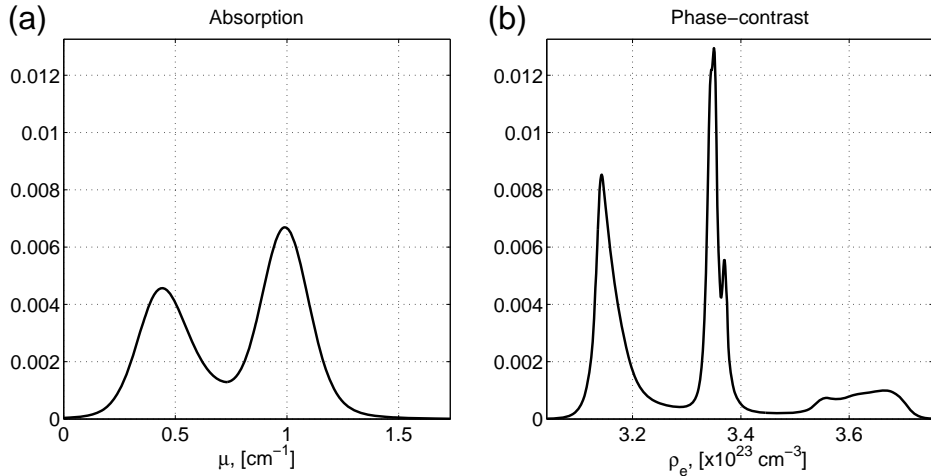


Figure 3.7. (a) Histogram of the absorption-contrast. (b) Histogram of the phase-contrast. Both are generated from the full 3D data-sets.

resentation of the two data-sets. The histograms are displayed in Figure 3.7. For the absorption we see two wide distributions. By comparing Figure 3.6a and Figure 3.7a we see the fat and the plastic cylinder are included in the left distribution and water and dermis in the right distribution. The distributions of the individual constituents are so broad and overlapping, that they cannot be individually distinguished. For the phase-contrast histogram we see at least 7 different distributions. On the left the fat and the plastic cylinder are again overlapping. In the middle two narrow peaks represent the water inside and outside the sample container. The water inside the cylinder has a slightly lower density due to dissolution of material from the samples. Finally the dermis is represented by three or more overlapping regions near $\rho_e = 3.6 \times 10^{23} [\text{cm}^{-3}]$. In the histograms we again see the clear separation between the water and the dermis. The narrow distributions in the phase-contrast histogram shows the increased signal to noise ratio.

The paper further goes on to investigate density variations in the both the fat and the rind. Note that all of the reconstructions presented in this paper are presented on an absolute scale. As with the previous paper it is of great significance that the method of grating based phase-contrast tomography has been demonstrated using standard laboratory x-ray sources (Pfeiffer et al. 2006, Bech et al. 2009b, Donath et al. 2010), thus making its use in widespread use in the food industry feasible. We believe that the results of Paper II will constitute the next step towards a new concept for x-ray imaging in the food industry.

3.3 Outlook and applications

We have in this chapter and in Papers I-II demonstrated two new applications of grating based x-ray phase-contrast tomography.

Both of the papers presented results obtained with a synchrotron x-ray source. The experiments thus benefitted from all of the advantages a synchrotron beam can provide with regards to flux, monochromaticity, and coherence. Both studies were also aimed at demonstrating applications of widespread interest to hospitals and the food industry. For these widespread applications to be implemented it requires the results to be translated to laboratory set-ups. In general grating based phase-contrast imaging has the advantage compared to other phase-contrast imaging methods that it can be translated into the laboratory using existing x-ray sources without requiring unreasonable long exposure times.

The quality of the grating based phase-contrast images from a laboratory set-up are currently not as high as that of the images from a synchrotron source. The translation of the results to a laboratory source thus has to be investigated. However the results of these two papers demonstrate that it is worth investing time and effort in studying how much of the increased contrast provided at the synchrotrons can also be obtained in the laboratory.

The main limitation for widespread application is the commercial availability of grating based phase-contrast tomography set-ups. The first commercially available grating based phase-contrast tomography machine should be on the market soon. This machine will be suited for small animals or samples of same limited size. We thus envisage this as another step on the way to widespread application of grating based phase-contrast tomography in many different areas.

Paper I was the first paper to demonstrate diagnostic relevance for medical phase-contrast tomography. Previous work has demonstrated increase in contrast, but this paper goes on to demonstrate that the increased contrast can provide additional information of diagnostic relevance. This is the first in a hopefully long line of studies that in the future will further demonstrate in which areas grating based phase-contrast imaging can be beneficial. As mentioned above, the next natural step is to investigate which set-up is required to achieve similar diagnostic capabilities with a laboratory set-up. We have nearly finalized such a laboratory set-up to conduct these kind of studies at the Niels Bohr Institute.

Paper II was the first paper to focus on possible food industrial applications of grating based phase-contrast tomography. The food industry and other industrial fields are areas where x-ray imaging and especially x-ray CT has been receiving increased interest lately. We have at the Niels Bohr In-

stitute since 2009 participated in a research consortium called 'Center for Industrial Application of CT scanning' (CIA-CT) with a number of industrial partners including the Danish Meat Research Institute. The consortium is focused on developing technical solutions for industrial applications of CT imaging. We hope that this paper further aids to demonstrate the relevance of including also grating based phase-contrast tomography in the palette of methods available to the industry.

Regarding the specific application demonstrated in Paper II the goal for the future is to extend the results to laboratory use and to whole pig carcasses. If the method can be integrated directly into the production line of the abattoir this would provide a number of interesting possibilities. One is virtual dissection of the carcasses, so that cutting of the carcass can be financially optimized and further robotized (Vester-Christensen et al. 2009). A second opportunity could be quality evaluation, thus providing a nondestructive tool to measure meat quality parameters. These parameters could include the measure of the tenderness of a specific piece of meat. Such a result would be of significant value as producers could guarantee the end user a certain degree of tenderness of their meat.

We have so far been discussing only the food industrial complications of the results presented in Paper II. However pigs are often used as test animals for studies aimed at human applications. The skin is one area where pigs are used in model studies. The results in Paper II thus also have implications for imaging of humans. The study is actually the first phase-contrast tomography study that quantitatively reconstruct the electron density of non-fixed tissue samples. The results thus demonstrate that the application of phase-contrast tomography for imaging of human skin may be worth further investigating. Additional studies have to be made to further investigate these possibilities.

3.3.1 Dose considerations

We have so far not been discussing the dose delivered when performing phase-contrast tomography. For all types of imaging of live subjects the delivered dose is a very important factor. As x-rays are ionizing radiation they are potentially harmful to the exposed subjects, and there are limits to the amount of radiation subjects can be exposed to. The studies above do not include calculations on the delivered dose. If we had measured the delivered dose, it might have been higher than what would be normally allowable for the imaging of live subjects. This is not necessarily devastating for the applicability. There are several reasons for this.

First of all, we have conducted the experiments such that they were op-

timized for maximum contrast. The reasoning has been that if studies at maximum contrast proves unusable all further studies can be abandoned. On the other hand if studies at maximum contrast provides useful information, it is then subsequently possible to optimize the imaging system to minimize the delivered dose. Some of the ways that the dose can be reduced is by:

- Decreasing the number of phase-steps acquired. 3 steps are in principle enough.
- Decrease the number of projection angles and the detectors spatial resolution, so that excess spatial resolution is not recorded.
- Optimize the detector efficiency.

When discussing the delivered dose, we often prefer to compare the dose delivered using phase-contrast imaging to the dose delivered using standard absorption methods. For phase-contrast imaging N images are acquired as one of the gratings is scanned in N steps. This does not necessitate an increase in dose, as the dose can be fractioned over the N images. As the exposuretime for each image can thus also be reduced the necessary time for a phase-contrast tomography scan can thus be reduced to times similar to those necessary for standard absorption tomography scans. Recently it was also demonstrated that grating based phase-contrast tomography can be performed without stepping a grating (Zhu et al. 2010). This is a very interesting new approach, that however requires perfectly produced and aligned gratings, and samples that produce only negligible scattering.

The grating interferometer also absorbs half of the x-rays in the second grating, so the necessary dose to obtain absorption images of the same quality as without the gratings is thus doubled. However as the phase-contrast images may be orders of magnitude better than absorption-contrast, it should in principle be possible to make phase-contrast images of same quality as standard absorption-contrast images with a dose that is orders of magnitude smaller than the dose required with the standard absorption method.

This dose estimation holds for applications where we replace standard absorption images with phase-contrast images in areas where absorption images are presently used. The difficulty arises when we want to use the phase-contrast images for new types of images, such as in Paper I, for imaging of lymph nodes. Here we can not rely on a comparison with the dose delivered in absorption imaging, as absorption imaging does not provide the necessary contrast. For these applications thorough dose studies are needed before the method can be widely applied.

One final remark regarding the dose, is that when using phase-contrast imaging one can in principle increase the energy of the x-rays. Absorption

imaging requires the x-rays to be absorbed in the sample, which limits how high energy the x-rays can have. Phase-contrast imaging on the other hand does not require any photons to be absorbed. It is thus in principle possible to perform phase-contrast imaging at high energies with very little or no absorption at all. This would result in very little or no dose delivered to the subject. There is thus potential for a drastic reduction in delivered dose, by increasing the energy. One limitation for this approach is that the second absorption grating becomes very difficult to manufacture for high energy x-rays. At these high energies extremely high aspect ratios are required for the analyzer absorption grating. Work is being made to produce gold gratings with heights of 300 microns. This would be 91 percent efficient at 100 keV (Henke et al. 1993). A second approach could be to replace the second grating with a scintillator grating, and use that to analyze the interference pattern as proposed by Xin et al. (2010).

The question of dose is thus a question that is not fully resolved for phase-contrast tomography. As with all x-ray methods it will never be fully resolved but has to be kept in mind and probably investigated for all new applications.

Chapter 4

Directional x-ray dark-field imaging

This chapter serves as an introduction to Paper III (Jensen et al. 2010c) and IV (Jensen et al. 2010d). The two papers introduced the novel x-ray imaging method called directional x-ray dark-field imaging. The approach is based on the general concept of (synchrotron-based) x-ray dark-field imaging (Suzuki & Uchida 1995, Kagoshima et al. 2001, Ando et al. 2002, Olivo et al. 2002, Pagot et al. 2003, Levine & Long 2004, Ando et al. 2005) and in particular on the method of the dark-field scattering signal from the grating interferometer which was introduced in Chapter 2. The method utilizes the dark-field scattering signal from the grating interferometer which was introduced in chapter 2. The use of a grating interferometer for x-ray dark-field radiographic imaging was first introduced by Pfeiffer et al. (2008a, 2009). Subsequently the method has been extended to three dimensions using tomography (Wang et al. 2009, Chen et al. 2010, Yashiro et al. 2010, Bech et al. 2010) and to provide directional information using directional dark-field imaging (Jensen et al. 2010c,d). In this chapter we will describe how the 2D radiographic method can be extended to provide local textural information.

4.1 Theory

X-ray imaging in general is a powerful and wide spread method that is routinely used for medical diagnostics, non-destructive testing, and general research applications. The smallest length scale on which information on the structural variations can be obtained is typically determined by the spatial resolution of the imaging system. For some applications, however, it is desirable to obtain more information in a particular image pixel than just a

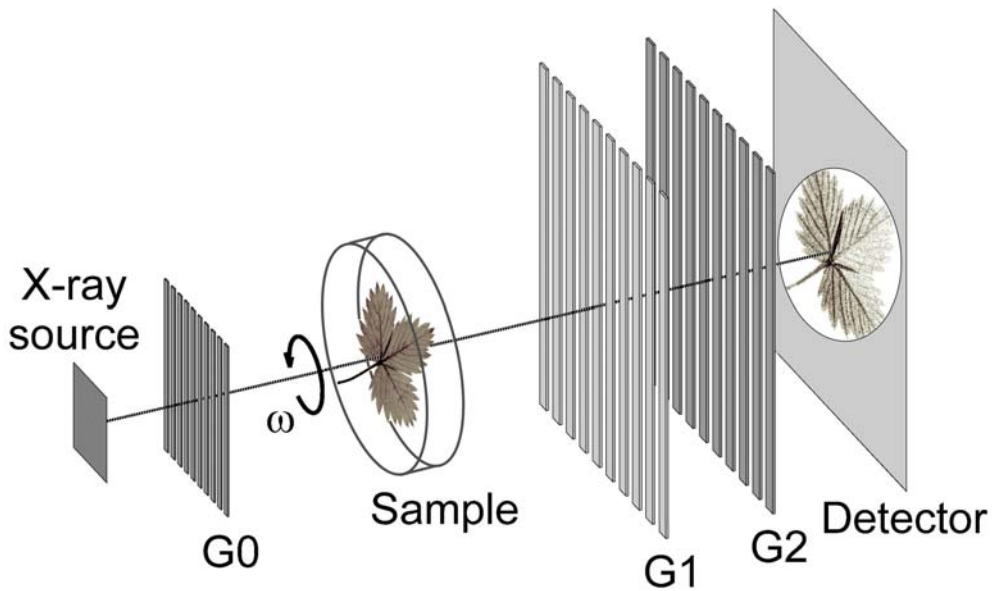


Figure 4.1. *Experimental set-up for directional dark-field imaging.*

(a) Set-up with a source grating G_0 , a phase grating G_1 and an analyzer absorption grating G_2 . The sample is mounted on a stage rotating around the optical axis. The horizontal component of the scattering is measured using the grating interferometer.

single value (e.g. density) that characterizes the material. This is resolved, for example, with Diffusion Tensor Imaging (Basser et al. 1994, Alexander et al. 2007), which is a special type of magnetic resonance imaging, where the diffusion tensor can be used to determine the magnitude, the degree of anisotropy and the orientation of directional diffusion in each image pixel.

In this chapter we introduce a new x-ray dark-field imaging based approach to obtain directional information on the structural variations in the sample on length scales smaller than the actual image pixel resolution. This new method can be used to map, e.g., local fibre orientation in an object. The approach is based on the concept of grating x-ray dark-field imaging introduced in Chapter 2. The dark-field signal is essentially a result of the integrated small- and ultrasmall-angle x-ray scattering from the sample (Pfeiffer et al. 2008a). The main idea is to use the inherent one dimensionality of the gratings to extract the orientational variation of this local small-angle x-ray scattering signal.

Experimental set-up

Figure 4.1 shows the experimental set-up. The grating interferometer has previously been described in Chapter 2. Directional dark-field images are collected for a number of different orientations where the sample is rotated around the optical axis of the set-up as seen in Figure 4.1.

The new aspect and principal idea of the method of directional x-ray dark-field imaging is to use the grating geometry in dark-field imaging to extract orientational information on structural details in the sub-micron regime beyond the spatial resolution of the detection system. In grating based dark-field imaging the contrast arises due to the scattering of x-rays in a direction perpendicular to the grating lines. X-rays scattered in a direction parallel to the grating lines only lead to a blur in the image, but not to any dark-field image contrast. This intrinsic physical property of the set-up can be utilized to extract orientational information about the angular variation of the local scattering power of the sample. This can be achieved by rotating the sample around the optical axis of the set-up, collecting a set of several dark-field images, each measuring the perpendicular component of the scattering for that particular orientation.

An example of how the visibility varies with sample orientation is seen in Figure 4.2 which is a series of dark-field images of a strawberry leaf (This example is taken from Paper III (Jensen et al. 2010c)). The grating lines were aligned vertically for this experiment. Figure 4.2a shows a standard absorption image of the leaf. Figure 4.2b shows three dark-field images of the same leaf recorded with the leaf rotated to different orientations. Note the clear variation in visibility with angle. One example is the petiole of the leaf (\blacktriangle) which shows strong scattering when aligned close to parallel with the grating lines (100°), while when aligned close to perpendicular (20°) only weak scattering is seen. The fibers in the petiole are oriented along the axis, and these fibers scatter primarily perpendicular to their axial direction giving rise to the observed contrast. The three images are from a series of a total of 18 dark-field images. Figure 4.2c shows the visibility as a function of angle for three different regions in the leaf sample. The angle of maximum scattering (minimum visibility) is clearly seen to vary between the blue and red curve.

The visibility in Figure 4.2 appears to vary sinusoidally as a function of rotation angle. In the following we will develop a general model to describe the variations of the visibility. This will include the development of a simple scattering model to account for the variations in the visibility.

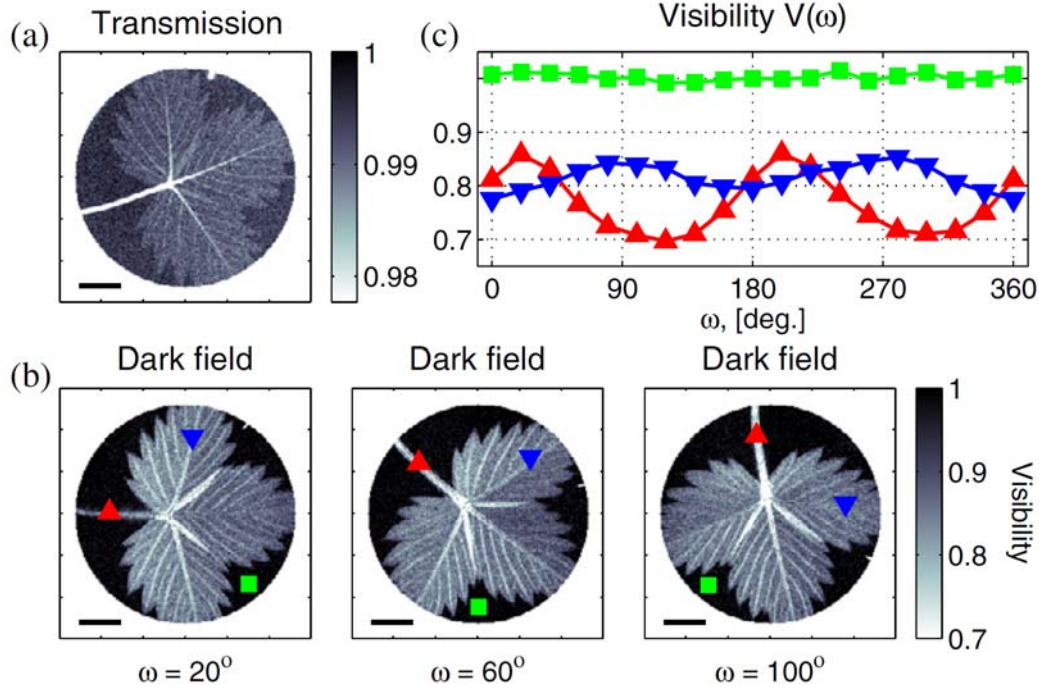


Figure 4.2. *Imaging of a test sample - a strawberry leaf.* (a) X-ray transmission image. (b) Dark-field images for three different sample orientations ω , showing a clear dependence on the orientation of the sample. (c) Visibility $V(j, k, \omega)$ as a function of ω for three different sample regions. The scale bars in (a) and (b) have a length of 5 mm.

The model

We will begin by assuming that the scattering from a single point on the sample will result in a 2D gaussian scattering intensity profile, S_2 at the plane of G2. Let the scattering profile S_2 be defined as follows.

$$\begin{aligned}
 S_2(x, y) &= \frac{1}{2\pi\sigma_1\sigma_2} \exp(-(ax^2 + 2bxy + cy^2)), \\
 a &:= \frac{\cos(\psi_1)^2}{2\sigma_1^2} + \frac{\sin(\psi_1)^2}{2\sigma_2^2}, \\
 b &:= \sin(\psi_1)\cos(\psi_1)\left(-\frac{1}{2\sigma_1^2} + \frac{1}{2\sigma_2^2}\right), \\
 c &:= \frac{\sin(\psi_1)^2}{2\sigma_1^2} + \frac{\cos(\psi_1)^2}{2\sigma_2^2}.
 \end{aligned} \tag{4.1}$$

S_2 is a 2D gaussian distribution with the width σ_1 and σ_2 in the two axial directions, and the first axis rotated by the angle ψ_1 . An example of how

$S_2(x, y)$ could look like for a given σ_1 , σ_2 and ψ_1 is shown in Figure 4.3.

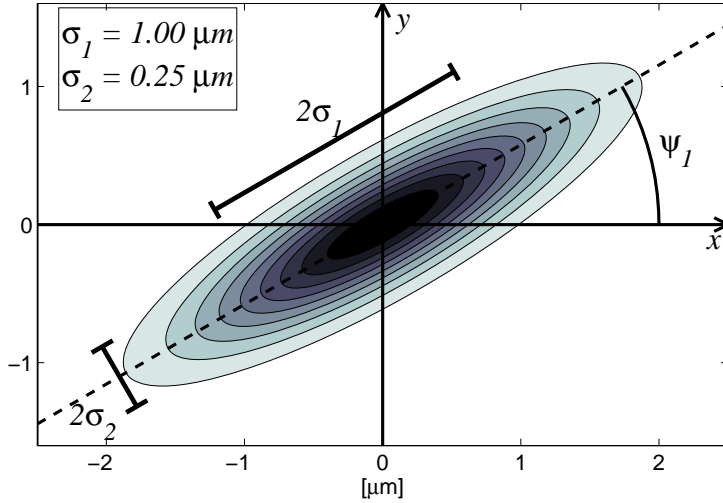


Figure 4.3. Illustration of 2D gaussian scattering function, $S_2(x, y)$, with $\psi_1 = 30^\circ$.

Since the grating interferometer is only sensitive to scattering perpendicular to the grating lines, the dark-field signal measures the projection of S_2 onto the x-axis. This corresponds to integrating S_2 along y ,

$$S(x) = \frac{1}{\sqrt{2\pi}\sigma^2} \exp\left(\frac{-x^2}{2\sigma^2}\right), \quad (4.2)$$

$$\sigma^2 = \frac{1}{2} (\sigma_1^2 + \sigma_2^2) + \frac{1}{2} (\sigma_1^2 - \sigma_2^2) \cos(2\psi_1 - \pi). \quad (4.3)$$

The projection of S_2 is thus another gaussian, S , with the width σ . As described in Chapter 2 on page 12, the variations in intensity in a pixel can be described as follows: $I^r(x) = a_0 + a_1 \cos\left(\frac{2\pi}{g_2}x - \phi_1\right)$. The influence of the scattering from the sample can be determined, by convoluting the original intensity function, $I^{(r)}(x)$ with the scattering function, $S(x)$.

$$\begin{aligned} I^s(x) &= I^r(x) \otimes S(x), \\ &= a_0 + a_1 \exp\left(\frac{-2\pi^2\sigma^2}{g_2^2}\right) \cos\left(\frac{2\pi}{g_2}x - \phi_1\right). \end{aligned} \quad (4.4)$$

Recalling the definition of the visibility $(V \equiv \frac{a_1^s/a_0^s}{a_1^r/a_0^r})$ from equation (2.19) on page 14 and combining with equation (4.4) we see that the visibility varies

as,

$$\begin{aligned} V(\psi_1) &= \exp\left(\frac{-\pi^2}{g_2^2}(\sigma_1^2 + \sigma_2^2)\right) \dots \\ &\quad \cdot \exp\left(\frac{-\pi^2}{g_2^2}(\sigma_1^2 - \sigma_2^2) \cos(2\psi_1 - \pi)\right). \end{aligned} \quad (4.5)$$

If we include the rotation of the sample, ω , during measurement we can rewrite equation (4.5) as:

Case II

$$\begin{aligned} V(\omega) &= \exp\left(\frac{-\pi^2}{g_2^2}(\sigma_1^2 + \sigma_2^2)\right) \dots \\ &\quad \cdot \exp\left(\frac{-\pi^2}{g_2^2}(\sigma_1^2 - \sigma_2^2) \cos(2[\omega - \psi_1] - \pi)\right). \end{aligned} \quad (4.6)$$

Equation (4.6) is a full description of how the visibility changes as a function of $(\sigma_1, \sigma_2, \psi_1, \omega)$. For reasons we will return to, we will call this type of visibility variations for 'Case II'.

We will now take a look at two special cases.

Weakly oriented scatterers

In cases of weakly oriented scatterers it can be shown that the visibility variations are sinusoidal. Let $K_1 \equiv \frac{\pi^2|\sigma_1^2 - \sigma_2^2|}{g_2^2}$. The parameter K_1 describes how eccentric the scattering profile is relative to the grating period. We note that in the special case where $K_1 \sim 0$, we can Taylor expand the second exponential of equation (4.6):

Case I

$$\begin{aligned} V(\omega) &= b_0 + b_1 \cos(2[\omega - \psi_1(j, k)] - \pi), \\ b_0 &= \exp\left(\frac{-\pi^2}{g_2^2}(\sigma_1^2 + \sigma_2^2)\right), \\ b_1 &= -\frac{\pi^2}{g_2^2}(\sigma_1^2 - \sigma_2^2) \exp\left(\frac{-\pi^2}{g_2^2}(\sigma_1^2 + \sigma_2^2)\right). \end{aligned} \quad (4.7)$$

We note that in equation (4.7) the visibility varies sinusoidally. From this we can conclude that if $K_1 \sim 0$, that is if the scattering profile has widths that are small compared to the period of the second grating, g_2 ,

or if the difference between the widths of the scattering profile are small compared to the period of the second grating, g_2 , then the visibility varies sinusoidal. Weakly scattering samples and samples that are not strongly oriented will thus produce sinusoidal visibility variations. This sinusoidal behavior corresponds well with the visibility variations we saw in the leaf in Figure 4.2 on page 42. As the cosine variation is the most simple visibility variation to describe we call this case for 'Case I'.

Unscattered photons

In the general model described above (equations (4.6)) we have assumed that the entire beam is scattered and no part of it pass the sample without being scattered. Only the part of the beam that is scattered can contribute to the reduction in visibility, so if a part of the beam passes through the sample without being scattered then the visibility can not be reduced to zero no matter the width of the scattering profile of the scattered part of the beam. If e.g. 40% of the beam is not scattered then the visibility will take values greater than 0.4. Such transmission can be included in the model using a constant taking the not scattered part of the beam into account. Let α be the proportion of the beam that has been scattered. Then equation (4.4) is replaced by,

$$\begin{aligned} I^s(x) &= I^r(x) \otimes ((1 - \alpha)\delta(x) + \alpha S(x)), \\ &= a_0 + \left((1 - \alpha) + \alpha \exp\left(\frac{-2\pi^2\sigma^2}{g_2^2}\right) \right) \dots \\ &\quad \cdot a_1 \cos\left(\frac{2\pi}{g_2}x - \phi_1\right), \end{aligned} \tag{4.8}$$

and the visibility takes the form,

Case III

$$\begin{aligned} V(\omega) &= (1 - \alpha) + \alpha \exp\left[\frac{-2\pi^2\sigma^2}{g_2^2}\right], \\ \sigma^2 &= \frac{1}{2} (\sigma_1^2 + \sigma_2^2) + \frac{1}{2} (\sigma_1^2 - \sigma_2^2) \cos(2[\omega - \psi_1] - \pi). \end{aligned} \tag{4.9}$$

The sinusoidal behavior for $K_1 \sim 0$ is still valid when we use equation (4.9) to describe the visibility. However when the visibility varies sinusoidally then the parameters $(\sigma_1, \sigma_2, \alpha)$ can no longer be uniquely determined. With the visibility varying sinusoidally the variations can be described by the mean and oscillation amplitude, and it is thus not possible to determine three

independent parameters. This does introduce an ambiguity in our model. It does not limit the ability to describe and predict visibility variations, but it can limit the ability to quantify the measured scattering profiles.

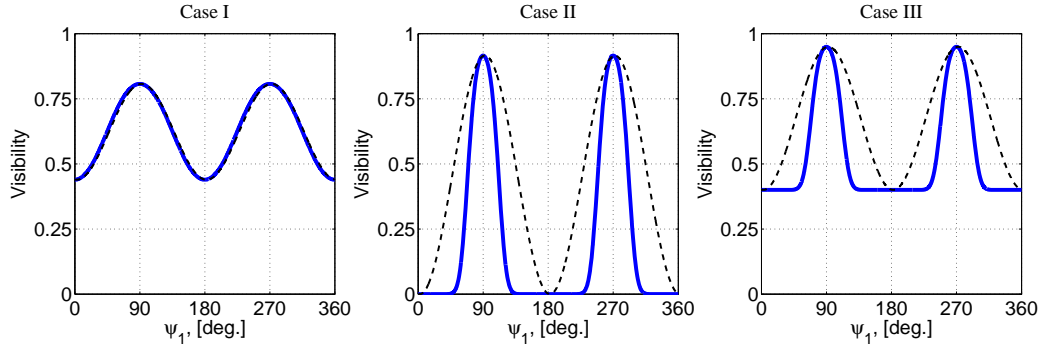


Figure 4.4. The three different cases of visibility changes. **Case I** Sinusoidal behavior when $K < 1$. **Case II** Nonsinusoidal behavior with $K > 1$ and $\alpha = 1$. **Case III** Nonsinusoidal behavior with $K > 1$ and $\alpha = 0.6$. Note how the baseline of the visibility variations has been shifted upwards. In all figures the corresponding cosine function is plotted as dashed black lines.

We have now presented three different cases:

Case I For weakly oriented samples where $K_1 \sim 0$ the visibility varies sinusoidally as seen in equation 4.7. An example of the visibility variations in this case is shown in Figure 4.4a.

Case II For strongly oriented and strongly scattering samples where $K_1 \sim 0$ and $\alpha = 1$ the visibility varies as seen in equation 4.6. An example of the visibility variations in this case is shown in Figure 4.4b.

Case III For strongly oriented and weakly scattering samples where $K_1 \sim 0$ and $\alpha < 1$ the visibility varies as seen in equation 4.9. An example of the visibility variations in this case is shown in Figure 4.4c.

In all three panels in Figure 4.4 the corresponding cosine function is plotted as dashed black lines for easier interpretation.

We already saw how the visibility varied sinusoidally for the leaf presented in Figure 4.2. The leaf thus falls in the Case I category. Examples of the two other cases are presented in Section 4.2.2 and Paper V (Jensen et al. 2010d).

Representing orientational information

In general a wide variety of information is recorded using directional dark-field imaging. Some of the information is listed here:

1. The standard absorption image is recorded for every rotation angle.
2. The differential phase-contrast images are recorded for every rotation angle.
3. The average scattering power can be determined, as the average of all the dark-field images. In Case I this corresponds to b_0 .
4. The degree of orientation. That is how large the difference is between minimum and maximum scattering power, relative to the average scattering power. In Case I this corresponds to b_1/b_0 .
5. The preferred scattering direction. For all three cases this is described by the parameter ψ_1 .
6. Depending on the case number additional information about α , σ_1 and σ_2 can be obtained.

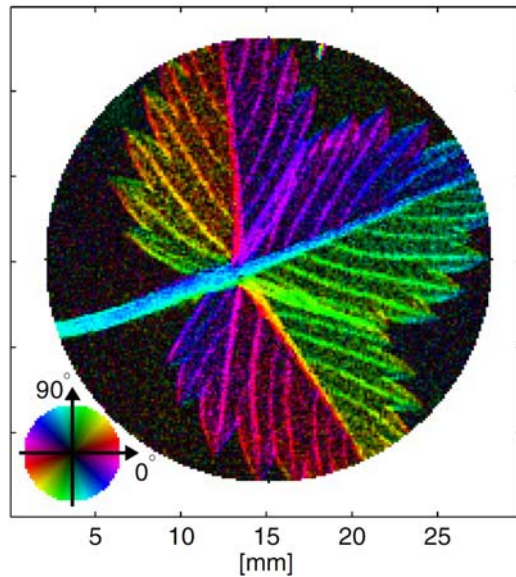


Figure 4.5. Combined color representation of the degree of orientation (mapped onto the image brightness) and the preferred scattering direction (mapped onto the image color, using the color wheel displayed in the bottom left corner) of the underlying texture micro-structure in the sample. This should be related to the visibility variations in Figure 4.2b and 4.2c. It is clearly seen how the fibers in the support structure of the leaf are aligned.

One convenient way to combine the information is to combine the degree of orientation and the preferred scattering direction in a color plot. This type

of plot highlights areas of strongly aligned structures, while showing their ordering direction. The preferred scattering direction (or sometimes the preferred ordering direction which is perpendicular to the prior) is mapped onto the color. Then the degree of orientation is mapped onto the brightness of the colors. An example of such a map is shown in Figure 4.5, which is a color representation of the leaf shown in Figure 4.2. The resulting image clearly highlights the presence of strongly aligned structural details (fibers), and their respective preferred alignment angle in the supporting branch structures of the leaf. A more thorough discussion of the different types of signals recorded using directional dark-field imaging will follow in Section 4.3. In that section we relate the results obtained with directional dark-field imaging to results obtained using synchrotron small-angle x-ray scattering mapping.

In summary we have introduced the novel imaging technique of directional dark-field imaging. We have also developed a simple scattering model to describe the angular variations of the visibility in grating based directional dark-field imaging. This model provides the foundation for the technique. In the following we will introduce the two papers that first introduced the method of directional dark-field imaging.

4.2 Introduction to Paper III and Paper IV

In this section we summarize the most important points of Papers III (Jensen et al. 2010c) and IV (Jensen et al. 2010d). These two papers introduced the novel method of directional x-ray dark-field imaging. Important key figures are included. For the full details of the papers the reader is referred to the full version of the papers in Appendix B.

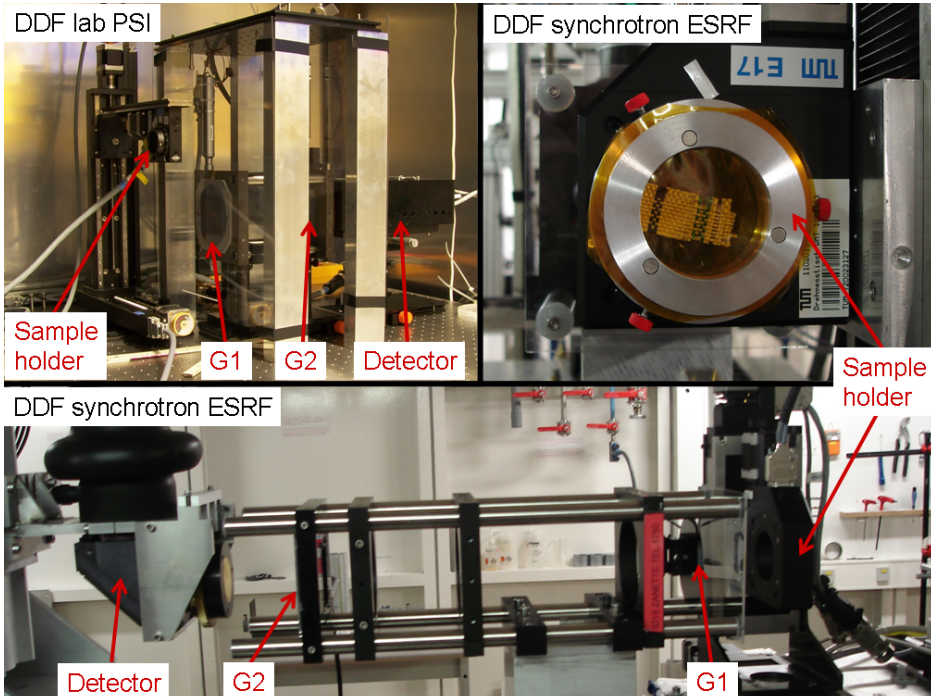


Figure 4.6. Picture of the two experimental set-ups used for directional x-ray dark-field imaging. On the top left is a picture of the set-up used in the laboratory at PSI. The set-up at ID19 at the ESRF is shown in the other two images. The set-ups consist of a phase grating G1 and an analyzer absorption grating G2. The sample is rotated around the optical axis. In the picture from PSI the sample holder is translated out of the beam.

Shown in Figure 4.6 are photographs of the two experimental set-ups used for Papers III and IV. For Paper III the experiments were conducted at the PSI with a laboratory source. For Paper IV the experiments were conducted at ID19 at the ESRF. Both set-ups consist of a sample holder, a grating interferometer with a phase and an absorption grating and a detector. The sample holder can rotate the sample around the optical axis of the set-up. Not visible in the picture of the laboratory set-up at the PSI is the

third grating used for that experiment. A noteworthy difference between the two set-ups is the difference in the intergrating distances. At the PSI the intergrating distance was 200 millimeter, while it was 447 millimeter at ID19 at the ESRF. Additional experimental details can be found in Table 2.2 on page 23. Shown in the third picture is the specially developed sample holder in the set-up at ID19 at the ESRF. Mounted in the sample holder is the fiber mesh sample imaged in Paper IV.

4.2.1 Introduction to Paper III

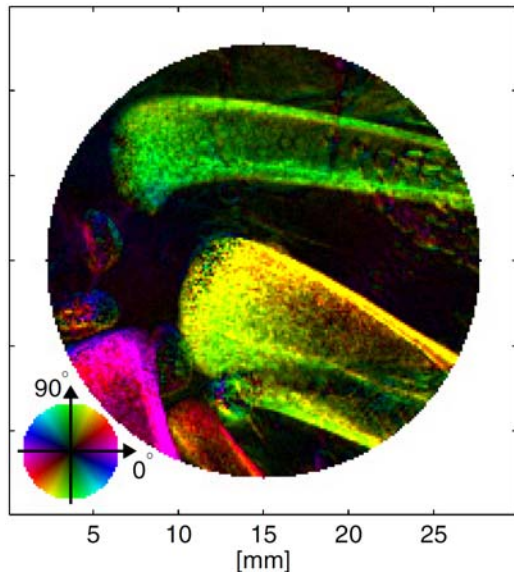


Figure 4.7. Imaging of a biological specimen - a chicken wing. Combined color representation of the degree of orientation (mapped onto the image brightness) and the preferred scattering direction (mapped onto the image color, using the color wheel displayed in the bottom left corner) of the underlying texture micro-structure in the sample. In many parts of the sample, we observe a strong dark-field signal that exhibits clear orientational preference in correspondence with the underlying bone ultra-structure.

Paper III has the title: 'Directional x-ray dark-field imaging' (Jensen et al. 2010c). The paper introduced for the first time the method of directional x-ray dark-field imaging. The paper does so by introducing the physical principle behind the effect of how one can take advantage of the grating geometry to extract directional information about the local integrated scattering amplitude.

After presenting the principle the paper goes on to experimentally demonstrate the technique. This is done using the leaf presented in Figures 4.2 and 4.5. The interpretation of the data obtained using directional x-ray dark-field imaging is in the paper supported by complementary small-angle x-ray scattering measurements made on the same leaf sample. (A full discussion of the comparison of directional x-ray dark-field imaging and small-angle x-ray scattering is given in Section 4.3 on page 54.) Having demonstrated the method with a leaf it was successfully applied to several specimens of different character, proving the method to be useful for a broad range of applications. The results on a biological sample - a chicken wing are reported in detail. The color representation of that sample is shown in Figure 4.7. The natural function of bones is to take up force at the dense bone heads and transmit it through the middle section to the other end. We would thus expect to see strong axial alignment in the middle section of the bone, and stronger scattering with less defined orientations at the bone ends. In Figure 4.7 the expected features are clearly seen. The angle of orientation in the middle section of the bones is aligned with the bone axes, whereas the orientation becomes less defined in the bone heads.

The results presented in Paper III are all explained using the Case I model of sinusoidal variation of the visibility. The model is in this paper founded on empirical observations. The general model described in Section 4.1 was introduced in the following paper (Paper IV, (Jensen et al. 2010d)).

One very important feature of Paper III is that all of the results were obtained using a conventional x-ray tube. We thus demonstrated that directional x-ray dark-field imaging can be conducted in the home laboratory. This enables widespread application of the method.

As the directional x-ray dark-field imaging is a new imaging contrast developed during the PhD, all code to analyze the data and display the results needed to be developed and written. In Appendix A an example of the code used for this is attached.

4.2.2 Introduction to Paper IV

Paper IV has the title: 'Directional x-ray dark-field imaging of strongly ordered systems' (Jensen et al. 2010d). In Paper IV the method of directional x-ray dark-field imaging is extended to cover the special case of strongly ordered systems. Where Paper III studied only Case I systems, this paper focuses on Case II and Case III systems. In Paper III we demonstrate how the directional dark-field signal of certain strongly ordered systems can not be satisfactorily described using the Case I methodology of sinusoidal visibility variations presented in Paper III. We develop the simple scattering model

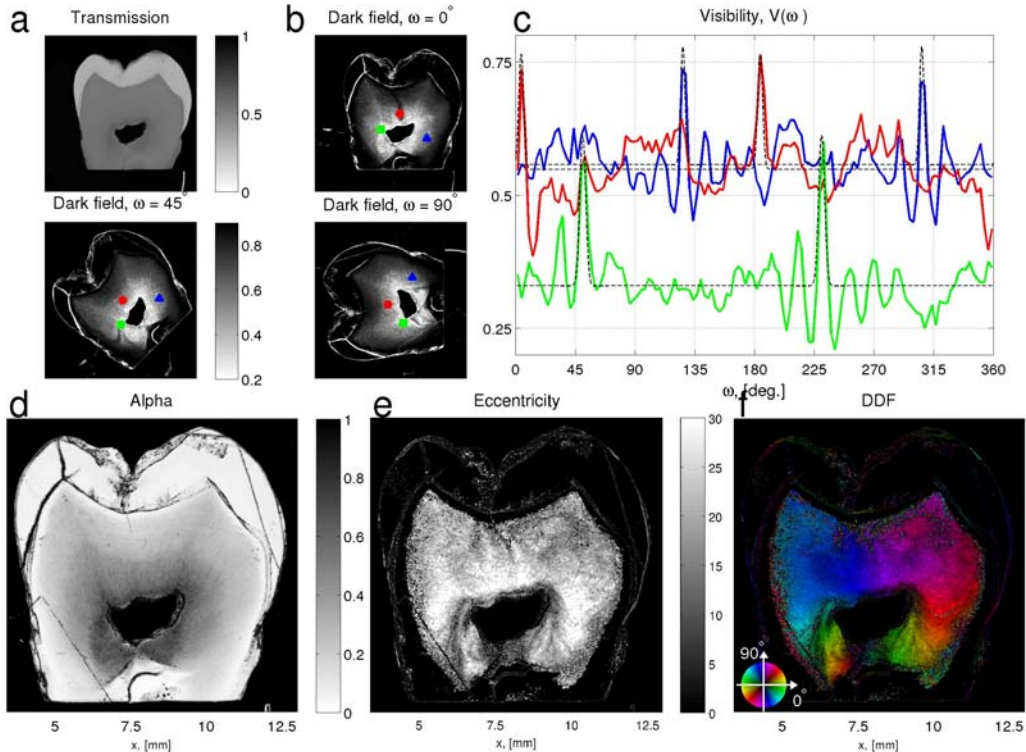


Figure 4.8. Imaging of a tooth slice. (a) X-ray transmission image. (b) Dark-field images for three different sample orientations ω . (c) Visibility $V(j, k, \omega)$ as a function of ω for three different sample regions. The dashed black lines are model fits to the measured values using the Case III model. (d) The parameter α describing the proportion of the beam that has been scattered. (e) Map of the eccentricity of the fitted local scattering profile. (f) Combined color representation. The eccentricity is mapped onto the image brightness and the angle of orientation of the tubuli in the dentin ($\psi_1 + 90^\circ$) is mapped onto the image color, using the color wheel displayed in the bottom left corner. Length scale given in (d-f).

described in Section 4.1 to account for these new observations, and subsequently verify the model using experimental data. The experimental data includes directional dark-field images of polypropylene fibers and a human tooth slice. The results of the tooth slice are shown in Figure 4.8. The tooth represents a Case III type system where $K_1 > 0$ and $\alpha \neq 1$. This can be seen when comparing the visibility variations in Figures 4.4 and 4.8c. We see that the visibility in Figure 4.8c varies non-sinusoidally and with a non-zero baseline characteristic of Case III systems.

Using directional dark-field imaging, we image the orientation of the tubuli in the tooth (Figure 4.8f), even though they are highly oriented and thus have 2D scattering profiles that are very eccentric. This high degree of orientation manifests it self as very narrow peaks in the visibility in Figure 4.8c, and high values of the eccentricity ($e \equiv (\sqrt{\sigma_1^2 - \sigma_2^2}) / \sigma_1$) in Figure 4.8e. The study of the tubuli in dentin in teeth will be particularly interesting when the method is extended to three dimensions. This however still requires the development of novel tensorial x-ray computer tomography reconstruction algorithms, which presently do not exist.

The model presented in Paper IV adds to the possible application of directional dark-field imaging for nondestructive testing of for example fiber reinforced materials. The results in Paper IV were all obtained using synchrotron radiation. However as Paper III demonstrated the technique also works with a conventional x-ray tube and the new results are thus directly applicable also to laboratory experiments using x-ray tubes. One can thus envisage widespread application of the method.

With these two papers the technique of directional dark-field imaging has been introduced and demonstrated for a wide variety of samples. In the following section we will go into detail with investigating the different signals obtainable with directional x-ray dark-field imaging. These are compared to measurements conducted using small-angle x-ray scattering mapping.

4.3 Directional dark-field imaging vs small-angle x-ray scattering mapping

In directional dark-field imaging a grating interferometer is used to record the integrated small-and ultrasmall-angle x-ray scattering component perpendicular to the lines of the gratings. By rotating the sample the angular variation of the scattering signal is recorded and subsequently analyzed. A different way to measure the angular variations of the local scattering pattern is to use a small-angle x-ray scattering (SAXS) set-up with a pencil beam and a 2D detector. 2D scattering patterns are then recorded point by point thus mapping out the complete sample. An orientational analysis similar to the one made with directional dark-field imaging can be made by direct analysis of the 2D SAXS patterns. The method for the directional SAXS analysis has been outlined in the co-authored paper 'Multimodal x-ray scatter imaging' (Bunk et al. 2009).

In this section the principle behind 2D SAXS pattern analysis will be outlined, and the results will be compared to that of directional dark-field imaging. A comparison of the two methods will be made using the leaf presented in Figures 4.2 and 4.5 in Section 4.1. We conducted these complementary experiments to further verify the findings in Paper III (Jensen et al. 2010c) and demonstrate the origin of the different signals.

Experimental set-up for SAXS mapping

The SAXS mapping experiments were performed at the coherent Small-Angle X-Ray Scattering beamline (cSAXS) at the Swiss Light Source (SLS). The experimental set-up is shown in Figure 4.9. An x-ray energy of 8.7 keV was selected and focused to a horizontal spot on the sample of $30 \times 30 \mu\text{m}^2$ using beamline optics. The experimental setup then consisted of an x/y translation stage with the sample holder, a 7 m long evacuated flight-tube with a 3 mm diameter beam-stop in vacuo (not shown), immediately followed by a state-of-the-art pixelated single photon counting PILATUS detector (Brönnimann et al. 2006). Using the pencil beam the sample was scanned in x and y, such that the full 2D scattering patterns from more than 50'000 points on the sample were measured. (More experimental details are provided in Table 4.1 on page 56).

The scanning measurements for the SAXS mapping are repeated twice. The first time an attenuated beam is used, the beamstop is removed and the absorption of the sample is measured. The second time the beam is not attenuated, the beamstop is used to protect the detector from the direct

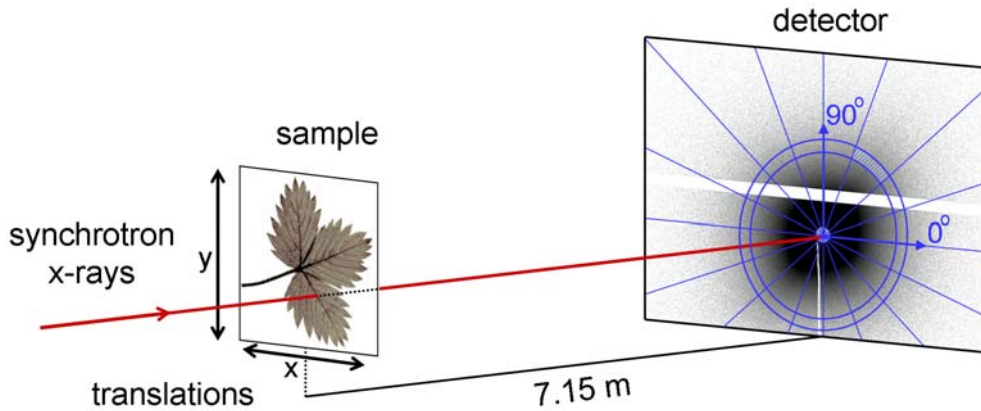


Figure 4.9. SAXS mapping set-up. The sample is mounted in the x-ray beam on an x/y translation stage. The SAXS pattern is recorded 7.15 meters from the sample with a PILATUS detector. To block the direct beam, a beam-stop was placed immediately in front of the detector. The white horizontal area across the displayed SAXS pattern is due to a dead area on the detector. The 2D scattering pattern is analyzed for orientation for a specific q -range. Figure not drawn to scale.

beam and the scattering from the sample is recorded. In that way the sample scattering as well as the sample absorption are accurately determined. For each step we move the sample (x_i, y_j) we record a full 2D scattering pattern $I(m, n)$ on our detector. The sample transmission can then be determined as,

$$T = \frac{\sum_{m,n} I_{bs\text{-out}}^s(m, n)}{\sum_{m,n} I^r(m, n)}, \quad (4.10)$$

where ^(*s*) refers to measurement made with sample, ^(*r*) to reference measurements without sample and ^(*bs-out*) to the fact that no beam stop was used and the beam was attenuated. The sum runs over all pixels (m, n) on the detector. This assumes that the scattering is negligible compared to the transmission, which was the case for the leaf sample under the applied conditions.

The scattering signal is recorded on a position sensitive detector. To reduce the data complexity it is convenient to describe the intensity as a function of radial distance to the center, r , and azimuthal angle, θ . For the postprocessing the detector is split into 16 azimuthal regions and 200 radial regions. An example of these regions can be seen in Figure 4.9.

The scattering in a region described by the azimuthal region Θ and the

radial region R can be described as follows,

$$S(R, \Theta) = \frac{\sum_{r \in R, \theta \in \Theta} I_{bs-in}^s(r, \theta) / A(r, \theta)}{T}, \quad (4.11)$$

where A is the area associated with each pixel and ($_{bs-in}$) refers to the fact that a beam stop was used and the beam was not attenuated.

For many typical SAXS samples with moderate ordering the scattering intensity is well approximated by a first order Fourier expansion (Bunk et al. 2009),

$$S(t, \theta) \approx c_0(r) + c_1(r) \cos(2[\theta - \varphi_1(r)]), \quad (4.12)$$

where c_0 describes the average scattering intensity, and c_1 the oriented part of the scattering. The shift of the cosine, φ_1 , describes the preferred orientation of the scattering. Note the close resemblance between equation (4.7) that describes the orientational variations of the SAXS signal and equation (4.12) which describes the Case I sinusoidal variations of the visibility. Equation (4.12) where S takes on the maximum value in the direction of maximum scattering does not include the factor of π included in equation (4.7) where the visibility takes on the minimum value in the direction of maximum scattering.

To outline the similarities and differences between the two methods as well as to build support for the claims of directional dark-field imaging made so far in this chapter we will now signal by signal compare the two methods.

	SAXS mapping	DDFI
X-ray source	Synchrotron	Fixed anode
Energy	8.7 keV	\sim 28 keV
Monochromatic	yes	no
Pixel size detector	172 μm	172 μm
Pixel size image	100 μm	142 μm
no. points	240 x 240	187 x 187
Beam size	30x30 μm^2	-
Field of view	24x24 mm 2	ϕ 26 mm
Total exp. time	35 min	96 min

Table 4.1. Table of experimental details for SAXS mapping and directional x-ray dark-field imaging experiments on leaf.

The experimental details for the two measurements are summarized in Table 4.1. Since the measurements were made at different energies a quantitative comparison is not possible even though the exact same sample was measured with the two methods.

Results

Absorption

For the grating interferometer, the absorption was measured for every orientation as outlined in equation (2.15) on page 14. The absorption was also measured using SAXS mapping as outlined in equation (4.10). The two results are shown in Figure 4.10. We should note that the energy for the SAXS mapping measurement at 8.7 keV was much lower than for the grating measurements at 28 keV, and the absorption subsequently higher. Generally it is also worth noting that the pixel size is a little bit smaller in the SAXS mapping measurements, and the resolution thus also slightly better.

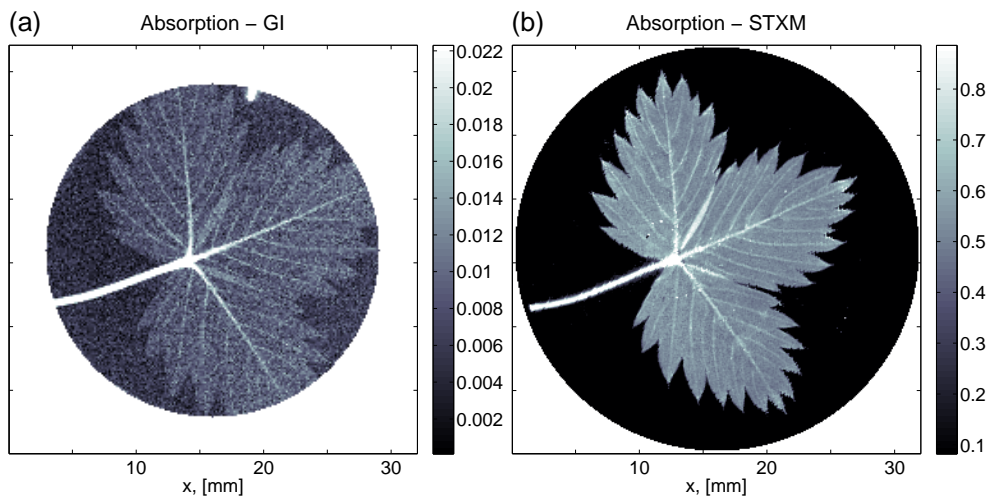


Figure 4.10. Comparison between grating interferometry and SAXS mapping - Absorption. (a-b) shows the absorption as measured with the grating interferometer and in the SAXS mapping experiment respectively.

Scattering in different directions

With the grating interferometer the scattering in different directions is measured by rotating the sample. The dark-field signal is extracted as explained in equation (2.19) on page 14. A similar contrast mechanism can be extracted from the SAXS mapping experiments, by using only one of the 16 angular ranges, Θ , described in equation 4.11. The scattering signal from the SAXS measurements are extracted by integrating over all the radial regions ($q \in [0.025 - 0.16] \text{ nm}^{-1}$) in each angular range. In Figure 4.11 a comparison between the two types of images are shown. The dark-field images have

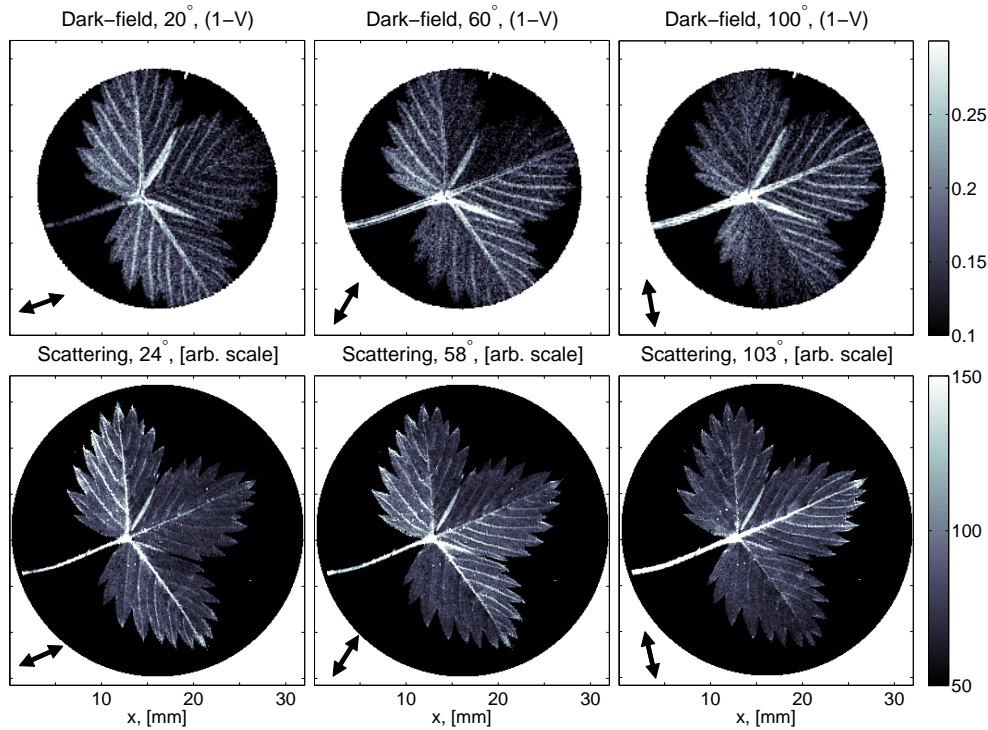


Figure 4.11. The angular variation of the scattering signal. First row: Dark-field images made using grating interferometry. The scattering amplitude(1-visibility) for different sample orientations is imaged. The dark-field images have been rotated back, so that the leaf is oriented the same in all images. The corner arrows show the probed scattering direction. Second row: SAXS images made by integrating scattering in only one angular direction. The arrow in the corner shows the scattering direction. The integrated q -range is: $[0.025-0.16] \text{ nm}^{-1}$.

been rotated back, so that the leaf is oriented the same in all images. The arrows in the bottom left corner shows the scattering direction used for producing each of the images. For the dark-field images the arrow thus show the direction perpendicular to the grating lines. Again we can only make a qualitative comparison as the measurements are made at different energies and thus cover different q -ranges. In all six panels we do see how the fibers aligned perpendicular to the scattering direction show the strongest scattering.

An important difference between the two measurements is the signal to noise ratio. For the SAXS mapping measurements we were using the full 10^6 dynamic range of the detector, having up to 10^9 counts per point, resulting in up to 10^8 counts per angular range as used for the images in Figure

4.11. In the grating measurements, we only had 10^4 counts per point for each of the 16 phase steps used to generate each image in Figure 4.11. Only a fraction of these counts were used to produce the dark-field image, as the unreduced oscillation amplitude was around 10%. We thus see that the counting statistics for the two measurements were significantly different. In the images this is also seen as a lower signal to noise ratio in the dark-field images. Both measurements were made using PILATUS detectors (Brönnimann et al. 2006).

Average scattering

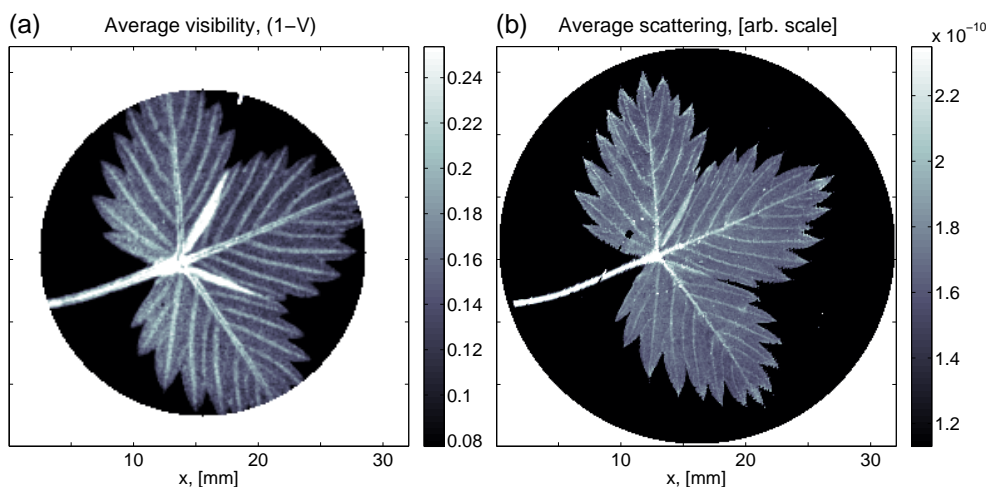


Figure 4.12. Comparison between grating interferometry and SAXS mapping- Average scattering. (a-b) The panels show the average scattering as measured using directional dark-field imaging and SAXS mapping respectively. This corresponds to the parameters b_0 and c_0 in equations (4.7) and (4.12) respectively.

Above we saw how the scattering varied in different directions. Having measured the scattering in directions over 360 degrees, the total average scattering can be determined. For the grating interferometer this corresponds to b_0 in equation (4.7). For the SAXS mapping experiments this corresponds to integrating the full 2D scattering pattern or the parameter c_0 in equation (4.12). The results are displayed in Figure 4.12. As with the measurements above we see that there is a qualitative agreement between the two measurements, even though the directional dark-field measurement suffers from poorer resolution and statistics. The strongest scattering takes place in the petiole and in the fibers extending from the center of the leaf.

Degree of orientation of scattering

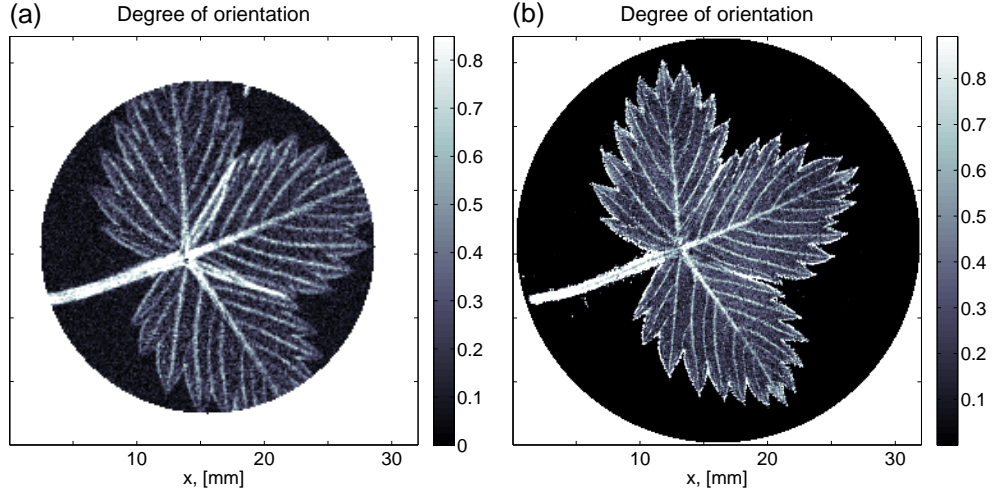


Figure 4.13. Comparison between grating interferometry and SAXS mapping - Degree of orientation. (a-b) The panels show the degree of orientation as measured with directional dark-field imaging and SAXS mapping respectively. This corresponds to the parameters b_1/b_0 and c_1/c_0 in equations (4.7) and (4.12) respectively. Note that the two images are plotted using the same color scale. We note good quantitative agreement.

One of the special features with directional dark-field imaging is the possibility to measure the angular variation of the strength of the scattering signal. This can be quantified in the degree of orientation, where the degree of orientation is defined as b_1/b_0 , and describes the relative variation of the scattering intensity. For the SAXS mapping measurements we can define a similar quantity. Using equation (4.12) we define the degree of orientation for the SAXS mapping measurements to be c_1/c_0 , describing the relative variation of the scattering intensity. These two signals are displayed in Figure 4.13. We note that even though the probed q -ranges are different these two signals can be quantitatively compared. The two images are thus displayed using the same color scale. The reason why this comparison is possible must be because the angular variation of the scattering amplitude is independent of the momentum transfer q . Even though these two images are recorded under two different experimental conditions they probe the same quantity. These SAXS measurements thus support the claims we have made above about how it is possible to map the angular variations of the scattering amplitude using directional x-ray dark-field imaging.

Combined color representation

There is one final signal we will examine. Using both types of measurements it is possible to determine the preferred scattering direction using equations (4.7) and (4.12). The preferred scattering direction corresponds to ψ_1 and φ in the two equations respectively. These directions of maximum scattering can be combined with the degree of orientation from above in a color representation. The preferred scattering direction is mapped onto the color and the degree of orientation is mapped onto the brightness of the colors. In Figure 4.14 the two color images obtained using SAXS mapping and directional dark-field imaging respectively are displayed. We see striking similarity between the two. Again we must remember that the two images display the same quantity, but have been recorded in two completely different experimental set-ups. The similarities however confirm our claims that we can use directional x-ray dark-field imaging to image the orientational variations of the local scattering amplitude.

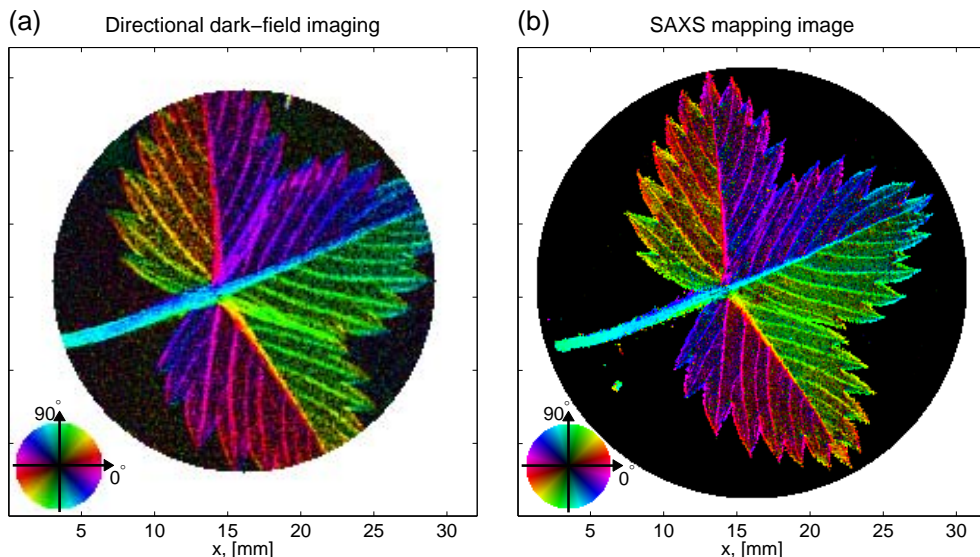


Figure 4.14. Comparison between grating interferometry and SAXS mapping - Color representation. Combined color representation of the degree of orientation (mapped onto the image brightness) and the angle of orientation (mapped onto the image color, using the color wheel displayed in the bottom left corner). (a) was measured using a grating interferometer in a laboratory set-up and (b) using a SAXS mapping with a synchrotron beam. We note good agreement between the two images.

We have now demonstrated how the different signals recorded in directional dark-field imaging can be related to measurements made using SAXS

mapping. We also demonstrated good qualitative agreement in the example of the strawberry leaf. These results further support the claims about the origin of the different directional dark-field signals made in Papers III and IV and in section 4.1.

We will end this comparison with a word of caution. The grating interferometer is in general sensitive to very small values of q . In (Jensen et al. 2010d) we demonstrate that the dark-field signal can be explained with a scattering curve of width 0.5-10 μm on the detector. This corresponds to q -values in the range $[1 \times 10^{-4} - 20 \times 10^{-4}] \text{ nm}^{-1}$. These q -values are much smaller than the values that can be probed with a standard small-angle x-ray scattering set-up. In our SAXS mapping experiment we probed q -vectors in the q -range, $[0.025-0.16] \text{ nm}^{-1}$. The grating interferometer and hence the directional x-ray dark-field signal can thus be sensitive to ultrasmall-angle x-ray scattering, which for hierarchical structures can differ from the small-angle x-ray scattering. For non-hierarchical samples this difference in probed q -ranges does not influence the results. The leaf is an example where no hierarchical structures are influencing our images as we can clearly see in Figure 4.14.

4.4 Outlook and applications

We have in this chapter as well as in Papers III-IV introduced and demonstrated the method of directional x-ray dark-field imaging (DDFI). Using DDFI we demonstrated how more information than just a single value for each pixel could be obtained by mapping the local texture of structural variations smaller than the actual image resolution.

It should be emphasized that some of the advantages of the presented DDFI approach are (a) that the information can be obtained with a conventional x-ray tube, which is a prerequisite for widespread practical applications, and (b) that a full two-dimensional image with information on the orientation and degree of structural ordering is acquired for all pixels in the image simultaneously, allowing fast and detailed investigation of large areas.

The possible applications that we foresee for this method are numerous. For widespread application this could include non-destructive testing and monitoring. As lightweight fiber-reinforced materials are being used more widely today (Gibson 2010), the quality testing of these materials could be one example. This could include testing of the integrity of the fibers after embedding or failure. One of the main advantages here is that DDFI can study these fiber structures even if they are buried in an embedding matrix. The study of fibers could also cover natural materials like wood. In Paper III we demonstrated that DDFI could be used to image the fiber orientation in wood as well as the presence and location of knots. This ability could be used for automatic positioning of the wood or for quality control.

One possibility is that DDFI could be integrated in a conveyor belt set-up for quality control. This could be done with as little as 9 line detectors, used in sets of 3 to record the dark-field signal in three different directions using the method of Kottler et al. (2007). The method could thus be integrated into a production line for online testing. The possible industrial applications are not limited to the few examples mentioned here. The method can be applied wherever the local texture is of interest.

Besides the industrial applications there are also a number of possible biomedical applications. For high resolution studies DDFI could be used to study the reorientation of collagen in cartilage, which is of great interest to osteoarthritis research and diagnostics (Shimao et al. 2005, 2006). Detailed structural investigation using DDFI of the bone-ultrastructure could benefit research and diagnostics of osteoporosis (Müller 2009). In osteoporosis it is very important for both research and diagnosis to be able to determine the local ordering which is important for the strength of the bone. SAXS mapping has been used for imaging of the orientation of the mineral particles in bone (Roschger et al. 2001), and the first test experiments on bone have

been performed. A second biological application for hard biological materials is demonstrated in Paper IV (Jensen et al. 2010d) where DDFI is used to image the dentin tubuli in teeth.

For biomedical applications on soft tissue we have tested several possibilities. MRI diffusion tensor imaging is used to map for example the fiber tracts in the brain by tracking the water diffusing along the nerve fibers. We tested whether we could directly image the scattering from these nerve fibers using DDFI. We had thin slices of rat brain nicely prepared, and used the 11th talbot distance at 17.6 keV at ID19 at the ESRF for the experiments. The scattering signal from the fibers were however too weak to be recorded. For the possibility of measuring these fibers directly an even more sensitive grating interferometer is thus needed.

Another possible soft biomedical application is the study of muscle fibers. If it is possible to demonstrate that the orientation of muscle fibers can be imaged using DDFI with a laboratory source this would have great medical implications. First test experiments were performed but further experiments will be needed to evaluate whether this is possible or not.

Finally there is the possibility to extend the method of DDFI to 3D. This extension would provide the local orientation of the scattering structures in three dimensions, so that e.g. the 3D local orientation of a fiber could be determined. For the reconstruction of the orientation of a single fiber this should be quite simple. For more complex structures this will however require the development of novel tensorial x-ray computer tomography reconstruction algorithms, which presently do not exist. One also has to consider how this information can practically be recorded in an experimental set-up. The extension will be extremely interesting for most of the examples mentioned above.

We believe that all of these possible applications could open up for the widespread application of the method. As the method is demonstrated with a laboratory x-ray source there are no fundamental limitations hindering this widespread application. Commercial availability of grating interferometers is presently the major limiting factor.

In the introduction to this chapter it was mentioned that x-ray dark-field imaging can be performed using alternate methods. One example is the Analyzer Based Imaging (ABI) approach. In ABI it is also only the scattering in a specific direction that is probed. The approach of directional x-ray dark-field imaging could thus also be used with ABI. This has yet to be experimentally demonstrated. Due to the limitations caused by the required monochromaticity and the limited field of view the ABI approach will be significantly slower for extended samples. Using ABI for directional dark-field imaging with a laboratory source will thus require substantial time. However

as ABI uses crystal reflections, one benefit would be that the method could be tuned to be sensitive to a specific momentum transfer, q . A second alternative approach for directional dark-field imaging was discussed in Section 4.3 on page 54 where small-angle x-ray scattering was used to generate dark-field contrast. The benefits and drawbacks of this method were also discussed.

So even though the method of directional x-ray dark-field has been developed using a grating interferometer, several of the results can be extended to other imaging approaches. These alternative approaches have different benefits and drawbacks. The main advantage for the grating based approach being that large areas can be probed simultaneously and that the method works with a laboratory x-ray source. We thus envisage that the grating based approach will be the one most easily developed for widespread use.

Chapter 5

Small-angle x-ray scattering tomography

In the previous chapters we have been focusing on results obtained using grating interferometry. In Chapter 3 we focused on tomographic reconstructions, while Chapter 4 focused on analyzing the scattering signals. In this chapter we will combine these two approaches and investigate the tomographic reconstruction of the scattering signal.

As mentioned in Chapter 4 it is possibly to use the dark-field signal for dark-field tomography (Wang et al. 2009, Chen et al. 2010, Yashiro et al. 2010, Bech et al. 2010). We will not go into detail about dark-field tomography. But inspired by the possibilities of grating based dark-field tomography and the success with 2D SAXS mapping in section 4.3 we did investigate the possibilities of extending SAXS mapping from 2D to 3D using tomography.

This chapter serves as an introduction to Papers V (Jensen et al. 2010e) and VI (Jensen et al. 2010f). The two papers demonstrated for the first time high resolution small-angle x-ray scattering computed tomography (SAXS-CT) and presented results on two different types of SAXS-CT.

5.1 Theory

The properties and functions of many soft matter systems such as soft tissues are often strongly related to the structure at the micro- and nanolevel. Detailed imaging of these structures can provide insight into this correlation. Small-angle x-ray scattering (SAXS) is a widely used method to probe the micro- and nanostructure of noncrystalline materials (Guinier & Fournet 1955, Glatter & Kratky 1982, Narayanan 2009). Structural variations in heterogeneous samples have been mapped out using a scanning-based set-up and

a pencil beam (Gourrier et al. 2007, Bunk et al. 2009). These experiments provide 2D structural information, but often do require destructive sample preparation and provide no depth-resolved information about the sample. One way to overcome this limitation is to use x-ray tomography. Standard x-ray absorption computed tomography (CT) has been used for many years for non-invasive 3D studies (Kalender 2006). CT provides access to volume-resolved information and requires little sample preparation. While providing excellent spatial resolving power, CT has an inherent lack of information about the nanoscale structure of the sample.

It is possible to combine SAXS and CT to small-angle x-ray scattering tomography (SAXS-CT). SAXS-CT has been demonstrated in a few cases with soft matter and biological samples[†] (Harding et al. 1985, 1987, Harding & Kosanetsky 1989, Kleuker et al. 1998, Schroer et al. 2006, Stock et al. 2008).

The combination of a scanning-probe imaging technique with tomography requires the acquisition of a vast amount of data. As a consequence, previous studies have been limited to comparatively low spatial resolution. Furthermore, the requirement of fast data acquisition has often compromised SAXS data quality such that only a qualitative analysis was possible, but the rich tools of quantitative SAXS analysis could not be brought to bear. The advent of brighter sources, fast and essentially noise-free detectors, and automated analysis schemes have made possible the efficient acquisition of hundreds of thousands of SAXS patterns. These larger number of patterns are required to spatially reconstruct and resolve the micro- and nanostructure of extended soft matter and biological samples.

Experimental set-up

Figures 5.1 and 5.2 shows the experimental set-up and principle of SAXS-CT. 2D SAXS patterns are recorded using a pencil beam. This is repeated for each horizontal sample translation, s , and rotation, ω , such that 2D SAXS patterns are collected point by point. In this way a full tomographic data set is collected point by point using a 1st generation tomography approach. The collected 2D SAXS patterns are azimuthally averaged and sinograms are generated for each value of q_r (Figure 5.2a). Each sinogram is used to reconstruct the differential scattering cross section for the associated value of q_r (Figure 5.2b). Once the reconstructions have been made for all values of q_r it is possible to extract full scattering curves for all voxels in the sample

[†]For strongly scattering crystalline samples extensive work has been performed using diffraction tomography (Nielsen et al. 2000, Bleuet et al. 2008).

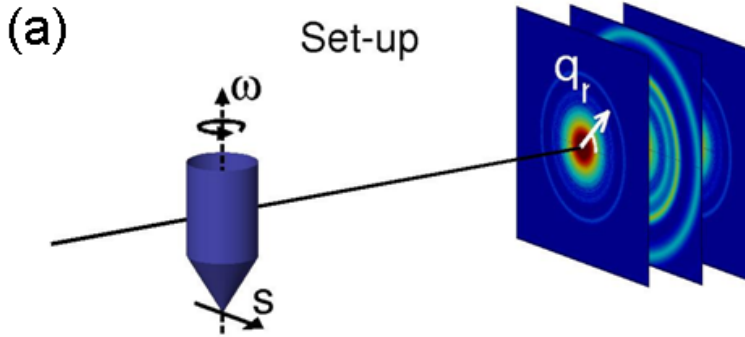


Figure 5.1. Small-angle x-ray scattering tomographic set-up. (a)

Using a pencil-beam, scattering patterns are collected by translating the sample through the beam (*s*), for different orientations (ω).

(Fig 5.2c). We note that in the example demonstrated in Figures 5.1-5.2 we see both the normal small-angle scattering curve at the smallest values of q as well as distinct Bragg peaks arising from different tissue types at larger values of q . In the following we will describe in detail how the reconstructions are performed.

Normally we define the scattering cross section $\frac{d\sigma}{d\Omega}$ through the following equation,

$$I(q) = (I_0/A_0) \frac{d\sigma}{d\Omega}(q) \Delta\Omega. \quad (5.1)$$

The scattered intensity from the whole sample, $I(q)$, in a certain solid angle $\Delta\Omega$ is given as the product of the incoming intensity per area I_0/A_0 , multiplied by the scattering cross section $\frac{d\sigma}{d\Omega}$, multiplied by the size of the solid angle $\Delta\Omega$. In the equation above the differential scattering cross section refers to the scattered intensity from the whole sample. If we now look at the scattering per unit volume $\frac{d\Sigma}{d\Omega} = \frac{d\sigma}{d\Omega} \frac{1}{V}$ (V being the scattering volume) we get,

$$I(q) = (I_0/A_0) V \frac{d\Sigma}{d\Omega}(q) \Delta\Omega. \quad (5.2)$$

Scattering from a sample can be then be described as,

$$I(s, \omega, q) = I_0 \int_0^L \underbrace{\left[e^{-\int_0^l \mu(\tilde{l}) d\tilde{l}} \right]}_{\text{Abs. before}} \underbrace{\frac{d\Sigma}{d\Omega}(l, q)}_{\text{Scattering}} \underbrace{\left[e^{-\int_l^L \mu(\tilde{l}) d\tilde{l}} \right]}_{\text{Abs. after}} dl \Delta\Omega. \quad (5.3)$$

The beam path through the sample defined by (s, ω) is parameterized by the variable l over which the integral runs. $I(q)$ is the scattered intensity for a

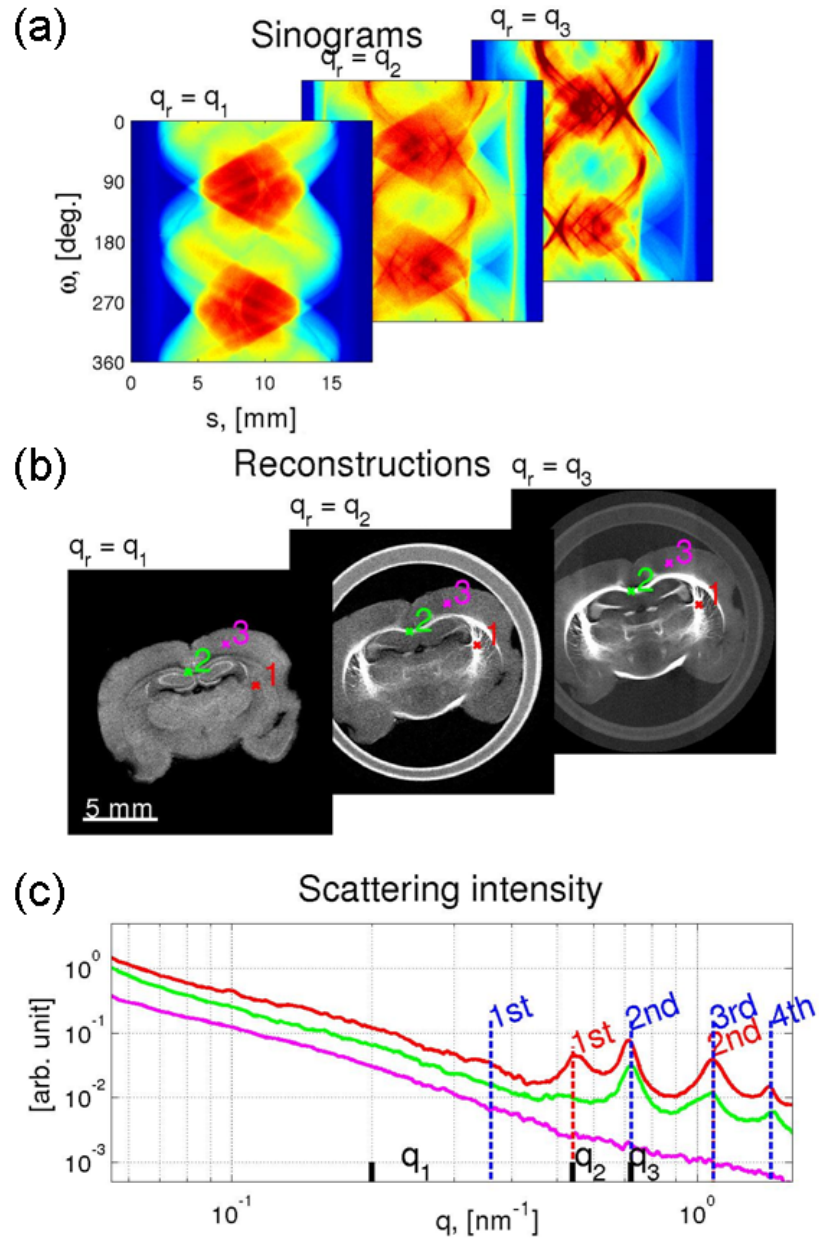


Figure 5.2. Small-angle x-ray scattering tomography working principle. (a) The scattering patterns that are collected point by point are azimuthal averaged and for each value of q_r , sinograms are generated. (b) These sinograms are used to reconstruct the differential scattering cross section for the associated value of q_r . (c) When the reconstructions are made it is then possible to extract complete scattering curves for all voxels in the sample, by combining the information from the slices reconstructed for each value of q_r . The curves shown here correspond to the points marked in (b). Bragg peak series from myelin sheaths (blue dashed lines) and cytoskeletal neurofilaments (red dashed lines) are marked in (c).

given q -vector, $\mu(l)$ is the local absorption length, and $\Delta\Omega$ is the solid angle covered by the detector element.

$\frac{d\Sigma}{d\Omega}(l, q)$ describes the scattering probability at a certain voxel in the sample. To determine the total scattered intensity we have to take the absorption taking place before and after the scattering events into account. Since all scattering occurs at small angles, the scattered photons can be assumed to exit the sample along the same path as the transmitted photons and it is thus possible to separate the absorption and scattering terms. We define the projected differential scattering cross section, $\mathcal{P}(s, \omega, q)$, and rewrite equation (5.3) as,

$$\begin{aligned}\mathcal{P}(s, \omega, q) &\equiv \frac{I(s, \omega, q)}{I_0 \cdot T(s, \omega) \cdot \Delta\Omega}, \\ &= \int_0^L \frac{d\Sigma}{d\Omega}(l, q) dl,\end{aligned}\quad (5.4)$$

where T is the sample transmission, $T(s, \omega) = e^{-\int_0^L \mu(l) dl}$. Equation (5.4) has the same form as the line integral of the attenuation coefficient known from absorption tomography seen in Chapter 3. We assume that the local differential scattering cross section is independent of the sample orientation such that the scattering is isotropic. It is then possible to reconstruct $\frac{d\Sigma}{d\Omega}(x, y, q)$ using a standard filtered backprojection algorithm for each value of q . We thus obtain spatially resolved scattering information about the micro- and nano-structures of a sample by reconstructing the local differential scattering cross section $\frac{d\Sigma}{d\Omega}(q)$ inside an extended sample using standard tomographic methods.

In the following we will introduce Papers V (Jensen et al. 2010e) and VI (Jensen et al. 2010f) that demonstrates the use of small-angle x-ray scattering tomography for imaging of soft tissue.

5.2 Introduction to Paper V and Paper VI

Paper V (Jensen et al. 2010e) and Paper VI (Jensen et al. 2010f) are both method papers on SAXS-CT. The main difference between the two are the q -ranges that are reconstructed and thus the origin of the scattering signals. In the following we will present the key results of the two papers. For the full details we refer to the Appendix where the complete papers are attached (Appendix B).

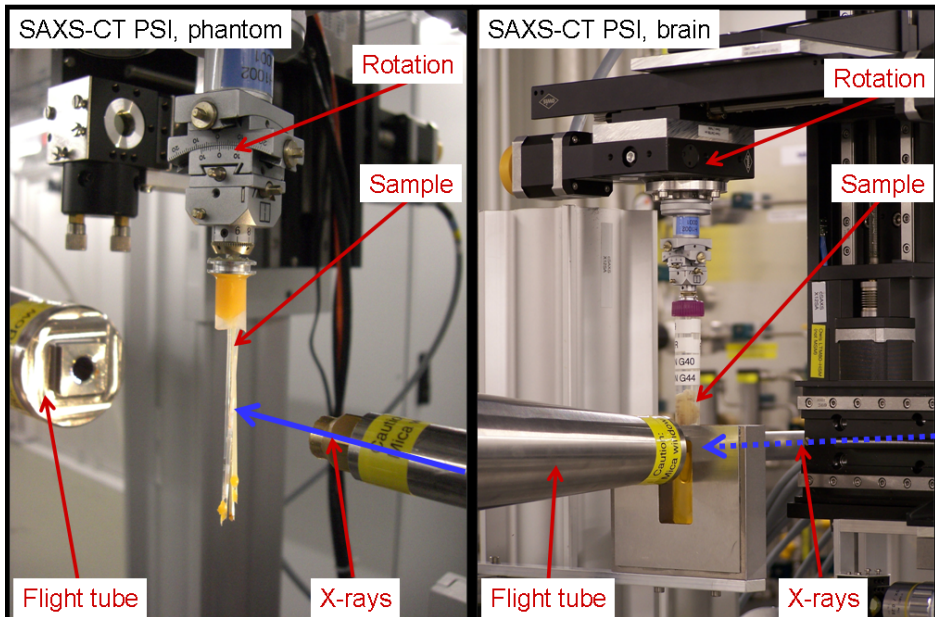


Figure 5.3. *Picture of the experimental set-up for SAXS-CT.* Picture of SAXS-CT set-up at the cSAXS beamline at the SLS two different samples mounted. On the left the phantom of Paper V is mounted. On the right the rat brains of Paper V and VI are mounted. The sample translation and rotation. The sample is in both cases translated through the pencil beam for each rotation angle, such that 2D SAXS patterns are collected point by point.

Shown in Figure 5.3 is two photographs of the experimental set-up used for Papers V and VI. The experiments were conducted at the cSAXS beamline at the SLS. The sample is translated through the pencil beam for each rotation angle, such that 2D SAXS patterns are collected point by point. Shown on the left is the phantom used in Paper V. Shown on the right are the two rat brains used in Paper V and VI. The brains are submerged in a water bath to avoid refraction and for optimizing the use of the dynamic range of the detector. The distance to the detector were for both experiments

longer than 7 meters.

5.2.1 Introduction to Paper V

Paper V has the title: 'Brain tumor imaging using small-angle x-ray scattering tomography' (Jensen et al. 2010e). The paper is a method paper demonstrating the possibilities of small-angle scattering tomography using two different samples.

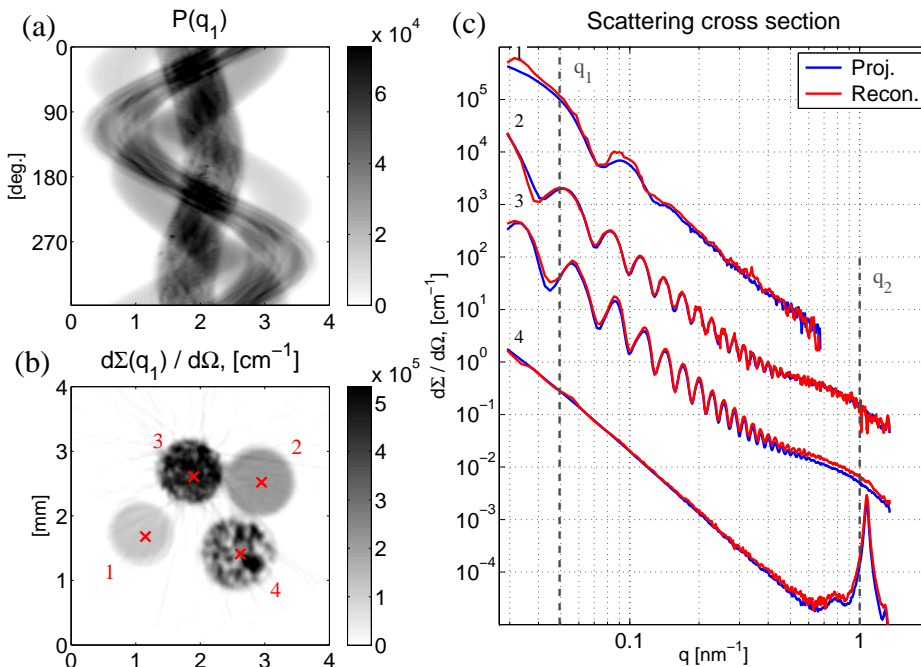


Figure 5.4. Reconstruction of phantom. SAXS-CT was performed on a phantom consisting of four capillaries. The capillaries were filled with a colloidal suspension (1), two concentrations of micelles (2-3) and silver behenate (4) respectively. (a)-(b) Show the scattering amplitude sinogram for a specific momentum transfer ($q_1 = 0.049 \text{ nm}^{-1}$), and the corresponding reconstructed differential scattering cross section of the sample. (c) Shows the reconstructed (red) and projection (blue) differential scattering cross sections for the four capillaries. The reconstructed scattering curves are taken from single voxels and are offset by two decades for clarity. Note that the reconstructed scattering curves span up to six decades, and that more than 20 size oscillations are clearly reconstructed in sample (3).

The first sample is a soft matter phantom with several standard SAXS samples. Figure 5.4 displays some of the experimental results for a single

tomographic slice through the phantom. In Figure 5.4a-b the projected differential scattering cross section sinogram and the reconstructed differential scattering cross sections for a specific q -value are displayed. Similar reconstructions were made for all recorded values of q , thus reconstructing the full differential scattering cross section for 189x189 different voxels in the slice. The reconstructed differential scattering cross section for four single voxels, each of volume $30 \times 30 \times 40 \mu\text{m}^3$ are displayed in Figure 5.4c. The reconstructed scattering curves of $\frac{d\Sigma}{d\Omega}(x_i, y_i, q)$ (shown in red) are compared to $\frac{d\Sigma}{d\Omega}(q)$ (shown in blue) obtained using the same samples in standard SAXS projection geometry. The latter were obtained from projections where only a single component was contributing to the signal, which corresponds to measurements using standard SAXS projection geometry. The projection scattering curves have been normalized to the sample transmission, and sample volume as known from absorption tomography. All curves are reconstructed on an absolute scale. We note that the reconstructed scattering curve of a single voxel inside the sample is identical to the scattering curves measured using standard SAXS projection geometry. In the paper we thus conclude that we can reconstruct the full SAXS curve associated with a small volume inside our sample.

The results in Figure 5.4 demonstrate that a quantitative reconstruction of the local differential scattering cross section is possible with SAXS-CT. The structural information on the nanoscale obtained through SAXS-CT clearly demonstrates its complementarity to tomography based on absorption or phase-contrast. Using the spatially resolved full scattering curves it is possible to identify the content of each of the four capillaries. Capillaries (1), (2) and (3) each contain monodisperse spheres with radius, $r \sim 60 \text{ nm}$, $r = 110 \text{ nm}$ and $r = 110 \text{ nm}$ respectively. The fourth capillary shows a Bragg peak corresponding to a period of 58.4 nm. We thus obtain important information about the nanostructure of the content of each capillary without having any *a priori* knowledge. We can even see the difference in concentration in capillaries (2) and (3) giving rise to a difference in the differential scattering cross section at small values of q due to the static structure factor of the interparticle interaction. The Bragg peak from the material in the fourth capillary is the (0 0 1) peak of the silver behenate crystal powder in the capillary.

Note how the reconstruction is obtained with high q -resolution, demonstrated by the resolving of more than 20 size oscillations in sample number 3. At the same time a high dynamic range is kept, with reconstructed SAXS curves in some cases spanning up to six decades. Even within a specific q -range the high dynamic range is obtained as seen at the first silver behenate peak where the scattering intensity varies by three decades between different

capillaries.

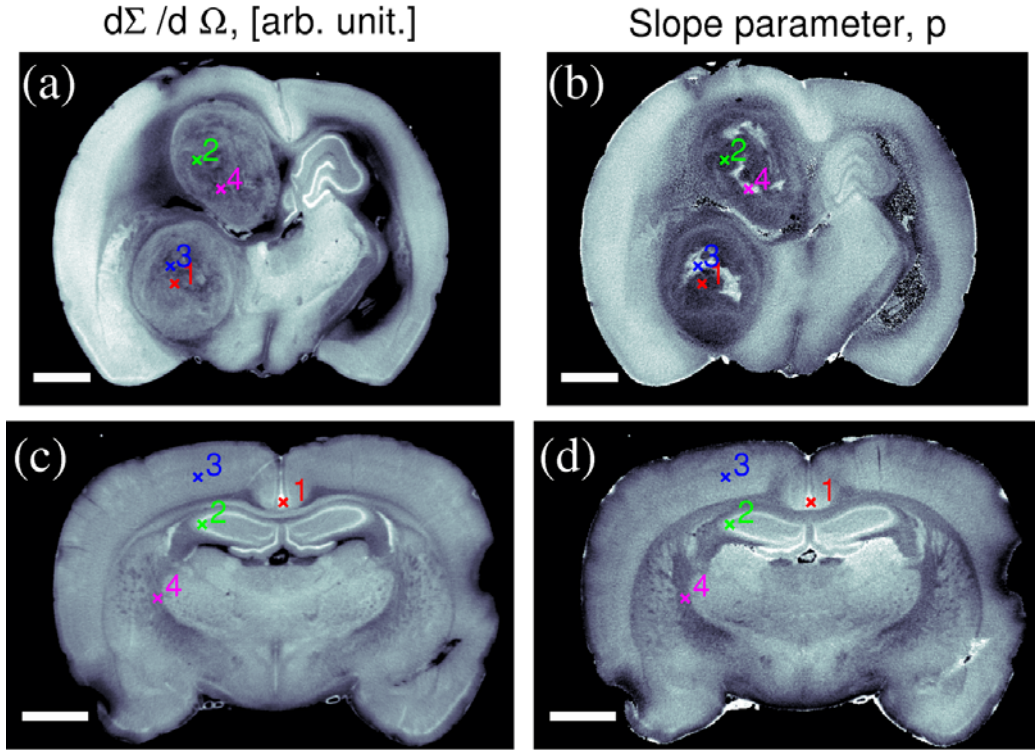


Figure 5.5. Biological example, rat brain. The two rows each represent two different tomographic sections of two rat brains. The first column (panels a and c) shows the local scattering cross section in a specific q -range ($q \in [0.071 - 0.39] \text{ nm}^{-1}$). The second column (panels b and d) shows the local slope of the scattering curve in the q -range $q \in [0.071 - 0.16] \text{ nm}^{-1}$ for the first row and in the q -range $q \in [0.071 - 0.39] \text{ nm}^{-1}$ for the second row. The scale bars have a length of 2 mm. All images are displayed with a linear grayscale with the following limits: a:[5.9-25.3], b:[1.34-2.52], c:[8.2-34.2] and d:[1.80-2.51].

Having introduced and demonstrated the method of SAXS-CT on a set of standard SAXS samples the paper goes on to demonstrate a potential biomedical application by investigating a weakly scattering soft tissue sample. Two formalin fixated rat brains were investigated using SAXS-CT. Some of the results are shown in Figure 5.5. Presented are two coronal slices from the two different brains. One brain has two large visible tumors (Figure 5.5a,b). A matching slice from the other brain without visible tumor is shown for comparison (Figure 5.5c,d).

In the paper we used the tomographic reconstructed local differential scattering cross section integrated over a certain q -range to generate contrast

(Figure 5.5a,c). The scattering signal provides anatomical maps of the brains. Several functional areas such as the corpus callosum (e.g. row 2 point 1), and internal capsule (row 2 point 4) are clearly visible, and the tumors (row 1 all points) are clearly delineated.

In Paper V we also introduce a new contrast mechanism. Since the full scattering curves are known for each voxel, one can conceive many different imaging contrasts signals. One way to analyze the scattering curves is to investigate the slope, p , of the scattering curves over a specific q -range by fitting them to a function of the form,

$$\frac{d\Sigma}{d\Omega}(q) = Cq^{-p}. \quad (5.5)$$

For large values of q this would be equivalent to a Porod-like analysis. The slope parameter is used to generate the image contrast in Figure 5.5 column 2.

From the slope parameter we can see increased contrast in several spots. In Figure 5.5b, the slope parameter helps to delineate substructures of the tumors that are less visible in the integrated differential scattering cross section image in Figure 5.5a. Especially, the necrotic part of the tumors is very well delimited on Figure 5.5b (white regions, points 3 and 4). In this way, using the slope parameter images can help to delineate the active part of the tumor. Also, the edema surrounding the tumors (in the hemisphere bearing the tumor) and the dilation of the ventricle (contralateral hemisphere) are very well defined and limited both on 5.5a and 5.5b.

Paper V thus demonstrates high resolution SAXS-CT over extended q -ranges of soft matter and tissue samples. With the first sample we validate the method and demonstrate the high dynamic range of the reconstructions. We also demonstrate how the SAXS signal provides nano-structural information about the samples. With the second set of samples we demonstrate the application of the method to tissue. We show how the nanostructural information can be used to provide clearly resolved anatomical maps of rat brains. We also introduce a novel contrast mechanism using the slope of the scattering curves and demonstrated how this slope can be used to provide additional contrast for both the functional areas and the tumor. The slope is used to delineation the necrotic regions of the tumor.

The two examples demonstrate how SAXS-CT complements and extends results obtainable with methods such as standard absorption tomography and histology.

Since the method is non-destructive, samples that cannot be sectioned can now be studied with SAXS. This could besides tissue samples include historic and cultural artifacts, and other uniquely valuable samples. It would

even be possible to study non fixated tissue, which would be impossible to slice. SAXS-CT could thus also be used to study what transformation tissue undergoes on the molecular level during fixation. For other types of applications, materials science could use SAXS-CT to study sintering of nano- or micro-powder samples. We believe that with this paper we have demonstrated how SAXS-CT may be used for high resolution and how the method can be applicable and beneficial in many cases.

5.2.2 Introduction to Paper VI

Paper VI has the title: 'Molecular x-ray computed tomography of myelin in a brain' (Jensen et al. 2010f). This second paper on SAXS-CT covers a different q -range than the first one. Paper VI still investigates scattering at small angles, but the angles are now large enough to observe the Bragg scattering from the myelin sheaths around the neuronal axons in a rat brain.

Myelin sheaths are lamellar membranes that wrap around neuronal axons. The sheaths are important for the central nervous system as they ensure rapid and secure communication of signals along axons. Structural changes of the myelin sheaths have been associated with a number of widespread neurodegenerative diseases such as cerebral malaria (Janota & Doshi 1979), multiple sclerosis (Prineas 1985, Peterson et al. 2001, Trapp et al. 1998) and Alzheimer's disease (Bartzokis 2004). The origin and evolution mechanisms of the diseases are still largely not understood, but they have been shown to be correlated with changes in the myelin formation and structure. A better understanding of the changes in the myelin sheath structure and its correlation to the pathologies is important for the development of methods for prevention or treatment of the diseases.

The changes in the myelin sheaths have been studied with a number of methods such as light (Trapp et al. 1998) and electron microscopy (Karlsson 1966, Sjöstrand 1953), magnetic resonance imaging (Hui et al. 2010) and x-ray diffraction (De Felici et al. 2008). All of these methods provide insight into the concentration and molecular structure of the myelin. While myelin sheaths from different types of nerves and in several different animal models have been extensively studied (Karlsson 1966, Marta et al. 2003), no mapping of the variations of the molecular structure of myelin sheaths in a complete brain has previously been achieved.

In Paper VI we use SAXS-CT to image the molecular variations of the myelin sheaths in a rat brain. We map these variations across the brain. Using SAXS-CT we reconstruct the full scattering curve from each point inside the brain. The myelin sheaths have a quasi periodical arrangement of their lamellar structure. This periodicity gives rise to Bragg scattering. By analyzing the peaks in the Bragg series we are able to extract information about the myelin sheaths. The method of SAXS-CT is highly selective. The myelin sheaths are the only tissue in the brain with a repetition unit of ~ 17.6 nm, we are thus certain to get information only about the myelin sheaths, when analyzing the associated Bragg series.

The strongest signal was associated with the second-order Bragg peak from the myelin sheaths. We fitted the intensity, position and width of this second-order Bragg peak. From the intensity of the peak we determined the

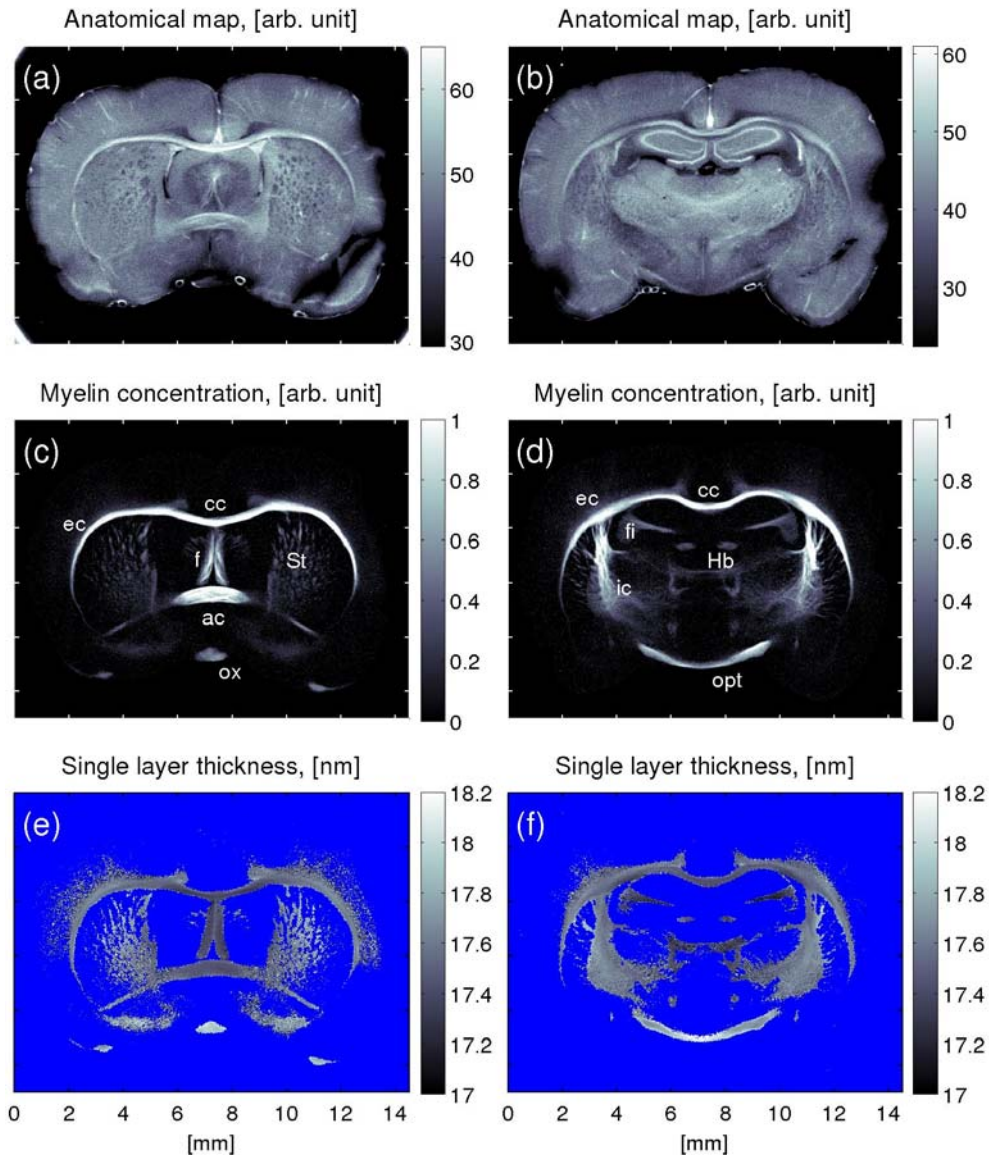


Figure 5.6. Myelin mapping. Two different brain slices are shown here.

(a,b) The integrated scattering cross section for $q_r = [0.05-1.4] \text{ nm}^{-1}$ provides anatomical maps of the brain slices to which we can relate the myelin maps. (c,d) Maps of the concentration of myelin in each voxel determined from the intensity of the 2nd-order Bragg peaks. (e,f) Maps of the periodicity of the lamellar structure of the myelin sheaths determined from the Bragg peaks positions. The blue color refers to areas with no or very low myelin content. A selection of structural labels are shown in column 2. (Detailed on page 80.)

local concentration of myelin. From the position we determined the period of the myelin sheaths and from the width we could determine a lower limit to the average thickness of the myelin sheaths. Some of the results are shown in Figure 5.6. The first row displays the integrated scattering cross section for $q_r = [0.05-1.4] \text{ nm}^{-1}$. The panels clearly show the overall anatomy of the imaged brain slices and are displayed to provide anatomical references to which we can relate the myelin maps.

The middle row of Figure 5.6 displays the myelin concentration. In Figure 5.6c the myelin is mainly associated with the corpus callosum(cc), external capsule(ec), the anterior commisure(ac), as well as the fornix(f). A somewhat lower concentration of myelin is associated with the striatum(st) and the optic chiasm(ox). In Figure 5.6d we again note the myelin associated with the corpus callosum and the external capsule. The myelin in the internal capsule(ic), as well as some of the connections between the internal and external capsule are also visible. Finally we note the myelin in the fimbria(fi) of the hippocampus as well as in the habenula(Hb) and the optical tract(opt).

We also determine the positions of the Bragg peaks, which are given by the period of the myelin sheaths. The period is equivalent to the thickness of a single myelin layer. Differences in period can occur both naturally and as a result of disease or treatment (Karlsson 1966, Marta et al. 2003). In Figure 5.6e,f the variations of the period are mapped. This molecular parameters can be used to distinguish different forms of myelin in the brain. In row 1 we note that the myelin in the optic chiasms in the bottom has a period that is significantly larger than the myelin in the corpus callosum and external capsule. In row 2 we see the difference between the corpus callosum and the optical tract. Additional molecular information such as a lower limit of the myelin sheath thickness as well as molecular information about cytoskeletal neurofilaments are also discussed in the paper.

We have in Paper VI thus demonstrated how SAXS-CT non-invasively can be used to map molecular information about the myelin sheaths in a rat brain. These molecular parameters of myelin are important for the understanding of the development of widespread neurodegenerative diseases such as cerebral malaria, multiple sclerosis and Alzheimer's disease. Using SAXS-CT we mapped the concentration and periodicity of the myelin sheaths. In this way we have seen how SAXS-CT is a new and valuable tool to study myelin and thus improve the understanding of a number of neurodegenerative diseases.

5.3 Outlook and applications

We have in this chapter as well as in Papers V and Paper VI demonstrated the method of small-angle x-ray scattering computed tomography (SAXS-CT) and several applications of the method. Using SAXS-CT we demonstrated how the full differential scattering cross section could be reconstructed volume resolved inside an extended sample, thus providing nanostructural information.

It should be emphasized that some of the advantages of the presented SAXS-CT approach are (a) that very little sample preparation is needed due to the tomographic nature of the method and (b) that the method is non-destructive.

Some of the limitations for the widespread use is the time needed to conduct the experiments. Each tomographic slice of the brains that were used in both Paper V and VI took around 24 hours to record. They included 400'000 SAXS patterns and an equivalent number of absorption measurements thus resulting in an effective recording rate of 9 images per second. This was done at a synchrotron x-ray source with high flux and a fast and very efficient detector. A PILATUS 2M detector was used for the experiments (Brönnimann et al. 2006, Henrich et al. 2009). The PILATUS 2M detector is essentially noise free and yields excellent statistics for the azimuthally averaged data with useable data for as low as 0.1 photons/pixel. The set-up is thus highly optimized for fast data collection. The time may still be reduced somewhat but the time required to record data for a single slice will remain substantial.

One way to significantly increase the speed of the data collection would be to parallelize it. As we assume the scattering is isotropic we only need to collect a 1D scattering pattern from each point on the sample. We could thus collect the scattering in the vertical direction, the direction parallel to the rotation axis. By using a flat wide beam, one could collect all scattering curves for each rotation angle at once. This would require some kind of Soller collimation of the scattered x-rays, so that only scattering from one point reaches each of the vertical lines of pixels on the detector. The construction of this collimation unit would be quite tricky, as the scattering angles are very small. This parallelization is thus not an easy step and has yet to be developed.

Full 3D high resolution studies are due to the required time still difficult to envisage at the moment, since each slice takes hours to record. With a laboratory source it will be possible to perform SAXS-CT. But due to the limited flux, only low resolution studies will be practical within reasonable time.

The possible applications we envisage for the methods are thus mainly

scientific research at highly specialized synchrotron beamlines. These applications are however still plentiful.

One biomedical application was demonstrated above where molecular imaging of the neuronal myelin sheaths in brain tissue was presented. The imaging of these molecular parameters may provide insight into a range of widespread neurodegenerative diseases. The imaging could also include other biomolecules. Paper VI demonstrated the possibility of studying cytoskeletal neurofilaments in this way. There is a range of biomolecules with periods long enough to be studied with small-angle x-ray scattering. This includes collagen which could be studied in bone and cartilage. Changes on the collagen have also been showed to be related to development of breast cancer (Fernandez et al. 2005). Using SAXS-CT one would be able to pinpoint the specific areas where the collagen has changed.

For biomedical applications it is always an issue of interest whether the imaging can be performed in-vivo. In principle there is nothing hindering SAXS-CT to be performed in-vivo. There are however some practical limitations. It could be an issue of concern that the sample is scanned rapidly back and forth, which poses some difficulties in handling the subject. More importantly is the time issue. As discussed above the necessary time for these types of images are quite long, and probably longer than what is acceptable in most in-vivo experiments. Finally there is the issue of the delivered dose. We have not discussed the delivered dose for these experiments so far. As we did our experiments ex-vivo, our main dose concern was physical beam damage. There was no beam damage observed in any of our samples. But the samples are exposed to a focused synchrotron beam for extended periods of time, and it is likely that the delivered dose exceeds the limits for in-vivo experiments. SAXS-CT is thus not directly applicable for in-vivo studies.

Aside from the in-vivo studies, we generally believe that SAXS-CT may be desirable and applicable in many cases. Since the method is non-destructive, samples that cannot be sectioned can now be studied with SAXS. This could include historic and cultural artifacts, and other uniquely valuable samples. It would even be possible to study non fixated tissue, which would be impossible to slice. SAXS-CT could thus also be used to study the transformation tissue undergoes on the molecular level during fixation.

For other types of applications, materials science could use SAXS-CT to study sintering of nano- or micro-powder samples. The use of small-angle x-ray scattering has over the last 10-15 years grown rapidly with the development of new analytical tools (Svergun 2010). Another area of possible expansion of SAXS-CT is the application of different types of small-angle scattering analysis. Since the full scattering curves are reconstructed all the analytical methods usually applied in small-angle scattering could also be

applied to the tomographically reconstructed data. SAXS-CT can thus be added as an extra tool to the small-angle scattering toolbox.

Finally it would be of great interest to extend SAXS-CT to cover the full reciprocal space. The extension of the method would be to reconstruct the differential scattering cross section in three dimensions. In that way a full 6D dataset is reconstructed, providing volume resolved 3D reciprocal space maps ($\frac{d\Sigma}{d\Omega}(x, y, z, q_x, q_y, q_z)$). We have successfully conducted the first experiments with this for 5 dimensions (2 real space, 3 reciprocal space (Böttiger 2010)), but the extension to 6D is not straight forward. Especially the way to record 6D information is tricky without putting additional constraints on the sample.

A simpler extension which is straight forward is the possibility of studying samples that scatter non-isotropically. The requirement for the tomographic reconstructions is that the reconstructed property of a given voxel is independent of which side the voxel is illuminated from. This is fulfilled when the scattering is isotropic as it is in the results presented in this chapter. The requirement is also fulfilled if only the scattering in the direction parallel to the rotation axis is reconstructed. We have conducted experiments on collagen samples, were a fraction of the collagen was strongly oriented. Since this orientation produced scattering parallel to the rotation axis it was possible to reconstruct both the oriented and the non-oriented part of the scattering signal, and thus separately visualize the oriented and non-oriented collagen (Thomsen 2009). This is a elegant way to study partial ordering of collagen.

Chapter 6

Conclusion

A number of novel refraction and scattering based x-ray imaging contrast mechanisms and their applications have been presented in this thesis. This includes an introduction to and the presentation of six original papers (Papers I-VI).

The principle behind an x-ray grating interferometer has been described. Using a grating interferometer the increase in contrast of phase-contrast tomography over standard absorption-contrast tomography was demonstrated. One application we demonstrated was that the identification of metastatic deposits in human lymph nodes is now possible with x-rays using phase-contrast tomography. Applications in the food industry were illustrated by imaging porcine fat and rind.

The grating interferometer was also used in a second method that was presented. The novel imaging method is called directional x-ray dark-field imaging. It was presented and experimentally verified for a number of different samples. The presented data included both biological sample (bones and tooth) and samples of industrial interest (fiber samples and wood). Some of the directional x-ray dark-field images were obtained using a conventional x-ray tube source, thus allowing for widespread use of the method. Comparison of grating based directional x-ray dark-field imaging and small-angle x-ray scattering mapping was performed, verifying the experimental results of directional x-ray dark-field imaging. The latter results are previously unpublished.

Small-angle x-ray scattering (SAXS) mapping was extended to 3D using tomography. High resolution reconstructions of weakly scattering samples were illustrated. The integrated scattering cross section demonstrated excellent contrast for imaging different functional areas of the brain. Analysis of scattering curves associated with each voxel was used to image the morphology of brain tumors with increased contrast. Molecular tomography was

also demonstrated using the Bragg peaks from neuronal myelin sheaths. Using SAXS-CT a number of molecular parameters for the neuronal myelin sheaths were determined. The changes in these parameters have been linked to a number of neurodegenerative diseases.

A copy of the six original articles are attached in Appendix B.

6.1 Outlook

The individual chapters in this thesis were to some extent independent of each other presenting different x-ray imaging methods. As a result we have already at the end of each chapter discussed the consequences of the presented results and the possible applications of the presented methods. Rather than repeating ourselves we will try to discuss some of the broad lines including possible applications and limitations.

In Chapter 3 we demonstrated two new applications of phase-contrast tomography. First we demonstrated that phase-contrast tomography can be used for identification of metastatic deposits in human lymph nodes. As the studies were performed with synchrotron radiation the next natural step is to investigate the possibilities with a laboratory x-ray source. This line of study will hopefully also inspire studies of imaging of other types of cancer or diseases. We have at the Niels Bohr Institute almost finalized a laboratory set-up that can be used for these studies.

The second demonstration regarded the increased contrast available with phase-contrast tomography when imaging porcine fat and rind. This is of interest to the food industry as a new method for noninvasive quality testing. As with the lymph node study, this study was also performed using synchrotron radiation. The next natural step is thus also to investigate the possibilities with a laboratory x-ray source. In order to implement the method in an abattoir or another place in the industry, the results need to be demonstrated with a laboratory x-ray source.

By demonstrating the possible applications of phase-contrast tomography we also demonstrate a market for commercial phase-contrast tomography set-ups. The studies presented in this thesis may thus aid to reduce the time until such set-ups become commercially available. Once set-ups are commercially available the number of researchers than can investigate and demonstrate more applications will drastically increase. This increase in number of demonstrated applications will generate an even larger demand. The key to get this positive feedback loop started is to make the first demonstration of applications such as the demonstrations we made with human lymph nodes and porcine fat and rind in Chapter 3. As previously mentioned the first

commercial phase-contrast tomography set-up should soon become available. This commercial availability of course rely on the production of x-ray gratings. This issue seems to have been overcome for energies below ~ 50 keV as the company microworks GmbH now sells such gratings (*microworks GmbH* 2010).

Another area of interest is the possibilities which become available with the advent of new bright and compact x-ray source. These sources include but are not limited to sources such as advanced micro focus sources like the metal-jet anode microfocus x-ray source of Excillum (Hemberg et al. 2004) and the Compact Light Source (CLS) from Lyncean Technologies (Huang & Ruth 1998). These new sources provide a high flux with a small source spot. Grating based phase-contrast imaging has already been demonstrated at the CLS (Bech et al. 2009a). Experiments were also performed at the CLS during this PhD, however without producing publishable new results. The important point is that these new and bright sources will in some form most likely become available in the near future. In that way some of the benefits which are today available only with synchrotron sources will become more broadly available.

As mentioned in the introduction to this thesis grating based phase-contrast imaging is not the only phase-contrast imaging method available. For broader applications propagation based imaging may also be a feasibility option. The method works well with a microfocus source with a broad energy spectrum and requires no specialized optical elements. Propagation based imaging has certain drawbacks. The field of view may be limited as high spatial resolution is needed to resolve the features used to generate the phase-contrast images. The need for variation of the sample to detector distance might also pose some technical challenges. It has been claimed by some of the people that first introduced the method that propagation based imaging has inferior contrast compared to other phase-contrast imaging methods (Nesterets & Wilkins 2008). Propagation based imaging also has the limitation that it does not provide the dark-field imaging capability. Whether propagation based imaging or grating based imaging will be the better or more widespread method will be seen in the years to come. Since both methods are phase-contrast imaging methods, applications demonstrated with one method may also be possible with the other. Comparisons then need to demonstrate which of the two provides the better results.

Besides experiments based on laboratory source a range of experiments at synchrotron sources should and will continue. The synchrotron sources still provide interferometers with superior contrast. For many research applications as well as for demonstrating new applications synchrotron sources will be the superior choice. As new synchrotron sources are build and old ones up-

dated with smaller spots and long(er) beamlines the phase-contrast imaging capabilities will also increase. There is also still a lot to be learned about the coherence properties of the different rings, insertion devices and beamlines and how these influence the image quality of grating interferometers.

As grating based phase-contrast imaging becomes more routine experiments at the synchrotron these may also become available to more general users. People who are not x-ray experts could benefit a great deal from the increased contrast available with phase-contrast imaging.

Far from all of the studies performed in this thesis have been able to demonstrate the applications we were testing. One such study was an extensive study of bone cancer in mice. The goal was to find a method to evaluate the size of the tumors without having to terminate the mice. Such a method would facilitate linear studies to be performed on a single mouse evaluating the correlation between the pain associated with the tumor and the size of the tumor. We tried several different approaches. Ex-vivo studies were performed using 2D SAXS mapping, SAXS-CT as well as grating based absorption, phase-contrast and dark-field tomography. In the end our conclusion was that we could not visualize the bone tumors. The line of studies were thus successful - we determined whether we could provide such a non-invasive method. The answer was however negative.

Phase-contrast imaging was not the only subject of this thesis. In Chapter 4 we demonstrated the novel method of directional x-ray dark-field imaging. Many of the considerations and comments regarding the use of phase-contrast tomography made above are also relevant for directional x-ray dark-field imaging. As mentioned in Chapter 4 we foresee a number of biomedical as well as industrial applications. As with phase-contrast imaging above this widespread use, depends on the availability of x-ray grating interferometers. Also in this case the commercial availability will be influenced by the number of practical applications that are demonstrated. Further research should thus aim to demonstrate such applications. In the case of directional x-ray dark-field imaging there are no other methods that can compete in providing this overview of local textural information. I personally believe that the greatest potential for the method lies within industrial nondestructive testing. The ability to see the ordering and orientation of fibers embedded in a material is unique and valuable tool for nondestructive testing of fiber-reinforced materials.

Directional x-ray dark-field imaging can with synchrotron sources also be of great interest for other e.g. biomedical applications. Whether the later can be translated to the laboratory only the future will show.

One important step for industrial applications could be to demonstrate directional x-ray dark-field imaging in a conveyer belt setup. Phase-contrast

imaging and hence dark-field imaging using a conveyer belt set-up with three line detectors has already been demonstrated (Kottler et al. 2007). In the simplest case of directional x-ray dark-field imaging only three sample orientations are needed. Directional x-ray dark-field imaging could thus be performed using only nine line-detectors, and without rotating the sample itself.

Another important next step is also the extension of directional x-ray dark-field imaging to 3D. This will open up for a range of new applications as also discussed in Chapter 4.

The final methods we demonstrated were methods using high resolution small-angle x-ray scattering computed tomography (SAXS-CT). This is probably the method least likely to achieve widespread application. There are experimental requirements as discussed in Chapter 5 that will probably limit the method to be used at synchrotron radiation sources.

Even though the methods will be limited to synchrotron sources the possible applications are still quite exciting. We already demonstrated the imaging of tumor morphology and molecular parameters of neuronal myelin sheaths in a brain. This molecular imaging has numerous applications and with SAXS-CT these molecules can now be probed *in-situ*. The use of more advanced SAXS analytical methods could also provide a range of new contrast mechanisms.

Another important range of applications is using the nondestructive nature of the method to allow studies of samples that may not or can not be sectioned for standard SAXS studies.

All of the novel methods presented in this thesis have a range of interesting applications worth further investigation. My hope is that some of them in the future will be put to practical use providing answers to practical questions whether it be to the benefit of patients in the hospitals or someone somewhere in the industry.

Bibliography

- Alexander, A. L., Lee, J. E., Lazar, M. & Field, A. S. (2007), 'Diffusion tensor imaging of the brain', *Neurotherapeutics* **4**, 316–329.
- Als-Nielsen, J. & McMorrow, D. (2001), *Elements of Modern X-ray Physics*, John Wiley & Sons Ltd.
- Ando, M., Maksimenko, A., Sugiyama, H., Pattanasiriwisa, W., Hyodo, K. & Uyama, C. (2002), 'Simple X-ray dark- and bright-field imaging using achromatic lane optics', *Jpn. J. Appl. Phys.* **41**(9A-B), L1016–L1018.
- Ando, M., Yamasaki, K., Toyofuku, F., Sugiyama, H., Ohbayashi, C., Li, G., Pan, L., Jiang, X., Pattanasiriwisa, W., Shimao, D., Hashimoto, E., Kimura, T., Tsuneyoshi, M., Ueno, E., Tokumori, K., Maksimenko, A., Higashida, Y. & Hirano, M. (2005), 'Attempt at visualizing breast cancer with X-ray dark field imaging', *Jpn. J. Appl. Phys.* **44**(16-19), L528–L531.
- Bartzokis, G. (2004), 'Quadratic trajectories of brain myelin content: unifying construct for neuropsychiatric disorders', *Neurobiol Aging* **25**, 49–62.
- Basser, P. J., Mattiello, J. & LeBihan, D. (1994), 'MR diffusion tensor spectroscopy and imaging', *Biophys. J.* **66**, 259–267.
- Bech, M. (2009), *PhD thesis, X-ray imaging with a grating interferometer, University of Copenhagen*, LAP Lambert Academic Publishing.
- Bech, M., Bunk, O., David, C., Ruth, R., Rifkin, J., Loewen, R., Feidenhans'l, R. & Pfeiffer, F. (2009a), 'Hard x-ray phase-contrast imaging with the compact light source based on inverse compton x-rays', *Journal of Synchrotron Radiation* **16**, 43–47.
- Bech, M., Bunk, O., Donath, T., Feidenhans'l, R., David, C. & Pfeiffer, F. (2010), 'Quantitative x-ray dark-field computed tomography', *Phys. Med. Biol.* **55**(18), 5529–5539.

- Bech, M., Jensen, T. H., Feidenhans'l, R., Bunk, O., David, C. & Pfeiffer, F. (2009b), 'Soft-tissue phase-contrast tomography with an x-ray tube source', *Physics in Medicine and Biology* **54**, 2747–2753.
- Bleuet, P., Welcomme, E., Dooryhee, E., Susini, J., Hodeau, J. L. & Walter, P. (2008), 'Probing the structure of heterogeneous diluted materials by diffraction tomography', *Nat. Mat.* **7**, 468–472.
- Bonse, U. & Hart, M. (1965), 'An x-ray interferometer', *Appl. Phys. Lett.* **6**, 155–156.
- Böttiger, A. P. L. (2010), Differential phase contrast imaging for diagnosis of metastatic cancer in lymph nodes and initial development of reciprocal space tomography, Master thesis, University of Copenhagen.
- Brönnimann, C., Eikenberry, E., Henrich, B., Horisberger, R., Huelsen, G., Pohl, E., Schmitt, B., Schulze-Briese, C., Suzuki, M., Tomizaki, T., Toyokawa, H. & Wagnera, A. (2006), 'The PILATUS 1M detector', *J. Syn. Rad.* **13**, 120–130.
- Bunk, O., Bech, M., Jensen, T. H., Feidenhans'l, R., Binderup, T., Menzel, A. & Pfeiffer, F. (2009), 'Multimodal x-ray scatter imaging', *New Journal of Physics* **11**.
- Chapman, D., Thomlinson, W., Johnston, R. E., Washburn, D., Pisano, E., Gmür, N., Zhong, Z., Menk, R., Arfelli, F. & Sayers, D. (1997), 'Diffraction enhanced x-ray imaging', *Physics in Medicine and Biology* **42**(11), 2015.
- Chen, G.-H., Bevins, N., Zambelli, J. & Qi, Z. (2010), 'Small-angle scattering computed tomography (SAS-CT) using a Talbot-Lau interferometer and a rotating anode x-ray tube: theory and experiments', *Opt. Exp.* **18**(12), 12960–12970.
- Cloetens, P., Barrett, R., Baruchel, J., Guigay, J. & Schlenker, M. (1996), 'Phase objects in synchrotron radiation hard x-ray imaging', *J. Phys. D* **29**(1), 133–146.
- Cloetens, P., Ludwig, W., Baruchel, J., Dyck, D. V., Landuyt, J. V., Guigay, J.-P. & Schlenker, M. (1999a), 'Holotomography: Quantitative phase tomography with micrometer resolution using hard synchrotron radiation x rays', *Appl. Phys. Lett.* **75**(19), 2912–2914.
- Cloetens, P., Pateyron-Salomé, M., Buffierè, J.-Y., Peix, G., Baruchel, J., Peyrin, F. & Schlenker, M. (1997), 'Observation of microstructure and

- damage in materials by phase sensitive radiography and tomography', *Journal of Applied Physics* **81**(9), 5878–5886.
- Cormack, A. M. (1963), 'Representation of a function by its line integrals, with some radiological applications', *J. Applied Physics* **34**, 2722.
- David, C., Nöhammer, B., Solak, H. H. & Ziegler, E. (2002), 'Differential x-ray phase contrast imaging using a shearing interferometer', *Appl. Phys. Lett.* **81**(17), 3287–3289.
- Davis, T. J., Gao, D., Gureyev, T. E., Stevenson, A. W. & Wilkins, S. W. (1995), 'Phase-contrast imaging of weakly absorbing materials using hard x-rays', *Nature* **373**, 595–598.
- De Felici, M., Felici, R., Ferrero, C., Tartari, A., Gambaccini, M. & Finet, S. (2008), 'Structural characterization of the human cerebral myelin sheath by small angle x-ray scattering', *Phys. Med. Biol.* **53**, 5675–5688.
- Donath, T., Pfeiffer, F., Bunk, O., Grünzweig, C., Hempel, E., Popescu, S., Vock, P. & David, C. (2010), 'Toward clinical x-ray phase-contrast CT demonstration of enhanced soft-tissue contrast in human specimen', *Invest. Radiol.* **7**, 445–52.
- Engelhardt, M., Kottler, C., Bunk, O., David, C., Schroer, C., Baumann, J., Schuster, M. & Pfeiffer, F. (2008), 'The fractional talbot effect in differential x-ray phase-contrast imaging for extended and polychromatic x-ray sources', *Journal of Microscopy* **232**(1), 145–157.
- Ferlay, J., Autier, P., Boniol, M., Heanue, M., Colombet, M. & Boyle, P. (2007), 'Estimates of the cancer incidence and mortality in Europe in 2006', *Ann. Oncol.* **18**(3), 581–592.
- Fernandez, M., Keyrilainen, J., Serimaa, R., Torkkeli, M., Karjalainen-Lindsberg, M., Leidenius, M., von Smitten, K., Tenhunen, M., Fiedler, S., Bravin, A., Weiss, T. & Suortti, P. (2005), 'Human breast cancer in vitro: matching histo-pathology with small-angle x-ray scattering and diffraction enhanced x-ray imaging', *Phys. Med. Biol.* **50**(13), 2991–3006.
- Gibson, R. F. (2010), 'A review of recent research on mechanics of multifunctional composite materials and structures', *Compos. Struct.* **92**(12), 2793–2810.
- Glatter, O. & Kratky, O. (1982), *Small angle X-ray scattering*, Academic, London.

- Goetz, K., Kalashnikov, M. P., Mikhailov, Y. A., Sklizkov, G. V., Fedotov, S. I., Foerster, E. & Zaumseil, P. (1979), 'Measurements of the parameters of shell targets for laser thermonuclear fusion using an x-ray schlieren method', *Soviet Journal of Quantum Electronics* **9**(5), 607.
- Gourrier, A., Wagermaier, W., Burghammer, M., Lammie, D., Gupta, H. S., Fratzl, P., Riekel, C., Wess, T. J. & Paris, O. (2007), 'Scanning x-ray imaging with small-angle scattering contrast', *J. Appl. Cryst.* **40**.
- Guinier, A. & Fournet, G. (1955), *Small-angle scattering of X-rays*, Wiley, New York.
- Gunin, A. (2009), 'Atlas of histology images', URL <http://www.histol.chuvashia.com/atlas-en/lymphoid-en.htm>.
- Gureyev, T. E., Mayo, S. C., Myers, D. E., Nesterets, Y., Paganin, D. M., Pogany, A., Stevenson, A. W. & Wilkins, S. W. (2009), 'Refracting Rontgen's rays: Propagation-based x-ray phase contrast for biomedical imaging', *Journal of Applied Physics* **105**(10).
- Harding, G. & Kosanetsky, J. (1989), 'Scattered x-ray beam nondestructive testing', *Nucl. Inst. and methods in Physics research A* **A280**, 517–528.
- Harding, G., Kosanetsky, J. & Neitzel, U. (1985), 'Elastic scatter computed tomography', *Phys. Med. Biol.* **30**, 183–186.
- Harding, G., Kosanetsky, J. & Neitzel, U. (1987), 'X-ray diffraction computed tomography', *Med. Phys.* **14**, 515–525.
- Hemberg, O., Otendal, M. & Hertz, H. M. (2004), 'Liquid-metal-jet anode X-ray tube', *Opt. Eng.* **43**(7), 1682–1688.
- Henke, B. L., Gullikson, E. M. & Davis, J. C. (1993), 'X-ray interactions: photoabsorption, scattering, transmission, and reflection at E=50-30000 eV, Z=1-92', *Atomic Data and Nuclear Data Tables* **54**(2), 181–342.
- Henrich, B., Bergamaschi, A., Broennimann, C., Dinapoli, R., Eikenberry, E. F., Johnson, I., Kobas, M., Kraft, P., Mozzanica, A. & Schmitt, B. (2009), 'PILATUS: A single photon counting pixel detector for x-ray applications', *Nucl Instrum Meth A* **607**(1), 247–249.
- Hounsfield, G. N. (1973), 'Computerized transverse axial scanning (tomography): Part I. description of system', *Br. J. Radiol.* **46**(552), 1016–1022.

- Huang, Z. & Ruth, R. D. (1998), 'Laser-electron storage ring', *Phys. Rev. Lett.* **80**(5), 976–979.
- Hui, E. S., Cheung, M. M., Chan, K. & Wu, E. X. (2010), 'B-value dependence of DTI quantitation and sensitivity in detecting neural tissue changes', *Neuroimage* **49**, 2366–2374.
- Ingal, V. & Beliaevskaya, E. (1995), 'X-ray plane-wave topography observation of the phase contrast from a non-crystalline object', *J. Phys. D Appl. Phys.* **28**, 2314–2317.
- Janota, I. & Doshi, I. (1979), 'Cerebral malaria in the united kingdom', *J. Clin. Pathol.* **32**, 769–772.
- Jensen, T. H., Bech, M., Binderup, T., Böttiger, A., David, C., Weitkamp, T., Zanette, I., Reznikova, E., Mohr, J., Rank, F., Feidenhans'l, R., Kjær, A., Højgaard, L. & Pfeiffer, F. (2010a), 'Imaging of metastatic lymph nodes by x-ray phase contrast tomography', *Submitted to Radiology*.
- Jensen, T. H., Bech, M., Böttiger, A., Weitkamp, T., Zanette, I., Reznikova, E., Mohr, J., Feidenhans'l, R. & Pfeiffer, F. (2010b), 'X-ray phase-contrast tomography of porcine fat and rind', *Submitted to Meat Science*.
- Jensen, T. H., Bech, M., Bunk, O., Donath, T., David, C., Feidenhans'l, R. & Pfeiffer, F. (2010c), 'Directional x-ray dark-field imaging', *Phys. Med. Biol.* **55**, 3317–3323.
- Jensen, T. H., Bech, M., Bunk, O., Menzel, A., Bouchet, A., Le Duc, G., Feidenhans'l, R. & Pfeiffer, F. (2010f), 'Molecular x-ray computed tomography of myelin in a brain', *Submitted to Nature Communications*.
- Jensen, T. H., Bech, M., Bunk, O., Thomsen, M., Menzel, A., Bouchet, A., Le Duc, G., Feidenhans'l, R. & Pfeiffer, F. (2010e), 'Brain tumor imaging using small-angle x-ray scattering tomography', *Submitted to Phys. Med. Biol.*.
- Jensen, T. H., Bech, M., Zanette, I., Weitkamp, T., David, C., Deyhle, H., Rutishauser, S., Reznikova, E., Mohr, J., Feidenhans'l, R. & Pfeiffer, F. (2010d), 'Directional x-ray dark-field imaging of strongly ordered systems', *Submitted to Phys. Rev. B*.
- Judas, M., Höreth, R. & Dobrowolski, A. (2006), 'Computertomografie als methode zur analyse der schlachtkörper von schweinen', *Fleischwirtschaft* **12**(102-105).

- Kagoshima, Y., Takai, K., Ibuki, T., Yokoyama, Y., Hashida, T., Yokoyama, K., Takeda, S., Urakawa, M., Miyamoto, N., Tsusaka, Y., Matsui, J. & Aino, M. (2001), 'Scanning hard X-ray microscope with tantalum phase zone plate at the Hyogo-BL (BL24XU) of SPring-8', *Nucl. Inst. Meth. A* **467**(Part 2), 872–876.
- Kak, A. C. & Slaney, M. (2001), *Principles of Computerized Tomographic Imaging*, Society for Industrial and Applied Mathematics.
- Kalender, W. A. (2006), 'X-ray computed tomography', *Phys. Med. Biol.* **51**(13), R29–R43.
- Karlsson, U. (1966), 'Comparison of the myelin period of peripheral and central origin by electron microscopy', *J. Ultrastructure Research* **15**, 451–468.
- Kleuker, U., Suortti, P., Weyrich, W. & Spanne, P. (1998), 'Feasibility study of x-ray diffraction computed tomography for medical imaging', *Phys. Med. Biol.* **43**, 2911–2923.
- Kottler, C., Pfeiffer, F., Bunk, O., Gruenzweig, C. & David, C. (2007), 'Grating interferometer based scanning setup for hard x-ray phase contrast imaging', *Rev. Sci. Instrum.* **78**(4).
- Landbrug & Fødevare* (2010), homepage as seen Oct. 12th, URL http://www.lf.dk/Tal_og_Analyser/Fakta_om_landbrugsfoedvareprod/Den_danske_svinesektor.aspx.
- Levine, L. E. & Long, G. G. (2004), 'X-ray imaging with ultra-small-angle x-ray scattering as a contrast mechanism', *J. Appl. Cryst.* **37**, 757–765.
- Marta, C. B., Paez, P., Lopez, M., Pellegrino de Iraldi, A., Soto, E. F. & Pasquini, J. M. (2003), 'Morphological changes of myelin sheaths in rats intracranially injected with apotransferrin', *Neurochemical Research* **28**, 101–110.
- microworks GmbH* (2010), homepage as seen Oct. 6th, URL <http://www.micro-works.de/index.html>.
- Momose, A. (1995), 'Demonstration of phase-contrast x-ray computed tomography using an x-ray interferometer', *Nuclear Instruments and Methods in Physics Research Section A: Accelerators, Spectrometers, Detectors and Associated Equipment* **352**(3), 622 – 628.

- Momose, A. (2003b), 'Phase-sensitive imaging and phase tomography using x-ray interferometers', *Optics Express* **11**(19), 2303–2314.
- Momose, A., Kawamoto, S., Koyama, I., Hamaishi, Y., Takai, K. & Suzuki, Y. (2003a), 'Demonstration of x-ray talbot interferometry', *Jpn. J. Appl. Phys.* **42**, L866–L868.
- Momose, A., Takeda, T., Itai, Y. & Hirano, K. (1996), 'Phase-contrast x-ray computed tomography for observing biological soft tissues', *Nat. Med.* **2**(4), 473–475.
- Momose, A., Yashiro, W., Takeda, Y., Suzuki, Y. & Hattori, T. (2006), 'Phase tomography by x-ray talbot interferometry for biological imaging', *Jpn. J. Appl. Phys.* **45**(6A), 5254–5262.
- Müller, R. (2009), 'Hierarchical microimaging of bone structure and function', *Nat. Rev. Rheumatol.* **5**(7), 373–381.
- Narayanan, T. (2009), 'High brilliance small-angle X-ray scattering applied to soft matter', *Curr. Opin. Colloid Interface Sci.* **14**(6), 409–415.
- Nesterets, Y. I. & Wilkins, S. W. (2008), 'Phase-contrast imaging using a scanning-double-grating configuration', *Opt Express* **16**(8), 5849–5867.
- Nielsen, S., Wolf, A., Poulsen, H., Ohler, M., Lienert, U. & Owen, R. (2000), 'A conical slit for three-dimensional XRD mapping', *J Synchrotron Radiat.* **7**, 103–109.
- Olivo, A., Arfelli, F., Dreossi, D., Longo, R., Menk, R. H., Pani, S., Poropat, P., Rigon, L., Zanconati, F. & Castelli, E. (2002), 'Preliminary study on extremely small-angle x-ray scatter imaging with synchrotron radiation', *Phys. Med. Biol.* **47**, 469–480.
- Pagot, E., Cloetens, P., Fiedler, S., Bravin, A., Coan, P., Baruchel, J., Härtwig, J. & Thomlinson, W. (2003), 'A method to extract quantitative information in analyzer-based x-ray phase contrast imaging', *Appl. Phys. Lett.* **82**, 3421–3423.
- Peterson, J. W., Bö, L., Mörk, S., Chang, A. & Trapp, B. D. (2001), 'Transected neurites, apoptotic neurons, and reduced inflammation in cortical multiple sclerosis lesions', *Annals of Neurology* **50**, 389–400.
- Pfeiffer, F., Bech, M., Bunk, O., Donath, T., Henrich, B., Kraft, P. & David, C. (2009), 'X-ray dark-field and phase-contrast imaging using a grating interferometer', *Journal of Applied Physics* **105**, 102006.

- Pfeiffer, F., Bech, M., Bunk, O., Kraft, P., Eikenberry, E. F., Brönnimann, C., Grünzweig, C. & David, C. (2008a), 'Hard-x-ray dark-field imaging using a grating interferometer', *Nat. Mater.* **7**, 134–137.
- Pfeiffer, F., Bunk, O., David, C., Bech, M., Le Duc, G., Bravin, A. & Cloetens, P. (2007c), 'High-resolution brain tumor visualization using three-dimensional x-ray phase contrast tomography', *Phys. Med. Biol.* **52**.
- Pfeiffer, F., Bunk, O., Kottler, C. & David, C. (2007b), 'Tomographic reconstruction of three-dimensional objects from hard x-ray differential phase contrast projection images', *Nucl. Instr. Meth. A* **580**, 925–928.
- Pfeiffer, F., Bunk, O., Schulze-Briese, C., Diaz, A., Weitkamp, T., David, C., van der Veen, J. F., Vartanyants, I. & Robinson, I. K. (2005), 'Shearing interferometer for quantifying the coherence of hard x-ray beams', *Phys. Rev. Lett.* **94**, 164801.
- Pfeiffer, F., Kottler, C., Bunk, O. & David, C. (2007a), 'Hard x-ray phase tomography with low-brilliance sources', *Phys. Rev. Lett.* **98**, 108105.
- Pfeiffer, F., Weitkamp, T., Bunk, O. & David, C. (2006), 'Phase retrieval and differential phase-contrast imaging with low-brilliance x-ray sources', *Nat. Phys.* **2**, 258–261.
- Prineas, J. W. (1985), *Handbook of clinical neurology. Demyelinating disease, vol 3*, Elsevier, Amsterdam, chapter The neuropathology of multiple sclerosis, pp. 213–257.
- Rigon, L., Besch, H. J., Arfelli, F., Menk, R. H., Heitner, G. & Plothow-Besch, H. (2003), 'A new DEI algorithm capable of investigating sub-pixel structures', *J. Phys. D* **36**(10A, Sp. Iss. SI), A107–A112.
- Röntgen, W. C. (1895), 'Über eine neue art von strahlen', *Sitzungsberichte der Physikalisch-Medizinischen Gesellschaft in Würzburg* **137**, 132–141.
- Roschger, P., Grabner, B., Rinnerthaler, S., Tesch, W., Kneissel, M., Berzlanovich, A., Klaushofer, K. & Fratzl, P. (2001), 'Structural development of the mineralized tissue in the human L4 vertebral body', *J. Struct. Biol.* **136**(2), 126–136.
- Schroer, C., Kuhlmann, M., Roth, S. V., Gehrke, R., Stribeck, N., Almendarez-Camarillo, A. & Lengeler, B. (2006), 'Mapping the local nanostructure inside a specimen by tomographic small-angle x-ray scattering', *Appl. Phys. Lett.* **88**.

- Shimao, D., Sugiyama, H., Hyodo, K., Kunisada, T. & Ando, M. (2005), 'Evaluation of x-ray dark-field imaging in visualization of nearly clinical articular cartilage', *Nucl. Inst. Meth. A* **548**, 129–134.
- Shimao, D., Sugiyama, H., Kunisada, T. & Ando, M. (2006), 'Articular cartilage depicted at optimized angular position of laue angular analyzer by x-ray dark-field imaging', *Appl. Radiat. Iso.* **64**, 868–874.
- Sjöstrand, S. F. (1953), 'The lamellated structure of the nerve myelin sheath as revealed by high-resolution electron microscopy', *Experientia* **9**(2), 68–69.
- Snigirev, A., Snigireva, I., Kohn, V., Kuznetsov, S. & Schelokov, I. (1995), 'On the possibilities of x-ray phase contrast microimaging by coherent high-energy synchrotron radiation', *Rev. Sci. Instrum.* **66**(12), 5486–5492.
- Stock, S., de Carlo, F. & Almer, J. (2008), 'High energy x-ray scattering tomography applied to bone', *J. Struct. Biol.* **161**, 144–150.
- Suzuki, Y. & Uchida, F. (1995), 'Dark-field imaging in hard x-ray scanning microscopy', *Rev. Sci. Instrum.* **66**, 1468–1470.
- Svergun, D. I. (2010), 'Small-angle X-ray and neutron scattering as a tool for structural systems biology', *Biol. Chem.* **391**(7), 737–743.
- Thomsen, M. (2009), SAXS-tomografi - en ny metode til at danne kontrast mellem væv, (SAXS-tomography - a novel contrast mechanism for tissue contrast), Bachelor thesis, Niels Bohr Institute, University of Copenhagen.
- Trapp, B. D., Peterson, J., Ransohoff, R. M., Rudick, R., Mörk, S. & Bö, L. (1998), 'Axonal transection in the lesions of multiple sclerosis', *New England Journal of Medicine* **338**, 278–285.
- Veronesi, U., Paganelli, G., Viale, G., Luini, A., Zurruda, S., Galimberti, V., Intra, M., Veronesi, P., Maisonneuve, P., Gatti, G., Mazzarol, G., De Cicco, C., Manfredi, G. & Fernandez, J. R. (2006), 'Sentinel-lymph-node biopsy as a staging procedure in breast cancer: update of a randomised controlled study', *Lancet Oncol.* **7**(12), 983–990.
- Vester-Christensen, M., Erbou, S. G. H., Hansen, M. F., Olsen, E. V., Christensen, L. B., Hviid, M., Ersbøll, B. K. & Larsen, R. (2009), 'Virtual dissection of pig carcasses', *Meat Science* **52**(291–297).

- Wang, Z.-T., Kang, K.-J., Huang, Z.-F. & Chen, Z.-Q. (2009), ‘Quantitative grating-based x-ray dark-field computed tomography’, *Appl. Phys. Lett.* **95**(9).
- Weitkamp, T., David, C., Bunk, O., Bruder, J., Cloetens, P. & Pfeiffer, F. (2008), ‘X-ray phase radiography and tomography of soft tissue using grating interferometry’, *European Journal of Radiology* **68**(3), 13–17.
- Weitkamp, T., David, C., Kottler, C., Bunk, O. & Pfeiffer, F. (2006), Tomography with grating interferometers at low-brilliance sources, in ‘Developments in X-Ray Tomography V’, Vol. 6318, Proc. SPIE, p. 631828.
- Weitkamp, T., Diaz, A., David, C., Pfeiffer, F., Stampanoni, M., Cloetens, P. & Ziegler, E. (2005), ‘X-ray phase imaging with a grating interferometer’, *Opt Express* **12**(16), 6296–6304.
- Wernick, M. N., Wirjadi, O., Chapman, D., Zhong, Z., Galatsanos, N. P., Yang, Y., Brankov, J. G., Oltulu, O., Anastasio, M. A. & Muehleman, C. (2003), ‘Multiple-image radiography’, *Physics in Medicine and Biology* **48**, 3875–3895.
- Wilkins, S. W., Gureyev, T. E., Gao, D., Pogany, A. & Stevenson, A. W. (1996), ‘Phase-contrast imaging using polychromatic hard x-rays’, *Nature* **384**, 335–337.
- Xin, L., Jin-Chuan, G. & Han-Ben, N. (2010), ‘A new method of detecting interferogram in differential phase-contrast imaging system based on special structured x-ray scintillator screen’, *Chinese Phys. B* **19**(7), 070701.
- Yashiro, W., Terui, Y., Kawabata, K. & Momose, A. (2010), ‘On the origin of visibility contrast in x-ray Talbot interferometry’, *Opt. Exp.* **18**(16), 16890–16901.
- Zhong, Z., Thominson, W., Chapman, D. & Sayers, D. (2000), ‘Implementation of diffraction-enhanced imaging experiments: at the NSLS and APS’, *Nucl. Instr. Meth. A* **450**, 556–567.
- Zhu, P., Zhang, K., Wang, Z., Liu, Y., Liu, X., Wu, Z., McDonald, S. A., Marone, F. & Stampanoni, M. (2010), ‘Low-dose, simple, and fast grating-based X-ray phase-contrast imaging’, *Proc. Nat. Acad. Sci. USA* **107**(31), 13576–13581.

Appendix A

Matlab script for directional dark-field imaging

Several thousand lines of code were developed for Matlab for data analysis during the course of this PhD. As directional dark-field imaging was a developed during the PhD, all code to analyze the data and display the results needed to be developed and written. In this appendix an example of the code used for the analysis is displayed.

The script is written for Matlab and used for analyzing directional dark-field data. Parts of the code is reused and adapted from code by O. Bunk. The necessary input for the script is a stack of dark-field images recorded at different sample orientations. The code necessary for preprocessing of the individual projections to generate the dark-field images for each rotation angle is not included here. The dark-field images are rotated back, so the sample overlap in all images. Subsequently the image stack is Fourier analyzed. The generated output is the variables b_0 , b_1 , ψ_1 . The variables are determined according to the model in equation (4.7) on page 44. Besides determining and plotting the variables mentioned above, the code also generate the color representation seen in Figure 4.5 on page 47.

The code is printed on the following pages.

ddf_analyze_XXXX.m

```

1 % ddf_analyze_XXXX.m - Calculates ddf images
2 % Written by Torben Jensen, TorbenHaugaardJensen@gmail.com 20/01-2010
3 % Parts of the code reused and adapted from other routines by O. Bunk.
4 % Use the code ddf_find_rot_center.m to determine the rotation center.
5 % Please cite Jensen T H, Bech M, Bunk O, Donath T, David C, Feidenhans'l R, and Pfeiffer F.
6 % Directional x-ray dark-field imaging. Phys. Med. Biol. 55, 3317 (2010).
7 %% Input
8 % Needed scripts: rotate_image.m
9 clear all,close all, drawnow
10 %% -----
11 % Define input parameters
12 %-----
13 expdata      = 'leaf1/';
14 projdir      = ['/taxi/data2/ESRF_2010_jan/analysis/' expdata];
15 procdir      = projdir;
16
17 nperiods     = 1;    % no of periods
18 no_scans      = 16;   % no of angles
19 max_angle     = -180; % maximum angle
20 center01      = 38.35;% rotation center1
21 center02      = -7.8; % rotation center2
22 scaling       = (150+.44)/150; %enlargment due to projection
23 pysize        = 0.00746; %pixelsize in mm
24 crop_in       = [00 00 00 00];
25 resize        = 1;
26 ang_offset    = 0; % angular offset for plotting
27 screensz     = get(0,'screensize');
28 %% -----
29 % Read in data from stack of dark-field images
30 % rotate images so they overlap
31 %-----
32 angles        = 0:max_angle/(no_scans):max_angle-1; %The rotation angles
33 proj_arr      = 1:no_scans; tic;
34 for proj_count=proj_arr;
35   %load dark-field images
36   temp          = load([procdir 'dci_' num2str(proj_count, '%04d') '.mat'],'dci');
37   %rotate dark-field images
38   [dci_rot0 diff] = rotate_image(0,center01,center02,1, ...
39                                 angles(proj_count)+ang_offset,temp.dci);
40   % resize
41   dci_rot(:,:,proj_count) = single(imresize(dci_rot0(1+crop_in(1):end-crop_in(2), ...
42                                               1+crop_in(3):end-crop_in(4)),resize,'bicubic'));
43   %remove areas with insufficient data
44   if proj_count==1
45     [x1 x2]=meshgrid(1:size(dci_rot,1),1:size(dci_rot,2));
46     [th,r]=cart2pol(x1-x1(end)/2,x2-x2(end)/2);bc=single(r<x1(end)/2)';
47   end
48   dci_rot(:,:,proj_count) = bc.*dci_rot(:,:,proj_count);
49   disp(['num2str(proj_count) ', ' processed, (time since start ', num2str(toc) ')']);
50 end
51 %% -----
52 % Fourier processing of the rotated dark-field images
53 %-----
54 fftdatm2      = fft(dci_rot(:,:,1:end),[],3);
55 ammdat       = abs(fftdatm2(:,:,1))/(no_scans);
56 dpcdat        = angle(fftdatm2(:,:,1+nperiods));
57 dcidat       = 2*abs(fftdatm2(:,:,1+nperiods))/no_scans;
58 %correcting phase data
59 temp          = isnan(dpcdat);dpcdat(temp)= 0;

```

```

60 %% -----
61 % Plot direct results
62 % -----
63 figure(200),clf,      set(gcf,'position',[0 0 screensz(3)*3/4 screensz(4)])
64 %b_0
65 subplot(2,2,1),      imagesc(ampdat),          title('b_0'),
66 %b_1
67 subplot(2,2,2),      imagesc(dciddat),        title('b_1'),
68 %b_1 / b_0
69 subplot(2,2,[2 4]),  imagesc(dciddat./ampdat),title('b_1/b_0'),
70 %\psi_1
71 figure(201),
72 clf, set(gcf,'position',[screensz(3)*3/4 0 screensz(3)*1/4 screensz(4)])
73 imagesc(dpcdat),      title('\psi_1'),
74 colorbar,axis image,colormap gray
75 %\psi_1
76 figure(201),
77 clf, set(gcf,'position',[screensz(3)*3/4 0 screensz(3)*1/4 screensz(4)])
78 imagesc(dpcdat),      title('\psi_1'),
79 colorbar,axis image,colormap jet
80 %% -----
81 %Produce color directional dark-field image
82 %-----
83 % rescale phase to degrees
84 f2phase = dpcdat / pi * 90.0;
85 sc      = max(dciddat./ampdat-.0,0);%remove background
86 %rescale intensity
87 sc      = sc.*5; sc = min(sc,1); sc = sc/max(sc(:));
88 %define colormap for phase-plot
89 c_map   = flipud(hsv(361));
90 % define colrcircle
91 sze     = min(size(sc));
92 bege    = round( 0+.02*sze);% begining of circle
93 ende    = round( 0+.20*sze);% end of circle
94 radio   = (ende-bege)/2;      % radius outside
95 cene    = (.5*(ende+bege)).*[1 1]; % center pixel of circle
96 minang  = -90;
97 for i=bege:ende
98     for j=bege:ende
99         rpix=((i-cene(1))^2 +(j-cene(2))^2);
100        if (rpix<(radio)^2)
101            f2phase(i+0,j) = atand((i-cene(1))/(j-cene(2)))+90;
102            f2phase(i+0,j) = -(minang + mod(f2phase(i+0,j)+90 -minang, 180));
103            sc(i+0,j)      = sqrt(rpix)/radio;
104        end
105    end
106 % Define color image function pl
107 f2phase_lin      = reshape(f2phase,size(f2phase,1)*size(f2phase,2),1);
108 pl                = c_map( round(2 * (f2phase_lin+90) +1), : ); clear f2phase_lin;
109 pl                = reshape( pl, size(f2phase,1), size(f2phase,2), 3 );
110 pl(:,:,1)        = sc .* pl(:,:,1);
111 pl(:,:,2)        = sc .* pl(:,:,2);
112 pl(:,:,3)        = sc .* pl(:,:,3);
113 y                = (1:size(pl,1))*pxsize/scaling;
114 x                = (1:size(pl,2))*pxsize/scaling;
115 figure(500),      clf, set(gcf,'position',[0 0 screensz(3)/2 screensz(4)])
116 imagesc(x,y,pl)
117 title('DDFI, Image showing the direction and amplitude of the visibility variation', 'fontsize',14)
118 axis on; axis xy; axis image;xlabel('x [mm]'); ylabel('y [mm]');

```


Appendix B

Publications

Papers I-VI are attached here.

Publication I

Submitted to Radiology

T.H. Jensen, M. Bech, T. Binderup, A. Böttiger, C. David, T. Weitkamp,
I. Zanette, E. Reznikova, J. Mohr, F. Rank, R. Feidenhans'l, A. Kjær, L.
Højgaard and F. Pfeiffer

Imaging of Metastatic Lymph Nodes by X-ray Phase Contrast Tomography
Submitted to Radiology

Imaging of Metastatic Lymph Nodes by X-ray Phase-Contrast Micro-Tomography

T. H. Jensen¹, M. Bech², T. Binderup^{3,4}, A. Böttiger¹, C. David⁴, T. Weitkamp⁵, I. Zanette⁵, E. Reznikova⁶, J. Mohr⁶, F. Rank³, R. Feidenhans'l¹, A. Kjær^{3,4}, L. Højgaard^{3,4}, F. Pfeiffer²

¹Niels Bohr Institute, Faculty of Natural Sciences, University of Copenhagen, Copenhagen, Denmark

²Department of Physics, Technical University Munich, 85747 Garching, Germany

³Dept. of Clinical Physiology, Nuclear Medicine and PET, Rigshospitalet, Copenhagen, Denmark

⁴Cluster for Molecular Imaging, Faculty of Health Sciences, University of Copenhagen, Denmark

⁴Paul Scherrer Institut, 5232 Villigen PSI, Switzerland

⁵European Synchrotron Radiation Facility, 38043 Grenoble Cedex, France

⁶Karlsruhe Institute of Technology, Institute for Microstructure Technology, 76021 Karlsruhe, Germany

Manuscript submitted to Radiology.

Abstract

Purpose:

Invasive cancer causes a change in density in the affected tissue which can be visualized by x-ray phase-contrast tomography. Therefore, the purpose of this study was, in a double blinded study, to investigate whether malignancy could be revealed by non-invasive x-ray phase-contrast tomography in lymph nodes from breast cancer patients.

Methods:

Seventeen formalin-fixed paraffin-embedded lymph nodes from 10 female patients (age range 37 – 83 years) diagnosed with invasive ductal carcinomas were analyzed by X-ray phase-contrast tomography. Ten lymph nodes had metastatic deposits and 7 were benign. The phase-contrast images were analyzed according to standards for conventional CT images looking for characteristics usually only visible by pathological examinations. For calculation of sensitivity, specificity, positive predictive value and negative predictive value of the image analyses the χ^2 test was used.

Results:

The diagnostic sensitivity of the image analysis was 100% and the specificity was 87 %. The positive predictive value was 91 % and the negative predictive value was 100%.

Conclusion:

X-ray phase-contrast imaging can accurately detect density variations to obtain information regarding lymph node involvement previously inaccessible with standard absorption x-ray imaging.

Introduction:

Breast cancer is the leading cause of death in cancer among women (1). Early diagnosis and accurate staging of the disease are crucial for proper treatment and improved prognosis. It is of major importance whether the cancer is confined to the breast or has spread to the adjacent lymph nodes. The current state-of-the-art method to investigate the regional axillary lymph nodes is the sentinel node (SNL) technique (2). Prior to the final surgical intervention, a quantity of radio-labeled colloid is injected into the breast, usually in the region around the tumor. The distribution of the radiotracer is visualized by a gamma camera image, revealing the lymph nodes that are draining the breast tissue with the tumor. These local lymph nodes, usually 1-3, are called the sentinel nodes. The surgeon identifies the sentinel node with a small Geiger probe and removes the nodes for investigation by the pathologist. This is done either per-operatively or following the primary operation. If the nodes show histological metastatic deposits, an axillary dissection is performed (3).

The sensitivity and specificity of the SNL technique is generally high. However, the technique may not be feasible for all breast cancer patients, and a non-invasive tool for identification of malignant lymph nodes would be of particular interest for non-SNL candidates. Suggested contra-indications for SNL are multifocal or multicentric lesions, previous axillary surgery, previous irradiation therapy, and neo-adjuvant chemotherapy (4-6), although large investigations regarding these contraindications are still requested.

Due to the high prognostic implication of axillary lymph node involvement, it is of paramount importance to identify a possible spread of disease for proper staging and thereby choice of treatment strategy. Especially false negative cases should be minimized for improved prognosis but also false positive cases, since removal of the whole axilla are associated with significant morbidity such as lymphoedema in the affected arm and limitations of shoulder movement (7;8). Thus, the development of a safe pre-operative, non-invasive imaging technique to identify lymph node metastases would be of paramount interest. Such an imaging technique could spare the patient axillary surgery if negative, and if positive, the primary tumor and the

affected nodes could be removed during the same operation and proper treatment initiated faster.

Tiny density variations in human tissue – below 0.1 % - can be visualized by grating-based phase-contrast X-ray tomography (9;10). Due to the wave-optical interaction of x-rays with matter, the contrast available with phase-contrast imaging is much better than standard X-ray absorption imaging. Hence, the density variations caused by invasive cancer can be visualized. Here we report the first high contrast biomedical phase-contrast imaging. The purpose of this study was, in a double blinded study, to investigate whether malignancy could be revealed by non-invasive x-ray phase-contrast tomography in lymph nodes from breast cancer patients.

Materials and Methods:

Samples:

Seventeen formalin-fixed, paraffin-embedded axillary lymph nodes were used for the study, all from axillary dissection specimens from women with invasive ductal breast carcinoma. All lymph nodes were weighted, measured on the longest diameter and cut in half prior to formalin-fixation. One half of the formalin fixed-paraffin-embedded lymph node was used for the study and the other for routine histological examination.

Haematoxylin and eosin staining (H&E-staining) was performed according to routine procedures on 10 μm sections from all samples on the experimental half of the lymph node to verify the diagnosis. In addition to the H&E-staining, each sample was imaged using phase-contrast tomography.

Phase-contrast micro-tomography:

The x-ray imaging measurements were carried out at the ID19 beamline at the European Synchrotron Radiation Facility (ESRF), in Grenoble, France. A grating interferometer was placed 150 meters from the wiggler source (see Figure 1). The principle and set-up of the x-ray grating interferometer has previously been described in detail (9;11-14). Using a monochromatic x-ray beam at 23 keV (0.54 Å), the interferometer was optimized and used for the 9th fractional Talbot distance with a grating separation of 480 mm. The Si phase grating (G1, π -phase shifting) was placed after the sample, had period of $g_1 = 4.785 \mu\text{m}$ and a height of $h_1 = 29.5 \mu\text{m}$ and was produced using photolithography and

wet chemical etching (14). The Au absorption grating (G2) was placed in front of the detector, had period of $g_2 = 2.400 \mu\text{m}$ and a height of $h_2 = 50 \mu\text{m}$ and was produced using soft X-ray lithography (15). A FReLoN CCD detector with an effective pixel size of $14.9 \times 14.9 \mu\text{m}^2$ with 1024×1024 pixels was used. Due to the limited height of the beam the field-of-view was reduced to $15.3(\text{h}) \times 13.7(\text{v}) \text{ mm}^2$.

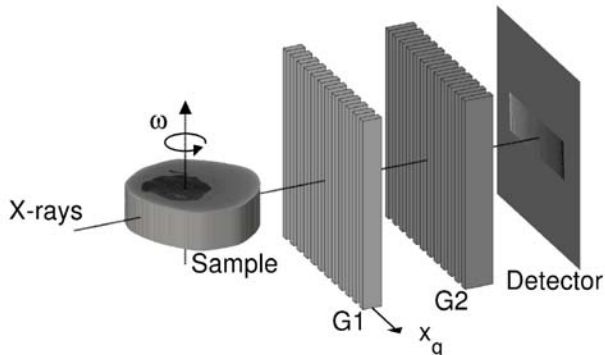


Figure 1

Experimental setup. Not to scale.

The sample is placed in front of the interferometer consisting of two x-ray optical transmission gratings, G1 and G2. The detector is placed immediately after G2. The phase-contrast images are collected for each rotation angle ω by scanning G1, along the x_g direction in four steps.

For each tomographic dataset four phase step projections with an exposure time of 0.5 seconds each were collected for 701 angles evenly distributed over 360 degrees. This resulted in a total exposure time of 24 minutes. Due to the large field-of-view four samples could be measured simultaneously. The data was reconstructed using a Hilbert-filter-based phase-contrast filtered back-projection algorithm (16). A phase unwrapping procedure was applied prior to reconstruction to suppress cupping artifacts. For each sample the dataset included (depending on the size of the sample) 100-225 adjacent $14.9 \mu\text{m}$ thick slices, thus providing a full 3D image of the sample. A movie showing the full data set for a single lymph node is presented in Appendix A (online¹).

Data analysis and statistics:

Each image was converted to DICOM format and imported into the Inveon Software (Siemens

Medical Solutions, Inc., Knoxville, TN, USA) for analysis by two experts in Nuclear Medicine. The two Nuclear Medicine Physicians who evaluated the images were both professors with 16 and 14 years of experience in Nuclear Medicine respectively.

The study was double-blinded and retrospective. Since the technique was so new and the images unlike prior absorption x-ray images, the experts who analyzed the scans first looked at three images and set their diagnosis, then they were given the correct diagnosis before completing the rest of the image analysis. This was done in order to know which features to look for in the benign and malignant lymph nodes respectively. The reference standard for metastatic disease was histopathology diagnosis set by an expert in pathology with more than 30 years of experience who was blinded to the x-ray phase-contrast results.

For calculation of sensitivity, specificity, positive predictive value and negative predictive value of the image analyses the χ^2 test was used. For comparison between groups for diameter and weight an independent-samples t-test was used. The statistical analyses were calculated using SPSS version 17.0 (SPSS Inc, Chicago, IL). $P < 0.05$ was considered significant.

Results:

Twenty-three samples were visualized by phase-contrast micro-tomography and 6 samples were excluded before the final image analysis due to technical challenges in the data processing resulting in poor image quality. Therefore, seventeen lymph nodes from 10 patients were included in the final analysis. The age range of the 10 patients was 37 – 83 years (median age 60 years).

The 17 included lymph nodes were collected from 10 patients with clinical suspiciousness of nodal involvement and all underwent complete axillary resection. Of these 10 patients, 1 had no metastasis in the resected axillary specimen, 3 had 1-3 affected nodes, 3 had 4 – 6 affected nodes and 3 had > 6 affected nodes.

Of the 17 included axillary lymph nodes, histological examination confirmed that $n = 10$ were infiltrated with invasive ductal breast carcinoma and $n = 7$ were without metastatic deposits. All lymph nodes with metastatic deposits that were included in the study had macro-

¹ http://www.fys.ku.dk/~torbenj/Sample_05_movie.avi

metastases. The 10 lymph nodes with cancer infiltration had a weight of $4.1 \text{ g} \pm 3.3$ (mean \pm SD), and a diameter of $24 \text{ mm} \pm 6.8$ (mean \pm SD). The lymph nodes without malignancy had a weight of $0.6 \text{ g} \pm 0.4$ (mean \pm SD), and a diameter of $14 \text{ mm} \pm 4.3$ (mean \pm SD). The malignant lymph nodes had a significantly higher weight and larger diameter than the non-malignant lymph nodes ($p = 0.015$ and $p = 0.005$, respectively).

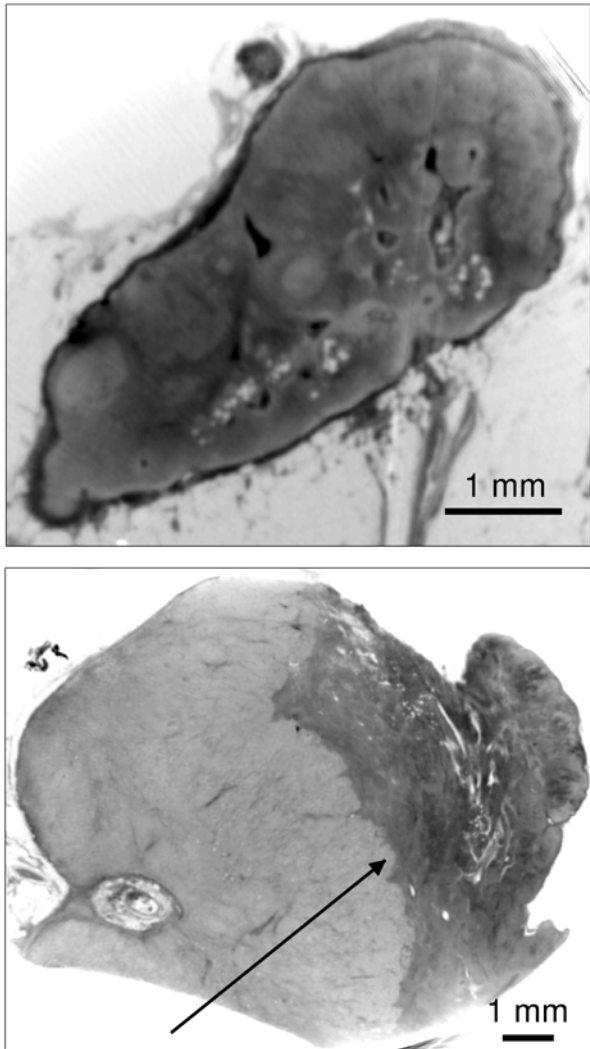


Figure 2

Phase-contrast tomography images of lymph nodes without (top panel) and with (lower panel) metastatic deposits from two patients with invasive ductal breast carcinoma. The lymphoid follicles can easily be distinguished in the image of the benign lymph node. In the lower panel the invasive edge (arrow) clearly marks the border between the metastatic majority (lighter, left) part of the lymph node and the smaller part of the node with intact normal cells (darker, right).

All of the 10 metastatic lymph nodes had a longest diameter that was above 10 mm, which is the criterion for considering the lymph node suspicious of malignancy on CT. Two lymph nodes were however close to 10 mm with the longest diameter of 12 and 13 mm respectively, which could be within the range of measurement inconsistency on CT images, and the lymph nodes could be considered non-malignant on conventional CT.

The raw data and image reconstruction was carried out by experts in x-ray physics. The final images were analyzed by two experts in nuclear medicine and both the physicists and the physicians were blinded to the diagnosis of the lymph nodes. Each of the 2 experts in Nuclear Medicine who analyzed the images had 1 false positive result and no false negative results. The false positive sample was however different for the two experts. Thus, the interobserver agreement was 88 % (15 of 17 lymph nodes) for classification of the lymph nodes as malignant or benign. The diagnostic sensitivity of the image analysis was 100% and the specificity was 87 %. The positive predictive value was 91 % and the negative predictive value was 100%. The features that were characteristic of the benign lymph nodes were an ordered structure with clearly visible lymphoid follicles (see figure 2a), whereas the malignant lymph nodes had features such as calcification, changed morphology, and a general disorganized appearance. From the example in figure 2b the border between the cancer infiltrated and the non-infiltrated part of the lymph node can be seen with a clear color difference due to the changed density of the tissue caused by the cancer infiltration. An overview showing a single slice from each sample is presented in Appendix B (online²).

Discussion:

The axillary status is one of the most important prognostic factors for breast cancer patients. Therefore, correct assessment of nodal involvement is of outmost importance, and the sentinel node technique has evolved as a mandatory part in the evaluation and staging of breast cancer patients. However, the SNL is not always indicated, e.g. for patients undergoing neo-adjuvant chemotherapy, and other approaches for axillary assessment are warranted.

² Attached following this paper.

Conventional imaging cannot accurately assess axillary lymph node involvement. Different imaging approaches have been evaluated for the use in axillary staging, and currently computer tomography and ultrasonography are the most widely used. However, no imaging modality has yet shown satisfactory sensitivity or specificity in this respect. Factors such as size and shape have been used to discriminate between malignant and benign lymph nodes, but these evaluation criterions have their obvious limitations.

A newer approach using dynamic contrast-enhanced magnetic resonance seems promising for evaluation of primary tumors for breast cancer patients after neo-adjuvant chemotherapy and has been evaluated as a surrogate marker for prediction of nodal status (17). This indirect assessment of nodal involvement may however be associated with an unsatisfactory high false-negative rate.

The diagnostic value of F-18 -Fluorodeoxy-glucose-Positron Emission Tomography (F-18-FDG-PET) with or without full-dose CT has also been evaluated as a tool for preoperative axillary staging (18;19). But again, a sensitivity around 60-70% seems unsatisfactory compared to SNL verified by histopathological examination.

Using x-ray phase-contrast tomography we demonstrate here a high sensitivity (100 %) as well as specificity (86 %), positive predictive value (91 %) and negative predictive value (100 %) with no false-negative cases. In the non-metastatic lesions the lymphoid follicles were clearly visible whereas the metastatic lesions had lost this ordered morphology. This change in morphological characteristics was clearly visible upon image analysis. This is the first time that a non-invasive imaging modality has demonstrated the ability to visually identify morphological differences between malignant and benign lymph nodes. Accordingly, x-ray phase-contrast micro-tomography gives histological information in a non-invasive manner which allows for discrimination between benign and malignant lymph nodes.

In this study, micro-metastases were not analyzed, and the detection limit for identification of metastatic deposits in lymph nodes is so far not known for this imaging approach. However, given the high morphological information achievable with x-ray phase-contrast tomography, we believe that this technique is more powerful than imaging

approaches otherwise available. In addition, it is questionable what the prognostic implication of micro-metastases is. It is known that intra-operative false-negative cases are often micro-metastases or isolated tumor cells. Two studies investigated the role of intra-operative false-negative cases. In these studies, 75% of the false-negative cases were micro-metastases or isolated tumor cells. There was no significant difference in recurrence rate between patients with true-negative SNL and patients with intra-operative false-negative SNL not undergoing axillary lymph node dissection (20;21). Thus, from the results of these studies it seems possible, that the clinical significance of micro-metastases is minor.

The non-invasive diagnostic method proposed here, based upon x-ray phase-contrast imaging, can be used for identification of metastatic deposits in lymph nodes. After developed into a clinical routine this x-ray phase-contrast imaging methodology could have a great impact on diagnosis and treatment in patients with breast cancer. The present sentinel node technique might then be replaced by a non-invasive preoperative x-ray phase-contrast evaluation of lymph node involvement in patients with breast cancer, and surgical intervention could be reduced to one operation, and perhaps more importantly, proper choice of treatment could be initiated faster.

The method of grating-based x-ray phase-contrast imaging has already been demonstrated using standard laboratory x-ray sources (10), making its use in the clinic feasible. We believe that the images presented here will constitute the next step towards a new concept for imaging cancer and possibly other diseases.

In conclusion, this study shows that there is a high sensitivity and specificity of this new modality of phase-contrast tomography, which may gain a pivotal role in the future for axillary staging of breast cancer patients.

Acknowledgements

This work was supported by the Danish Cancer Society (T.B., A.K.), by DANSCATT (M.B., T.H.J., A.B., and R.F.), by the DFG excellence cluster 'Munich-Centre for Advanced Photonics' (M.B. and F.P.). and by the European Synchrotron Radiation Facility (project MD-404) by allocation

of beam time. We thank The John and Birthe Meyer Foundation and the Danish National Advanced

Technology Foundation;

Reference List

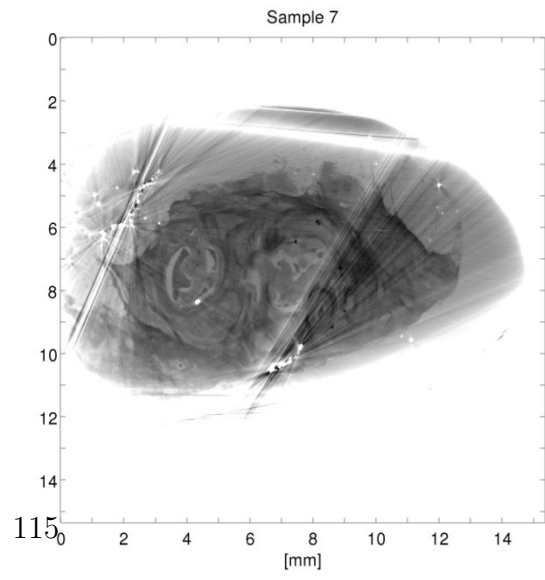
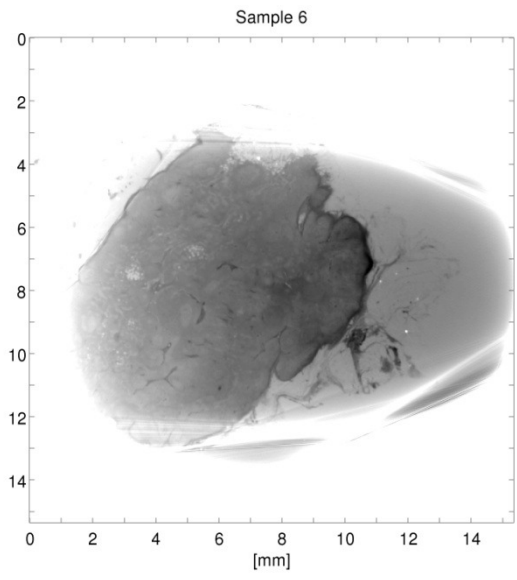
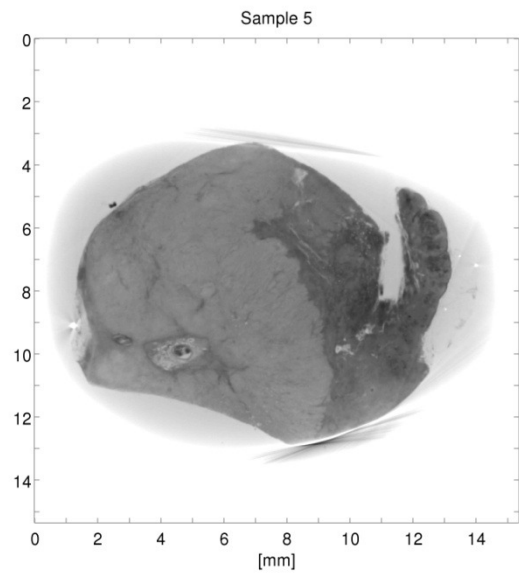
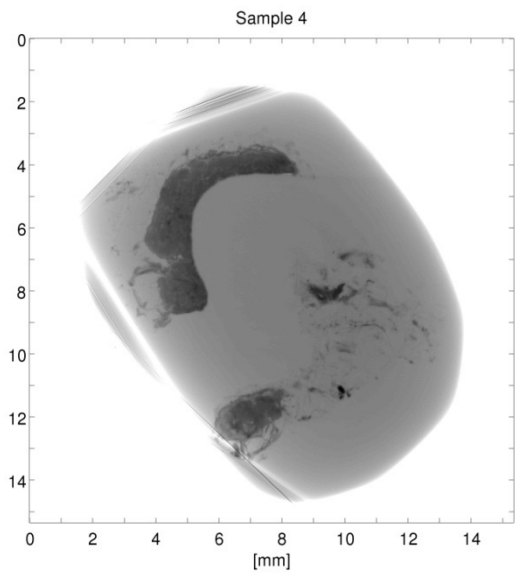
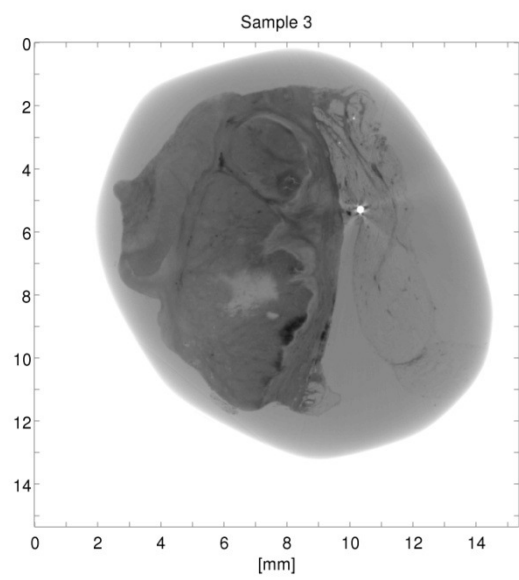
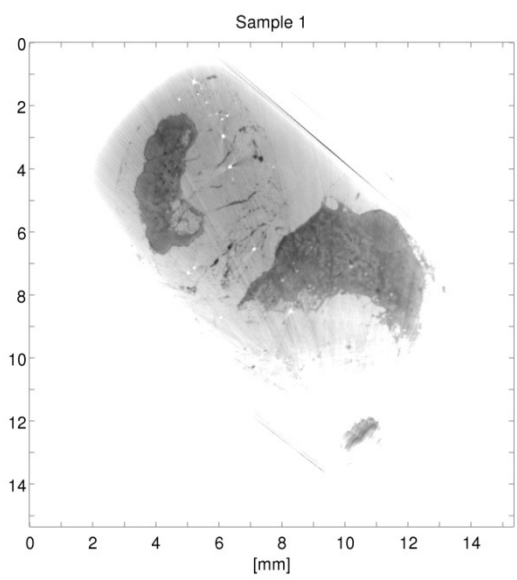
- (1) Ferlay J, Autier P, Boniol M, Heanue M, Colombet M, Boyle P. Estimates of the cancer incidence and mortality in Europe in 2006. *Ann Oncol* 2007 Mar;18(3):581-92.
- (2) Veronesi U, Paganelli G, Viale G, Luini A, Zurrida S, Galimberti V, et al. Sentinel-lymph-node biopsy as a staging procedure in breast cancer: update of a randomised controlled study. *Lancet Oncol* 2006 Dec;7(12):983-90.
- (3) Samphao S, Eremin JM, El-Sheemy M, Eremin O. Management of the axilla in women with breast cancer: current clinical practice and a new selective targeted approach. *Ann Surg Oncol* 2008 May;15(5):1282-96.
- (4) Shien T, Akashi-Tanaka S, Yoshida M, Hojo T, Iwamoto E, Miyakawa K, et al. Evaluation of axillary status in patients with breast cancer using thin-section CT. *Int J Clin Oncol* 2008 Aug;13(4):314-9.
- (5) Anderson BO. Sentinel lymphadenectomy in breast cancer: an update on the NCCN clinical practice guidelines. *J Natl Compr Canc Netw* 2003 Jan;1 Suppl 1:S64-S70.
- (6) Reintgen D, Giuliano R, Cox C. Lymphatic mapping and sentinel lymph node biopsy for breast cancer. *Cancer J* 2002 May;8 Suppl 1:S15-S21.
- (7) Schulze T, Mucke J, Markwardt J, Schlag PM, Bembenek A. Long-term morbidity of patients with early breast cancer after sentinel lymph node biopsy compared to axillary lymph node dissection. *J Surg Oncol* 2006 Feb 1;93(2):109-19.
- (8) Peintinger F, Reitsamer R, Stranzl H, Ralph G. Comparison of quality of life and arm complaints after axillary lymph node dissection vs sentinel lymph node biopsy in breast cancer patients. *Br J Cancer* 2003 Aug 18;89(4):648-52.
- (9) Pfeiffer F, Bunk O, David C, Bech M, Le Duc G, Bravin A, et al. High-resolution brain tumor visualization using three-dimensional x-ray phase contrast tomography. *Phys Med Biol* 2007 Dec 7;52(23):6923-30.
- (10) Pfeiffer F, Weitkamp T, Bunk O, David C. Phase retrieval and differential phase-contrast imaging with low-brilliance X-ray sources. *Nat Phys* 2006 Apr;2(4):258-61.
- (11) David C, Weitkamp T, Pfeiffer F, Diaz A, Bruder J, Rohbeck T, et al. Hard X-ray phase imaging and tomography using a grating interferometer. *Spectrochimica Acta Part B: Atomic Spectroscopy* 2007 Jul;62(6-7):626-30.
- (12) Weitkamp T, Diaz A, David C, Pfeiffer F, Stampanoni M, Cloetens P, et al. X-ray phase imaging with a grating interferometer. *Opt Express* 2005 Aug 8;13(16):6296-304.
- (13) Momose A, Yashiro W, Takeda Y, Suzuki Y, Hattori T. Phase Tomography by X-ray Talbot Interferometry for Biological Imaging. *Jpn J Appl Phys* 2006 Jun 8;45(6A):5254-62.
- (14) David C, Nöhammer B, Solak HH, Ziegler E. Differential x-ray phase contrast imaging using a shearing interferometer. *Applied Physics Letters* 2002 Oct 21;81(17):3287-9.
- (15) Reznikova E, Mohr J, Boerner M, Nazmov V, Jakobs PJ. Soft X-ray lithography of high aspect ratio SU8 submicron structures. *Microsystem Technologies* 2008 Oct 1;14(9):1683-8.
- (16) Pfeiffer F, Kottler C, Bunk O, David C. Hard x-ray phase tomography with low-brilliance sources. *Phys Rev Lett* 2007 Mar 9;98(10):108105.
- (17) Hsiang DJ, Yamamoto M, Mehta RS, Su MY, Baick CH, Lane KT, et al. Predicting nodal status using dynamic contrast-enhanced magnetic resonance imaging in patients with locally advanced breast cancer undergoing neoadjuvant chemotherapy with and without sequential trastuzumab. *Arch Surg* 2007 Sep;142(9):855-61.
- (18) Fuster D, Duch J, Paredes P, Velasco M, Munoz M, Santamaria G, et al. Preoperative staging of large primary breast cancer with [18F]fluorodeoxyglucose positron emission tomography/computed tomography compared with conventional imaging procedures. *J Clin Oncol* 2008 Oct 10;26(29):4746-51.
- (19) Heusner TA, Kuemmel S, Hahn S, Koeninger A, Otterbach F, Hamami ME, et al. Diagnostic value of full-dose FDG PET/CT for axillary lymph node staging in breast cancer patients. *Eur J Nucl Med Mol Imaging* 2009 Oct;36(10):1543-50.
- (20) Takei H, Kurosumi M, Yoshida T, Ishikawa Y, Hayashi Y, Ninomiya J, et al. Axillary lymph node dissection can be avoided in women with breast cancer with intraoperative, false-negative sentinel lymph node biopsies. *Breast Cancer* 2010;17(1):9-16.
- (21) Taras AR, Hendrickson NA, Lowe KA, Atwood M, Beatty JD. Recurrence rates in breast cancer patients with false-negative intraoperative evaluation of sentinel lymph nodes. *Am J Surg* 2010 May;199(5):625-8.

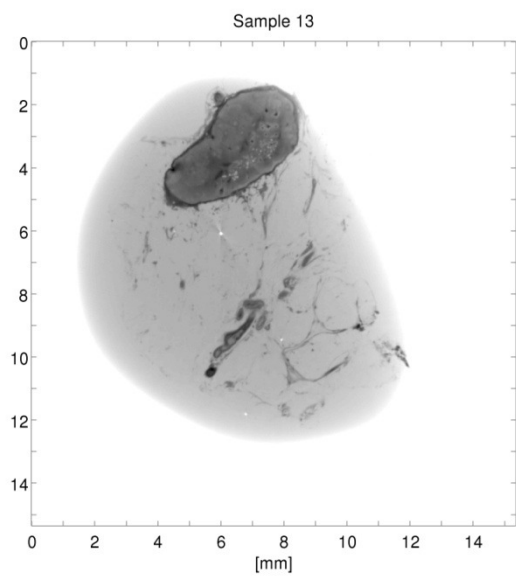
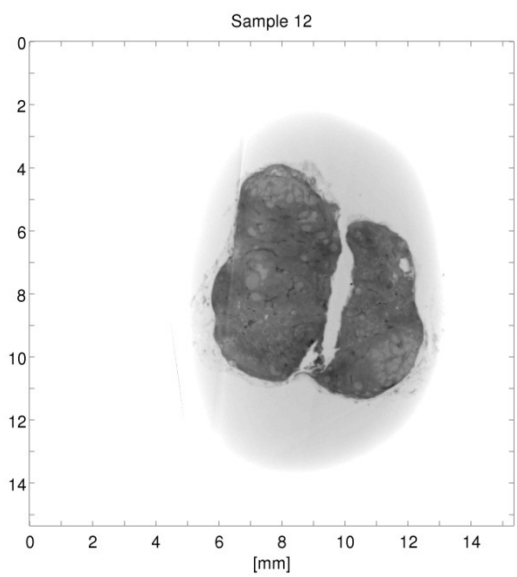
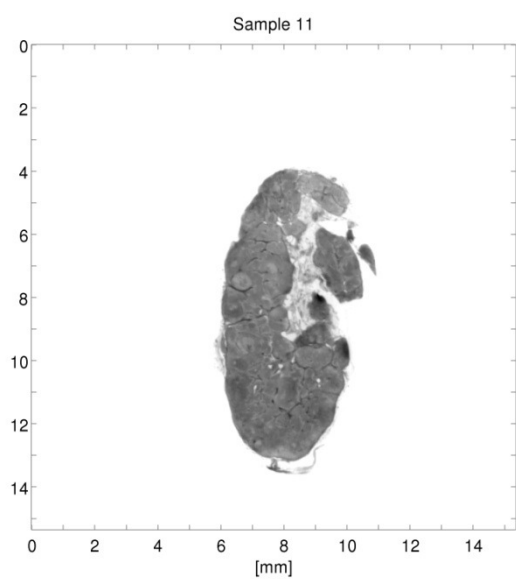
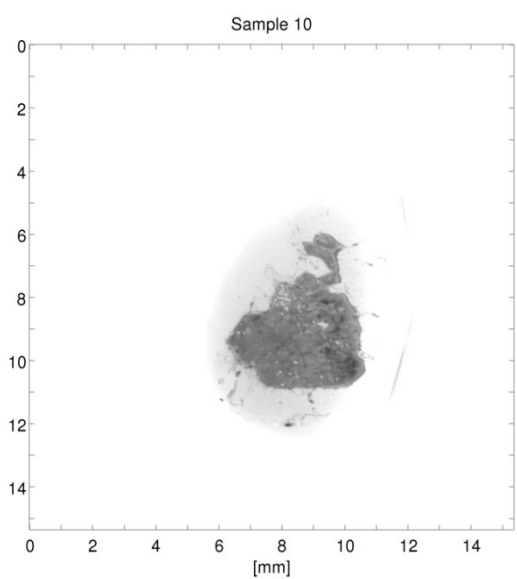
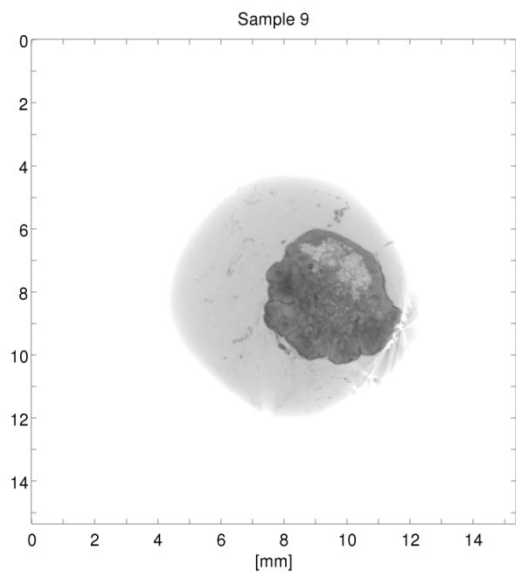
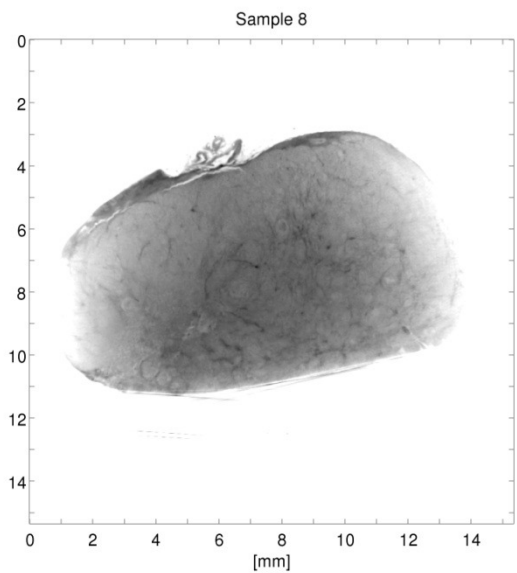
Overview of samples

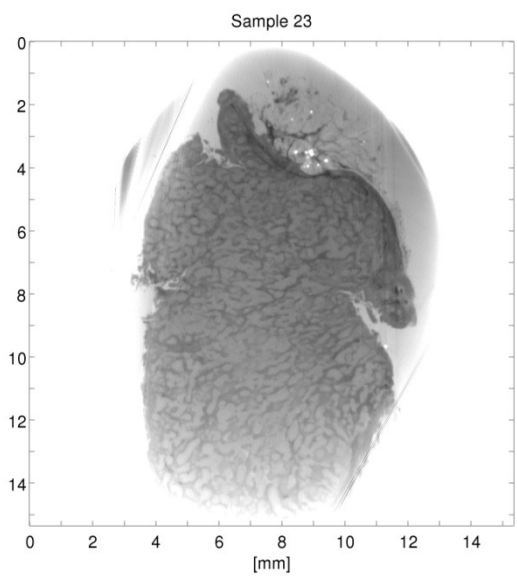
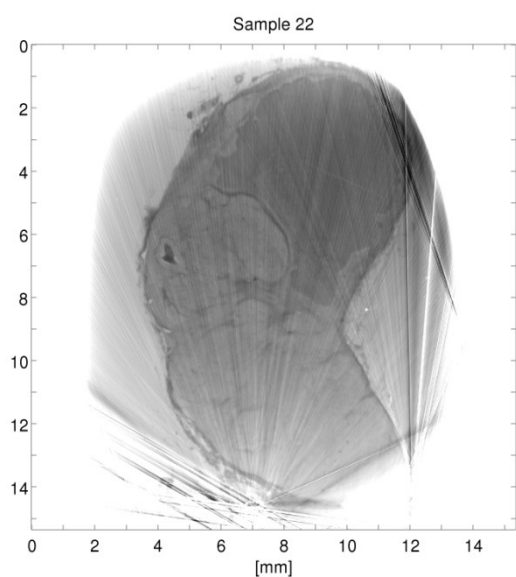
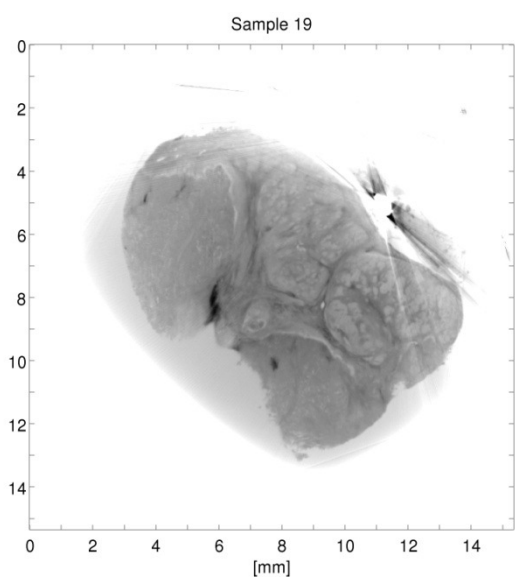
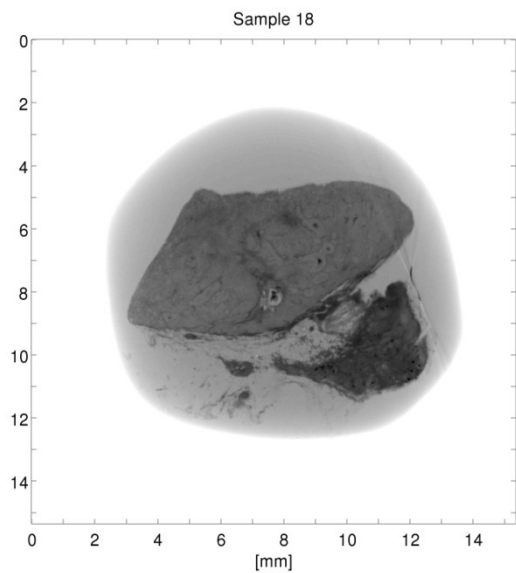
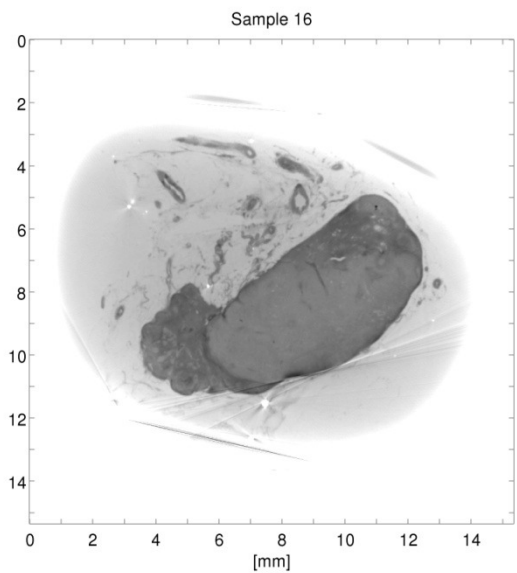
List of sample and their diagnosis as determined from histological examination. Twenty-three samples were visualized by phase-contrast micro-tomography and 6 samples were excluded before the final image analysis due to technical challenges in the data processing resulting in poor image quality.

Sample no	Diagnosis	Excluded
1	Benign	
2		X
3	Malignant	
4	Benign	
5	Malignant	
6	Benign	
7	Malignant	
8	Malignant	
9	Benign	
10	Benign	
11	Benign	
12	Malignant	
13	Benign	
14		X
15		X
16	Malignant	
17		X
18	Malignant	
19	Malignant	
20		X
21		X
22	Malignant	
23	Malignant	

A single slice from each sample is shown below. Note that for each sample 100-225 slices were available in full 1024x1024 resolution. These full 3D data sets were used for diagnosis.







Publication II

Submitted to Meat Science

T.H. Jensen, A. Böttiger, M. Bech, I. Zanette, T. Weitkamp, S. Rutishauser, C. David, E. Reznikova, J. Mohr, L. Bager Christensen, E. Olsen, R. Feidens'l, and F. Pfeiffer

X-ray phase-contrast tomography of porcine fat and rind
Submitted to Meat Science

X-ray phase-contrast tomography of porcine fat and rind

Torben H. Jensen¹, Arvid Böttiger¹, Martin Bech², Irene Zanette³, Timm Weitkamp³, Simon Rutishauser⁴, Christian David⁴, Elena Reznikova⁵, Jürgen Mohr⁵, Lars Bager Christensen⁶, Eli V. Olsen⁶, Robert Feidenhans'l¹, Franz Pfeiffer²

¹ *Niels Bohr Institute, University of Copenhagen, Copenhagen, Denmark*

² *Department of Physics, Technical University of Munich, Garching, Germany*

³ *European Synchrotron Radiation Facility, Grenoble, France*

⁴ *Paul Scherrer Institut, Villigen PSI, Switzerland*

⁵ *Karlsruhe Institute of Technology, Institute for Microstructure Technology, Karlsruhe, Germany*

⁶ *DMRI/Danish Technological Institute, Roskilde, Denmark*

Abstract

X-ray computed tomography (CT) has recently received increased attention in the food science community. The aim of this paper is to demonstrate how grating based phase-contrast CT can provide contrast superior to standard absorption based CT. We apply the method of phase-contrast CT to porcine subcutaneous fat and rind. The additional contrast obtained may be used for quality testing and to investigate variations in fatty acid composition of the fat-fraction, or water holding capacity in the meat-fraction. The possibility of integrating the method into an abattoir environment is discussed.

Keywords: Phase-contrast CT, X-ray computed tomography, Fatty acids, Image analysis, Pig, Meat quality,

1. Introduction

X-ray computed tomography (CT) has over the last 40 years become a valuable tool for non-destructive three dimensional imaging (Kalender, 2006), mainly in human medical applications, but also emerging in various applications based in the food science community (Fournols et al., 2009; Vester-Christensen et al., 2009; Kongsro et al., 2009; Prieto et al., 2010; Judas et

al., 2006). The applications include classification of pig carcasses into lean meat, fat and bone composition (Vester-Christensen et al., 2009; Judas et al., 2006), determination of the lean meat percentage (Fournols et al., 2009; Vester-Christensen et al., 2009; Judas et al., 2006) and selection of the best breeding individuals in a sheep breeding program (Kongsro et al., 2009).

While CT works well for classification of pig carcasses into three tissue classes: lean meat, fat and bone, CT is limited when investigating subtle differences within the individual fractions. This could e.g. include investigations into the fatty acid composition of the fat-fraction, or water holding capacity in the meat-fraction. Methods such as MRI have been demonstrated to provide contrast superior to standard CT (Perez-Palacios et al., 2010). However MRI is very expensive and very time consuming.

Recently a novel grating based x-ray phase-contrast tomographic method with increased contrast was demonstrated (David et al., 2002; Momose et al., 2003; Weitkamp et al., 2005; Bech et al., 2010). The method exploits the full complex refractive index of the x-rays, and uses the refraction of the x-rays for image generation. Due to the wave-optical interaction of x-rays with matter, the contrast available with phase-contrast imaging is much better than standard x-ray absorption imaging.

The aim of this article is to demonstrate how this new phase-contrast methodology can be used for imaging of porcine meat and fat. Grating based x-ray phase-contrast CT has recently been used to demonstrate increased contrast in a number of biomedical applications (Pfeiffer et al., 2007a; Bech et al., 2009; Donath et al., 2010). One important feature of the method is that it has been demonstrated in a set-up using a conventional x-ray tube (Pfeiffer et al., 2006, 2007b; Bech et al., 2009; Donath et al., 2010; Momose, 2005; Momose et al., 2006). This may allow the integration of the method in an abattoir environment.

2. Material and methods

2.1. Experimental set-up

The x-ray phase-contrast tomography measurements were carried out using a grating interferometric set-up at the ID19 beamline at the European Synchrotron Radiation Facility (ESRF), in Grenoble, France. The grating interferometer outlined in Fig. 1 has previously been described in detail (Weitkamp et al., 2005; Pfeiffer et al., 2006, 2007a, 2008a,b). It consists of a phase grating (G1), and an analyzer absorption grating (G2). The first

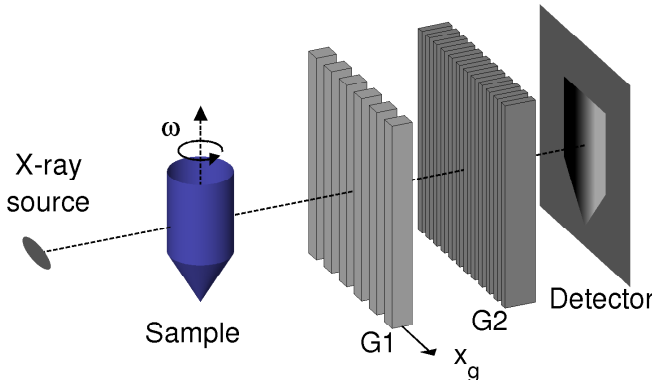


Figure 1: X-ray grating interferometer. (a) Set-up with a phase grating G1 and an analyzer absorption grating G2. The sample is rotated around a vertical axis parallel to the grating lines. G1 is scanned in the direction of x_g to determine the position of the interference pattern generated at the plane of G2.

grating, (G1) generates a periodic intensity modulation at the position of the second grating (G2). The second grating is used to analyze the position and amplitude of the intensity modulation. The gratings periods were $g_1 = 4.79 \mu\text{m}$ and $g_2 = 2.40 \mu\text{m}$. The heights of the grating structures were $23 \mu\text{m}$ (G1) and $50 \mu\text{m}$ (G2). The height of G1 was optimized for π -phaseshift at the used x-ray energy of 17.6 keV ($\lambda = 0.70 \text{ \AA}$). G1 was produced using photolithography and wet chemical etching (David et al., 2002, 2007). G2 was produced using soft X-ray lithography (Reznikova et al., 2008). The distance between G1 and G2 was 447 mm, corresponding to the eleventh fractional Talbot distance (Bech et al., 2009). The images were recorded using a FReLoN 2000 CCD with 2048×2048 pixels with an effective pixel size of $7.46 \times 7.46 \mu\text{m}^2$. The sample was mounted in a plastic cylinder which was submerged in a water bath during measurements. For the tomographic data-set four phase step projections with an exposure time of 4.5 seconds each were collected for 1000 angles evenly distributed over 360 degrees. This resulted in a total exposure time of 5 hours. In an optimized set-up phase-contrast tomography will require times similar to standard absorption tomography measurements in the range of minutes.

2.2. Data acquisition and processing

In standard absorption-contrast x-ray tomography the imaginary part of the complex refractive index is recorded and reconstructed. For x-rays the

complex refractive index is often described as,

$$n = 1 - \delta + i\beta. \quad (1)$$

In absorption-contrast it is thus the quantity β that is reconstructed. This is related to the often used absorption length μ through (Als-Nilsen and McMorrow, 2001),

$$\mu \equiv \frac{4\pi}{\lambda} \beta, \quad (2)$$

where λ is the wavelength of the x-rays.

In phase-contrast tomography the real part of the refractive index is reconstructed. The real part, δ , is directly related to the electron density, ρ_e , (Als-Nilsen and McMorrow, 2001)

$$\rho_e = \frac{2\pi r_0}{\lambda^2} \delta, \quad (3)$$

where $r_0 = 2.82 \times 10^{-15}$ m is the Thomson scattering length. The electron density, ρ_e is thus often used when presenting phase-contrast tomographic results.

The advantage for phase-contrast imaging is that the real part of the refractive index is orders of magnitude larger than the imaginary part. For water at 17.6 keV, $\delta = 7.45 \times 10^{-7}$ and $\beta = 5.43 \times 10^{-10}$ (Henke et al., 1993). This difference in magnitude offers the possibility of a substantial increase in image contrast with phase-contrast tomography over standard absorption-contrast tomography.

2.3. Fat sampling and analysis

The two fat samples were extracted from two individual pig carcasses finished at a Danish commercial abattoir. The two carcasses were treated by similar standard slaughter procedure including scalding, dehairing before slaughter and using a tunnel chilling procedure storing in the equalization room for 24 hours. After excision the samples were frozen, and defrosted shortly before imaging. The two carcasses were part of a larger feeding experiment focused on the effect on fat quality from using two different feeding strategies: high wheat content vs. high maize content. The feed composition is summarized in Table 1.

Diet treatment	I	II
Number of pigs	30	29
Soybean meal, peeled	17.92	25.01
Barley	8	8
Wheat	68.74	1.7
Maize (grounded)	0	60
FESv ^a /kg	1.13	1.17
Digestible protein/FESv	130	130
Crude fat/FESv	3.23	4.03

Table 1: Description of experimental diet for the two feeding strategies. (^a) FESv = Danish feed unit for growing pigs.

3. Results

To test the applicability of phase-contrast tomography for imaging of porcine fat, we measured two fat samples.

Figure 2 shows an example of the results. The two pieces of fat are mounted in a small plastic cylinder. The bottom sample (sample B) is mounted so that the dermis is on top and two layers of subcutaneous fat below. The top most sample (sample A) is mounted sideways with the dermis to the right. Both images are scaled with two times the standard deviation. Sample A followed diet treatment II and Sample B diet treatment I (Table 1). We notice that in the absorption image (Fig. 2a) we can distinguish the fat from the water it is submerged in, but there is no difference in contrast between the dermis and the water in the sample container. In the phase-contrast image, this is much different. We can clearly separate the dermis and the water. It is even possible to see contrast differences within the dermis.

To provide a quantitative comparison of the absorption-contrast to phase-contrast, Fig. 2a displays the values along the dashed lines in Figs. 2a,b. The two axes have been scaled for the curves to overlap. We observe that the difference between the water and the dermis in the absorption-contrast is lower than the noise level, whereas it is clearly resolved in the phase-contrast. We also note the clear difference in signal to noise ratio. The noise is significantly reduced in the phase-contrast images. Based on the standard devi-

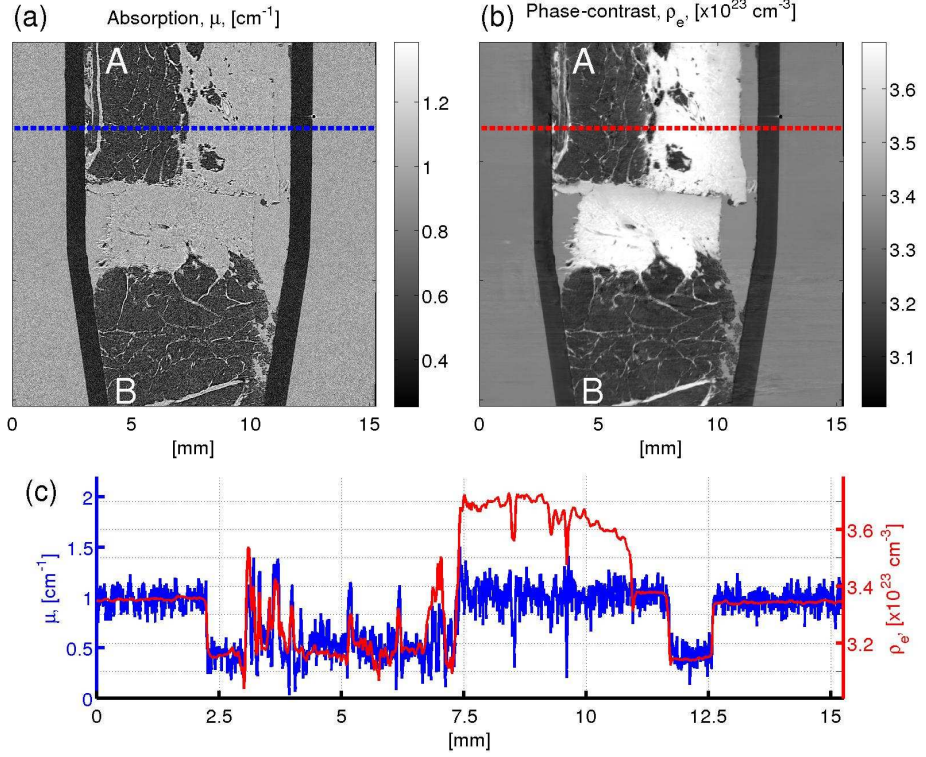


Figure 2: (a) Frontal slice through the tomographic reconstruction of the absorption-contrast. (b) Frontal slice through the tomographic reconstruction of the phase. (a) and (b) are scaled displayed on a linear gray scale corresponding to $\pm 2\sigma$, where σ is the standard deviation of the pixel gray values in the image. (c) Plot of the absorption-contrast and phase-contrast through the lines marked in (a) and (b).

ation of the gray values in water regions of the reconstructed tomographic slices, we deduced from the phase-contrast measurements an electron density sensitivity of $9.0 \times 10^{20} \text{ cm}^{-3}$ corresponding to a mass density sensitivity of approximately 2.7 mg cm^{-3} for aqueous specimens. From the absorption-contrast measurements we deduced a measurement sensitivity for the absorption length of 0.10 cm^{-1} corresponding to a mass density sensitivity of approximately 100 mg cm^{-3} for aqueous specimens. The phase-contrast measurements thus have a forty-fold increase in sensitivity for aqueous specimens in this experiment.

These differences can be further explored by studying the histogram representation of the two data-sets. The histograms are displayed in Fig. 3. For

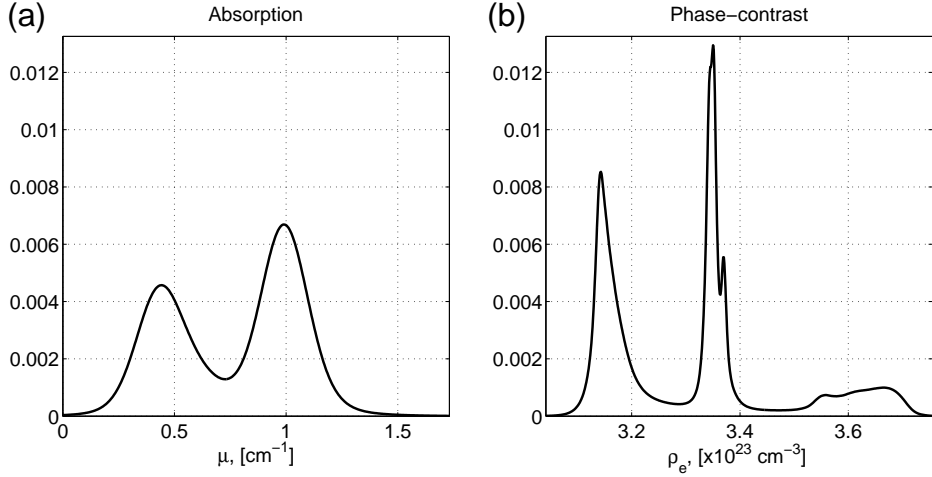


Figure 3: (a) Histogram of the absorption-contrast. (b) Histogram of the phase-contrast. Both are generated from the full 3D data-sets.

the absorption we see two wide distributions. By comparing Fig. 2a and Fig. 3a we see the fat and the plastic cylinder are included in the left distribution and water and dermis in the right distribution. The distributions of the individual constituents are so broad and overlapping, that they cannot be individually distinguished. For the phase-contrast histogram we see at least 7 different distributions. On the left the fat and the plastic cylinder are again overlapping. In the middle two narrow peaks represent the water inside and outside the sample container. The water inside the cylinder has a slightly lower density due to dissolution of material from the samples. Finally the dermis is represented by three or more overlapping regions near $\rho_e = 3.6 \times 10^{23} \text{ cm}^{-3}$. In the histograms we again see the clear separation between the water and the dermis. The narrow distributions in the phase-contrast histogram shows the increased signal to noise ratio. Besides the increase in signal to noise it is also worth noticing the increase in the contrast to noise ratio (CNR). In the absorption data there is no visible contrast between the rind and the water, so $\text{CNR} \approx 0$. While for the phase-contrast data, we see a clear difference in contrast between the water and the rind, with $\text{CNR} \approx 30$.

In the following we will look a little closer at the histograms of the rind and fat fractions.

In Figure 4 we investigate the variation in electron density of the sub-

cutaneous fat. We have determined the histogram of two regions of interest (ROI) of subcutaneous fat. One volume is taken from each sample. The two volumes are marked in Fig. 4a. In Fig. 4b the corresponding histograms are shown. We immediately see that there is a difference between the two distributions. Sample B seems to have a slightly higher electron density. The differences are quite small, the relative change in peak position is only 0.18%. Even though the differences are small they are still quite clear. The electron densities for different common fatty acids are varying in the 0.5-5.0%-range (Henke et al., 1993; Manohara et al., 2008). We thus believe that phase-contrast tomography could be a non-destructive method to investigate the fatty acid composition of porcine fat. The origin of the observed difference may be the different feeding strategies of the pigs from which the two samples were taken that was outlined in Table 1. Systematic studies have to be performed to finally validate this assumption.

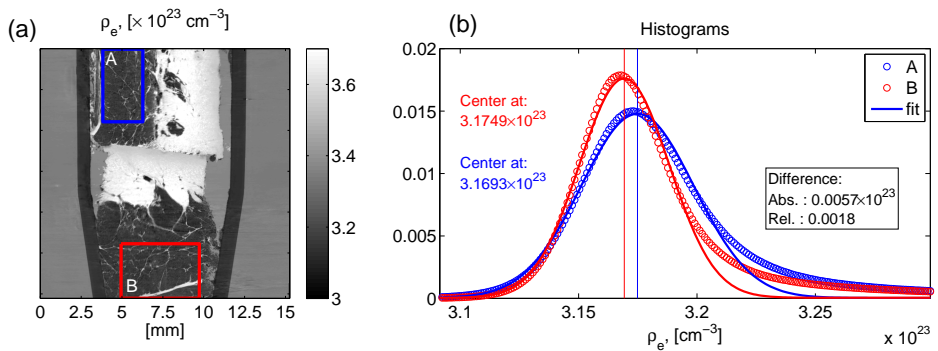


Figure 4: Variations in the fat density **(a)** Overview of the probed regions. Full 3D volumes were probed. **(b)** Histogram of the electron density of the fat in the two different samples. We do see a significant difference in the mean electron density of the two samples.

In Figure 5 we investigate the variation in electron density of the dermis layer. We determined the variation in electron density as a function of distance to the surface. This was done in 3D, so a 2D slice was investigated for each distance. Both samples were investigated showing similar features. We here show the results for sample A. In Fig. 5a a slice of the investigated sample is imaged. In Fig. 5b the histograms corresponding to the four distances marked in Fig. 5a are shown. The histograms are colour coded according to the marks in Fig. 5a. We see that there are large variations in electron density. The peaks for different distances are completely separated. In Fig. 5c the position of the peaks in Fig. 5b are plotted as a function of distance from

the surface. We see that the density is lowest at the surface and increases linearly for about 2 mm, followed by a decrease to the fat compartments. This goes to demonstrate that different parts of the dermis can easily be separated using phase-contrast. With absorption contrast this is not possible due to the poorer signal to noise ratio and resulting broad distributions. The sample was heat treated, and this might influence the density through absorption of water from the chilling procedure due to condensation. Further research has to be conducted on this topic to confirm these speculations.

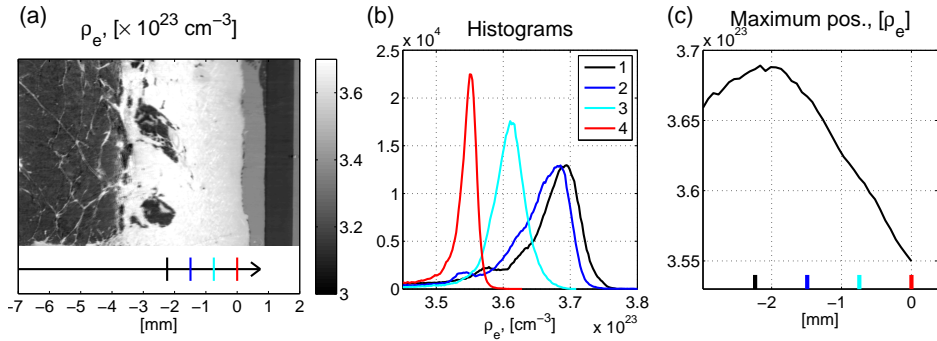


Figure 5: Variations in the rind density (a) Overview of the probed regions. 2D vertical slices transverse to the image was probed. (b) Histogram of four different slices at different distances to the surface. The slices are marked by colour in (a). (c) The mean electron density as a function of distance to the surface of the sample. The rind has a lower density at the surface, which increases for about 2 mm. The variation is up to 4%.

4. Conclusion and Implications

We have demonstrated that grating based x-ray phase-contrast tomography of porcine fat and rind provides a significant increase in the image contrast compared to standard absorption based CT. This increased contrast can be used to investigate the individual fractions of the porcine tissue, such as the fatty acid composition of the fat-fraction and the density variations in the rind. It may also be used to obtain a better understanding of fat and meat quality and how treatment influences this.

A second possible use of the increased contrast is to use this to reduce the required exposure time. With phase-contrast CT images of sufficient quality can be obtained a lot faster than with standard methods due to the increased sensitivity of the method. This will result in a reduction in the dose delivered

to the sample, as well as an increase in the capacity (products/second) of the imaging system. The increased speed could be used to integrate online CT into production environments. As discussed above the method of grating based CT has already been demonstrated with a standard x-ray tube source.

Acknowledgements

We gratefully acknowledge Keld Theodor for technical support. M.B. and F.P. acknowledge financial support through the DFG Cluster of Excellence Munich-Centre for Advanced Photonics and the European Research Council (FP7, Starting grant #240142). T.H.J. and A.B. acknowledges support from the Danish Natural Science Research Council through DANSCATT. This work was supported by the European Synchrotron Radiation Facility (project MI-1001) by allocation of beam time.

References

- Als-Nielsen, J. and McMorrow, D. (2001). *Elements of Modern X-ray Physics*, John Wiley & Sons Ltd.
- Bech, M., Jensen, T.H., Feidenhans'l, R., Bunk, O., David, C. and Pfeiffer, F. (2009). Soft-tissue phase-contrast tomography with an x-ray tube source. *Phys. Med. Biol.*, 54, 2747-2753.
- Bech, M., Jensen, T.H., Bunk, O., Donath, T., David, C., Weitkamp, T., Le Duc, G., Bravin, A., Cloetens, P. and Pfeiffer, F. (2010). Advanced contrast modalities for X-ray radiology: Phase-contrast and dark-field imaging using a grating interferometer. *Z. Med. Phys*, 20, 7-16.
- Donath, T., Pfeiffer, F., Bunk, O., Grünzweig, C., Hempel, E., Popescu, S., Vock, P. and David, C. (2010). Toward Clinical X-ray Phase-Contrast CT Demonstration of Enhanced Soft-Tissue Contrast in Human Specimen. *Invest. Radiol.*, 7, 445-52.
- David, C., Nöhammer, B., Solak, H.H. and Ziegler, E. (2002). Differential x-ray phase contrast imaging using a shearing interferometer. *Appl. Phys. Lett.*, 81, (17) 3287-3289.
- David, D., Bruder, J., Rohbeck, T., Grünzweig, C., Kottler, C., Diaz, A., Bunk, O. and Pfeiffer, F. (2007). Fabrication of diffraction gratings for hard X-ray phase contrast imaging. *Microel. Eng.*, 84, 1172-1177.

- Fournols, M.F., Teran, M.F. and Gispert, M. (2009). Estimation of lean meat content in pig carcasses using x-ray computed tomography and PLS regression. *Chemometrics and Intelligent Laboratory Systems*, 98(1), 31-37.
- Henke, B.L. and Gullikson, E.M. and Davis, J.C. (1993). X-ray interactions: photoabsorption, scattering, transmission, and reflection at $E=50\text{-}30000$ eV, $Z=1\text{-}92$. *Atomic Data and Nuclear Data Tables*, 54, 181-342.
- Judas, M., Höreth, R. and Dobrowolski, A. (2006). Computertomografie als Methode zur Analyse der Schlachtkörper von Schweinen. *Fleischwirtschaft*, 12, 102-105.
- Kalender, W.A. (2006). X-ray computed tomography. *Phys. Med. Biol.*, 51, R29-R43.
- Kongsro, J., Røe, M., Kvaal, K., Aastveit, A.H. and Egelandsdal B.. (2009). Prediction of fat, muscle and value in Norwegian lamb carcasses using EUROP-classification, carcass shape and length measurements, visible light reflectance and computer tomography (CT). *Meat Science*, 81, 102-107.
- Manohara, S.R., Hanagodimath, S.M. and Gerward, L. (2008). Studies on effective atomic number, electron density and kerma for some fatty acids and carbohydrates. *Phys. Med. Biol.*, 20, N377-N386.
- Momose, A. (2003). Phase-sensitive imaging and phase tomography using X-ray interferometers. *Opt. Exp.*, 11, (19) 2303-2314.
- Momose, A. (2005). Recent Advances in X-ray Phase Imaging. *Jpn. J. Appl. Phys.*, Vol. 44, No. 9A (2005)
- Momose, A., Yashiro, W., Takeda, Y., Suzuki, Y. and Hattori, T. (2006). Phase Tomography by X-ray Talbot Interferometry for Biological Imaging. *Jpn. J. Appl. Phys.*, Vol. 45, No. 6A (2006)
- Perez-Palacios, T., Antequera, T., Luisa Duran, M., Caro, A., and Rodriguez, P.G., and Ruiz, J. (2010). MRI-based analysis, lipid composition and sensory traits for studying Iberian dry-cured hams from pigs fed with different diets. *Food Research Int.*, 43, 248-254.

- Pfeiffer, F., Weitkamp, T., Bunk, O. and David, C. (2006). Phase retrieval and differential phase-contrast imaging with low-brilliance X-ray sources. *Nature Phys.*, *2*, 258-261.
- Pfeiffer, F., Bunk, O., David, C., Bech, M., Le Duc, G., Bravin, A. and Cloetens, P. (2007a). High-resolution brain tumor visualization using three-dimensional x-ray phase contrast tomography. *Phys. Med. Biol.*, *52*, 692330.
- Pfeiffer, F., Kottler, C., Bunk, O., and David, C. (2007b). Hard X-ray phase tomography with low-brilliance sources. *Phys. Rev. Lett.*, *98* 108105.
- Pfeiffer, F., Bech, M., Bunk, O., Kraft, P., Eikenberry, E.F., Brönnimann, C.H., Grünzweig, C. and David, C. (2008a). Hard-X-ray dark-field imaging using a grating interferometer. *Nature Mat.*, *7*, 134-137.
- Pfeiffer, F., Bech, M., Bunk, O., Donath, T., Henrich, B., Kraft, P. and David, C. (2008b). X-Ray Dark-Field and Phase-Contrast Imaging using a Grating Interferometer. *J. Appl. Phys.*, *105*, 102006.
- Prieto, N., Navajas, E.A., Richardson, R.I., Ross, D.W., Hyslop, J.J., Simm, G. and Roehe R. (2010). Predicting beef cuts composition, fatty acids and meat quality characteristics by spiral computed tomography. *Meat Science*, *86*, 770-779.
- Reznikova, E., Mohr, J., Boerner, M., Nazmov, V., and Jakobs, P. (2008). Soft X-ray lithography of high aspect ratio SU8 submicron structures. *Microsyst. Technol.*, *14*, 1683-1688.
- Vester-Christensen, M., Erbou, S.G.H., Hansen, M.F., Olsen, E.V., Christensen, L.B. Hviid, M., Ersbøll, B.K. and Larsen, R. (2009). Virtual dissection of pig carcasses. *Meat Science*, *52*, 291-297.
- Weitkamp, T., Diaz, A., David, C., Pfeiffer, F., Stampanoni, M., Cloetens, P. and Ziegler, E. (2005). X-ray phase imaging with a grating interferometer. *Opt. Exp.*, *13*, (16), 62966304.

Publication III

Physics in Medicine and Biology (2010)

T.H. Jensen, M. Bech, O. Bunk, T. Donath, C. David, R. Feidenhans'l and F. Pfeiffer

Directional x-ray dark-field imaging

Physics in Medicine and Biology 55 (2010) 3317-3323

Directional x-ray dark-field imaging

Torben H Jensen¹, Martin Bech^{1,3}, Oliver Bunk², Tilman Donath²,
Christian David², Robert Feidenhans'l¹ and Franz Pfeiffer³

¹ Niels Bohr Institute, University of Copenhagen, DK-2100 Copenhagen, Denmark

² Paul Scherrer Institut, CH-5232 Villigen PSI, Switzerland

³ Department of Physics, Technical University of Munich, 85747 Garching, Germany

E-mail: torbenj@fys.ku.dk and franz.pfeiffer@tum.de

Received 22 January 2010, in final form 30 March 2010

Published 18 May 2010

Online at stacks.iop.org/PMB/55/3317

Abstract

We introduce a novel x-ray imaging approach that yields information about the local texture of structures smaller than the image pixel resolution inside an object. The approach is based on a recently developed x-ray dark-field imaging technique, using scattering from sub-micron structures in the sample. We show that the method can be used to determine the local angle and degree of orientation of bone, and fibers in a leaf. As the method is based on the use of a conventional x-ray tube we believe that it can have a great impact on medical diagnostics and non-destructive testing applications.

 Online supplementary data available from stacks.iop.org/PMB/55/3317/mmedia

1. Introduction

X-ray imaging is a powerful and widespread method that is routinely used for medical diagnostics, non-destructive testing and general research applications. The smallest length scale on which information on the structural variations can be obtained is typically determined by the spatial resolution of the imaging system. For some applications, however, it is desirable to obtain more information in a particular image pixel than just a single value (e.g. density) that characterizes the material. This is resolved, for example, with diffusion tensor imaging (Basser *et al* 1994, Alexander *et al* 2007), a special type of magnetic resonance imaging, where the diffusion tensor can be used to determine the magnitude, the degree of anisotropy and the orientation of directional diffusion in each image pixel. Here we introduce a new x-ray-based approach to obtain directional information on the structural variations in the sample on length scales smaller than the actual image pixel resolution. This new method can be used to map, e.g. local fiber orientation in an object. The approach is based on the general concept of (synchrotron-based) x-ray dark-field imaging (Suzuki and Uchida 1995, Kagoshima *et al* 2001, Olivo *et al* 2002, Pagot *et al* 2003, Levine *et al* 2004, Bech *et al* 2009) and our recently

developed alternative approach using three transmission gratings (Pfeiffer *et al* 2008, 2009, Schwarzschild 2008) in particular. To show the potential for widespread clinical and industrial application, we demonstrate the method using a conventional x-ray tube source.

2. Materials and methods

2.1. Experimental set-up

Figure 1 shows the experimental set-up. The grating interferometer has previously been described in detail (Pfeiffer *et al* 2008, 2009, 2006, Kottler *et al* 2007). It consists of a source grating (G0), a phase grating (G1) and an analyzer absorption grating (G2) (figure 1(a)). The source grating (G0) allows the use of conventional x-ray tube sources with square-millimeter-sized focal spots. The image contrast is formed through the combined effect of the phase grating and the absorption grating. The second grating (G1) acts as a periodic phase mask, and through the Talbot effect this periodic phase modulation is transformed into a periodic intensity modulation at the position of the third grating (G2). The intensity modulation is imaged using the analyzer grating. When the analyzer grating is scanned along the direction perpendicular to the beam and the grating lines, the intensity signal $I(j, k)$ for each pixel with coordinates (j, k) will oscillate as a function of grating position x_g (figure 1(c)). Previous work has demonstrated how the intensity can be described through a Fourier expansion (Pfeiffer *et al* 2008):

$$\begin{aligned} I(j, k, \omega, x_g) &= \sum_{n=0}^{\infty} a_n(j, k, \omega) \cos \left[\frac{2\pi n}{g_2} x_g - \phi_n(j, k, \omega) \right] \\ &\approx a_0(j, k, \omega) + a_1(j, k, \omega) \cos \left[\frac{2\pi n}{g_2} x_g - \phi_1(j, k, \omega) \right], \end{aligned} \quad (1)$$

where a_n are the amplitude coefficients, ϕ_n are the corresponding phase coefficients, g_2 is the period of G2 and ω is the rotation angle of the sample around the optical axis. Scattering in the sample will degrade the oscillation amplitude at the position of the second grating (figure 1(b)). Defining the visibility $V^s(j, k, \omega) \equiv a_1^s(j, k, \omega)/a_0^s(j, k, \omega)$, the dark-field scatter signal can then be quantified through the normalized visibility (Pfeiffer *et al* 2008):

$$V(j, k, \omega) \equiv V^s(j, k, \omega)/V^r(j, k). \quad (2)$$

The superscripts s and r denote the values measured with the specimen in place (s) and as a reference without (r). As previously demonstrated (Bech *et al* 2009, Pfeiffer *et al* 2008, 2009), the quantity $V(j, k, \omega)$ is an inverse measure for the effective integrated local small- (and ultrasmall-) angle scattering power of the sample. For homogeneous specimens and for samples with negligible small-angle x-ray scattering contribution, the value for the visibility remains unchanged and $V(j, k, \omega) = 1$. For specimens that show strong internal density fluctuations on the sub-micron length scale, the visibility is significantly reduced yielding the values of $V < 1$.

The new aspect and principal idea of the work presented here is to demonstrate how the grating geometry in dark-field imaging can be used to extract orientational information of structural details in the sub-micron regime beyond the spatial resolution of the detection system. In grating-based dark-field imaging the contrast arises due to the scattering of x-rays in a direction perpendicular to the grating lines. X-rays scattered in a direction parallel to the grating lines only lead to a blur in the image, but not to any dark-field image contrast. This intrinsic physical property of the set-up can be utilized to extract orientational information about the angular variation of the local scattering power of the sample. This can be achieved

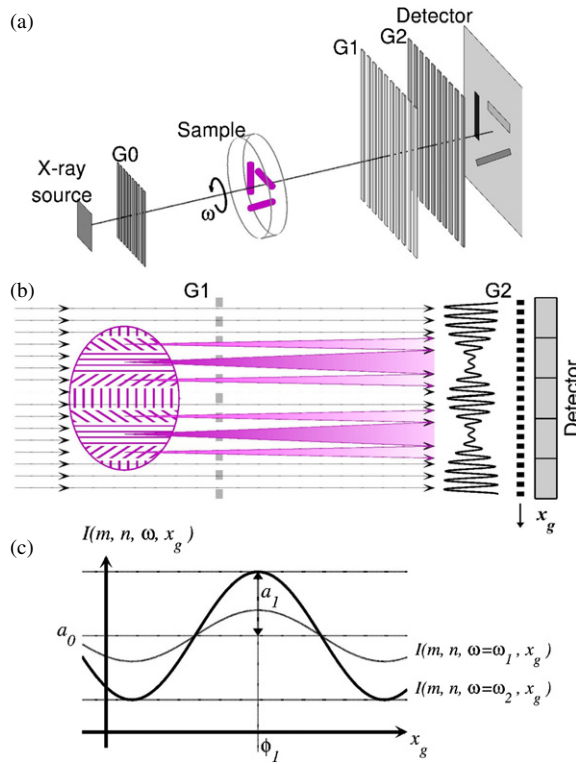


Figure 1. X-ray grating interferometer. (a) Set-up with a source grating G0, a phase grating G1 and an analyzer absorption grating G2. The sample is rotated around the optical axis. (b) Through the Talbot effect a periodic fringe pattern is created behind G1 in the plane of G2. The contrast of the fringe pattern is an inverse measure of the scattering in the sample and is used to extract the dark-field image contrast. (c) For each angular position, the grating G2 is scanned along x_g , yielding an intensity modulation $I(j, k, \omega, x_g)$ for each pixel (j, k) on the two-dimensional image detector.

by rotating the sample around the optical axis of the set-up, collecting a set of several dark-field images, each measuring the perpendicular component of the scattering for that particular orientation.

In analogy to the treatment above, this set of images can be analyzed to yield the average scattering power, the degree of asymmetry and the preferred direction of the underlying structure. Due to the oscillatory behavior, the visibility variations are well described by the first two orders of the Fourier expansion:

$$\begin{aligned} V(j, k, \omega) &= \sum_{n=0}^{\infty} b_n(j, k) \cos[2n(\omega - \psi_n(j, k)) + \pi] \\ &\approx b_0(j, k) + b_1(j, k) \cos[2(\omega - \psi_1(j, k)) + \pi]. \end{aligned} \quad (3)$$

Whereas in equation (1), a_0 , ϕ_1 and a_1 represent the absorption, phase-contrast and dark-field images, respectively, the corresponding coefficients in equation (3) can be interpreted as follows: b_0 describes the local average scattering power of the sample (the average here refers to the average with respect to the angle), b_1 holds information on the asymmetry of the scattering and ψ_1 is the preferred scattering direction. Note that the preferred scattering

direction is the direction with the lowest visibility. For randomly disordered samples that scatter isotropically, there is no variation in $V(j, k, \omega)$ for a given pixel (j, k) , and hence $b_1(j, k) = 0$. In the opposite case, a locally strongly oriented system scattering in only one direction would result in the values of b_1 close to b_0 . The degree of orientation is hence defined as the ratio b_1/b_0 . This ratio describes how strong the orientation of the local structure causing the scattering is.

2.2. Experimental details

The directional dark-field experiments were carried out at the Paul Scherrer Institut using a Seifert ID 3000 x-ray generator. We used a tungsten (W) line focus tube (DX-W8 \times 0.4 L) with a focus size of 8 (horizontal) \times 0.4 (vertical) mm², operated at 1 kW (40 kV/25 mA). The inclination of the target with respect to the optical axis was 6°, causing an effective source size of 0.8 (h) \times 0.4 (v) mm².

The gratings were fabricated by a process involving photolithography, deep etching into silicon and electroplating of gold (David *et al* 2007). While G0 and G2 were gold gratings, G1 was a silicon grating. The grating periods were $p_0 = 14.1$ μm, $p_1 = 3.5$ μm and $p_2 = 2.0$ μm. The heights of the grating structures were 42 μm (G0), 35 μm (G1) and 26 μm (G2). The height of G1 was optimized for a mean x-ray energy of 28 keV. The distance between G0 and G1 was 1.40 m and the distance between G1 and G2 was 0.20 m, corresponding to the fifth fractional Talbot distance. The images were recorded using a PILATUS 100 K pixel detector (Brönnimann *et al* 2006, Bech *et al* 2008, Kraft *et al* 2009). A single module of 487 \times 195 pixels was used, with a pixel size of 0.172 \times 0.172 mm².

For generating the directional dark-field images, raw images were acquired for 16 grating positions in x_g and 18 angular positions in ω . The acquisition time for each image was 20 s resulting in a total exposure time of 96 min. Note that the total exposure time can be greatly reduced by (i) acquiring only nine projections (three grating steps and three angular positions), (ii) using a rotating anode with a power of tens of kW, instead of the current 1 kW anode, and (iii) using a more efficient detector, increasing the efficiency from present 10%.

To extract the dark-field, phase and absorption contrast signals from the measured intensity modulation $I(j, k, \omega, x_g)$, one-dimensional discrete fast Fourier transforms were computed for each pixel for each rotation angle. The resulting values for the Fourier coefficients were normalized to the corresponding values obtained without the specimen in place. The degree and angle of orientation were then extracted from the visibility for each pixel for each rotation angle $V(j, k, \omega)$ using an additional one-dimensional discrete fast Fourier transforms. On a standard personal computer (1.66 GHz processor, 1 GB memory), the processing time needed for a series of 10^2 images with 10^5 pixels was of the order of tens of seconds.

3. Results

Figure 2 displays the experimental results for a biological test sample: a small strawberry leaf. The conventional transmission image is shown in figure 2(a). The panels in figure 2(b) display dark-field images for three different rotation angles, showing a clear variation with the angle. One example is the petiole of the leaf (red ▲) which shows strong scattering when aligned close to parallel with the grating lines (100°), while when aligned close to perpendicular (20°) only weak scattering is seen. The fibers in the petiole are oriented along the axis, and these fibers scatter primarily perpendicular to their axial direction giving rise to the observed contrast. Figure 2(c) shows the visibility as a function of angle for three different regions in

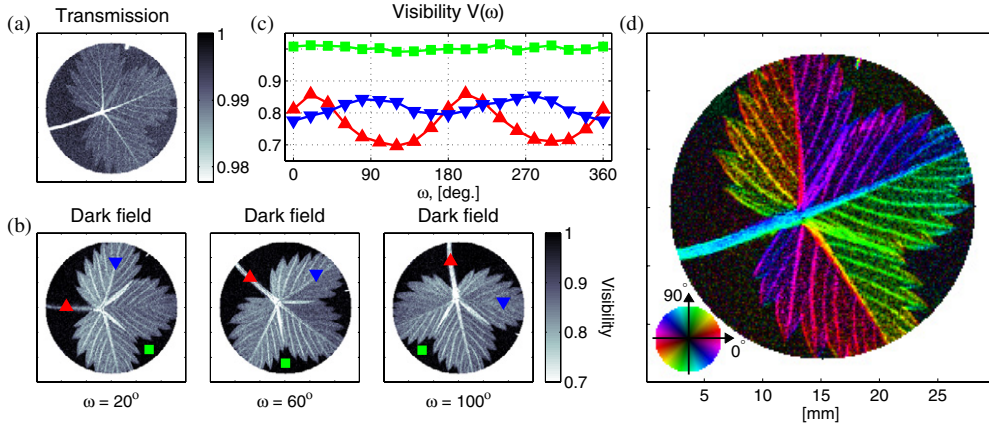


Figure 2. Imaging of a test sample (strawberry leaf). (a) X-ray transmission image. (b) Dark-field images for three different sample orientations ω , showing a clear dependence on the orientation of the sample. (c) Visibility $V(j, k, \omega)$ as a function of ω for three different sample regions. (d) Combined color representation of the degree of orientation (mapped onto the image brightness) and the angle of orientation (mapped onto the image color, using the color wheel displayed in the bottom-left corner) of the underlying texture micro-structure in the sample. It is clearly seen how the fibers in the support structure of the leaf are aligned. Length scale given in (d).

the leaf sample. The preferred angle of orientation is clearly seen to vary between the blue and red curves.

The spatially resolved information on the degree of orientation (b_1/b_0) and the angle of orientation (ψ_1) for each image pixel can conveniently be combined into a single color representation, as displayed in figure 2(d). This is achieved by mapping the degree of orientation (b_1/b_0) onto the brightness of each image pixel, and the angle of orientation (ψ_1) onto its color, according to a certain color map. The resulting image (figure 2(d)) clearly highlights the presence of strongly aligned structural details (fibers) and their respective preferred alignment angle in the supporting branch structures of the leaf. To support the measurements, we have carried out supplementary micro-beam small-angle x-ray scattering (SAXS) experiments at a highly brilliant synchrotron x-ray radiation facility on the corresponding regions in the sample. These results are detailed in the supplementary information available at stacks.iop.org/PMB/55/3317/mmedia (figure S1), and the asymmetries and preferred orientations deduced from the two-dimensional SAXS diffraction patterns agree well with the dark-field imaging results discussed above. It should be emphasized that the main advantages of the presented directional dark-field imaging approach are (a) that this information is obtained with a conventional x-ray tube, which is a prerequisite for widespread practical applications, and (b) that a full two-dimensional image with information on the orientation and degree of structural ordering is acquired for all pixels in the image simultaneously, allowing fast and detailed investigation of large areas.

This new x-ray imaging method has successfully been applied to several specimens of different characters, proving the method to be useful for a broad range of applications. In the following, we report in detail on another result obtained for a biological sample (two additional examples are provided in the supplementary information, available at stacks.iop.org/PMB/55/3317/mmedia figures S2 and S3). The example shown here (in figure 3) concerns the results obtained on a part of a chicken wing.

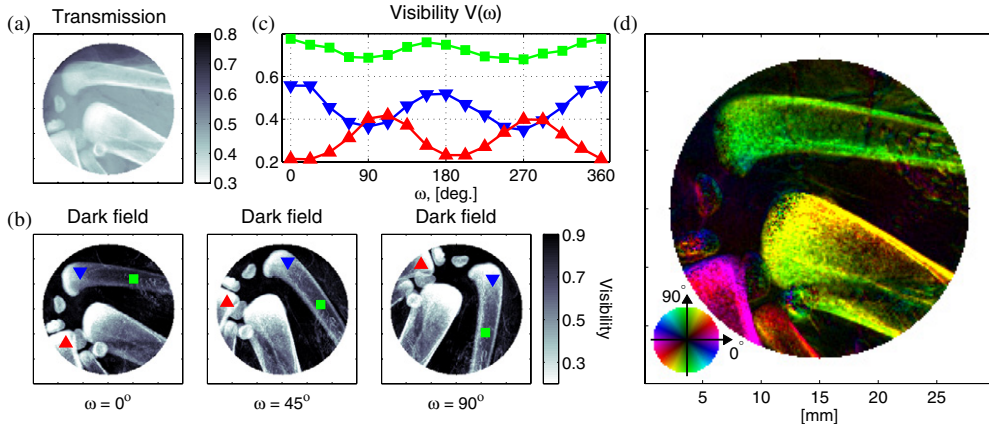


Figure 3. Imaging of a biological specimen (chicken wing). (a) X-ray transmission image. (b) Dark-field images for three different sample orientations ω . (c) Visibility $V(j, k, \omega)$ as a function of ω for three different sample regions. (d) Combined color representation of the degree of orientation (mapped onto the image brightness) and the angle of orientation (mapped onto the image color, using the color wheel displayed in the bottom-left corner) of the underlying texture micro-structure in the sample. In many parts of the sample, we observe a strong dark-field signal that exhibits clear orientational preference in correspondence with the underlying bone ultra-structure. Length scale given in (d).

Figures 3(a) and (b) displays the transmission and the corresponding dark-field images. As previously reported (Pfeiffer *et al* 2008, 2009), the highly porous bone structure causes strong scattering and renders them clearly visible in the dark-field images, with better contrast than in the transmission image. Beyond this we observe a strong angular dependence of the dark-field signal as a function of ω , hinting at strong asymmetries in the alignment of the underlying bone ultra-structure on the sub-micron length scale. The visibility changes in three different points are shown in figure 3(c). It is clearly seen how the degree and angle of orientation varies for different parts of the sample. The natural function of bones is to take up force at the dense bone heads and transmit it through the middle section to the other end. We would thus expect to see strong axial alignment in the middle section of the bone, and stronger scattering with less-defined orientations at the bone ends. In the combined representation (figure 3(d)) the expected features are clearly seen. The angle of orientation in the middle section of the bones is aligned with the bone axes, whereas the orientation becomes less defined in the bone heads, despite of a generally higher scattering signal in these parts.

4. Conclusions

In summary, we have demonstrated a novel x-ray imaging method, which provides information on the local degree of scattering asymmetry and angle of orientation for every pixel in the two-dimensional image. Since this additional information is obtained essentially through small-angle scattering effects, it provides access to the local texture of the specimen on the sub-micron length scale. This is achieved, even though the actual resolution element in the image acquisition can be orders of magnitude larger.

We have experimentally demonstrated the approach using a conventional x-ray tube, and hence envisage widespread applications including in particular medical diagnostics, non-destructive testing and fundamental research. In the context of medical imaging the

approach could yield information on the orientation of collagen in cartilage (Shimao *et al* 2005, 2006), which is of great importance in osteoarthritis research and diagnostics. Detailed structural investigation of the bone-ultrastructure could furthermore benefit research and diagnostics of osteoporosis where the local ordering is important for the strength of the bone. Other applications could include quality control through online screening of fiber-reinforced materials or mapping of fiber orientations in muscles.

We believe that this method can be extended into a non-destructive three-dimensional characterization method that could ultimately yield an orientation tensor describing the degree and direction of ordering of the underlying textured micro-structure in every voxel of a three-dimensional specimen. This, of course, would first require the development of novel tensorial x-ray computer tomography reconstruction algorithms, which presently do not exist.

Acknowledgments

We gratefully acknowledge C Grünzweig for help with the grating fabrication and B Henrich, P Kraft, C Brönnimann and E Eikenberry for providing the detector. FP acknowledges support through the DFG excellence cluster ‘Munich-Centre for Advanced Photonics’.

References

- Alexander A L, Lee J E, Lazar M and Field A S 2007 Diffusion tensor imaging of the brain *Neurotherapeutics* **4** 316–29
 Basser P J, Mattiello J and LeBihan D 1994 MR diffusion tensor spectroscopy and imaging *Biophys. J.* **66** 259–67
 Bech M, Bunk O, David C, Ruth R, Rifkin J, Loewen R, Feidenhans'l R and Pfeiffer F 2009 Hard x-ray phase-contrast imaging with the compact light source based on inverse Compton x-rays *J. Synchrotron Radiat.* **16** 43–7
 Brönnimann Ch *et al* 2006 The PILATUS 1M detector *J. Synchrotron Radiat.* **13** 120–30
 Bech M, Bunk O, David C, Kraft P, Brönnimann Ch, Eikenberry E F and Pfeiffer F 2008 X-ray imaging with the PILATUS 100K detector *Appl. Radiat. Isotopes* **66** 474–8
 David D, Bruder J, Rohbeck T, Grünzweig C, Kottler C, Diaz A, Bunk O and Pfeiffer F 2007 Fabrication of diffraction gratings for hard x-ray phase contrast imaging *Microel. Eng.* **84** 1172–7
 Kagoshima Y *et al* 2001 Scanning hard x-ray microscope with tantalum phase zone plate at the Hyogo-BL (BL24XU) of SPring-8 *Nucl. Instrum. Methods A* **467–468** 872–6
 Kottler C *et al* 2007 Phase contrast x-ray imaging of large samples using an incoherent laboratory source *Phys. Stat. Sol. a* **204** 2728–33
 Kraft P *et al* 2009 Characterization and calibration of PILATUS detectors *IEEE Trans. Nucl. Sci.* **56** 758–64
 Levine L E and Long G G 2004 X-ray imaging with ultra-small-angle x-ray scattering as a contrast mechanism *J. Appl. Cryst.* **37** 757–65
 Olivo A, Arfelli F, Dreossi D, Longo R, Menk R H, Pani S, Poropat P, Rigon L, Zanconati F and Castelli E 2002 Preliminary study on extremely small-angle x-ray scatter imaging with synchrotron radiation *Phys. Med. Biol.* **47** 469–80
 Pagot E, Cloetens P, Fiedler S, Bravin A, Coan P, Baruchel J, Härtwig J and Thominson W 2003 A method to extract quantitative information in analyzer-based x-ray phase contrast imaging *Appl. Phys. Lett.* **82** 3421–3
 Pfeiffer F, Bech M, Bunk O, Kraft P, Eikenberry E F, Brönnimann CH, Grünzweig C and David C 2008 Hard-x-ray dark-field imaging using a grating interferometer *Nat. Mat.* **7** 134–7
 Pfeiffer F, Bech M, Bunk O, Donath T, Henrich B, Kraft P and David C 2009 X-ray dark-field and phase-contrast imaging using a grating interferometer *J. Appl. Phys.* **105** 102006
 Pfeiffer F, Weitkamp T, Bunk O and David C 2006 Phase retrieval and differential phase-contrast imaging with low-brilliance x-ray sources *Nat. Phys.* **2** 258–61
 Suzuki Y and Uchida F 1995 Dark-field imaging in hard x-ray scanning microscopy *Rev. Sci. Instrum.* **66** 1468–70
 Schwarzschild B 2008 Dark-field imaging is demonstrated with a conventional hard-x-ray source *Phys. Today* **3** 12
 Shimao D, Sugiyama H, Hyodo K, Kunisada T and Ando M 2005 Evaluation of x-ray dark-field imaging in visualization of nearly clinical articular cartilage *Nucl. Instrum. Methods A* **548** 129–34
 Shimao D, Sugiyama H, Kunisada T and Ando M 2006 Articular cartilage depicted at optimized angular position of Laue angular analyzer by x-ray dark-field imaging *Appl. Radiat. Iso.* **64** 868–74

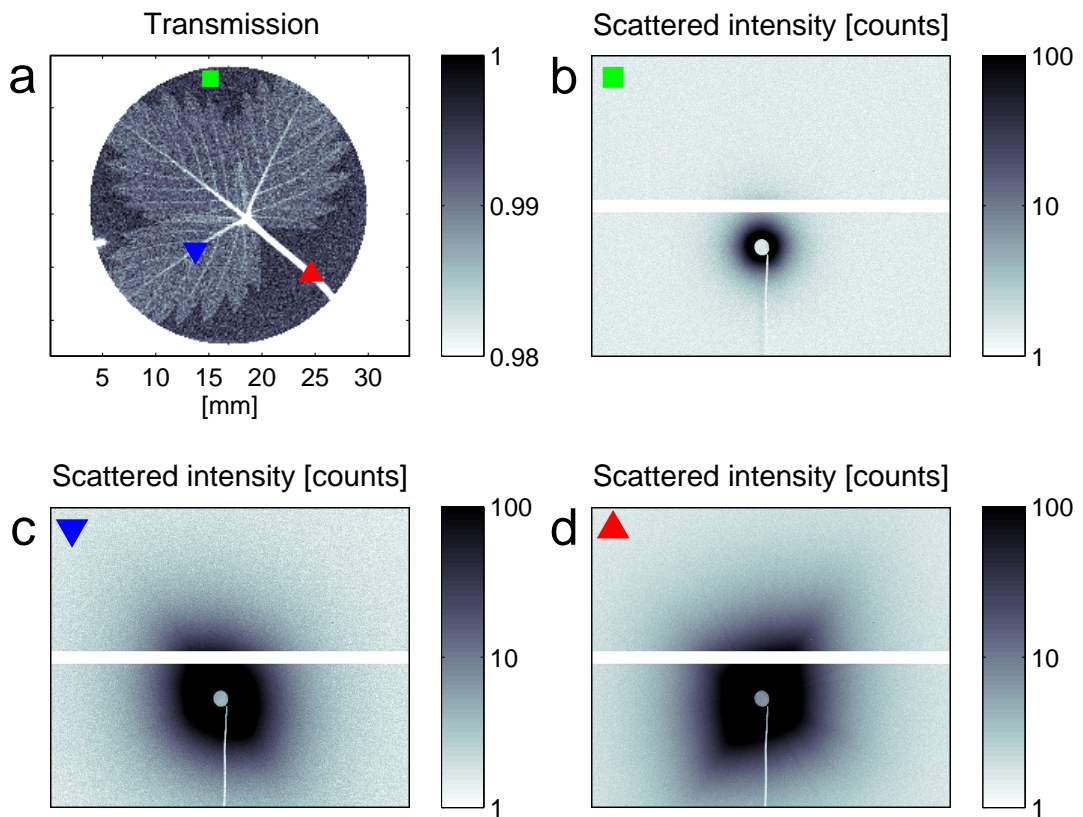


Figure S1. Complementary micro-beam small-angle x-ray scattering results on the leaf sample. The leaf in this figure is the same that was also used to obtain the results presented in Figure 2. (a) Conventional transmission image of the leaf (from the results presented in Fig. 2). (b-d) Small-angle scattering patterns recorded for three different regions in the samples (marked by the corresponding symbols). The images are displayed using a logarithmic gray scale and cover the scattering vector q -range $[9.5 \times 10^{-3} - 0.37] \text{ nm}^{-1}$. The white line is from a gap between the detector modules. Strong and asymmetric scattering patterns with distinct, but different preferred scattering directions are clearly observed. The asymmetries observed in these diffraction patterns confirm our interpretation of the results obtained with the new directional dark-field imaging method presented in the main article. This demonstrates that directional dark-field imaging can indeed reveal the strength and directional preference in the local scattering amplitude, and thus yield information on the local micro-texture of the specimen.

II. Application example, wood

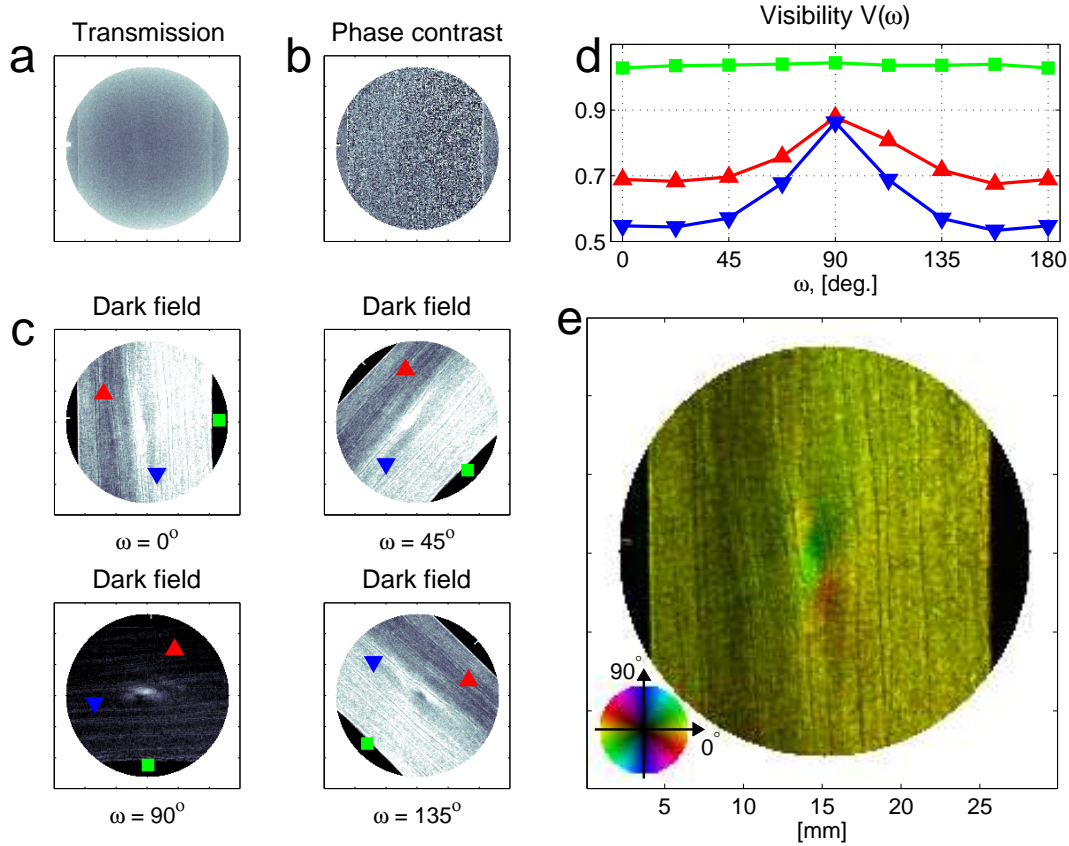


Figure S2. Imaging of a material science specimen (balsa wood). (a) Conventional x-ray transmission image. (b) Phase-contrast image. (c) Dark-field images for four different sample orientations ω . We clearly observe the angular dependence of the dark-field image, and that the scattering is strongest in the direction perpendicular to the wood fibers. (d) Visibility $V(j, k, \omega)$ as a function of ω for three different sample regions, extracted from a series of phase-stepping scans recorded for several ω positions. (e) Combined color representation of the degree of orientation (mapped onto the image brightness) and the angle of orientation (mapped onto the image color, using the color wheel displayed in the bottom left corner) of the underlying texture micro-structure in the sample. The wood fibers are all oriented in the same direction, except around the knot in the middle of the wood. The sample thickness was 1 mm. Length scale given in (e).

III. Application example, mushroom

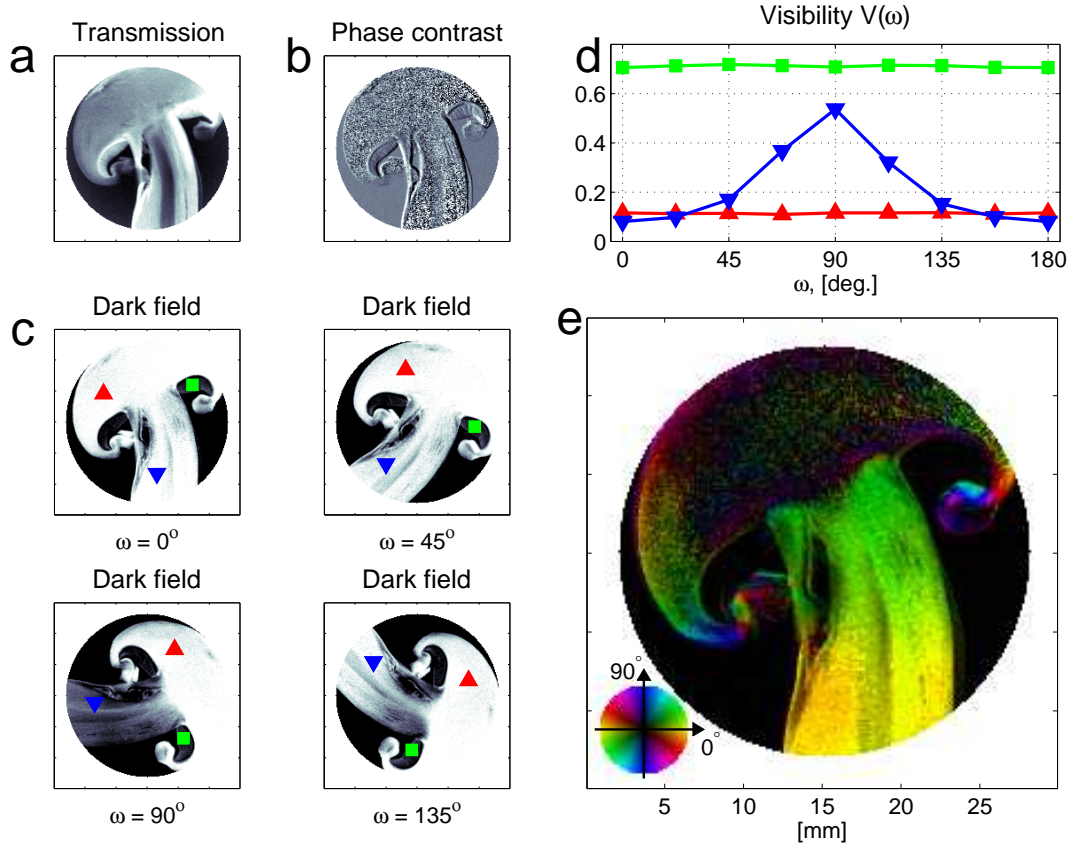


Figure S3. Imaging of a mushroom slice. (a) Conventional x-ray transmission image. (b) Phase-contrast image. (c) Dark-field images for four different sample orientations ω . (d) Visibility $V(j, k, \omega)$ as a function of ω for three different sample regions, extracted from a series of phase-stepping scans recorded for several ω positions. (e) Combined color representation of the degree of orientation (mapped onto the image brightness) and the angle of orientation (mapped onto the image color, using the color wheel displayed in the bottom left corner) of the underlying texture micro-structure in the sample. The fibers in the stipe are aligned in the growth direction, while the micro-structures of the pileus scatters so strongly that the dark-field signal saturates. The sample thickness was 1 mm. Length scale given in (e).

Publication IV

Submitted to Physical Review B

T.H. Jensen, M. Bech, I. Zanette, T. Weitkamp, C. David, H. Deyhle, S. Rutishauser, E. Reznikova, J. Mohr, R. Feidenhans'l and F. Pfeiffer

Directional x-ray dark-field imaging of strongly ordered systems

Submitted to Physical Review B

Directional x-ray dark-field imaging of strongly ordered systems

Torben Haugaard Jensen,¹ Martin Bech,² Irene Zanette,³ Timm Weitkamp,³ Christian David,⁴ Hans Deyhle,^{5,6} Simon Rutishauser,⁴ Elena Reznikova,⁷ Jürgen Mohr,⁷ Robert Feidenhans'l,¹ and Franz Pfeiffer²

¹*Niels Bohr Institute, University of Copenhagen, 2100 Copenhagen, Denmark*

²*Department of Physics, Technical University of Munich, 85747 Garching, Germany*

³*European Synchrotron Radiation Facility, 38043 Grenoble, France*

⁴*Paul Scherrer Institut, 5232 Villigen PSI, Switzerland*

⁵*Biomaterials Science Center, University of Basel, 4031 Basel, Switzerland*

⁶*Institute for Materials Science, School of Dental Medicine, University of Basel, 4031 Basel, Switzerland*
⁷*Karlsruhe Institute of Technology, Institute for Microstructure Technology, 76021 Karlsruhe, Germany*

(Dated: October 13, 2010)

Recently a novel grating based x-ray imaging approach called directional x-ray dark-field imaging was introduced. Directional x-ray dark-field imaging yields information about the local texture of structures smaller than the pixel size of the imaging system. In this work we extend the theoretical description and data processing schemes for directional dark-field imaging to strongly scattering systems, which could not be described previously. We develop a simple scattering model to account for these new observations and subsequently demonstrate the model using experimental data. The experimental data includes directional dark-field images of polypropylene fibers and a human tooth slice.

PACS numbers: 07.85.-m, 62.20.-x, 78.70.Ck, 87.59.-e

I. INTRODUCTION

Grating-based x-ray imaging has recently been used to demonstrate a variety of different contrast mechanisms^{1–17}. These include phase contrast imaging^{1–8}, dark-field imaging^{4,7,9–16}, and lately also directional dark-field imaging (DDFI)¹⁷. The latter provides information on structures in the sample on length scales smaller than the actual image resolution. The method can be used to map, e.g., local fibre orientations and has been demonstrated in a set-up using a conventional x-ray tube. DDFI analyzes the angular variation of the scattering signal. In the first presentation of the method by Jensen *et al.*¹⁷ the visibility variations were described by a Fourier series expansion up to the first order, i.e., by a sinusoidal behavior.

$$V(j, k, \omega) \approx b_0(j, k) + \dots \\ b_1(j, k) \cos(2[\omega - \psi_1(j, k)] + \pi). \quad (1)$$

In this paper we will extend our previously introduced theoretical basis and data interpretation schemes for DDFI to strongly ordered systems. This becomes necessary as strongly ordered systems produce highly eccentric scattering patterns, which can no longer be sufficiently described by the previously introduced sinusoidal data interpretation for DDFI.

II. EXPERIMENTAL SET-UP

The experimental set-up is shown in Fig. 1. The grating interferometer has previously been described in detail^{3,5,6,9,10,17}. It consists of a phase grating (G1), and an analyzer absorption grating (G2). The first grating,

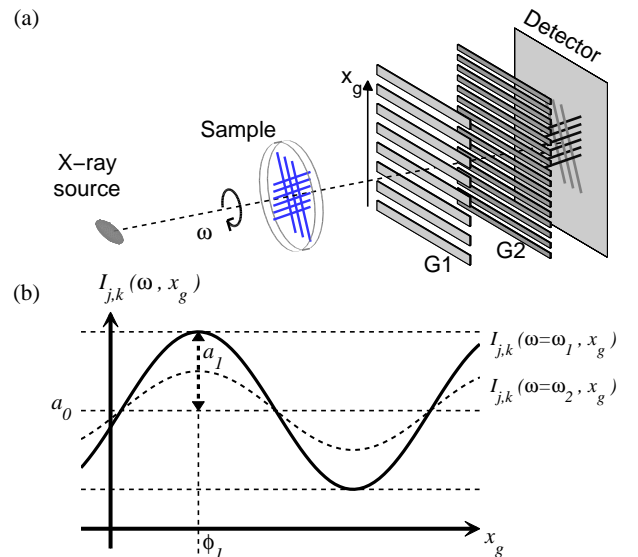


FIG. 1: X-ray grating interferometer. (a) Set-up with a phase grating G1 and an analyzer absorption grating G2. The sample is rotated around the optical axis. (b) For each angular position, the grating G1 is scanned along x_g , yielding an intensity modulation $I_{j,k}(\omega, x_g)$ for each pixel (j, k) on the two-dimensional image detector.

(G1) generates a periodic intensity modulation at the position of the second grating (G2). The second grating is used to analyze the position and amplitude of the intensity modulation. When the phase grating is scanned in the direction perpendicular to the optical axis and the grating lines, the intensity signal $I(j, k)$ for each pixel with coordinates (j, k) will oscillate as a function of grating position x_g (Fig. 1b). Previous work has demon-

strated how the intensity can be well described by a first order Fourier expansion^{4,9}:

$$\begin{aligned} I(j, k, \omega, x_g) &\approx a_0(j, k, \omega) + \dots \\ a_1(j, k, \omega) \cos\left(\frac{2\pi}{g_2}x_g - \phi_1(j, k, \omega)\right) \end{aligned} \quad (2)$$

where g_2 is the period of G2, and ω the rotation angle of the sample around the optical axis.

Scattering in the sample will reduce the oscillation amplitude. The dark-field scatter signal is called the visibility and describes the reduction in oscillation amplitude. The visibility is defined as:

$$V(j, k, \omega) \equiv \frac{a_1^s(j, k, \omega)/a_0^s(j, k, \omega)}{a_1^r(j, k, \omega)/a_0^r(j, k, \omega)}. \quad (3)$$

The superscripts s and r denote the values measured with the specimen in place (s) and as a reference without (r). The visibility, $V(j, k, \omega)$ is an inverse measure of the effective integrated local small- (and ultrasmall-) angle scattering power of the sample^{7,9,10,17}. It will have a value close to 1 for samples with negligible scattering. For strongly scattering samples the visibility will be reduced yielding values of $V < 1$.

As described by Jensen *et al.*¹⁷ the dark-field contrast arises due to the component of the scattering that happens perpendicular to the grating lines. The scattering component parallel to the grating lines will produce only negligible dark-field contrast. In the following we will develop a model to describe how the dark-field signal varies as a function of angle.

III. THE MODEL

We will begin by assuming that the scattering from a single point on the sample will result in a 2D gaussian scattering intensity profile, S_2 at the plane of G2. This assumption of a Gaussian scattering distribution corresponds well to assumptions made when using the dark-field signal for tomography¹³⁻¹⁵. Let the scattering profile S_2 be defined as follows.

$$\begin{aligned} S_2(x, y) &= \frac{1}{2\pi\sigma_1\sigma_2} \exp(-(ax^2 + 2bxy + cy^2)), \\ a &:= \frac{\cos(\psi_1)^2}{2\sigma_1^2} + \frac{\sin(\psi_1)^2}{2\sigma_2^2}, \\ b &:= \sin(\psi_1)\cos(\psi_1)\left(-\frac{1}{2\sigma_1^2} + \frac{1}{2\sigma_2^2}\right), \\ c &:= \frac{\sin(\psi_1)^2}{2\sigma_1^2} + \frac{\cos(\psi_1)^2}{2\sigma_2^2}. \end{aligned}$$

S_2 is a 2D gaussian distribution with the width σ_1 and σ_2 in the two axial directions, and the first axis rotated by the angle ψ_1 . An example of how $S_2(x, y)$ could look like for a given σ_1 , σ_2 and ψ_1 is shown in Fig. 2. Since the gratings are only sensitive to scattering perpendicular to

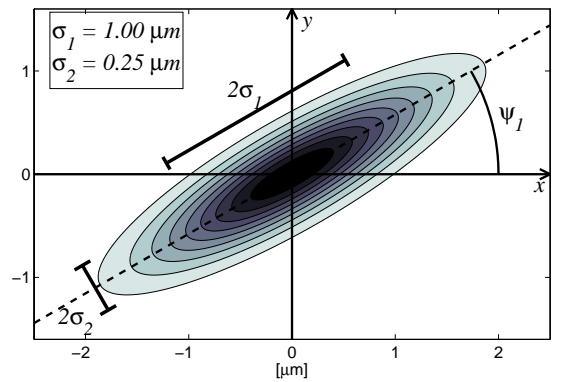


FIG. 2: Illustration of 2D gaussian scattering function, $S_2(x, y)$, with $\psi_1 = 30^\circ$.

the grating lines, the dark-field signal will be measuring the projection of S_2 onto the x -axis. This corresponds to integrating S_2 along y :

$$S(x) = \frac{1}{\sqrt{2\pi\sigma^2}} \exp\left(\frac{-x^2}{2\sigma^2}\right), \quad (4)$$

$$\sigma^2 = \frac{1}{2} (\sigma_1^2 + \sigma_2^2) + \frac{1}{2} (\sigma_1^2 - \sigma_2^2) \cos(2\psi_1 - \pi). \quad (5)$$

The projection of S_2 is thus another gaussian, S , with the width σ . As mentioned above, the variations in intensity in a pixel can be described as follows: $I^r(x) = a_0 + a_1 \cos\left(\frac{2\pi}{g_2}x - \phi_1\right)$. Since the scattering from a single point is described by $S(x)$ at the position of the second grating, the perturbed intensity variation can be found as the convolution of the original intensity function, $I^r(x)$ and the scattering function, $S(x)$.

$$\begin{aligned} I^s(x) &= I^r(x) \otimes S(x), \\ &= a_0 + a_1 \exp\left(\frac{-2\pi^2\sigma^2}{g_2^2}\right) \cos\left(\frac{2\pi}{g_2}x - \phi_1\right). \end{aligned} \quad (6)$$

Recalling the definition of the visibility from eq. (3) and combining with eq. (6) we see that the visibility varies as:

$$\begin{aligned} V(\psi_1) &= \exp\left(\frac{-\pi^2}{g_2^2}(\sigma_1^2 + \sigma_2^2)\right) \dots \\ &\cdot \exp\left(\frac{-\pi^2}{g_2^2}(\sigma_1^2 - \sigma_2^2) \cos(2\psi_1 - \pi)\right). \end{aligned} \quad (7)$$

If we include the rotation of the sample, ω , during measurement we can rewrite eq. (7):

$$\begin{aligned} V(\omega) &= \exp\left(\frac{-\pi^2}{g_2^2}(\sigma_1^2 + \sigma_2^2)\right) \dots \\ &\cdot \exp\left(\frac{-\pi^2}{g_2^2}(\sigma_1^2 - \sigma_2^2) \cos(2[\omega - \psi_1] - \pi)\right) \end{aligned} \quad (8)$$

Equation (8) is a full description of how the visibility changes as a function of $(\sigma_1, \sigma_2, \psi_1, \omega)$.

We will now take a look at two special cases.

A. Weakly oriented scatterers

In the previous study¹⁷, it was assumed that the visibility variations were sinusoidal. From the model developed above (equation(8)) we know this is not generally the case. Let $K_1 \equiv \frac{\pi^2 |\sigma_1^2 - \sigma_2^2|}{g_2^2}$. The parameter K_1 describes how eccentric the scattering profile is relative to the grating period. We note that in the special case where $K_1 \sim 0$, we can Taylor expand the second exponential of eq. (8):

$$V(\omega) \approx \exp\left(\frac{-\pi^2}{g_2^2} (\sigma_1^2 + \sigma_2^2)\right) \dots \\ \cdot \left(1 - \frac{\pi^2}{g_2^2} (\sigma_1^2 - \sigma_2^2) \cos(2[\omega - \psi_1] - \pi)\right). \quad (9)$$

We note that in eq. (9) the visibility varies sinusoidally. From this we can conclude that if $K_1 \sim 0$, that is if the scattering profile has widths that are small compared to the period of the second grating, g_2 , or if the difference between the widths of the scattering profile are small compared to the period of the second grating, g_2 , then the visibility varies sinusoidal. So weakly scattering samples and samples that are not strongly oriented will produce sinusoidal visibility variations. The new model presented here is thus consistent with the previously published methodology for samples with $K_1 \sim 0$. For samples with highly eccentric scattering profiles, the parameter K_1 will be much greater than 0, and the visibility variations will no longer be sinusoidal.

B. Unscattered photons

In the model described above (equations (8) and (9)) we have assumed that the entire beam is scattered and no part of it pass the sample without being scattered. Only the part of the beam that is scattered can contribute to the reduction in visibility, so if a part of the beam passes through the sample without being scattered then the visibility can not be reduced to zero no matter the width of the scattering profile of the scattered part of the beam. If e.g. 40% of the beam is not scattered then the visibility will take values greater than 0.4. Such transmission can be included in the model using a constant taking the not scattered part of the beam into account. Let α be the proportion of the beam that has been scattered. Then eq. (6) is replaced by:

$$I^s(x) = I^r(x) \otimes ((1 - \alpha)\delta(x) + \alpha S(x)), \\ = a_0 + \left((1 - \alpha) + \alpha \exp\left(\frac{-2\pi^2\sigma^2}{g_2^2}\right)\right) \dots \\ \cdot a_1 \cos\left(\frac{2\pi}{g_2}x - \phi_1\right), \quad (10)$$

and the visibility takes the form:

$$V(\omega) = (1 - \alpha) + \alpha \exp\left[\frac{-2\pi^2\sigma^2}{g_2^2}\right], \quad (11)$$

$$\sigma^2 = \frac{1}{2} (\sigma_1^2 + \sigma_2^2) + \dots \\ \frac{1}{2} (\sigma_1^2 - \sigma_2^2) \cos(2[\omega - \psi_1] - \pi). \quad (12)$$

The sinusoidal behavior for $K_1 \sim 0$ is still valid when we use equations (11-12) to describe the visibility. With the visibility varying sinusoidally the variations can be described by the mean and oscillation amplitude, and it is thus not possible to determine three independent parameters, hence $(\sigma_1, \sigma_2, \alpha)$ can no longer be uniquely determined. This does introduce an ambiguity in our model, which does not limit the ability to describe and predict visibility variations, but can limit the ability to quantify the measured scattering profiles.

In the following we will present experimental data with $K_1 > 1$ where the visibility does not vary sinusoidally. The two examples described will be cases with $\alpha = 1$ and $\alpha < 1$ respectively. The experimental data will be well described by the model presented above.

IV. RESULTS

A. Experimental details

The directional dark-field experiments were conducted at beamline ID19 of the European Synchrotron Radiation Facility (ESRF, Grenoble) using monochromatic x-rays at an energy of 17.6 keV.

The grating interferometer was placed 150 meters from the wiggler source. The silicon phase grating was fabricated by a process involving photolithography and anisotropic wet etching into silicon¹⁸. The absorption gold grating was fabricated by a process involving deep x-ray lithography and gold electroplating¹⁹. The gratings periods were $g_1 = 4.79 \mu\text{m}$ and $g_2 = 2.40 \mu\text{m}$. The heights of the grating structures were $23 \mu\text{m}$ (G1) and $50 \mu\text{m}$ (G2). The height of G1 was optimized for π -phaseshift at an x-ray energy of 17.6 keV. The distance between G1 and G2 was 447 mm, corresponding to the eleventh fractional Talbot distance⁸. The gratings were mounted with the grating lines horizontally to use the greater coherence in the vertical direction. The images were recorded using a FReLoN 2000 CCD with 2048×2048 pixels with an effective pixel size of $7.46 \times 7.46 \mu\text{m}^2$.

Each dark-field image was generated using raw images recorded for 16 different grating position in x_g over two periods. The dark-field signal was extracted from the intensity modulation $I(j, k, \omega, x_g)$ for each rotation angle using one-dimensional fast Fourier transforms.

B. Fibers

We use a mesh of polypropylene fibers (PP) to illustrate the model in a case where $\alpha = 1$. The experiments were made with 90 angular rotation steps over 180 degrees. The exposure time for each image was 1.5 seconds, resulting in a total exposure time of 36 minutes. In Fig. 3.a and 3.b we see the average visibility of the fiber mesh. In Fig. 3 we identified sets of ten distinct points with no fibers, single fibers and coaxially overlapping pairs of fibers respectively. In Fig. 3.b, a magnified section of Fig. 3.a, examples of spots with 0, 1, 2 and several fibers are marked. In the images we clearly see that point (b) is placed in the middle of one fiber and point (c) is placed where two fibers overlap. The fiber diameters are 32 μm , and the pixel size is 7.46 μm . It is thus possible to effectively probe only x-rays that have passed through the middle of one or two fibers.

The visibility variation of the four points marked in Fig. 3.b are plotted in Fig. 3.c. Upon inspection we see great variation in the visibility curves for the four different spots. We also note that some of these visibility variations are clearly not sinusoidal. The visibility variations for the four shown points as well as the 30 other identified points have been thoroughly analyzed using the model we developed above (eq. (8)). For all the points the visibility variations were fitted using the parameters σ_1, σ_2 and ψ_1 . We see no effects from the not scattered part of the beam (except in points with no fibers). The parameter α is thus set to $\alpha = 1$ for all fits. In Fig. 3.c the fits are plotted for the four curves with black dashed lines. We see that the model described above can be used to accurately fit the experimentally recorded visibility variations²¹. The fitted parameters for all points are printed in Table I. Along with the fitted parameters σ_1, σ_2 and ψ_1 , the derived parameter K_1 and the standard x-ray absorption for all points are also printed in the table. The 30 points were analyzed to give an estimate of the uncertainty in the measurements. The noted uncertainty for the associated fitted parameters are the standard deviations over ten points. Upon analysis of the fitted parameters we see that the width of two fibers (as in point (c)) is double that of the width of one fiber (as in point (b)). Once the magnitude of the widths of the scattering profiles have been calibrated we see that with excellent signal to noise ratio we can distinguish one and two fibers. Note this is not possible with the absorption information in this case, where the signal to noise ratio is too low to infer usable information. The noise is also the origin of the negative absorption in the point without a fiber. In point (d) multiple fibers are overlapping. We see that there is a negligible increase in σ_2 for that point. So we can conclude that all of the fibers overlap coaxially and thus produce no scattering in the direction perpendicular to their axes.

In the presentation of the model above, we developed a criteria ($K_1 \sim 0$) for when our model predicted the previously described sinusoidal behavior. The parameter K_1 is

tabulated in Table I. In Fig. 3 we note that for one fiber the visibility variation is sinusoidal as reported in Jensen *et al.*¹⁷ while for two and more fibers the visibility clearly does not vary sinusoidally. For the points with one fiber we note that $K_1 = 0.3 \sim 0$ which was the criteria for sinusoidal behavior. For two and multiple fibers we have that $K_1 > 1$ as expected for nonsinusoidal behavior. The observations in Fig 3.c thus corresponds well with our discriminatory parameter, K_1 . We can conclude that not all of the experimental data presented here could satisfactorily have been described by simple sinusoidal behavior. Our new model however provides an accurate description of the variations.

The results clearly demonstrate that for strongly oriented samples the sinusoidal approach is no longer suitable for describing the visibility variations. These fibers were in a simple mesh. Since we use x-rays for this investigation, the method would have worked equally well if the fibers had been embedded. The method could thus be used for quality control for fiber reinforced materials.

Besides using the model for determining the location, orientation and number of overlapping fibers in each point, the model presented here could be used to design optimal grating parameters if interested in a specific problem. If the Talbot distance is doubled, the width of the gaussian scattering function on the detector will double. The effect of a change in Talbot distance can thus be predicted using the model. A second important factor is the energy. A change in energy will both influence the width of the scattering function on the detector and also reduce the scattering cross section. The changes in energy and Talbot distance could be tailored to provide a suitable use of the dynamic range of the visibility for a given task.

C. Tooth

We use a second sample to illustrate the extended version of the model with $\alpha < 1$. The sample is a vertical slice of a human tooth²². The experiments were made with 128 angular rotation steps over 360 degrees. The exposure time for each image was 1.5 seconds, resulting in a total exposure time of 51 minutes. The results are shown in Fig. 4. In Fig. 4.a the x-ray transmission is shown outlining the enamel, dentin and pulp cavity of the tooth. Dark-field images of the visibility for three different orientations are shown in Fig. 4.b, whiter represents stronger scattering. Note that the dentin has the strongest dark-field signal. In the dentin narrow dark bands displays small areas of low scattering for the different orientations (most clearly visible near the red circle for $\omega = 0^\circ$). In Fig. 4.c the visibilities for the three points marked in Fig. 4.b are plotted. Narrow peaks of high visibility show that the scattering is strongly oriented. The peaks are located at different angles, corresponding to different orientation of the scattering structures in the dentin in each of the three points. The fits made using the extended model (equations (11)-(12)) are plotted as

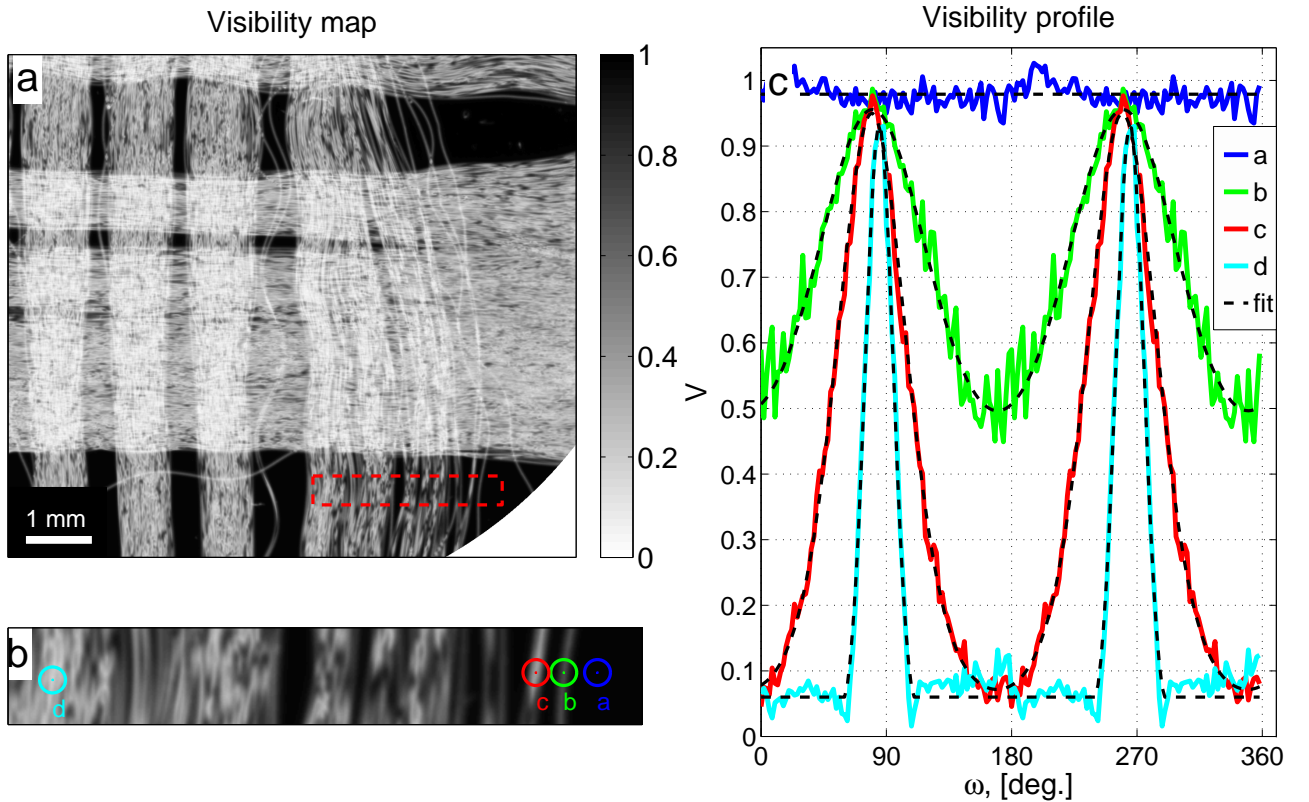


FIG. 3: (a) Average visibility of a polypropylene (PP) fiber mesh. (b) Enlargement of part of (a), height 0.5 mm. (c) Visibility variation as a function of rotation angle for four different points marked in (b). Note the nonsinusoidal behavior of the read and cyan lines. The dashed black lines are model fits to the measured values.

Name	# Fibers	Fitted parameters			Meas. Param.	Deriv. Param.
		σ_1	σ_2	ψ_1	absorption	K_1
	10 x 0	$0.06 \pm 0.004 \mu\text{m}$	$0.06 \pm 0.004 \mu\text{m}$	0	$0.6 \pm 0.4\%$	0
	10 x 1	$0.46 \pm 0.02 \mu\text{m}$	$0.11 \pm 0.01 \mu\text{m}$	-	$1.5 \pm 0.5\%$	0.3
	10 x 2	$0.87 \pm 0.04 \mu\text{m}$	$0.13 \pm 0.03 \mu\text{m}$	-	$2.3 \pm 0.8\%$	1.3
(a)	0	$0.08 \mu\text{m}$	$0.08 \mu\text{m}$	0.0°	-0.2%	0
(b)	1	$0.45 \mu\text{m}$	$0.12 \mu\text{m}$	169.9°	1.2%	0.3
(c)	2	$0.88 \mu\text{m}$	$0.12 \mu\text{m}$	169.5°	2.8%	1.3
(d)	multiple	$2.19 \mu\text{m}$	$0.14 \mu\text{m}$	174.9°	5.5%	8.2

TABLE I: Fitted parameters for points with 0, 1, 2 and several overlapping fibers. The fits were made using eq. (8). Included are also the derived parameter K_1 as well as the measured absorption.

dashed black lines. We see that the baselines vary and are greater than 0. The narrow peaks and the nonzero baseline shows that a part of the beam has not been scattered. This partially scattered beam indicates that $\alpha < 1$ and the extended model is needed to describe the observed visibility changes. The variation in baseline shows that a different proportion of the beam is unscattered through different parts of the tooth.

Some of the visibility curves show more than two peaks. The multiple peaks could be caused by the overlapping of different structures due to the thickness of the sample (500 μm). In our analysis we have focused on the most

pronounced peaks for each point.

We believe that the dentin tubuli are the origin of the scattering signal. The sample was dry when measured, and the empty tubuli hence will produce a very strong small angle scattering signal. It is also possible to use the widths of the fitted gaussian scattering profile to estimate the q-space scattering vector they correspond to. For the dentin the gaussian has a fitted major (minor) axis on G2 of ~ 11 (~ 0.5) μm (data not shown). One can use this and the G1-G2 distance to calculate the corresponding reciprocal scattering vector. The reciprocal scattering vectors corresponds to a real space distance of

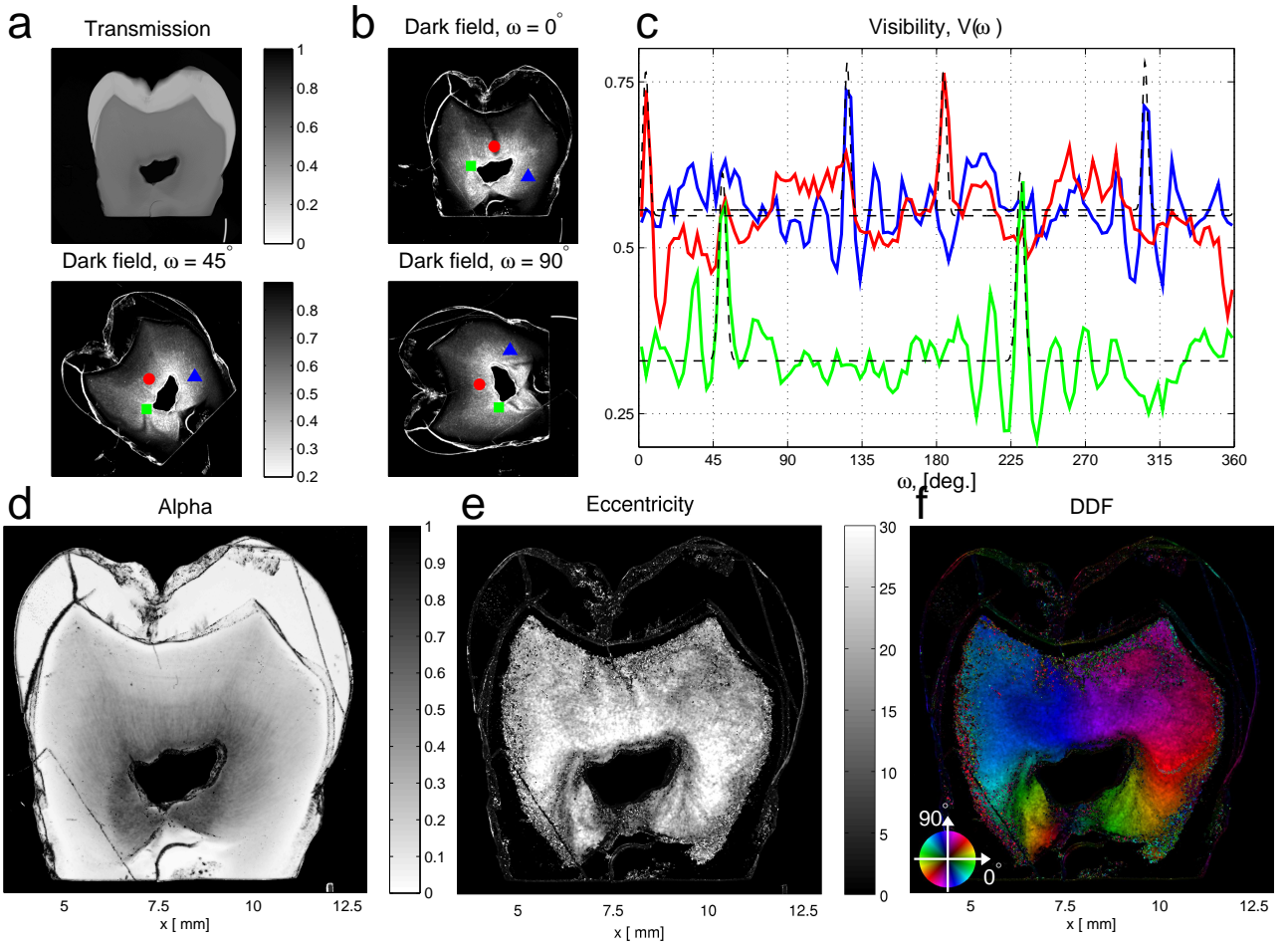


FIG. 4: Imaging of a tooth slice. (a) X-ray transmission image. (b) Dark-field images for three different sample orientations ω . (c) Visibility $V(j, k, \omega)$ as a function of ω for three different sample regions. The dashed black lines are model fits to the measured values. (d) The parameter α describing the proportion of beam that has been scattered. (e) Map of the eccentricity of the fitted local scattering profile. (f) Combined color representation. The eccentricity is mapped onto the image brightness and the angle of orientation of the tubuli in the dentin ($\psi_1 + 90^\circ$) is mapped onto the image color, using the color wheel displayed in the bottom left corner. Length scale given in (d-f). Large version of Fig. 4 in Appendix I.

~ 2.5 (~ 50) μm . We recognize the shorter distance to be close to the known size of the dentin tubuli, while the long distance corresponds to the coherence length of the beam, which is thus the limiting factor for the narrow part of the scattering function. This supports the notion that the tubuli are the origin of the scattering signal.

The fits shown in Fig. 4.c were made for all points on the sample. In Fig. 4.d the parameter α is plotted showing the part of the beam that has been scattered. Note how the scattering decreases away from the pulp cavity. This corresponds well with the known property that the tubuli exists in higher concentrations closer to the pulp cavity. Note also that we can detect little or no scattering in the enamel and near the dentin-enamel junction. In Fig. 4.d points with no sample have been colored black for clarity.

The local eccentricity ($e \equiv (\sqrt{\sigma_1^2 - \sigma_2^2}) / \sigma_1$) is plotted in Fig. 4.e. The eccentricity shows the dentin is most strongly aligned close to the pulp. The eccentricity has

values up to more than 30. This indicates a very strong preferred orientation and correlates well with the observation of the very narrow peaks in the visibility in Fig. 4.c and the narrow dark bands in Fig. 4.b. Only when the tubuli are aligned with a couple of degrees of parallel with the grating lines do they produce no signal in the visibility.

The eccentricity has in Fig. 4.f been combined with the ordering direction of the tubuli in the dentin. The color wheel shows the orientation of tubuli in the dentin, corresponding to the position of the peak ($+90^\circ$) in the visibility in Fig. 4.c. In the figure the eccentricity is mapped onto the intensity of the colors. The orientation we see in Fig. 4.f corresponds to the dentin tubuli which are mainly oriented radially away from the pulp cavity. For both Fig 4.e and 4.f only points with $\alpha > 0.15$ have been plotted for clarity, thus omitting pixels where only a small part of the beam has been scattered. The orientation in the enamel is not observable in the presented measurements.

The results presented in Fig. 4 demonstrate how the parameter α included in the extended model can help us understand the visibility variations of strongly aligned samples. The observed visibility is clearly not sinusoidal and the novel model presented here is hence necessary to interpret the results. It is noteworthy that this is an extreme case of strongly oriented scattering.

We also see how the directional dark-field measurement provides multiple images containing complementary information. The absorption provides information about the density in the sample, the eccentricity about the degree of ordering, ψ_1 about the ordering direction and α about the integrated scattering cross section. All of these parameters can be combined to get a better understanding of the investigated samples.

The orientation of the tubuli in the dentin is important for a number of reasons. The orientation is necessary to understand and model the mechanical properties of teeth. Recently it has also been suggested that future dental filling should mimic the micro and nanostructure of the teeth²⁰. For this to be possible it is necessary to image and understand the nanostructure of the teeth. The use of directional dark-field imaging for this purpose will be particularly interesting when the method is extended into three dimensions. This however still requires the development of novel tensorial x-ray computer tomography reconstruction algorithms, which presently do not exist.

V. CONCLUSION

We have developed a simple scattering model to describe the angular variations of the visibility in grating based directional dark-field imaging. The new model is consistent with previously described methodology, while extended to cover also strongly ordered systems which are not well described by the previous model. The novel model was experimentally verified using a fiber mesh sample and a slice of a tooth.

We demonstrated an example of how directional dark-field could be used to determine both the position and orientation of fibers as well as being used to, once calibrated, count the number of overlapping fibers in a given point.

This novel model adds to the possible application of directional dark-field imaging for non destructive testing of for example fiber reinforced materials. It is important to note that the method has previously been demonstrated with a conventional x-ray tube¹⁷, and one could thus envisage widespread application of the method.

We developed the model further including a term accounting for the not scattered part of the beam. This was used to map the orientation and the eccentricity of the scattering of the tubuli in the dentin. This example demonstrated that directional dark-field imaging can be used for samples exhibiting highly eccentric scattering profiles.

The study of the tubuli in the dentine in teeth will be particularly interesting when the method is extended to three dimensions. As mentioned this however still requires the development of novel tensorial x-ray computer tomography reconstruction algorithms, which presently do not exist.

Acknowledgements

We thank Stefan Buser and the clinic for parodontology, endodontontology and cariology of the school for dental medicine (Uni Basel) for sample preparation and Keld Theodor for technical support. F.P. and M.B. acknowledges support through the DFG excellence cluster 'Munich-Centre for Advanced Photonics'. T.H.J. acknowledges support from the Danish Natural Science Research Council through DANSCATT. This work was supported by the European Synchrotron Radiation Facility (project MI-1001) by allocation of beam time.

-
- ¹ David C., Nöhammer B., Solak H.H. and Ziegler E. *Appl. Phys. Lett.* **81** (17) 3287-3289 (2002).
- ² Momose A. *Opt. Exp.* **11**, (19) 2303 (2003).
- ³ Weitkamp T, Diaz A, David C, Pfeiffer F, Stampaconi M, Cloetens P and Ziegler E. *Opt. Exp.* **13**, (16) 6296 (2005)
- ⁴ Bech M, Jensen T H, Bunk O, Dontah T, David C, Weitkamp T, Le Duc G, Bravin A, Cloetens P and Pfeiffer P. *Z. Med. Phys* **20**, 7 (2010).
- ⁵ Pfeiffer F, Weitkamp T, Bunk O and David C. *Nature Phys.* **2**, 258 (2006).
- ⁶ Pfeiffer F, Bunk O, David C, Bech M, Le Duc G, Bravin A and Cloetens P. *Phys. Med. Biol.* **52**, 6923 (2007).
- ⁷ Bech M, Bunk O, David C, Ruth R, Rifkin J, Loewen R, Feidenhans'l R and Pfeiffer F. *J. Synchrotron Radiat.* **16**, 43 (2009).
- ⁸ Bech M, Jensen T H, Feidenhans'l R, Bunk O, David C and Pfeiffer F. *Phys. Med. Biol.* **54**, 2747 (2009).
- ⁹ Pfeiffer F, Bech M, Bunk O, Kraft P, Eikenberry E F, Brönnimann CH, Grünzweig C and David C. *Nature Mat.* **7**, 134 (2008).
- ¹⁰ Pfeiffer F, Bech M, Bunk O, Donath T, Henrich B, Kraft P and David C. *J. Appl. Phys.* **105** 102006 (2009).
- ¹¹ Schwarzschild B. *Phys. Today Vol.* **3** 12 (2008).
- ¹² Bech M. X-ray imaging with a grating interferometer. PhD thesis, University of Copenhagen, 2009.
- ¹³ Wang, Z.-T., Kang, K.-J., Huang, Z.-F. and Chen, Z.-Q. (2009), 'Quantitative grating-based x-ray dark-field computed tomography', *Appl. Phys. Lett.* 95(9).
- ¹⁴ Chen, G.-H., Bevins, N., Zambelli, J. and Qi, Z. (2010), 'Small-angle scattering computed tomography (SAS-CT) using a Talbot-Lau interferometer and a rotating anode x-ray tube: theory and experiments', *Opt. Exp.* 18(12), 12960-12970.
- ¹⁵ Bech, M., Bunk, O., Donath, T., Feidenhans'l, R., David,

- C. and Pfeiffer, F. (2010), 'Quantitative x-ray dark-field computed tomography', *Phys. Med. Biol.* **55**(18), 5529-5539.
- ¹⁶ Yashiro, W., Terui, Y., Kawabata, K. and Momose, A. (2010), 'On the origin of visibility contrast in x-ray Talbot interferometry', *Opt. Exp.* **18**(16), 16890- 16901.
- ¹⁷ Jensen T H, Bech M, Bunk O, Donath T, David C, Feidenhans'l R, and Pfeiffer F. *Phys. Med. Biol.* **55** 3317 (2010).
- ¹⁸ David D, Bruder J, Rohbeck T, Grünzweig C, Kottler C, Diaz A, Bunk O and Pfeiffer F. *Microel. Eng.* **84** 1172 (2007).
- ¹⁹ Reznikova E, Mohr J, Boerner M, Nazmov V, and Jakobs P. *Microsyst. Technol.* **14** 1683 (2008).
- ²⁰ Deyhle H, Bunk O, Buser S, Krastl G, Zitzmann N U, Ilgenstein B, Beckmann F, Pfeiffer F, Weiger R, and Müller B. *Proc. SPIE* **7401** 74010E (2009).
- ²¹ Due to noise, a minimal visibility of 0.06 has been used in the fits. We would expect a noise level of this magnitude and thus believe this is not an effect of the not scattered part of the beam.
- ²² The human tooth was an extracted non-restored molar tooth of the fourth quadrant. A saw (Exact Apparatebau GmbH, Norderstedt, Germany) equipped with a 0.2 mm cutting diamond band was used to make a 500 μm thick slice parallel to the tooth axis.

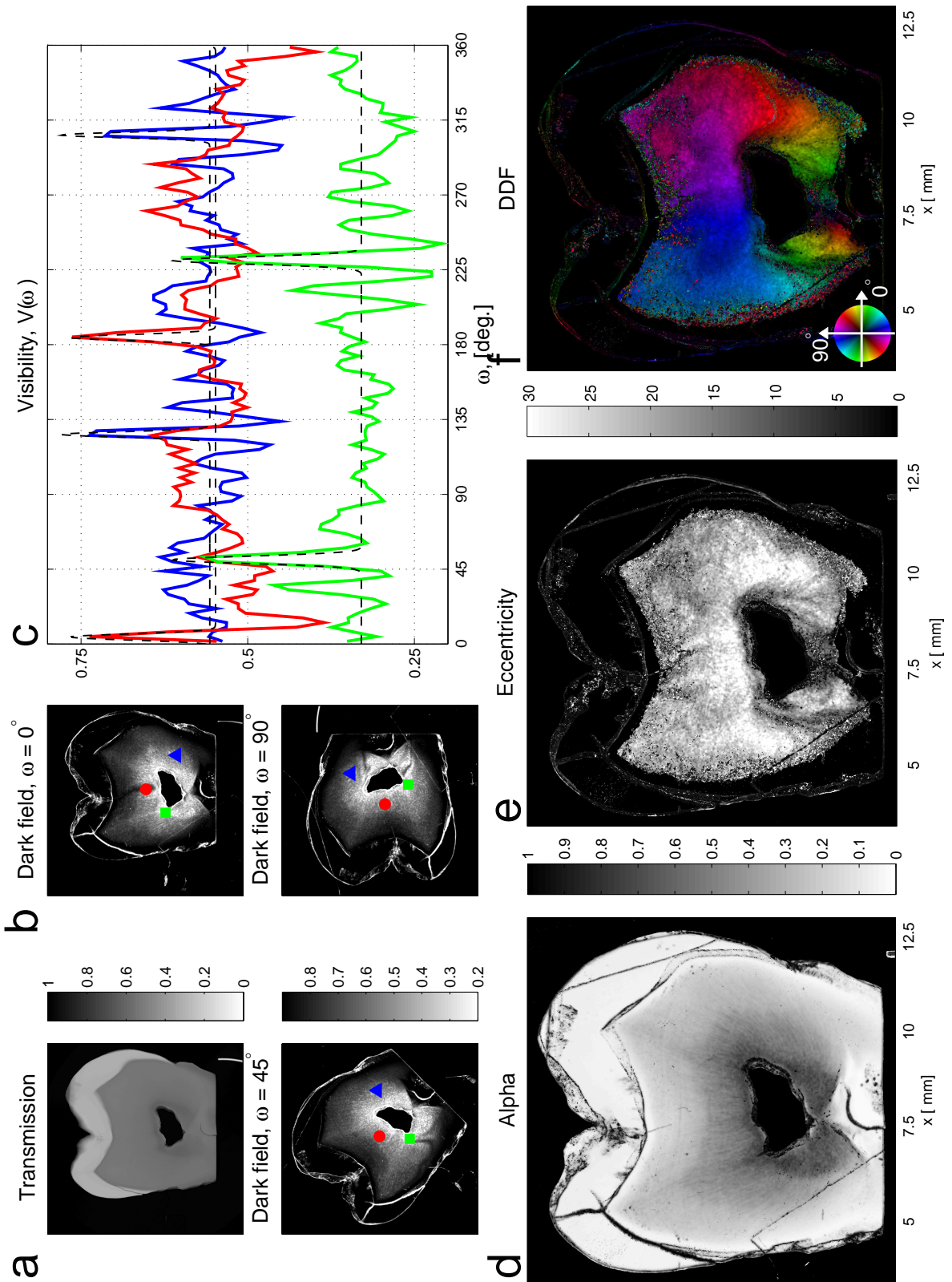


FIG. 5: Enlarged version of Fig. 4. Imaging of tooth slice (a) X-ray transmission image. (b) Dark-field images for three different sample orientations ω . (c) Visibility $V(j, k, \omega)$ as a function of ω for three different sample regions. (d) The parameter α describing the proportion of beam that has been scattered. (e) Map of the eccentricity of the fitted local scattering profile. (f) Combined color representation. The eccentricity is mapped onto the image brightness and the angle of orientation of the tubuli in the dentin ($\psi_1 + 90^\circ$) is mapped onto the image color, using the color wheel displayed in the bottom left corner. Length scale given in (d-f).

Publication V

Submitted to Physics in Medicine and Biology

T.H. Jensen, M. Bech, O. Bunk, M. Thomsen, A. Menzel, A. Bouchet, G. Le Duc, R. Feidenhans'l and F. Pfeiffer

Brain tumor imaging using small-angle x-ray scattering tomography

Submitted to Physics in Medicine and Biology

Brain tumor imaging using small-angle x-ray scattering tomography

T. H. Jensen,¹ M. Bech,² O. Bunk,³ M. Thomsen,¹ A. Menzel,³
A. Bouchet,^{4,5} G. Le Duc,⁴ R. Feidenhans'l,¹ and F. Pfeiffer²

¹*Niels Bohr Institute, University of Copenhagen, 2100 Copenhagen, Denmark*

²*Department of Physics, Technical University of Munich, 85748 Garching, Germany*

³*Paul Scherrer Institut, 5232 Villigen PSI, Switzerland*

⁴*European Synchrotron Radiation Facility, 38043 Grenoble, France*

⁵*Grenoble Institute of Neurosciences (Team 7), 38000 Grenoble, France*

(Dated: October 11, 2010)

We demonstrate high-resolution small-angle x-ray scattering computed tomography (SAXS-CT) of soft matter and soft tissue samples. Complete SAXS patterns over extended ranges of momentum transfer are reconstructed spatially resolved from volumes inside an extended sample. Several SAXS standard samples are used to quantitatively validate the method and demonstrate its performance. Further results on biomedical tissue samples (rat brains) are presented that demonstrate the advantages of the method compared to existing biomedical x-ray imaging approaches. Functional areas of the brains as well as tumor morphology are imaged. By providing insights into the structural organization at the nanolevel, SAXS-CT complements and extends results obtainable with standard methods such as x-ray absorption tomography and histology.

INTRODUCTION

The properties and functions of many soft matter systems such as soft tissues are often strongly related to the structure at the micro- and nanolevel. Detailed imaging of these structures can provide insight into this correlation. Small-angle x-ray scattering (SAXS) is a widely used method to probe the micro- and nanostructure of noncrystalline materials[1–3]. Structural variations in heterogenous samples have been mapped out using a scanning-based set-up and a pencil beam[4, 5]. These experiments provide 2D structural information, but often require destructive sample preparation and provide no depth-resolved information about the sample. One way to overcome this limitation is to use x-ray tomography. Standard x-ray absorption computed tomography (CT) has been used for many years for non-invasive 3D studies[6]. CT provides access to volume-resolved information and requires little sample preparation. While providing excellent spatial resolving power, it has an inherent lack of information about the nanoscale structure of the sample.

It is possible to combine SAXS and CT to small-angle x-ray scattering tomography (SAXS-CT). SAXS-CT has been demonstrated in a few cases with soft matter and biological samples[7–12].

The combination of a scanning-probe imaging technique with tomography requires the acquisition of a vast amount of data. As a consequence, previous studies have been limited to comparatively low spatial resolution. Furthermore, the requirement of fast data acquisition has often compromised SAXS data quality such that only a qualitative analysis was possible, but the rich tools of quantitative SAXS analysis could not be brought to bear. The advent of brighter sources, fast and essentially noise-free detectors, and automated analysis schemes

have made possible the efficient acquisition of hundreds of thousands of SAXS patterns that are required to spatially resolve the micro- and nanostructure of extended samples.

In this paper we demonstrate how SAXS-CT can deliver biomedical images that highlight structural (and functional) details of the soft tissue on the nanoscale. We particularly report results of SAXS-CT experiments performed on a soft matter phantom and on tumors implanted rat brains. Our results on the phantom demonstrate the sensitivity of the method. The obtained information is used to accurately identify and describe the nanostructure of the different samples in the phantom. With the results from the rat brains we demonstrate the use of the structural information for imaging substructures of brain tumors as well as important functional areas of the brain.

MATERIALS AND METHODS

Figure 1a shows the experimental set-up. The idea of the set-up is to use tomographic methods to reconstruct spatially resolved small-angle x-ray scattering curves. Small-angle x-ray scattering is collected in a 1st-generation tomography approach: Using a pencil-beam, 2D SAXS patterns are collected point by point for each horizontal sample translation s , and rotation ω . Figure 1b is a sketch of a sample containing four sample capillaries, with four different beam paths indicated. In Fig. 1c the corresponding azimuthally averaged SAXS curves are shown.

In order to enable tomographic reconstruction of the SAXS signal one of the following demands must be fulfilled: (1) Only the scattering parallel to the ro-

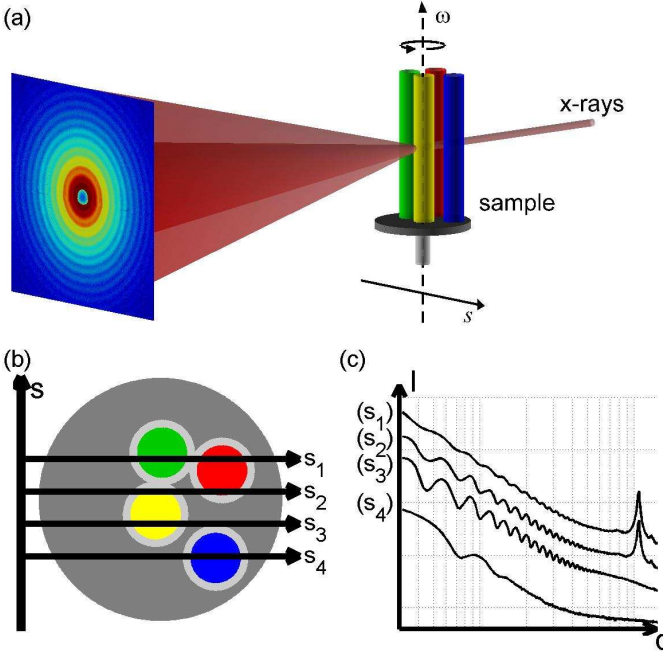


FIG. 1: **Small-angle x-ray scattering tomographic set-up.** (a) Using a pencil-beam, scattering patterns are collected by translating the sample through the beam (s), for different orientations (ω) (b)-(c) An example with scattering patterns collected for 4 different projections are shown.

tation axis is reconstructed. (2) The sample scatters isotropically[11]. In this paper all our samples will be isotropically scattering samples. From this point on the momentum transfer q will hence be treated as a scalar. Scattering from a sample can be described by the differential scattering cross section per unit volume $\frac{d\Sigma}{d\Omega}$:

$$I(s, \omega, q) = I_0 \int_0^L \underbrace{\left[e^{-\int_0^l \mu(\tilde{l}) d\tilde{l}} \right]}_{\text{Abs. before}} \underbrace{\frac{d\Sigma}{d\Omega}(l, q)}_{\text{Scattering}} \underbrace{\left[e^{-\int_l^L \mu(\tilde{l}) d\tilde{l}} \right]}_{\text{Abs. after}} dl \Delta\Omega. \quad (1)$$

The beam path through the sample defined by (s, ω) is parameterized by the variable l over which the integral runs. $I(q)$ is the scattered intensity for a given q -vector, I_0 is the incident intensity, $\mu(l)$ is the local absorption length, and $\Delta\Omega$ is the solid angle covered by the detector element.

$\frac{d\Sigma}{d\Omega}(l, q)$ describes the scattering probability at a certain voxel in the sample. To determine the total scattered intensity we have to take the absorption happening before and after the scattering events into account. Since all scattering occurs at small angles, the scattered photons can be assumed to exit the sample along the same path as the transmitted photons and it is thus possible to separate the absorption and scattering terms. We define the projected differential scattering cross section $\mathcal{P}(s, \omega, q)$ and rewrite equation (1) as:

$$\begin{aligned} \mathcal{P}(s, \omega, q) &\equiv \frac{I(s, \omega, q)}{I_0 \cdot T(s, \omega) \cdot \Delta\Omega} \\ &= \int_0^L \frac{d\Sigma}{d\Omega}(l, q) dl, \end{aligned} \quad (2)$$

where T is the sample transmission, $T(s, \omega) = e^{-\int_0^L \mu(l) dl}$. Equation (2) has the same form as the line integral of the attenuation coefficient known from absorption tomography [13]. It is thus possible to reconstruct $\frac{d\Sigma}{d\Omega}(x, y, q)$ using standard CT reconstruction algorithms for each q . We thus obtain spatially resolved scattering information about the micro- and nano-structures of a sample by reconstructing the local SAXS signal $\frac{d\Sigma}{d\Omega}(q)$ inside an extended sample using standard tomographic methods.

RESULTS

The SAXS-CT experiments were carried out at the cSAXS beamline at the Swiss Light Source (SLS). Using a monochromatic x-ray beam focused at the sample position, scattering was recorded with a PILATUS 2M detector[14]. The PILATUS 2M detector is essentially noise free and yields excellent statistics for the azimuthally averaged data with useable data for as low as 0.1 photons/pixel.

To demonstrate the sensitivity of the method a soft matter phantom with several standard SAXS samples was imaged[15]. The phantom was constructed to test the dynamic range as well as the reciprocal space resolution of the set-up. The phantom consisted of four capillaries filled with a colloidal suspension, two types of micelles and silver behenate powder, respectively. Figure 2 displays the experimental results for a single tomographic slice through the phantom. The standard projected absorption sinogram and the corresponding reconstructed absorption lengths are shown in Fig. 2a,b[16]. Using absorption tomography the four capillaries are clearly localized, but only little information on the micro- and nanoscale of the contents are obtained. Specifically, no information from structures smaller than the voxel size of $30 \times 30 \times 40 \mu\text{m}^3$ can thus be resolved. In Fig. 2c-f the projected differential scattering cross section sinograms and the reconstructed differential scattering cross sections for two different q -values are displayed. These reveal information about the samples at the nanoscale. We should note that the momentum transfers we are probing corresponds to real space distances of 4-200 nm. With SAXS-CT we are thus probing length scales that are smaller than the voxel size. Similar reconstructions were made for all recorded values of q , thus reconstructing the full differential scattering cross section for 189x189 different voxels in the slice. The reconstructed differential scattering cross section for four single voxels, each of volume

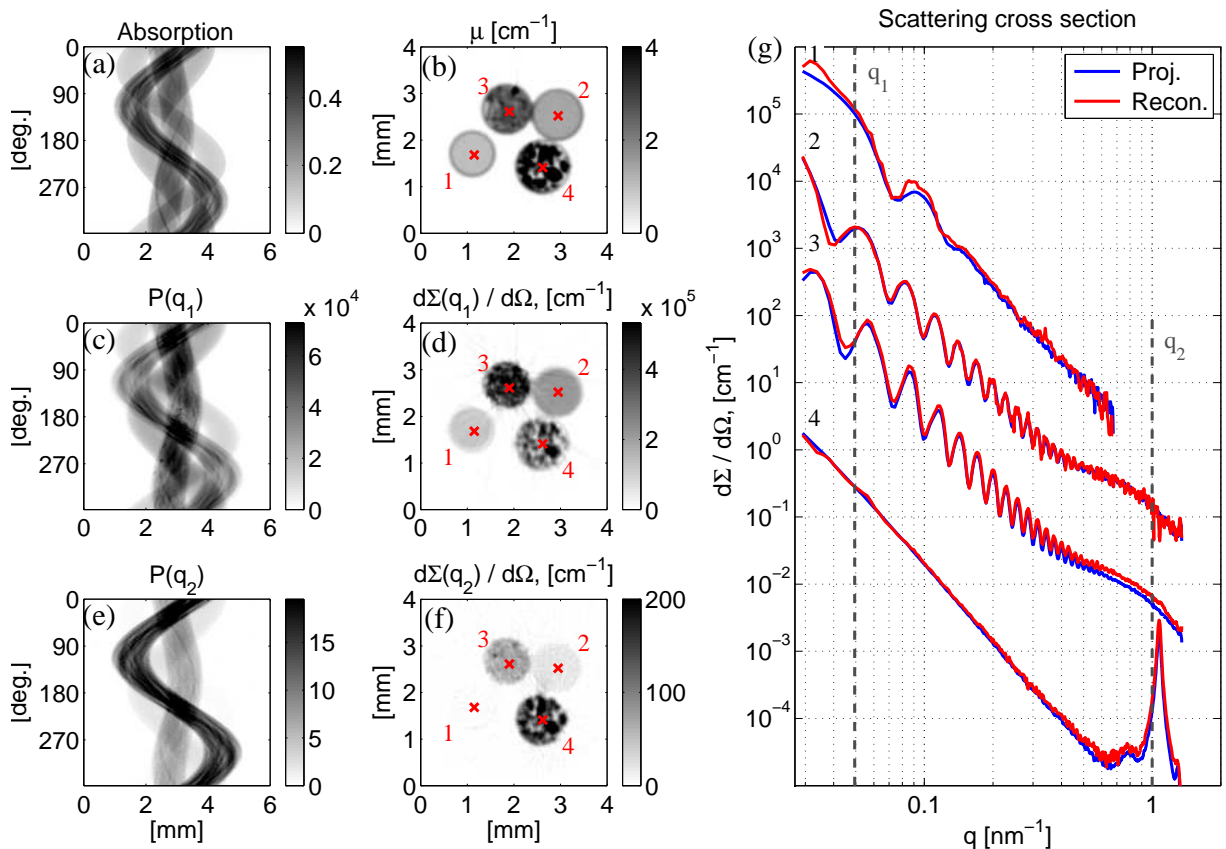


FIG. 2: Sinograms and reconstructions. SAXS-CT was performed on a phantom consisting of four capillaries. The capillaries were filled with a colloidal suspension (1), two concentrations of micelles (2-3) and silver behenate (4) respectively. (a)-(b) Shows the absorption sinogram and the corresponding reconstruction for a single slice through the sample. (c)-(d) Shows the scattering amplitude sinogram for a specific momentum transfer ($q_1 = 0.049 \text{ nm}^{-1}$), and the corresponding reconstructed differential scattering cross section of the sample. (e)-(f) The same information as (c)-(d), but for a different momentum transfer ($q_2 = 1.0 \text{ nm}^{-1}$). (g) Reconstructed (red) and standard (blue) differential scattering cross sections for the four different capillaries. The reconstructed scattering curves are taken from single voxels (marked in panels b,d and f) and curves from the four capillaries are each offset by two decades for clarity.

$30 \times 30 \times 40 \mu\text{m}^3$ are displayed in Fig. 2g. Their locations are shown in panels b, d and f. The reconstructed scattering curves of $\frac{d\Sigma}{d\Omega}(x_i, y_i, q)$ (shown in red) are compared to $\frac{d\Sigma}{d\Omega}(q)$ (shown in blue) obtained using the same samples in standard SAXS projection geometry. The latter were obtained from projections where only a single component was contributing to the signal, which corresponds to measurements using standard SAXS projection geometry. The projection scattering curves have been normalized to the sample transmission, and sample volume as known from absorption tomography. All curves are reconstructed on an absolute scale. We note that the reconstructed scattering curve of a single voxel inside the sample is identical to the SAXS measured using standard SAXS projection geometry. We thus conclude that we can reconstruct the full SAXS curve associated with a small volume inside our sample.

Since the full scattering curves are known for each voxel, we can conceive many different imaging contrasts

signals. In Fig. 2d,f the scattering cross section for a specific q -value is used as imaging signal. A more extensive curve analysis can also be used to generate the image contrast. One way to analyze the curves is to investigate the slope, p , of the scattering curves over a specific q -range by fitting them to a function of the form:

$$\frac{d\Sigma}{d\Omega}(q) = Cq^{-p}. \quad (3)$$

For large values of q this would be equivalent to a Porod-like analysis. One could also make Guinier-like analysis of the curves. Many other, and possibly more advanced or specialized analysis methods can be used to generate image contrast.

The results in Figure 2 demonstrate that a quantitative reconstruction of the local differential scattering cross section is possible with SAXS-CT. The extra structural information on the nanoscale obtained through SAXS-CT now clearly demonstrates its complementarity to to-

mography based on absorption or phase contrast. Using the spatially resolved full scattering curves it is possible to identify the content of each of the different capillaries. Capillaries (1), (2) and (3) each contains monodisperse spheres with radius, $r \sim 60$ nm, $r = 110$ nm and $r = 110$ nm respectively. The fourth capillary shows a Bragg peak corresponding to a period of 58.4 nm. We thus obtain important information about the nanostructure of the content of each capillary without having any *a priori* knowledge. We can even see the difference in micelle concentration in capillaries (2) and (3) giving rise to a difference in the differential scattering cross section at small values of q due to static structure factor of the interparticle interaction. The Bragg peak from the material in the fourth capillary is the (0 0 1) peak of the silver behenate crystal powder in the capillary.

Note how the reconstruction is obtained with high q -resolution, demonstrated by the resolving of more than 20 size oscillations in sample number 3. At the same time a high dynamic range is kept, with reconstructed SAXS curves in some cases spanning up to six decades. Even within a specific q -range the high dynamic range is obtained, as seen at the first silver behenate peak where the scattering intensity varies by three decades between different capillaries.

Having introduced and demonstrated the method of SAXS-CT on a set of standard SAXS samples we demonstrate a potential biomedical application by investigating a weakly scattering soft tissue sample. Two formalin fixed rat brains[17] were investigated using SAXS-CT[21]. The results are shown in Figure 3. Presented here are three coronal slices from the two different brains. The three different slices are presented in three rows. One brain has two large visible tumors (Fig. 3a,b), a matching slice from the other brain without visible tumor is shown for comparison (Fig. 3c,d). A second slice from the brain without visible tumor is also shown (Fig. 3e,f). Panel a in Fig. 3 show the tomographic reconstructed local differential scattering cross section integrated over $q \in [0.071 - 0.16] \text{ nm}^{-1}$, panels c and e the cross section integrated over $q \in [0.071 - 0.39] \text{ nm}^{-1}$. The intervals are marked by vertical black dashed lines in the plots in Fig. 4. The integrated differential scattering cross section demonstrates sufficient contrast to clearly identify different parts of the brain. The scattering signal provides anatomical maps of the brains. Several functional areas such as the corpus callosum (e.g. Fig. 3f point 4), and the hippocampus (Fig. 3d point 2) are clearly visible, and the tumors (Fig. 3a all points) are clearly delineated. For each voxel in each slice the full scattering curve has been reconstructed. A few of these scattering curves are shown in Fig. 4. The curves are displayed in Kratky plots ($q, \frac{d\Sigma}{d\Omega} q^2$) and offset by a factor of 2 for clarity. The points from where the scattering curves are taken are marked in column 1 and 2 in the corresponding rows of Fig. 3.

The slope parameter analysis introduced in eq. (3) was performed on all scattering curves of all three slices. The slope parameter, p is displayed in Figure 3 column 2 and was determined over the same q -range as the cross section in column 1.

From the slope parameter we can see increased contrast in several spots. In Fig. 3b, the slope parameter helps to delineate substructures of the tumors that are less visible in the integrated differential scattering cross section image in Fig. 3a. Especially, the necrotic part of the tumors is very well delimited on Fig. 3b (white regions, points 3 and 4). In such a way, using the slope parameter images might help to delineate the active part of the tumor. Also, the edema surrounding the tumors (in the hemisphere bearing the tumor) and the dilation of the ventricle (contralateral hemisphere) are very well defined and limited both on 3a and 3b.

In Fig. 3f the anterior commissure (point 3) is clearly visible when analyzing the slope parameter. Finally in Fig. 3d we can see some of the connections between the internal and external capsule near point 4.

The images in column 2 clearly demonstrate that curve analysis can be used to generate additional image contrast, and hence obtain additional information about the brain and the tumors. In principle all the methods regularly used in small-angle x-ray scattering could also be applied in the analysis of the spatially resolved scattering curves for image contrast and possibly tissue identification.

Although row 1 and 2 show slices through the same region of the brain, only very little of the original structure is left in the tumor invaded brain in row 1. In the tumor invaded brain it is possible to recognize parts of hippocampus and corpus callosum, but the structure is strongly disturbed by the tumors.

CONCLUSION

In summary, we have demonstrated a high-resolution SAXS-CT over extended q -ranges, which provides information on the local scattering inside an extended sample. This information is obtained by using SAXS in a tomographic approach, thus providing the information in a non-invasive way. Small-angle x-ray scattering curves spanning up to six decades in intensity were reconstructed, with hundreds of thousands of SAXS patterns reconstructed.

We validated the method of SAXS-CT using a phantom comprising several SAXS standards. We thus could demonstrate the range and accuracy to which the scattering curves could be reconstructed. We further showed how the nanostructural information can be used to provide clearly resolved anatomical maps of rat brains. We also demonstrated how the slope of the scattering curves

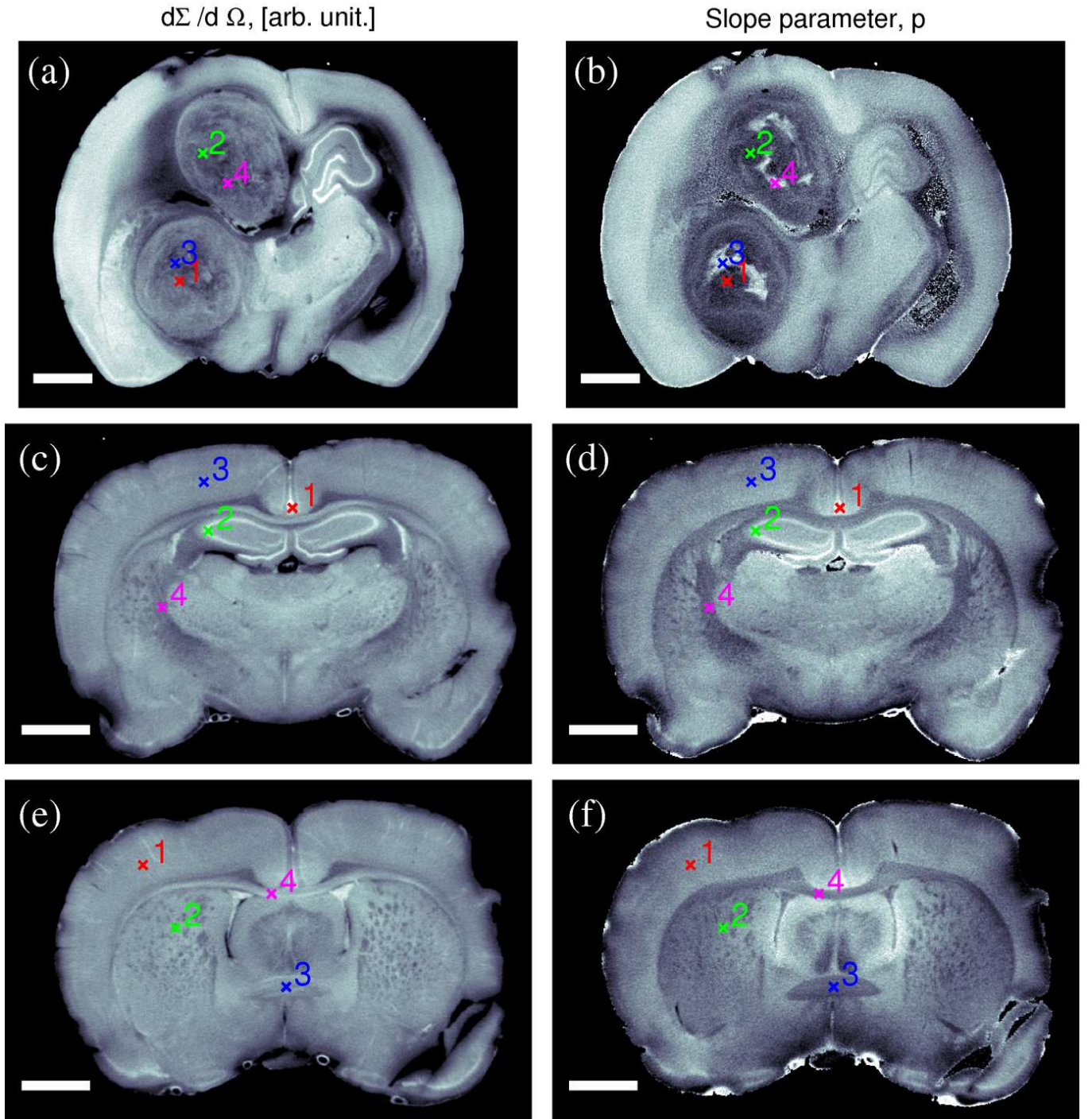


FIG. 3: Biological example, rat brain. The three rows, each represent three different tomographic sections of two rat brains. The first column (panels a, c and e) shows the local scattering cross section in a specific q -range ($q \in [0.071 - 0.39] \text{ nm}^{-1}$). The second column (panels b, d and f) shows the local slope of the scattering curve in the q -range $q \in [0.071 - 0.16] \text{ nm}^{-1}$ for the first row and in the q -range $q \in [0.071 - 0.39] \text{ nm}^{-1}$ for the second and third row. The scattering curves corresponding to the points marked in this figure are plotted in Fig. 4. The scale bars have a length of 2 mm. All images are displayed with a linear grayscale, with the following limits: a:[5.9-25.3], b:[1.34-2.52], c,e:[8.2-34.2] and d,f:[1.80-2.51].

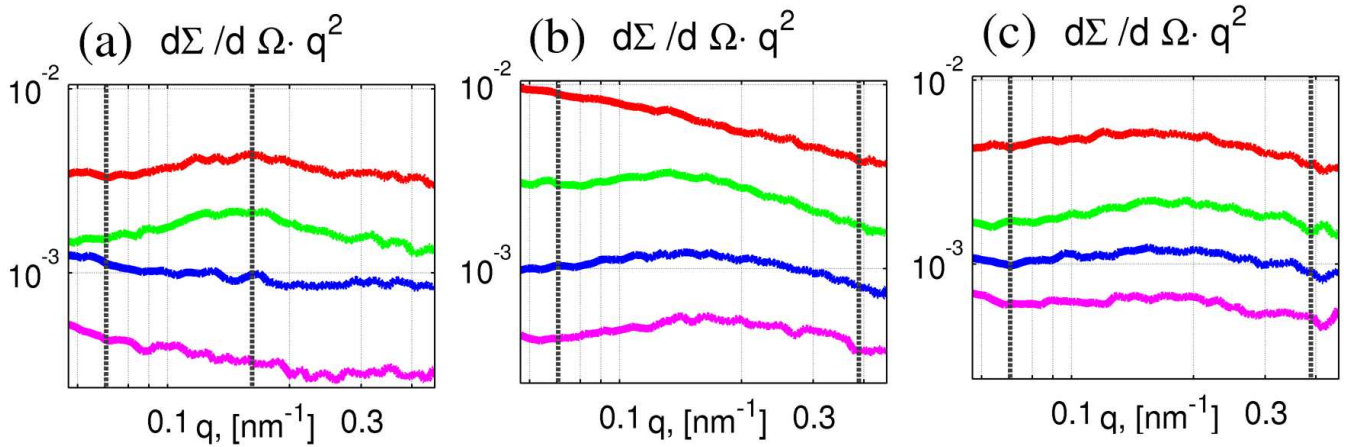


FIG. 4: **Biological example, rat brain.** Panels a, b and c shows the reconstructed small-angle scattering curves for 4 selected points from each of the rows in Fig. 3. The panels a, b and c corresponds to row 1, 2 and 3 respectively. The correspondence between the points in Fig. 3 and the scattering curves in this figure is shown by color and numbering. Each scattering curve is offset by a factor of 2 for clarity.

can be used for imaging providing additional contrast for both the functional areas and the tumor. Using the slope delineation of the necrotic regions of the tumor was possible.

The two examples demonstrated how SAXS-CT complements and extends results obtainable with methods such as standard absorption tomography and histology.

We believe that SAXS-CT may be desirable and applicable in many cases. Since the method is non-destructive, samples that cannot be sectioned can now be studied with SAXS. This could include historic and cultural artifacts, and other uniquely valuable samples. It would even be possible to study non fixed tissue, which would be impossible to slice. SAXS-CT could thus also be used to study what transformation tissue undergoes on the molecular level during fixation. For other types of applications, materials science could use SAXS-CT to study sintering of nano- or micro-powder samples.

Acknowledgements

We gratefully acknowledge Keld Theodor and Xavier Donath for technical support. F.P. and M.B. acknowledges support through the DFG excellence cluster 'Munich-Centre for Advanced Photonics'. T.H.J., M.B., M.T. and R.F. acknowledges support from the Danish Natural Science Research Council through DANSCATT. The experiments were performed at the cSAXS beamline [5] of the Swiss Light Source, Paul Scherrer Institut, Villigen, Switzerland.

-
- [1] Guinier, A. & Fournet, G. *Small-angle scattering of X-rays* (Wiley, New York, 1955).
 - [2] Glatter, O. & Kratky, O. *Small angle X-ray scattering* (Academic, London, 1982).
 - [3] Narayanan, T. High brilliance small-angle X-ray scattering applied to soft matter. *Curr. Opin. Colloid Interface Sci.* **14**, 6, 409-415 (2009).
 - [4] Gourrier, A. *et al.* Scanning X-ray imaging with small-angle scattering contrast. *J. Appl. Cryst.* **40**, 7882 (2007).
 - [5] Bunk, O. *et al.* Multimodal x-ray scatter imaging. *New Jour. of Phys.* **11**, 123016 (2009).
 - [6] Kalender, W. A. X-ray computed tomography. *Phys. Med. Biol.* **51**, R29-R43 (2006).
 - [7] Harding, G., Kosanetzky, J., & Neitzel, U. Elastic Scatter computed tomography. *Phys. Med. Biol.* **30**, 183-186 (1985).
 - [8] Harding, G., Kosanetzky, J., & Neitzel, U. X-ray diffraction computed tomography. *Med. Phys.* **14**, 515-525 (1987).
 - [9] Harding, G., & Kosanetzky, J. Scattered x-ray beam non-destructive testing. *Nucl. Inst. and methods in Physics research A* **A280**, 517-528 (1989).
 - [10] Kleuker, U., Suortti, P., Weyrich, W., & Spanne, P. Feasibility study of x-ray diffraction computed tomography for medical imaging. *Phys. Med. Biol.* **43**, 2911-2923 (1998).
 - [11] Schroer, C. G. *et al.* Mapping the local nanostructure inside a specimen by tomographic small-angle x-ray scattering. *Appl. Phys. Lett.* **88**, 164102 (2006).
 - [12] Stock, S. R., de Carlo, F., & Almer, J. D. High energy X-ray scattering tomography applied to bone. *J. Struct. Biol.* **161**, 144-150 (2008).
 - [13] Kak, A. C., & Slaney, M. *Principles of Computerized Tomographic Imaging* (IEEE Press, New York, 1988).
 - [14] Henrich, B. *et al.* PILATUS: A single photon counting pixel detector for X-ray applications. *Nucl Instrum Meth A* **607**, 247-249 (2009).

- [15] The following parameters were used for the data acquisition for the phantom: x-ray energy 18.6 keV, focus spot size $40 \times 40 \mu\text{m}^2$, sample to detector distance 7212 mm, $30 \mu\text{m}$ step size, 201 steps, 181 angles over 360 degrees. Exposure time 200 ms for both scattering and absorption measurements. The total acquisition time for the scattering and absorption measurements for one tomographic slice was 4.5 hours. In total 72'000 scattering patterns were collected per slice.
- [16] Absorption was measured in the same set-up using the same method, but with an attenuated beam and no beam-stop.
- [17] Brain tumor inoculation. The 9L gliosarcoma cell line was originally established by Benda et al.[18]. The 9L gliosarcoma cells were implanted in the brain of male Fisher 344 rats (Charles River, France) as previously described[19]. Cells were grown with complete medium at 37C. The male Fisher 344 rats (180-280 g, Charles River, L' Arbresle, France) were anesthetized with 4% isoflurane inhalation followed by an intraperitoneal injection of xylazine/ketamine (64.5/5.4 mg/kg). They were placed on a stereotactic head holder (model 900, David Kopf Instruments, Tujunga, USA). At D0, 104 cells were suspended into 1 μl DMEM with antibiotics (1%) then injected using a 1 μl Hamilton syringe through a burr hole in the right caudate nucleus (9 mm anterior to the ear-bars i.e. at bregma site, 3.5 mm lateral to the midline, 5.5 mm depth from the skull)[20]. The rats were euthanized at different stages of the tumor growth (Day 17 and Day 7 for the two brains respectively). No tumor was visible in the slices from the Day 7 rat. The brains were then sampled and fixed in 10% formalin 10 days minimum prior to any experiment. All operative procedures related to animal care strictly conformed to the Guidelines of the French Government with licenses 380825 and B3818510002 and they were reviewed by the Internal Evaluation Committee for Animal Welfare and Rights of the ESRF.
- [18] Benda, P., Someda, K., Messer, J., & Sweet W. H. Morphological and immunochemical studies of rat glial tumors and clonal strains propagated in culture. *J. Neurosurg.* **34**, 310-23 (1971).
- [19] Regnard, P. et al. Irradiation of intracerebral 9L gliosarcoma by a single array of microplanar x-ray beams from a synchrotron: balance between curing and sparing. *Phys. Med. Biol.* **bf 53**, 4, 861-78 (2008).
- [20] Paxinos, G. & Watson, C. eds. *The rat brain in stereotaxic coordinates* (New York: Academic Press, 1986).
- [21] The following parameters were used for the data acquisition for the rat brain sample: x-ray energy 18.58 keV, focus spot size $25 \times 25 \mu\text{m}^2$, sample to detector distance 7117 mm, $25 \mu\text{m}$ step size, 720 steps, 541 angles over 360 degrees. Exposure time 150 ms for scattering measurements and 10 ms for absorption measurements. The total acquisition time for the scattering and absorption measurements for one tomographic slice approximately 24 hours. In total 390'061 scattering patterns were collected per slice.

Publication VI

Submitted to Nature Communications

T.H. Jensen, M. Bech, O. Bunk, A. Menzel, A. Bouchet, G. Le Duc, R. Feidenhans'l and F. Pfeiffer

Molecular x-ray computed tomography of myelin in a brain
Submitted to Nature Communications

Molecular x-ray computed tomography of myelin in a brain

T. H. Jensen,¹ M. Bech,^{1,2} O. Bunk,³ A. Menzel,³ A. Bouchet,^{4,5} G. Le Duc,⁴ R. Feidenhans'l,¹ and F. Pfeiffer²

¹*Niels Bohr Institute, University of Copenhagen, 2100 Copenhagen, Denmark*

²*Department of Physics, Technical University of Munich, 85748 Garching, Germany*

³*Paul Scherrer Institut, 5232 Villigen PSI, Switzerland*

⁴*European Synchrotron Radiation Facility, 38043 Grenoble, France*

⁵*Grenoble Institute of Neurosciences (Team 7), 38000 Grenoble, France*

(Dated: October 11, 2010)

We demonstrate the method of small-angle x-ray scattering computed tomography (SAXS-CT) for non-invasive molecular imaging of myelin sheaths in a rat brain. We investigate the variations in myelin concentration and periodicity. We also report data on the total thickness of the myelin sheaths. A wealth of additional information can be extracted from the SAXS-CT data, and we demonstrate imaging of the concentration of cytoskeletal neurofilaments. The imaging of these molecular variations could provide a general means for understanding how these molecular variations relate to a number of neurodegenerative diseases.

Myelin sheaths are lamellar membranes that wrap around neuronal axons. The sheaths are important for the central nervous system as they ensure rapid and secure communication of signals along axons. Structural changes of the myelin sheaths have been associated with a number of widespread neurodegenerative diseases such as cerebral malaria [1], multiple sclerosis [2–4] and Alzheimer's disease [5]. The origin and evolution mechanisms of the diseases are still largely not understood, but it is hypothesized that it is correlated with changes in the myelin formation and structure. A better understanding of the changes in the myelin sheath structure and its correlation to the pathologies is important for the development of methods for prevention or treatment of the diseases.

The changes in the myelin sheaths have been studied with a number of methods such as light [4] and electron microscopy [6, 7], magnetic resonance imaging [8] and x-ray diffraction [9]. All of these methods provide insight into the concentration and molecular structure of the myelin. While myelin sheaths from different types of nerves and in several different animal models have been extensively studied[6, 10], no mapping of the variations of the molecular structure of myelin sheaths in a complete brain has been achieved.

In this paper we introduce a novel method to visualize molecular variations of the myelin structure in a rat brain. Our novel approach is based on the fusion of two well-established biomedical investigation methods: Small-angle x-ray scattering (SAXS) and computed tomography (CT). Combined with a specially developed data processing schemes, our approach delivers non-invasive volume-resolved studies of the molecular variations of the myelin sheaths in a whole rat brain.

SAXS-CT has been demonstrated previously in a few cases with soft matter and biological samples[11–16]. However the combination of SAXS and CT requires the acquisition of vast amounts of data. Previous studies have as a consequence been limited to a comparatively

low resolution. The development of fast and essentially noise-free detectors, bright sources and automated analysis schemes have facilitated the efficient acquisition and processing of the hundreds of thousands of SAXS patterns needed for the high resolution SAXS-CT studies necessary for molecular imaging.

RESULTS

SAXS-CT methodology and data processing

Figure 1 shows the experimental set-up and principle of SAXS-CT. 2D SAXS patterns are recorded using a pencil beam. This is repeated for each horizontal sample translation, s , and rotation, ω , such that 2D SAXS patterns are collected point by point (Fig. 1a). In this way a full tomographic data set is collected point by point using a 1st generation tomography approach. The 2D SAXS patterns are azimuthally averaged and sinograms are generated for each value of q_r (Fig. 1b). Each sinogram is used to reconstruct the differential scattering cross section for the associated value of q_r (Fig. 1c). Once the reconstructions have been made for all values of q_r it is possible to tomographically extract full scattering curves in a non-destructive manner for all voxels in the sample (Fig 1d).

Mapping the myelin sheath concentration

To demonstrate the potential of the new method, particularly for biomedical applications, a formalin-fixed rat brain was investigated using SAXS-CT. Figure 1c,d shows an example of a reconstruction of such a brain with a few associated reconstructed scattering patterns. In the scattering patterns we note several distinct Bragg peaks. One of the series of Bragg peaks is associated with the quasi periodical arrangement of the lamellar structure of

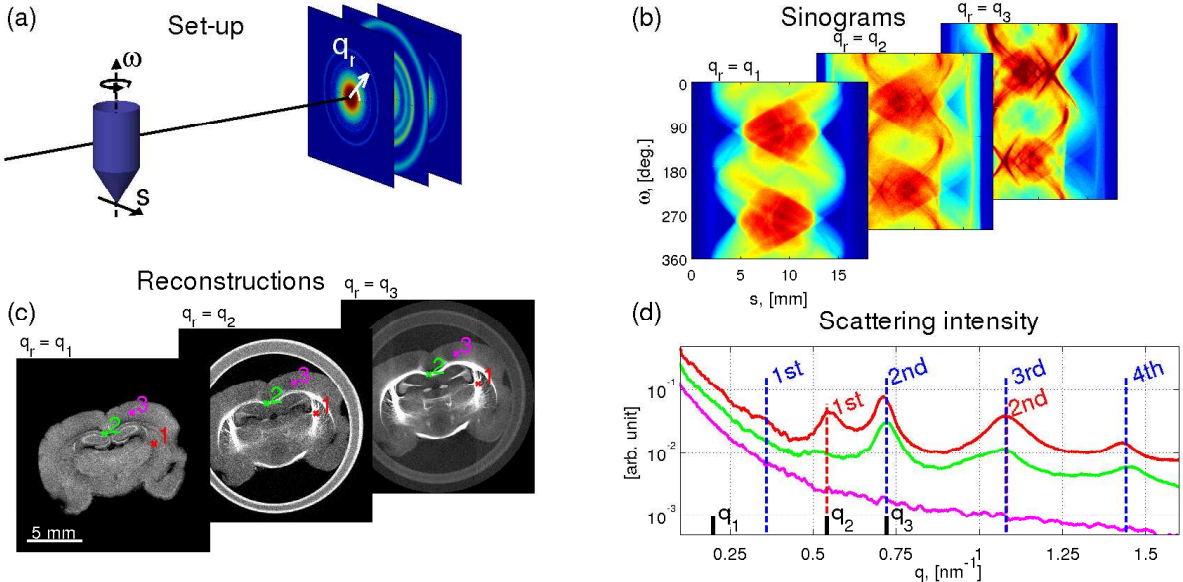


FIG. 1: Experimental set-up and principle of SAXS-CT. (a) Using a pencil-beam(1^{st} generation CT geometry), scattering patterns are collected by translating the sample through the beam, s , at different orientations, ω . (b) The scattering patterns are azimuthally averaged and for each value of q_r sinograms are generated. (c) These sinograms are used to reconstruct the differential scattering cross section for the associated value of q_r . (d) When the reconstructions are made it is then possible to extract complete scattering curves for all voxels in the sample, by combining the information from the slices reconstructed for each value of q_r . The curves shown here correspond to the points marked in (c). Bragg peak series from myelin sheaths (blue) and cytoskeletal neurofilaments (red) are marked in (d).

the myelin sheaths. The peaks provide information about the molecular organization of the myelin. In point 1 (Fig. 1c,d) a second Bragg peak series is present. This second series is probably associated with the cytoskeleton neurofilaments [9]. In the following we will further analyze the two Bragg series. Two different coronal slices from the brain are presented in Fig. 2. In the first row maps of the integrated scattering cross section for $q_r = [0.05-1.4] \text{ nm}^{-1}$ are shown. The scattering cross section is a term used in x-ray scattering which describes the samples ability to scatter x-rays in a specific direction. The panels clearly show the overall anatomy of the imaged brain slices and are displayed to provide anatomical references to which we can relate the myelin maps.

Knowing the full scattering curve in each voxel, we fitted the intensity, position and width of the second-order Bragg peak associated with the myelin series. The peak was fitted with a gaussian profile with a linear background. The intensity of the peak is proportional to the amount of myelin in each voxel, which represents a volume of $25 \times 25 \times 25 \mu\text{m}^3$. The middle row of Fig. 2 displays the myelin concentration. In Fig. 2c the myelin is mainly associated with the corpus callosum(cc), external capsule(ec), the anterior commisure(ac), as well as the fornix(f). A somewhat lower concentration of myelin is associated with the striatum(st) and the optic chiasm(ox). In Fig. 2d we again note the myelin associated with the corpus callosum and the external capsule. The

myelin in the internal capsule(ic), as well as some of the connections between the internal and external capsule are also visible. Finally we note the myelin in the fimbria(fi) of the hippocampus as well as in the habenula(Hb) and the optical tract(opt). These maps of the myelin concentration correlate well with the location and concentration of myelin known from anatomy and histology.

The method of SAXS-CT is highly selective. The myelin sheaths are the only tissue in the brain with a repetition unit of $\sim 17.6 \text{ nm}$, we are thus certain to get information only about the myelin sheaths, when analyzing the associated Bragg series. Other methods such as e.g. histology can also selectively image myelin. With histology it is possible to stain for and image specific molecules, such as myelin basic protein (MBP). It is however associated with great difficulty to quantify the concentration of these proteins. Demyelination and hence the concentration of myelin is important for several of the diseases mentioned above. With SAXS-CT it is possible to quantify exactly what the concentration of myelin is in a specific volume and thus use it to study partial demyelination.

Mapping the myelin sheath period

The local concentration of myelin is not the only information we obtain from the fits. We also determine

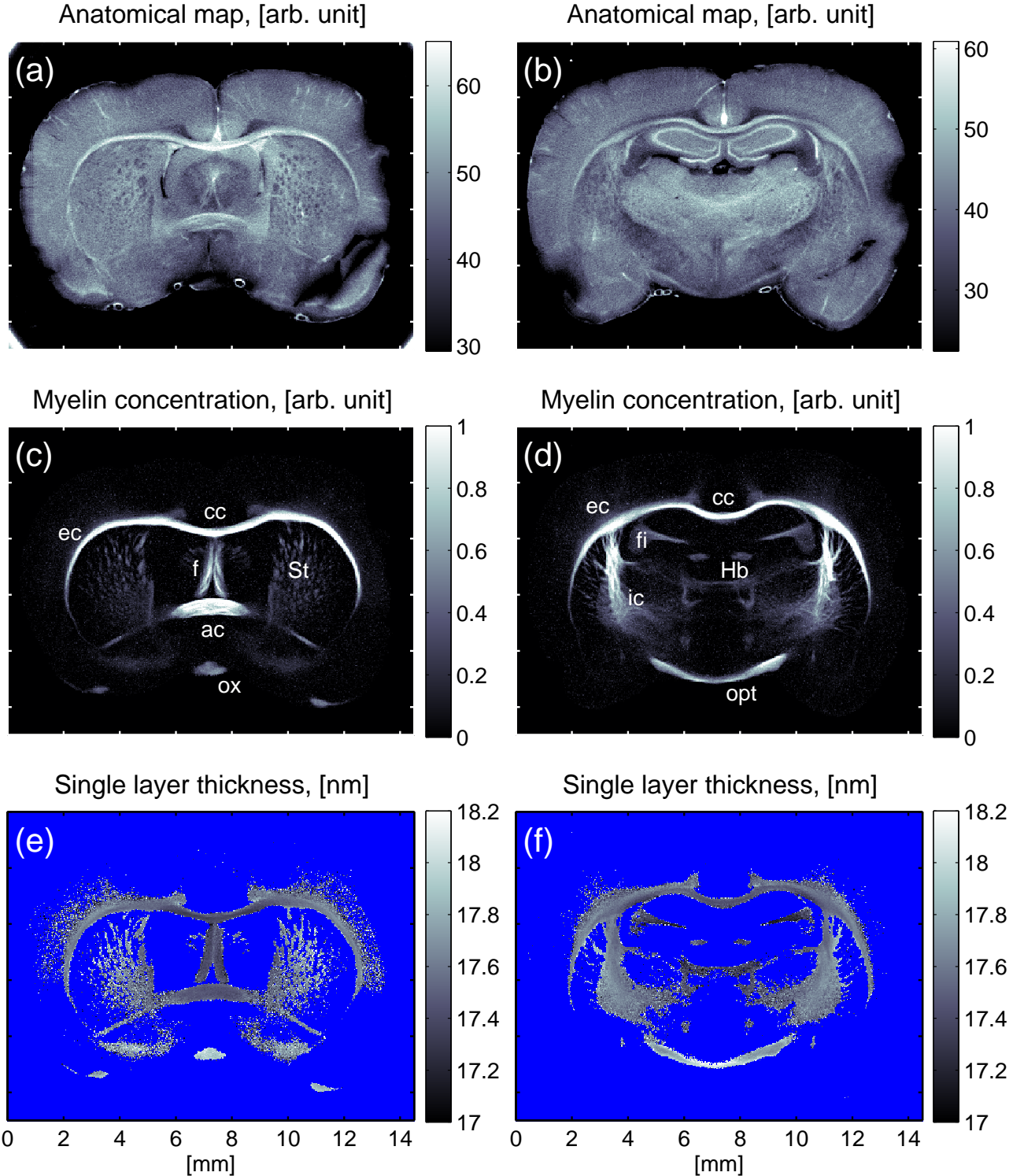


FIG. 2: **Myelin mapping.** Two different brain slices are shown here. **(a,b)** The integrated scattering cross section for $q_r = [0.05-1.4] \text{ nm}^{-1}$ provides anatomical maps of the brain slices to which we can relate the myelin maps. **(c,d)** Maps of the concentration of myelin in each voxel determined from the intensity of the 2nd-order Bragg peaks. **(e,f)** Maps of the periodicity of the lamellar structure of the myelin sheaths determined from the Bragg peaks positions. The blue color refers to areas with no or very low myelin content. A selection of structural labels are shown in column 2.

the positions of the Bragg peaks, which are given by the period of the myelin sheaths. The period is equivalent to the thickness of a single myelin layer. Differences in period can occur both naturally and as a result of disease or treatment [6, 10]. In Fig. 2e,f the variations of the period is mapped. This molecular parameters can be used to distinguish different forms of myelin in the brain. In row 1 we note that the myelin in the optic chiasms in the bottom has a period that is significantly larger than the myelin in the corpus callosum and external capsule. In row 2 we see the difference corpus callosum and the optical tract.

Mapping the thickness of the myelin sheath

As we determine the position of the peak we also determine the width of the peak. The width is mainly controlled by the total thickness of the myelin sheaths and the periodicity variation within a single voxel. If several peaks in a series are fitted it is possible to deconvolve the two effects. The 3rd-order peak of myelin overlaps with a peak from the neurofilament series and the 4th-order peak is in most cases not strong enough to extract useable information from. With the present data a voxel by voxel deconvolution is thus not possible. This is however not an intrinsic limitation of the method.

Since the total thickness and the periodicity variation both contribute positively to the width of the peak we can determine a lower limit to the total thickness of the myelin sheaths. These results are shown in Fig. 3a,b. From three points chosen in the corpus callosum and external capsule where the 4th-order peak is significant we determined that the actual thickness is 30-50% larger than the lower limit shown in the Fig. 3.

With the knowledge of the total thickness of the myelin sheaths it is possible to combine this with the single layer thickness to make a map of the average number myelin layers in a sheath.

The average number of layers in the myelin sheaths is very important when trying to understand how demyelination takes place. Maps such as those shown in Fig. 3a,b would be able to tell whether demyelination take place with a part of the axons loosing all of their myelin or all of the axons loosing a part of their myelin. Deconvolution of the two signals would also provide the periodicity variation which has also been linked to treatment and diseases [10].

Complementary molecular information

All of the above results were deduced from the myelin Bragg peak series. With SAXS-CT a range of complementary information is automatically included. One type of information is the information available from

the second series of Bragg peaks. The series probably arises from the cytoskeletal neurofilaments. The neurofilaments are a part of the axons that the myelin sheaths are wrapped around. Correlation between neurofilament changes and neurodegenerative diseases has demonstrated[18]. Shown in Fig. 4a,b are maps of the concentration of neurofilaments determined from the intensity of the 1st-order peak. We note that the location of the neurofilaments is closely correlated to the location of the myelin, as expected. However there seem to be uncorrelated variations in the concentration of the two when comparing Fig. 2b,e and Fig. 4a,b. This is also seen in Fig. 1c,d where the scattering curve from point 1 in the internal capsule shows a distinct Bragg peak from the neurofilaments while the scattering curve from point 2 in the corpus callosum shows no Bragg peak from the neurofilaments, while having similar amounts of myelin. All of the analysis made on the Bragg peak series of myelin presented above can also be made on the peaks of the neurofilaments. A full discussion of the correlations between variations of molecular parameters and different pathologies are left for future studies.

DISCUSSION

We have in this paper demonstrated how SAXS-CT non-invasively can be used to map molecular information about the myelin sheaths in a rat brain. The molecular parameters of myelin are important for the understanding of the development of widespread neurodegenerative diseases such as cerebral malaria, multiple sclerosis and Alzheimer's disease. Using SAXS-CT we mapped the concentration and periodicity of the myelin sheaths. We also demonstrated how the method can be used to determine the local average thickness of the myelin sheaths as well as the local average periodicity variation. Finally we demonstrated that the method also provides molecular information about the cytoskeletal neurofilaments of the axons and how this information correlates with the myelin information. SAXS-CT thus provides a new and valuable tool to study myelin and improve the understanding of a number of neurodegenerative diseases.

METHODS

Sample preparation

The rat brain used for this study, was a tumor inoculated brain. However the rat was euthanized on day 7, so we would expect only a very small tumor. No tumor was imaged, and the tumor type does not to our knowledge interfere with the myelin sheaths. The inoculation and preparation of the brain took place as follows. The 9L gliosarcoma cell line was originally established by

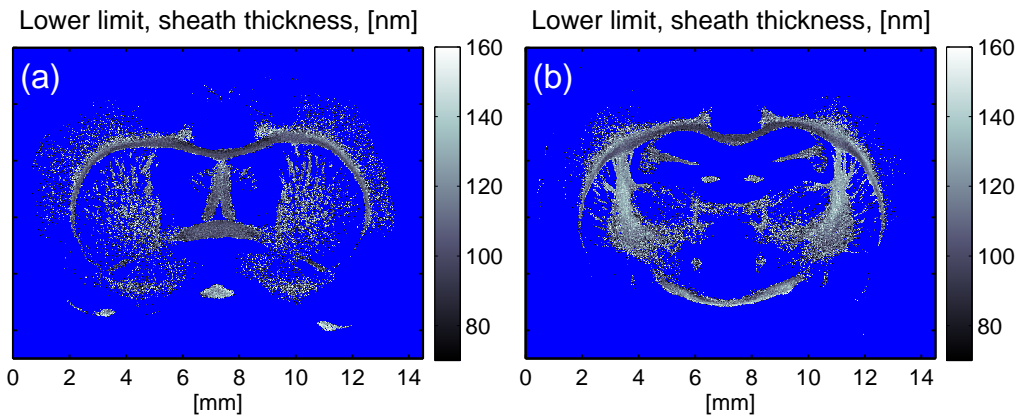


FIG. 3: Thickness of myelin sheaths. (a,b) Maps of the lower boundary of the thickness of the myelin sheaths as determined from the width of the Bragg peaks. The actual thickness has in some cases been determined to be 30-50% greater than the lower boundary. (a) and (b) corresponds to the two slices shown in Fig. 2c,d.

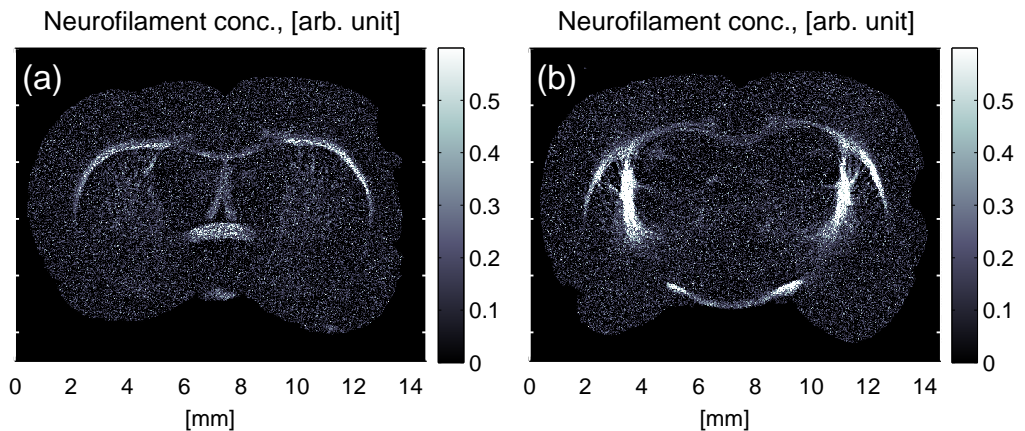


FIG. 4: Density of cytoskeletal neurofilaments. (a,b) Maps of the density of cytoskeletal neurofilaments determined from the first-order Bragg peak. (a) and (b) corresponds to the two slices shown in row 1 and 2 of Fig. 2. Note that the neurofilament location is closely correlated to the location of myelin, though there are some uncorrelated variations in density, when comparing to Fig. 2c,d.

Benda et al.[19]. The 9L gliosarcoma cells were implanted in the brain of a male Fisher 344 rat (Charles River, France) as previously described[20]. Cells were grown with complete medium at 37C. The male Fisher 344 rat (180-280 g, Charles River, L' Arbreles, France) was anesthetized with 4% isoflurane inhalation followed by an intraperitoneal injection of xylazine/ketamine (64.5/5.4 mg/kg). It was placed on a stereotactic head holder (model 900, David Kopf Instruments, Tujunga, USA). At D0, 104 cells were suspended into 1 μ l DMEM with antibiotics (1%) then injected using a 1 μ l Hamilton syringe through a burr hole in the right caudate nucleus (9 mm anterior to the ear-bars i.e. at bregma site, 3.5 mm lateral to the midline, 5.5 mm depth from the skull)[21]. The rat was euthanized at Day 7. The brain was then sampled and fixed in 10% formalin 10 days minimum prior to any experiment. All operative procedures related to animal

care strictly conformed to the Guidelines of the French Government with licenses 380825 and B3818510002 and they were reviewed by the Internal Evaluation Committee for Animal Welfare and Rights of the ESRF.

Data collection

The SAXS-CT measurements were performed at the cSAXS beamline [22] of the Swiss Light Source. The following parameters were used for the data acquisition: X-ray energy 18.58 keV, focus spot size 25x25 μm^2 , sample to detector distance 7117 mm. The sample was imaged from 541 equidistant angles over 360 degrees. 720 scattering patterns were collected for each angle using a step size of 25 μm . The exposure time was 150 ms for scattering measurements and 10 ms for absorption measurements. The total acquisition time for the scattering

and absorption measurements for one tomographic slice approximately 24 hours. A total of 390'061 scattering patterns were collected per slice.

Data processing

The 2D scattering patterns were azimuthally averaged using a customized in-house developed code. After correcting for absorption reconstructions were made for 1152 different values of momentum transfer using a standard filtered backprojection algorithm.

ACKNOWLEDGEMENTS

We gratefully acknowledge Keld Theodor and Xavier Donath for technical support, and Anders Skjolding and Casper Hempel for fruitful discussions. F.P. and M.B. acknowledges support through the DFG excellence cluster 'Munich-Centre for Advanced Photonics'. T.H.J. acknowledges support from the Danish Natural Science Research Council through DANSCATT. The experiment was performed at the cSAXS beamline of the Swiss Light Source, Paul Scherrer Institut, Villigen, Switzerland.

-
- [1] Janota, I. & Doshi, I. Cerebral malaria in the United Kingdom. *J. Clin. Pathol.* **32**, 769-772 (1979).
 - [2] Prineas, J.W. The neuropathology of multiple sclerosis. In: Koetsier J.C., ed. *Handbook of clinical neurology. Demyelinating disease, vol 3.* (Amsterdam, Elsevier, 1985) 213257.
 - [3] Peterson, J.W., Bö, L., Mörk, S., Chang, A.,& Trapp, B.D. Transected Neurites, Apoptotic Neurons, and Reduced Inflammation in Cortical Multiple Sclerosis Lesions. *Ann. Neurol.* **50**, 389-400 (2001).
 - [4] Trapp, B.D. et al. Axonal transection in the lesions of multiple sclerosis, *N. Eng. J. Med.* **338**, 278-285 (1998).
 - [5] Bartzokis G. Quadratic trajectories of brain myelin content: unifying construct for neuropsychiatric disorders. *Neurobiol. Aging* **25**, 49-62 (2004).
 - [6] Karlsson, U. Comparison of the Myelin Period of Peripheral and Central Origin by Electron Microscopy. *J. Ultra. Res.* **15**, 451-468 (1966).
 - [7] Sjöstrand, F. S., The lamellated structure of the nerve myelin sheath as revealed by high-resolution electron microscopy. *Experientia* **9**, 68-69 (1953).
 - [8] Hui, E.S., Cheung, M.M., Chan, K.,& Wu, E.X. B-value dependence of DTI quantitation and sensitivity in detecting neural tissue changes. *Neuroimage* **49**, 2366-2374 (2010).
 - [9] De Felici, M. et al. Structural characterization of the human cerebral myelin sheath by small angle x-ray scattering. *Phys. Med. Biol.* **53**, 5675-5688 (2008).
 - [10] Marta, C. B. et al. Morphological changes of myelin sheaths in rats intracranially injected with apotransferrin. *Neurochem. Res.* **28**, 101-110 (2003).
 - [11] Harding, G., Kosanetzky, J., & Neitzel, U. Elastic Scatter computed tomography. *Phys. Med. Biol.* **30**, 183-186 (1985).
 - [12] Harding, G., Kosanetzky, J., & Neitzel, U. X-ray diffraction computed tomography. *Med. Phys.* **14**, 515-525 (1987).
 - [13] Harding, G., & Kosanetzky, J. Scattered x-ray beam non-destructive testing. *Nucl. Inst. and methods in Physics research A* **A280**, 517-528 (1989).
 - [14] Kleuker, U., Suortti, P., Weyrich, W., & Spanne, P. Feasibility study of x-ray diffraction computed tomography for medical imaging. *Phys. Med. Biol.* **43**, 2911-2923 (1998).
 - [15] Schroer, C. G. et al. Mapping the local nanostructure inside a specimen by tomographic small-angle x-ray scattering. *Appl. Phys. Lett.* **88**, 164102 (2006).
 - [16] Stock, S. R., de Carlo, F., & Almer, J. D. High energy X-ray scattering tomography applied to bone. *J. Struct. Biol.* **161**, 144-150 (2008).
 - [17] Kak, A. C., & Slaney, M. *Principles of Computerized Tomographic Imaging* (IEEE Press, New York, 1988).
 - [18] Liu, Q. et al. Neurofilament proteins in neurodegenerative diseases. *Cell. Mol. Life Sci.* **61**, 3057-3075 (2004).
 - [19] Benda, P., Someda, K., Messer, J., & Sweet W. H. Morphological and immunochemical studies of rat glial tumors and clonal strains propagated in culture. *J. Neurosurg.* **34**, 310-23 (1971).
 - [20] Regnard, P. et al. Irradiation of intracerebral 9L gliosarcoma by a single array of microplanar x-ray beams from a synchrotron: balance between curing and sparing. *Phys. Med. Biol.* **bf 53**, 4, 861-78 (2008).
 - [21] Paxinos, G. & Watson, C. eds. *The rat brain in stereotaxic coordinates* (New York: Academic Press, 1986).
 - [22] Bunk, O. et al. Multimodal x-ray scatter imaging. *New Jour. of Phys.* **11**, 123016 (2009).